Exploring the local differences of M1-type mixed oxides by *quasi in-situ* (S)TEM

vorgelegt von

Master of Science

Liudmyla Masliuk

geb. in Kiev (Ukraine)

Von der Fakultät II – Mathematik und Naturwissenschaften

der Technischen Universität Berlin

Zur Erlangung des akademischen Grades

Doktor der Naturwissenschaften

Dr. rer. nat.

genehmigte Dissertation

Promotionsausschuss:

Vorsitzender: Prof. Dr. Martin Lerch

Gutachter: Prof. Dr. Robert Schlögl

Gutachter: Prof. Dr. Malte Behrens

Gutachter: Prof. Dr. Michael Lehmann

Tag der wissenschaftlichen Aussprache: 19.07.2018

Berlin 2018

Let's call it an accidental feature.

(Larry Wall)

Acknowledgements

holder and Dr. Marc Heggen from Forschungszentrum Jülich for discussions regarding most suitable tiling.

Finally, I would like to thank to my family for motivation, support, understanding and, especially, their patience.

Abstract

Heterogeneous catalysts have proven to increase the efficiency of many chemical reactions of industrial importance. The interaction between catalyst and reactant decreases energy barriers of the target reactions but it can also induce reversible or irreversible changes of the catalyst surface. Detailed knowledge of the underlying mechanisms of these changes can provide further pathways for an optimization of the performance of catalysts. The identical location imaging (ILI) concept, introduced earlier, enables to detect the structure responses of target samples to relevant catalytic conditions. ILI includes detailed investigations of the pristine structure of the target samples, exposure of the samples to relevant reaction conditions, and examination of the samples after the reaction. In the present study ILI using a specially designed TEM grid reactor was carried out for two model catalysts, $(Mo,V)O_x$ and $(Mo,V,Te,Nb)O_x$ with M1-type crystallographic structure, in order to investigate the interplay between structure response and catalytic properties.

In this study scanning transmission electron microscopy (STEM) measurements were performed to study local structure variations of pristine $(Mo,V)O_x$. Here the concept of tiling was applied to separate structural defects from the structure of the ideal orthorhombic bulk. In addition to the previously reported intergrown phases, several different kinds of extended defects and local structural motifs, which can be arranged further into extended defect structures, were detected and classified. Moreover, STEM combined with electron energy loss spectroscopy (EELS) was carried out to characterize variations of the local metal content and their correlation with local structure details.

Further, a *quasi in-situ* TEM grid reactor was developed in order to detect reaction induced structural changes at the nanoscale. Preliminary test experiments, such as thermal decomposition of lead carbonate and reduction of $Cu/ZnO/Al_2O_3$, ensured a precise temperature calibration and the possibility of a secure sample transfer between the TEM grid reactor and the microscope. Further, changes of the structures at the nanoscale and catalytic conversion were detected for the CO oxidation reaction over a Pt foil and Pt nanoparticles.

Comparative *quasi in-situ* and *in-situ* STEM studies were conducted to investigate structure responses of orthorhombic $(Mo,V)O_x$ samples to various conditions. Different responses of the surface, near-surface, and defect structure were observed and found to depend

on redox properties of the atmosphere and on pressure (N_2 or conditions relevant for the oxidative dehydrogenation of ethane; high vacuum). In addition, comparative studies of the structure responses of orthorhombic $(Mo,V)O_x$ and M1-type $(Mo,V,Te,Nb)O_x$ to the oxidative dehydrogenation of ethane reaction were performed under relevant conversion conditions. The differences between activation temperatures and observed responses were further linked to differences between the pristine structures of orthorhombic $(Mo,V)O_x$ and M1-type $(Mo,V,Te,Nb)O_x$.

In summary, the present thesis demonstrates the potential of identical location imaging to investigate structure changes at the nanoscale where orthorhombic $(Mo,V)O_x$ and M1-type $(Mo,V,Te,Nb)O_x$ samples serve as examples. Further, the results evidence correlations between the activity of these catalysts and the adaptabilities of their structures.

Kurzfassung

Heterogene Katalysatoren haben bewiesen, dass sie die Effizienz bei vielen chemischen Reaktionen von kommerzieller Bedeutung erheblich steigern können. Dabei werden Energiebarrieren der Reaktionen durch die Wechselwirkung zwischen dem Katalysator und den Reaktanten zwar gesenkt, jedoch kann die Wechselwirkung auch zu reversiblen oder irreversiblen Strukturänderungen der Katalysatoroberfläche führen. Eine detaillierte Kenntnis der grundlegenden Mechanismen dieser Strukturänderungen kann zusätzliche Information zur Optimierung der Leistung von Katalysatoren liefern. Das bereits eingeführte Konzept der Abbildung identischer Bereiche ("identical location imaging", ILI) erlaubt die Beobachtung von Strukturänderungen der Katalysatorprobe unter entsprechenden katalytischen Bedingungen. Dabei beinhaltet ILI genaue Untersuchungen der ursprünglichen Probenstruktur, die Durchführung entsprechender chemischer Reaktionen an der Probe sowie die Untersuchung der Probe nach der Reaktion. In der vorliegenden Arbeit wurde ILI mit einem speziell konstruierten TEM-Grid-Reaktor durchgeführt, um den Zusammenhang zwischen Strukturänderung und katalytischen Eigenschaften bei zwei Modellkatalysatoren, $(Mo,V)O_x$ und $(Mo,V,Te,Nb)O_x$ mit M1-artiger Kristallstruktur zu untersuchen.

In diesen Untersuchungen wurde Transmissionselektronen-Mikroskopie ("transmission electron microscopy", STEM) zur Analyse lokaler Strukturänderungen an der ursprünglichen $(Mo,V)O_x$ Probe eingesetzt. Dabei hat sich das theoretische Konzept des "Kachelns" (tiling) zur Unterscheidung zwischen Strukturdefekten und der Idealstruktur des orthorhombischen Volumens bewährt. Zusätzlich zu bereits bekannten Verwachsungsphasen wurden weitere ausgedehnte Defekte sowie lokale Strukturmotive, die sich zu größeren Defektstrukturen zusammenfügen, beobachtet und klassifiziert. Desweiteren ließ sich STEM mit Elektronenenergieverlust-Spektroskopie ("energy loss spectroscopy", EELS) kombinieren, um Änderungen im lokalen Metallgehalt der Proben und deren lokaler Struktur aufzuzeigen.

Zusätzlich kam ein neu entwickelter *quasi-in-situ*-TEM-Grid-Reaktor zum Einsatz, der die Beobachtung von reaktionsbedingten Strukturänderungen im Nanoskalenbereich ermöglicht. Erste Experimente zur thermischen Zersetzung von Bleikarbonat sowie der Reduktion von $Cu/ZnO/Al_2O_3$-Proben lieferten eine genaue Temperaturkalibrierung und zeigten die Möglichkeit eines sicheren Probentransfers zwischen TEM-Grid-Reaktor und Mikroskop. Außerdem wurden

bei der CO-Oxidation an Platin-Folien und Nanoteilchen Strukturänderungen im Nanobereich bei der katalytischen Konversion beobachtet.

Vergleichende *quasi-in-situ-* und *in-situ*-STEM-Messungen lieferten weiterhin Aussagen über Struktureinflüsse auf orthorhombische $(Mo,V)O_x$-Proben bei unterschiedlichen Reaktionsbedingungen. Die Ergebnisse zeigen verschiedene Einflüsse auf die Oberfläche, die oberflächennahen Bereiche und entsprechende Defektstrukturen, die von Redoxeigenschaften der Gasatmosphäre und dem Druck (N_2 oder Bedingungen bei der oxidativen Dehydrierung von Ethan; Hochvakuum) abhängen. Schließlich wurden vergleichende Untersuchungen zum Einfluss der oxidativen Dehydrierung von Ethan auf die Struktur von orthorhombischen $(Mo,V)O_x$- und M1-artigen $(Mo,V,Te,Nb)O_x$-Proben unter verschiedenen Konversionsbedingungen durchgeführt. Der unterschiedliche Zusammenhang zwischen Aktivierungstemperatur und Struktur konnte auf Unterschiede zwischen den ursprünglichen Kristallstrukturen der orthorhombischen $(Mo,V)O_x$-und M1-artigen $(Mo,V,Te,Nb)O_x$-Proben zurückgeführt werden.

Insgesamt zeigt die vorliegende Arbeit die Leistungsfähigkeit der Methode der Abbildung identischer Bereiche (ILI) bei der Untersuchung von Struktureinflüssen im Nanobereich, wobei orthorhombische $(Mo,V)O_x$- und M1-artige $(Mo,V,Te,Nb)O_x$-Proben als Beispiele dienen. Darüber hinaus zeigen die Ergebnisse den Zusammenhang zwischen der Aktivität dieser Katalysatoren und der Veränderbarkeit ihrer Strukturen.

Table of contents

1 Introduction

Heterogeneous catalysts can significantly increase the economical outcome of the industrial processes via decreasing the energy demand and improving the selectivity.[1-2], Common heterogeneous catalyst systems have highly sophisticated structures, which make further tailoring of the catalyst structure and composition towards the desired lifetime enhancement, activity and selectivity difficult. Moreover, the possibility of a catalyst to dynamically response to the reaction media can cause significant structural differences between the equilibrated catalyst that can be revealed by common *ex-situ* investigations and its reactive intermediate states, which involves the interaction of the catalyst with reactants, intermediates and/or products.[3-4] This interaction can induce the formation of thermodynamically more stable surface and can be influenced by the presence of defects.[5] Therefore, a catalyst can be considered as a living system that is composed of a dynamic surface layer stabilized by the bulk structure, which is influenced by the defect chemistry and forms the real structure of a catalyst.

Surface dynamics during a catalytic reaction have, for instance, already been reported for complex mixed molybdenum and vanadium based oxides.[6-7] In addition, this family of oxides represents suitable candidates for the investigation of the real structure and their structure responses to different atmospheres as various oxides with different composition can crystallize in the same orthorhombic structure, which is often referred to as M1-type.[8-9] Moreover, these oxides can be active and selective in the oxidative of small alkanes to functionalized hydrocarbons.[9-11] However, further lifetime and activity improvements require a detailed understanding of their real and working structure.

This thesis provides detailed structural insights of the real structure and composition of complex molybdenum and vanadium based mixed oxides and corresponding structural changes at the nanoscale, which are induced by the reaction media. Chapter 2 provides a catalogue of structural variations, which can occur in pristine $(Mo,V)O_x$ and is accompanied by a quantitative defect evaluation. Chapter 3 demonstrates the real composition of pristine $(Mo,V)O_x$ and reveals compositional details of the surface and extended defects. It further provides important correlations between structure and composition. Chapter 4 describes the concept of the *quasi in-situ* TEM reactor, which was used for identical location imaging and shows that it is possible to conduct catalytic experiments on a TEM grid under relevant conditions. Chapter 5 depicts the

influence of different atmospheres on orthorhombic $(Mo,V)O_x$ which was investigated by *quasi-in-situ* TEM and highlights the importance of the redox properties of the reaction media. Additionally the chapter provides *in-situ* heating experiment results, which show the influence of the pressure gap on the structure response. Chapter 6 provides comparative studies of the pristine orthorhombic $(Mo,V)O_x$ and M1-type $(Mo,V,Te,Nb)O_x$ as well as their structural changes induced by the oxidative dehydrogenation of ethane (ODE) investigated under relevant conditions. Chapter 7 presents the final conclusions with respect to the correlation of activity and stability.

1.1 Transmission electron microscopy

Transmission electron microscopy (TEM) is a powerful tool for the structural investigations down to the atomic level and to the lightest elements.[12-15] Various combinations of the analytical techniques, which are available in a modern TEM, provide outstanding performance for a thorough characterization of heterogeneous catalysts. For instance, these techniques include bright field and dark field imaging, which are based on the different origins of the main contrast and can, therefore, be sensitive to the different elements, energy X-ray dispersion (EDX) spectroscopy and electron energy loss spectroscopy (EELS), which are sensitive to the composition and can even provide information of the electronic states, and electron diffraction, which allows to determine the crystal structure.[16-20]

Moreover, two *in-situ* imaging techniques, environmental TEM (ETEM) and microelectromechanical systems (MEMS) were developed in order to track reaction induced changes under operando conditions.[21-22] In the ETEM approach the gas is directly incorporated into the octagon of the microscope. Thus, conventional TEM heating holder can be used, but a special microscope design is required, which relies on inserting differential pumping apertures at the pole pieces. The MEMS-based cell is a reaction chamber with two electron-transparent windows, made from Si_3N_x. The holder is further equipped with a gas inlet and outlet (usually with pressure controls) and a heating element.[21, 23-24] Unfortunately, both methods have some limitations. The operating pressure for ETEM is in the 1-10 mbar range, because otherwise multiple electron scattering from the gas in the system cause too much noise or the gas can damage the parts of the microscope, which require high vacuum in the operation mode, i.e. the electron source. If the reactants are, for instance, corrosive they cause additional limitations of

pressure, feed gas composition and flow.[25] The benefit of this method is a resolution of about 0.1 nm.[26] Compared to ETEM the MEMS-based calls can be operated at atmospheric or even higher pressure.[21, 27] However, light elements and detailed atomic resolution images, which would allow for the desired interpretative depth, cannot be obtained in this system because scattering from the windows and/or reaction gas will become too significant.

Convenient *ex-situ* imaging includes the comparison of two batches of the same catalyst imaged before and after the reaction. But the variation of the reaction conditions along the reactor can cause significant differences between probes, which were taken from different reactor parts.[28]

The disadvantages of the *ex-situ* and *in-situ* TEM can be balanced by the *quasi in-situ* TEM approach. This approach is based on identical location imaging (ILI) of the same catalyst location before and after reaction.[29] Currently there are several approaches, which are designed for different reaction conditions:

      a. The sample can be initially mounted on a TEM holder, which makes it easier to observe the same position.[30]

      b. The sample can be transferred between the reactor and the microscope without exposure to ambient atmosphere.[31-32]

Between all the *quasi in-situ* systems it is worse mention single crystal flow reactor that is designed to allow secure transfer to a TEM in any moment by a transfer system. Thus, the catalyst surface can be monitored at each step of the reaction.[33]

The *quasi in-situ* TEM reactor setup, which is applied in the present study is described in chapter 4 and provides ambient pressure conditions and allows for the detection of the catalytic conversion.

1.2 Target catalysts

Mixed metal oxides are promising candidates for a variety of catalytic reactions with high activity and selectivity.[34] The complex structure of these oxides provides different active centers on the same catalyst, which enables the same catalyst to stabilize a set of different reactions and/or several steps in multistep reactions.[35] In addition, the activity of a catalyst is influenced by the crystallographic structure – different phases or phase mixture can show different catalytic

behavior.[36] Even the same atoms, that occupy different crystallographic sites within the same phase, might possess different valence states and therefore show different catalytic properties.[8]

Molybdenum and vanadium based oxides are suitable targets to correlate the atomic structure of the catalyst and its activity because several oxides with different composition can crystallize in an orthorhombic or so-called "M1" phase (ICSD 55097, Figure 1-1).[37] This structure is composed of $\{(A)Mo_5\}$ pentagonal building blocks, where A=Mo,Nb, which are connected by linker sites with mixed Mo and V occupation, so that hexagonal and heptagonal channels are created. Te can be located inside the hexagonal channels and with lower probability inside the heptagonal channels.[8] In case of Te absence the hexagonal channels can be partially occupied by V (around 5% and 20%).[6, 38] Additionally, mixed molybdenum and vanadium based oxides can exist in different phases or as phases mixtures and/or exhibit structural defects. $(Mo,V)O_x$ can exist as orthorhombic, trigonal, tetragonal or amorphous phase.[39] The orthorhombic and trigonal phases are reported to be efficient catalysts, but the orthorhombic one exhibits higher activity for the ODE reaction, while both phases show high performance for partial oxidation of acrolein to acetic acid.[39-40] $(Mo,V,Te,Nb)O_x$ can also crystalize in the M2 phase (ISCD 55098).[41-42] Moreover, orthorhombic $(Mo,V)O_x$ and M1-type $(Mo,V,Te,Nb)O_x$ can exhibit trigonal or amorphous intergrown phases and other set of defects, which are further described in chapters 2 and 6.[43-44]
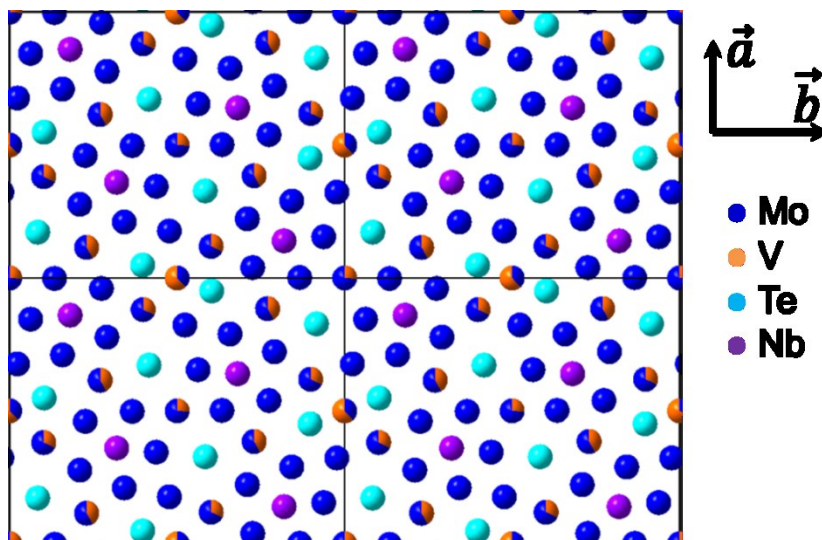

Figure 1-1 The M1 structure (ISCD 55097) viewed along the crystallographic c-direction, mixed colors: mixed site occupancies.

Molybdenum and vanadium based oxides were proposed to be active in the oxidation of ethane to ethylene in 1978.[45] Further studies enhanced the potential application range of these oxides family to several partial oxidation or ammoxidation reactions of light alkanes and are summarized in Table 1-1.

Table 1-1: partial oxidation reaction results over selected catalysts[*]

Target	Catalyst	Products reported	References
Ethane	$(Mo,V)O_x$	Ethylene, acetic acid, CO_x	[39, 46]
	$(Mo,V,Te,Nb)O_x$	Ethylene, CO_x	[47-49]
Propane	$(Mo,V)O_x$	Acrylic acid, propene, acetic acid, CO_x	[9, 37]
	$(Mo,V,Te,Nb)O_x$	Acrylic acid, propene, acetic acid, acrolein, acetone, CO_x	[35, 47, 50-57]
Propene	$(Mo,V)O_x$	Acrylic acid, acetic acid, acetone, CO_x	[9]
	$(Mo,V,Te,Nb)O_x$	Acrylic acid, acetaldehyde, acetic acid, acrolein, acetone, CO_x	[57]
N-butane	$(Mo,V,Te,Nb)O_x$	Maleic anhydride, acrylic acid, acetic acid, CO_x	[47]

*Products are listed even if they were detected only in trace amounts and/or specific conditions.

As demonstrated in the Table 1-1 the reaction products can differ for the two catalysts. For instance, it is reported that both $(Mo,V)O_x$ and $(Mo,V, Te,Nb)O_x$ oxides are efficient catalysts for the selective oxidation of propane, but $(Mo,V,Te,Nb)O_x$ is highly selective to acrylic acid while further oxidation to CO_x happen over $(Mo,V)O_x$.[9] Thus, these catalysts can show similar as well as different catalytic behavior during the same reaction, which provides the main hypothesis of this project: different M1 phases show different structure responses to the same applied chemical potential. The investigation of structural differences induced by the reaction conditions can clarify this hypothesis. In this thesis, the oxidative dehydrogenation of ethane (ODE) was chosen as the test reaction.

1.3 ODE

ODE can potentially reduce the costs for the production of ethylene by 20% compared to the currently applied steam cracking process.[58] However, additional to the formation of ethylene, further oxidation to acetic acid and CO_x can also occur. The oxidation process over $(Mo,V,Te,Nb)O_x$ is summarized in the kinetic model presented in Figure 1-2.[59]
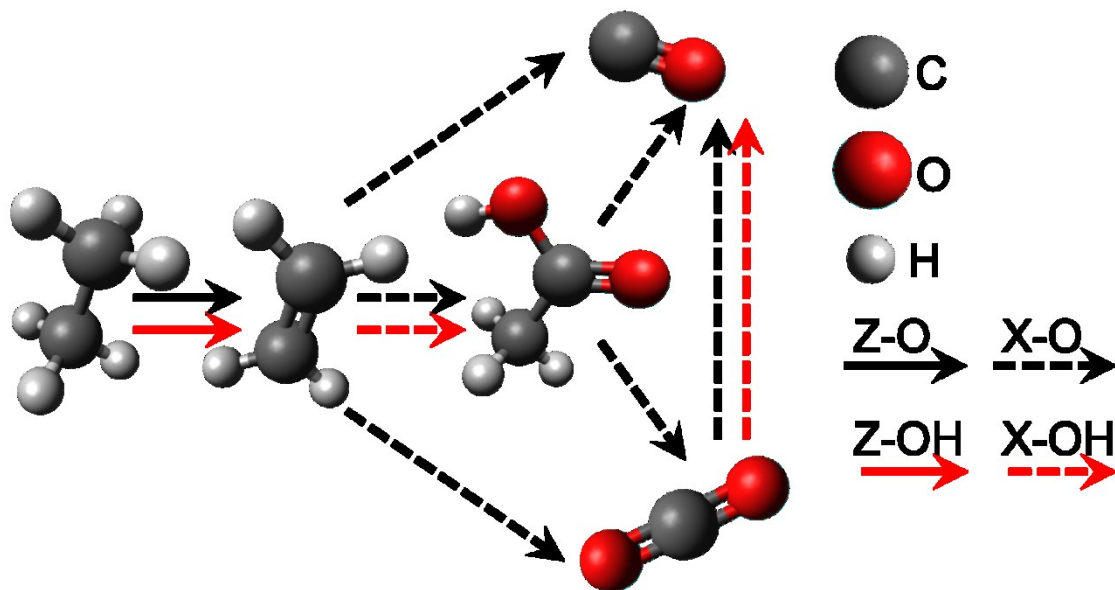
Figure 1-2: ODE reaction scheme reproduced from [59]. X and Z: two different sites; -O and –OH: oxidize and hydroxyl type centers respectively.

Despite the variety of different ODE studies, the information about structural changes, which were induced by the reaction conditions, is rather scarce. The available data are summarized in the Table 1-2. Unfortunately, the commonly used X-ray diffraction (XRD) is not sensitive enough to detect the local surface structure response. Reported ETEM experiments, which were carried out under vacuum conditions, might be affected by pressure-gap related effects. Meanwhile, *in-situ* X-ray photoelectron spectroscopy (XPS) suggests the possibility of surface modifications, demonstrating V enrichment under steam. [6, 51]

Table 1-2: Structural changes induced under ODE conditions

Structural investigation method	Catalyst	Pressure, bar	Feed composition(s), flow	Reaction temperature range, °C	Selectivity and conversion details	Structure response	Reference
ETEM	$(Mo,V,Te,Nb)O_x$	0.9E-3	He; $C_2H_6:O_2:He$ 3:2:5; O_2	400	N.r.[*]	Te depletion	[60]
XRD	$(Mo,V,(Bi))O_x$	~1	$C_2H_6:O_2:N_2$ 1:1:8;	240-390	Over 90% at less than 300°C, than CO_x increase, AcrA[**]<3%	No impurities detected	[61]
XRD	$(Mo,V,Te,(Nb))O_x$	~1	$C_2H_6:O_2:N_2$+ He 2:3:5	320-450	Lower conversion – higher selectivity to ethylene	MoO_3 formation in MoVTe, no changes MoVTeNb	[62]
ETEM	$(Mo,V,Te)O_x$	1E-3	$C_2H_6:O_2:N_2$ 3:6:11 $C_2H_6:O_2:$ (Ne+He) 3:2:5	350	N.r.	Te disappearance in reducing atmosphere	[7]
In-situ XRD	$(Mo,V)O_x$	~1	Air; $H_2:N_2(Ar)$ 1:19; $C_2H_6:N_2$ 1:9; $C_2H_6:O_2:N_2$ 1:1:8	300	Selectivity and conversion depend on pore size, which can be changed during the reaction as structure response to ODE	No impurities detected during reduction, but slight peak shifts and lattice parameters change; heptagonal channels size changes possible under redox treatment, but it can be reversed during ODE	[38]
XRD TEM	$(Mo,V,Te,Nb)O_x$	~1	$C_2H_6:O_2:N_2$ 9:7:84	440-550	Catalyst deactivation over 500°C	Over 500°C Te removal from M1, MoO_2 formation;	[63]

[*]N.r. – non-reported

[**]AcrA – acrylic acid

1.4 Outline of the thesis

Chapter 2 demonstrates the benefits of the concept of tiling for simplifying the structural description of orthorhombic $(Mo,V)O_x$ and further separation and classification of structural defects. The observed defects are further classified as local defects, which include triangular and linear structural motifs and can act as building blocks for larger defects arrangements, and extended defects, which include surface regions, different kinds of intergrowth and interstitial regions. The defects structures, occurrence and locations are summarized in a structural catalogue.

Chapter 3 shows compositional variations inside orthorhombic $(Mo,V)O_x$, which includes unit cell inhomogeneities related modifications and differences between the bulk, surface and grain boundaries (intergrown regions). The observed inhomogeneities are further correlated to different parts of the structure.

Chapter 4 provides the description of the *quasi in-situ* TEM grid reactor setup and shows the main benefits of the approach by using well-investigated model reactions. Temperature calibration was obtained by thermal decomposition of a lead carbonate, which has three distinct decomposition steps and can be correlated to thermogravimetric analysis (TGA). Detectable conversion is demonstrated for CO oxidation reaction over a polycrystalline Pt foil, where an oscillating behavior of CO and CO_2 signals was detected in the proton transfer reaction mass spectrometer (PTR-MS) traces. CO oxidation is also used to demonstrate nanoscale changes of Pt nanoparticles tracked via ILI. Secure sample transfer is confirmed using FHI Standard catalyst $(Cu/ZnO/Al_2O_3)$ for methanol synthesis, which exhibits Cu nanoparticles in the reductive atmosphere, that easily oxidize under ambient conditions.[64]

Chapter 5 demonstrates the differences of the structure responses of orthorhombic $(Mo,V)O_x$ at different conditions of heat treatment, which includes *in-situ* imaging under high vacuum and quasi *in-situ* imaging under N_2 atmosphere and ODE reaction, where the changes were tracked via ILI using the *quasi in-situ* TEM setup. The present study demonstrates a structural flexibility of defect-rich areas of the catalyst and suggests the migration of atoms into surface-near structural channels, which leads to structural reorganizations towards oxygen-deficient motifs as the main structure response mechanism under mild reducing conditions.

Chapter 6 provides differences between the pristine structures of orthorhombic $(Mo,V)O_x$ and M1-phase $(Mo,V,Te,Nb)O_x$ in terms of structural defects, which were observed in the two samples, and demonstrates the differences in their structure responses to relevant ODE conditions. This was further correlated to the flexibilities of the structures of the two examined catalysts.

In chapter 7 final conclusions obtained by this work are summarized.

1.5 References

1.   Heterogeneous Catalysis. In *Modern Heterogeneous Catalysis*, Wiley-VCH Verlag GmbH & Co. KGaA: 2017; pp 1-13.

2.   Boyes, E. D.; Gai, P. L., Environmental high resolution electron microscopy and applications to chemical science. *Ultramicroscopy* **1997,** *67* (1–4), 219-232.

3.   Schlögl, R., Heterogeneous Catalysis. *Angew. Chem., Int. Ed.* **2015,** *54* (11), 3465-3520.

4.   Vendelbo, S. B.; Elkjær, C. F.; Falsig, H.; Puspitasari, I.; Dona, P.; Mele, L.; Morana, B.; Nelissen, B. J.; van Rijn, R.; Creemer, J. F.; Kooyman, P. J.; Helveg, S., Visualization of oscillatory behaviour of Pt nanoparticles catalysing CO oxidation. *Nat. Mater.* **2014,** *13* (9), 884-890.

5.   Equilibrium Thermodynamics. In *Physics of Surfaces and Interfaces*, Ibach, H., Ed. Springer Berlin Heidelberg: Berlin, Heidelberg, 2006; pp 149-205.

6.   Trunschke, A.; Noack, J.; Trojanov, S.; Girgsdies, F.; Lunkenbein, T.; Pfeifer, V.; Hävecker, M.; Kube, P.; Sprung, C.; Rosowski, F.; Schlögl, R., The Impact of the Bulk Structure on Surface Dynamics of Complex Mo–V-based Oxide Catalysts. *ACS Catal.* **2017,** *7* (4), 3061-3071.

7.   Aouine, M.; Epicier, T.; Millet, J. M. M., In Situ Environmental STEM Study of the MoVTe Oxide M1 Phase Catalysts for Ethane Oxidative Dehydrogenation. *ACS Catal.* **2016,** *6* (7), 4775-4781.

8.   DeSanto, P.; Buttrey, D. J.; Grasselli, R. K.; Lugmair, C. G.; Volpe, A. F.; Toby, B. H.; Vogt, T., Structural characterization of the orthorhombic phase M1 in MoVNbTeO propane ammoxidation catalyst. *Top. Catal.* **2003,** *23* (1-4), 23-38.

9.   Ueda, W.; Vitry, D.; Katou, T., Crystalline Mo-V-O based complex oxides as selective oxidation catalysts of propane. *Catal. Today* **2005,** *99* (1-2), 43-49.

10.   Schlögl, R., Selective Oxidation: From a Still Immature Technology to the Roots of Catalysis Science. *Top. Catal.* **2016,** *59* (17), 1461-1476.

11.   Védrine, J., *Heterogeneous Partial (amm)Oxidation and Oxidative Dehydrogenation Catalysis on Mixed Metal Oxides*. 2016; Vol. 6, p 22.

12. MacLaren, I.; Ramasse, Q. M., Aberration-corrected scanning transmission electron microscopy for atomic-resolution studies of functional oxides. *International Materials Reviews* **2014,** *59* (3), 115-131.

13. Meyer, J. C.; Girit, C. O.; Crommie, M. F.; Zettl, A., Imaging and dynamics of light atoms and molecules on graphene. *Nature* **2008,** *454*, 319.

14. Lunkenbein, T.; Girgsdies, F.; Wernbacher, A.; Noack, J.; Auffermann, G.; Yasuhara, A.; Klein-Hoffmann, A.; Ueda, W.; Eichelbaum, M.; Trunschke, A.; Schlogl, R.; Willinger, M. G., Direct Imaging of Octahedral Distortion in a Complex Molybdenum Vanadium Mixed Oxide. *Angew. Chem., Int. Ed.* **2015,** *54* (23), 6828-6831.

15. Batson, P. E.; Dellby, N.; Krivanek, O. L., Sub-angstrom resolution using aberration corrected electron optics. *Nature* **2002,** *418* (6898), 617-620.

16. Tan, H.; Verbeeck, J.; Abakumov, A.; Van Tendeloo, G., Oxidation state and chemical shift investigation in transition metal oxides by EELS. *Ultramicroscopy* **2012,** *116* (Supplement C), 24-33.

17. Allen, L. J.; D'Alfonso, A. J.; Freitag, B.; Klenov, D. O., Chemical mapping at atomic resolution using energy-dispersive x-ray spectroscopy. *MRS Bulletin* **2012,** *37* (1), 47-52.

18. Pyrz, W. D.; Buttrey, D. J., Particle Size Determination Using TEM: A Discussion of Image Acquisition and Analysis for the Novice Microscopist. *Langmuir* **2008,** *24* (20), 11350-11360.

19. Williams, D. B.; Carter, C. B., Diffraction in TEM. In *Transmission Electron Microscopy: A Textbook for Materials Science*, Williams, D. B.; Carter, C. B., Eds. Springer US: Boston, MA, 2009; pp 197-209.

20. Koch, C., Conventional and Advanced Electron Transmission Microscopy. In *In-Situ Electron Microscopy*, Wiley-VCH Verlag GmbH & Co. KGaA: 2012; pp 39-69.

21. Creemer, J. F.; Helveg, S.; Hoveling, G. H.; Ullmann, S.; Molenbroek, A. M.; Sarro, P. M.; Zandbergen, H. W., Atomic-scale electron microscopy at ambient pressure. *Ultramicroscopy* **2008,** *108* (9), 993-998.

22. Ramachandramoorthy, R.; Bernal, R.; Espinosa, H. D., Pushing the envelope of in situ transmission electron microscopy. *ACS Nano* **2015,** *9* (5), 4675-85.

23.   Creemer, J. F.; Helveg, S.; Kooyman, P. J.; Molenbroek, A. M.; Zandbergen, H. W.; Sarro, P. M., A MEMS Reactor for Atomic-Scale Microscopy of Nanomaterials Under Industrially Relevant Conditions. *J Microelectromech S* **2010,** *19* (2), 254-264.

24.   Creemer, J. F.; Helveg, S.; Hoveling, G. H.; Ullmann, S.; Kooyman, P. J.; Molenbroeke, A. M.; Zandbergen, H. W.; Sarro, P. M., Mems Nanoreactor for Atomic-Resolution Microscopy of Nanomaterials in Their Working State. *Proc Ieee Micr Elect* **2009**, 76-79.

25.   Hansen, L. P.; Johnson, E.; Brorson, M.; Helveg, S., Growth Mechanism for Single- and Multi-Layer MoS2 Nanocrystals. *J. Phys. Chem. C* **2014,** *118* (39), 22768-22773.

26.   Boyes, E. D.; Gai, P. L., Visualising reacting single atoms under controlled conditions: Advances in atomic resolution in situ Environmental (Scanning) Transmission Electron Microscopy (E(S)TEM). *Comptes Rendus Physique* **2014,** *15* (2–3), 200-213.

27.   Creemer, J. F.; Santagata, F.; Morana, B.; Mele, L.; Alan, T.; Iervolino, E.; Pandraud, G.; Sarro, P. M. In *An all-in-one nanoreactor for high-resolution microscopy on nanomaterials at high pressures*, 2011 IEEE 24th International Conference on Micro Electro Mechanical Systems, 23-27 Jan. 2011; 2011; pp 1103-1106.

28.   Korup, O.; Goldsmith, C. F.; Weinberg, G.; Geske, M.; Kandemir, T.; Schlogl, R.; Horn, R., Catalytic partial oxidation of methane on platinum investigated by spatial reactor profiles, spatially resolved spectroscopy, and microkinetic modeling. *J. Catal.* **2013,** *297*, 1-16.

29.   Hodnik, N.; Dehm, G.; Mayrhofer, K. J. J., Importance and Challenges of Electrochemical In Situ Liquid Cell Electron Microscopy for Energy Conversion Research. *Accounts of Chemical Research* **2016,** *49* (9), 2015-2022.

30.   Malladi, S. R. K.; Tichelaar, F. D.; Xu, Q.; Wu, M. Y.; Terryn, H.; Mol, J. M. C.; Hannour, F.; Zandbergen, H. W., Quasi in situ analytical TEM to investigate electrochemically induced microstructural changes in alloys: AA2024-T3 as an example. *Corrosion Science* **2013,** *69*, 221-225.

31.   Janbroers, S.; Louwen, J. N.; Zandbergen, H. W.; Kooyman, P. J., Insights into the nature of iron-based Fischer–Tropsch catalysts from quasi in situ TEM-EELS and XRD. *J. Catal.* **2009,** *268* (2), 235-242.

32.   Vogelaar, B. M.; Steiner, P.; Dick van Langeveld, A.; Eijsbouts, S.; Moulijn, J. A., Deactivation of Mo/Al2O3 and NiMo/Al2O3 catalysts during hydrodesulfurization of thiophene. *Appl. Catal., A* **2003,** *251* (1), 85-92.

33.   Kuhrs, C.; Swoboda, M.; Weiss, W., Single crystal flow reactor for studying reactivities on metal oxide model catalysts at atmospheric pressure to bridge the pressure gap to the adsorption properties determined under UHV conditions. *Top. Catal.* **2001,** *15* (1), 13-18.

34.   Védrine, C. J., Heterogeneous Catalysis on Metal Oxides. *Catalysts* **2017,** *7* (11).

35.   Amakawa, K.; Kolen'ko, Y. V.; Villa, A.; Schuster, M. E.; Csepei, L.-I.; Weinberg, G.; Wrabetz, S.; Naumann d'Alnoncourt, R.; Girgsdies, F.; Prati, L.; Schlögl, R.; Trunschke, A., Multifunctionality of Crystalline MoV(TeNb) M1 Oxide Catalysts in Selective Oxidation of Propane and Benzyl Alcohol. *ACS Catal.* **2013,** *3* (6), 1103-1113.

36.   Kolen'ko, Y. V.; Amakawa, K.; d'Alnoncourt, R. N.; Girgsdies, F.; Weinberg, G.; Schlogl, R.; Trunschke, A., Unusual Phase Evolution in MoVTeNb Oxide Catalysts Prepared by a Novel Acrylamide-Gelation Route. *Chemcatchem* **2012,** *4* (4), 495-503.

37.   Ueda, W.; Vitry, D.; Kato, T.; Watanabe, N.; Endo, Y., Key aspects of crystalline Mo-V-O-based catalysts active in the selective oxidation of propane. *Res Chem Intermediat* **2006,** *32* (3-4), 217-233.

38.   Ishikawa, S.; Kobayashi, D.; Konya, T.; Ohmura, S.; Murayama, T.; Yasuda, N.; Sadakane, M.; Ueda, W., Redox Treatment of Orthorhombic $Mo_{29}V_{11}O_{112}$ and Relationships between Crystal Structure, Microporosity and Catalytic Performance for Selective Oxidation of Ethane. *J. Phys. Chem. C* **2015,** *119* (13), 7195-7206.

39.   Konya, T.; Katou, T.; Murayama, T.; Ishikawa, S.; Sadakane, M.; Buttrey, D.; Ueda, W., An orthorhombic Mo_3VO_x catalyst most active for oxidative dehydrogenation of ethane among related complex metal oxides. *Catal. Sci. Technol.* **2013,** *3* (2), 380-387.

40.   Chen, C.; Kosuke, N.; Murayama, T.; Ueda, W., Single-Crystalline-Phase Mo3VOx: An Efficient Catalyst for the Partial Oxidation of Acrolein to Acrylic Acid. *ChemCatChem* **2013,** *5* (10), 2869-2873.

41.   DeSanto, P.; Buttrey, D. J.; Grasselli, R. K.; Lugmair, C. G.; Volpe, A. F.; Toby, B. H.; Vogt, T., Structural aspects of the M1 and M2 phases in MoVNbTeO propane ammomidation catalysts. *Z. Kristallogr.* **2004,** *219* (3), 152-165.

42.   Holmberg, J.; Grasselli, R. K.; Andersson, A., Catalytic behaviour of M1, M2, and M1/M2 physical mixtures of the Mo–V–Nb–Te–oxide system in propane and propene ammoxidation. *Appl. Catal., A* **2004,** *270* (1–2), 121-134.

43.   Pyrz, W. D.; Blom, D. A.; Sadakane, M.; Kodato, K.; Ueda, W.; Vogt, T.; Buttrey, D. J., Atomic-level imaging of Mo-V-O complex oxide phase intergrowth, grain boundaries, and defects using HAADF-STEM. *P Natl Acad Sci USA* **2010,** *107* (14), 6152-6157.

44.   Masliuk, L.; Heggen, M.; Noack, J.; Girgsdies, F.; Trunschke, A.; Hermann, K. E.; Willinger, M.-G.; Schloegl, R.; Lunkenbein, T., Structural Complexity in Heterogeneous Catalysis: Cataloging Local Nano-Structures. *The Journal of Physical Chemistry C* **2017,** *121* (43), 24093-24103.

45.   Thorsteinson, E. M.; Wilson, T. P.; Young, F. G.; Kasai, P. H., The oxidative dehydrogenation of ethane over catalysts containing mixed oxides of molybdenum and vanadium. *J. Catal.* **1978,** *52* (1), 116-132.

46.   Ishikawa, S.; Tashiro, M.; Murayama, T.; Ueda, W., Seed-assisted synthesis of crystalline Mo_3VO_x oxides and their crystal formation mechanism. *Cryst. Growth Des.* **2014,** *14* (9), 4553-4561.

47.   Heine, C.; Havecker, M.; Sanchez-Sanchez, M.; Trunschke, A.; Schlogl, R.; Eichelbaum, M., Work Function, Band Bending, and Microwave Conductivity Studies on the Selective Alkane Oxidation Catalyst MoVTeNb Oxide (Orthorhombic M1 Phase) under Operation Conditions. *J. Phys. Chem. C* **2013,** *117* (51), 26988-26997.

48.   Nguyen, T. T.; Aouine, M.; Millet, J. M. M., Optimizing the efficiency of MoVTeNbO catalysts for ethane oxidative dehydrogenation to ethylene. *Catal. Commun.* **2012,** *21* (0), 22-26.

49.   Botella, P.; Dejoz, A.; Abello, M. C.; Vázquez, M. I.; Arrúa, L.; López Nieto, J. M., Selective oxidation of ethane: Developing an orthorhombic phase in Mo−V−X (X = Nb, Sb, Te) mixed oxides. *Catal. Today* **2009,** *142* (3–4), 272-277.

50.   Naumann d'Alnoncourt, R.; Csepei, L.-I.; Hävecker, M.; Girgsdies, F.; Schuster, M. E.; Schlögl, R.; Trunschke, A., The reaction network in propane oxidation over phase-pure MoVTeNb M1 oxide catalysts. *Journal of Catalysis* **2014,** *311*, 369-385.

51.   Hävecker, M.; Wrabetz, S.; Kröhnert, J.; Csepei, L.-I.; Naumann d'Alnoncourt, R.; Kolen'ko, Y. V.; Girgsdies, F.; Schlögl, R.; Trunschke, A., Surface chemistry of phase-pure M1 MoVTeNb oxide during operation in selective oxidation of propane to acrylic acid. *J. Catal.* **2012,** *285* (1), 48-60.

52.   Schlögl, R., Active Sites for Propane Oxidation: Some Generic Considerations. *Top. Catal.* **2011,** *54* (10-12), 627-638.

53.   Ramli, I.; Botella, P.; Ivars, F.; Pei Meng, W.; Zawawi, S. M. M.; Ahangar, H. A.; Hernández, S.; Nieto, J. M. L., Reflux method as a novel route for the synthesis of MoVTeNbOx catalysts for selective oxidation of propane to acrylic acid. *Journal of Molecular Catalysis A: Chemical* **2011,** *342–343* (0), 50-57.

54.   Naraschewski, F. N.; Praveen Kumar, C.; Jentys, A.; Lercher, J. A., Phase formation and selective oxidation of propane over MoVTeNbOx catalysts with varying compositions. *Appl. Catal., A* **2011,** *391* (1–2), 63-69.

55.   Kolen'ko, Y. V.; Zhang, W.; d'Alnoncourt, R. N.; Girgsdies, F.; Hansen, T. W.; Wolfram, T.; Schlogl, R.; Trunschke, A., Synthesis of MoVTeNb Oxide Catalysts with Tunable Particle Dimensions. *Chemcatchem* **2011,** *3* (10), 1597-1606.

56.   Sanfiz, A. C.; Hansen, T. W.; Teschner, D.; Schnorch, P.; Girgsdies, F.; Trunschke, A.; Schlogl, R.; Looi, M. H.; Hamid, S. B. A., Dynamics of the MoVTeNb Oxide M1 Phase in Propane Oxidation. *J. Phys. Chem. C* **2010,** *114* (4), 1912-1921.

57.   Ivars, F.; Solsona, B.; Hernández, S.; López Nieto, J. M., Influence of gel composition in the synthesis of MoVTeNb catalysts over their catalytic performance in partial propane and propylene oxidation. *Catal. Today* **2010,** *149* (3–4), 260-266.

58.   Cavani, F.; Ballarini, N.; Cericola, A., Oxidative dehydrogenation of ethane and propane: How far from commercial implementation? *Catal. Today* **2007,** *127* (1), 113-131.

59.   Che-Galicia, G.; Quintana-Solórzano, R.; Ruiz-Martínez, R. S.; Valente, J. S.; Castillo-Araiza, C. O., Kinetic modeling of the oxidative dehydrogenation of ethane to ethylene over a MoVTeNbO catalytic system. *Chemical Engineering Journal* **2014,** *252* (0), 75-88.

60.   Zhu, Y.; Sushko, P. V.; Melzer, D.; Jensen, E.; Kovarik, L.; Ophus, C.; Sanchez-Sanchez, M.; Lercher, J. A.; Browning, N. D., Formation of Oxygen Radical Sites on MoVNbTeOx by Cooperative Electron Redistribution. *J Am Chem Soc* **2017,** *139* (36), 12342-12345.

61.   Ishikawa, S.; Goto, Y.; Kawahara, Y.; Inukai, S.; Hiyoshi, N.; Dummer, N. F.; Murayama, T.; Yoshida, A.; Sadakane, M.; Ueda, W., Synthesis of Crystalline Microporous Mo–V–Bi Oxide for Selective (Amm)Oxidation of Light Alkanes. *Chem. Mater.* **2017,** *29* (7), 2939-2950.

62.   Nguyen, T. T.; Deniau, B.; Baca, M.; Millet, J. M. M., Influence of Nb Content on the Structure, Cationic and Valence Distribution and Catalytic Properties of MoVTe(Sb)NbO M1

Phase Used as Catalysts for the Oxidation of Light Alkanes. *Top. Catal.* **2016,** *59* (17-18), 1496-1505.

63.   Valente, J. S.; Armendáriz-Herrera, H.; Quintana-Solórzano, R.; Del Ángel, P.; Nava, N.; Massó, A.; López Nieto, J. M., Chemical, structural, and morphological changes of a MoVTeNb catalyst during oxidative dehydrogenation of ethane. *ACS Catal.* **2014,** *4* (5), 1292-1301.

64.   White, A. H.; Germer, L. H., The Rate of Oxidation of Copper at Room Temperature. *Transactions of The Electrochemical Society* **1942,** *81* (1), 305-319.

2 Structural complexity in heterogeneous catalysis: cataloging local nano-structures

2.1 Abstract

We present an analytical route towards a detailed and quantitative description of individual defects in heterogeneous catalysts. The investigation is based on a high resolution scanning transmission electron microscopy (STEM) study using complex $(Mo,V)O_x$ mixed oxide as an example. Tiling the structural regions simplifies the identification of local modifications in the microstructure. Up to 19 different structures were observed that can be listed and classified into different structural motifs, intergrowth, channels, interstitial regions, and inclinations. The observed defects are expressed by the rearrangement of the $\{(Mo)Mo_5O_{27}\}$ building blocks, exhibit different sizes, penetrate the bulk and can form decoupled surface regions that partially cover the crystallographic bulk. The evaluation of 31 crystals yields an average defect concentration of 3.3% and indicates the absence of identical particles. We have, for example, observed 54 of these rearranged structures close to the surface of one $(Mo,V)O_x$ particle (100x50 nm^2). A detailed analysis of the atomic arrangement at the surface of this particle suggests a surface composition of $(Mo_{610}V_{230}M_{70})O_x$ (M= Mo and/or V). The resulting catalog of motifs reproduces individual fragments of the real structure of a catalyst and can reveal detailed defect-activity correlations that will contribute to a better understanding of heterogeneous catalysis.

2.2 Introduction

Heterogeneous catalysis has emerged to a ubiquitous technology, whose products promote our everyday life. Parallel optimizations of catalytic and synthetic protocols of solid catalysts have rendered this technology into the future chemical approach for efficient energy conversion. Those solid catalysts are intrinsically composed of defects in their bulk and surface structure, which can significantly alter the catalytic performance.[1] Defects, however, are often

treated as white spots on the catalytic landscape since they are, due to the lack of translational symmetry, hard to pinpoint. Qualitative and quantitative defect estimation could reflect important defect-activity correlations, which will boost the understanding in heterogeneous catalysis and will simplify a prospective catalyst tailoring.

To bridge this knowledge gap, we focus on a real space, atomic-resolved quantitative defect description using local characterization techniques. Local insight into structural features of limited translational symmetry can be obtained by transmission electron microscopy (TEM) imaging. Recent developments in TEM allow for capturing local fluctuations of the crystallographic bulk structure at the atomic scale and have stimulated research in heterogeneous catalysis.[2-4] The local analytical strength of TEM has, for instance, provided valuable insights into the surface coverage of $Cu/ZnO/Al_2O_3$ catalysts for methanol synthesis or manganese surface enrichment in nanosized $MnWO_4$.[5-7]

Using aberration corrected scanning transmission electron microscopy (STEM) we explore local structural variations in activated orthorhombic $(Mo,V)O_x$, which selectively catalyzes the oxidative dehydrogenation (ODH) of ethane to ethene.[8] The structure of orthorhombic $(Mo,V)O_x$ is complex enough to compete as relevant oxidation catalysts. Its complexity further allows for a broad structural flexibility.[9] Although details of orthorhombic $(Mo,V)O_x$ have already been elucidated by STEM imaging using high angle annular dark field (HAADF) and annular bright field- (ABF) detectors, studies on the defect structures of M1 phase mixed oxides are rare.[9-12] However, an in-depth and quantitative defect analysis that describes local atomistic and chemical details of structural parameter alterations within this complex catalyst is missing.

In selective oxidation catalysis, a detailed knowledge of individual defects may be important for understanding oxygen activation, electron migration to the surface and reversible/irreversible surface enrichments.

Our approach is based on a simple visualization of local structural anomalies using the concept of structural tiling (Figure 2-1). In brief, the tiling covers the periodic structure with building blocks (tiles) of equal or different shape.[13-14] Clearly, 2D tiling does not reflect the complete 3D structural information. However, a proper tiling model can specifically highlight structural defects that break the perfect periodicity of the otherwise regular, crystalline structure.[15] Using the concept of tiling our detailed and local investigation identifies new

structural motifs that are expressed by new connectivities of $\{(Mo)Mo_5O_{27}\}$ building blocks, intergrowth regions, octagonal channels, interstitial regions, and inclinations. The results are complemented by a statistical analysis and grouped in catalog of local structures. In addition, alterations of the local composition induced by the structural re-arrangements and their general impact on heterogeneous catalysis are also discussed.

2.3 Results and discussion

2.3.1 The orthorhombic tiling

In general, orthorhombic $(Mo,V)O_x$ mixed oxides, crystallize in the so-called M1 structure and are composed of pentagonal $\{(M)Mo_5O_{27}\}$ building blocks that are connected via corner-sharing MoO_6 or VO_6 octahedra and form hexagonal and heptagonal channels (Figure 2-1a).[16-18] In ternary $(Mo,V)O_x$ mixed oxides the $\{(Mo)Mo_5O_{27}\}$ units can be differently connected and, thereby, determine the crystal structure.[16-17] The ideal microstructure of orthorhombic $(Mo,V)O_x$ viewed along the crystallographic *c*-axis is shown in Figure 2-1a. As suggested recently the ideal orthorhombic M1 structure can be described by combining the central cations of the pentagonal $\{(M)Mo_5O_{27}\}$ building blocks along the corner-sharing, neighboring, single octahedral sites (Figure 2-1).[19-20]

In the M1 unit cell the central Mo cations of the $\{(Mo)Mo_5O_{27}\}$ building blocks are situated in a common plane perpendicular to the crystallographic *c*-axis.[21] Thus, the Mo vertices of this tiling can be connected torsion free which allows for a direct measurement of the lengths and angles of the hexagonal tiles (Figure 2-1a-c). The present tiling is similar to that described for structurally complex, orthorhombic alloys that crystallize in the so called T-Al-Mn-Pd phase and exhibit a local 5-fold symmetry with respective tiling angles at the vertices of 72° and 144°.[15] As opposed to the complex metal alloys the ideal tiling of ternary, orthorhombic $(Mo,V)O_x$ mixed oxide derived from the crystal structureexhibits tiling angles of 77° and 141° (Figure 2-1b).[21] The deviation may result from the influence of the local distortion of different pentagonal blocks that are present in the M1 structure referenced with respect to the central Mo cation in $\{(Mo)Mo_5O_{27}\}$ and depends on the applied synthesis protocol: Each central Mo cation in $\{(Mo)Mo_5O_{27}\}$ is surrounded by five Mo cations where the Mo-Mo$_{central}$-Mo angle fluctuates between 68° and 71°.[22, 39] The corner sharing octahedra around the $\{(Mo)Mo_5O_{27}\}$ units also form a distorted pentagon that is rotated by 36° and exhibits M-Mo$_{central}$-M (M=Mo,V) angles

that vary between 70° and 74°. The corner sharing octahedra are surrounded by five channels (C), heptagonal and hexagonal, realizing C-Mo$_{central}$-C angles from 70° to 76°.[21] The distorted
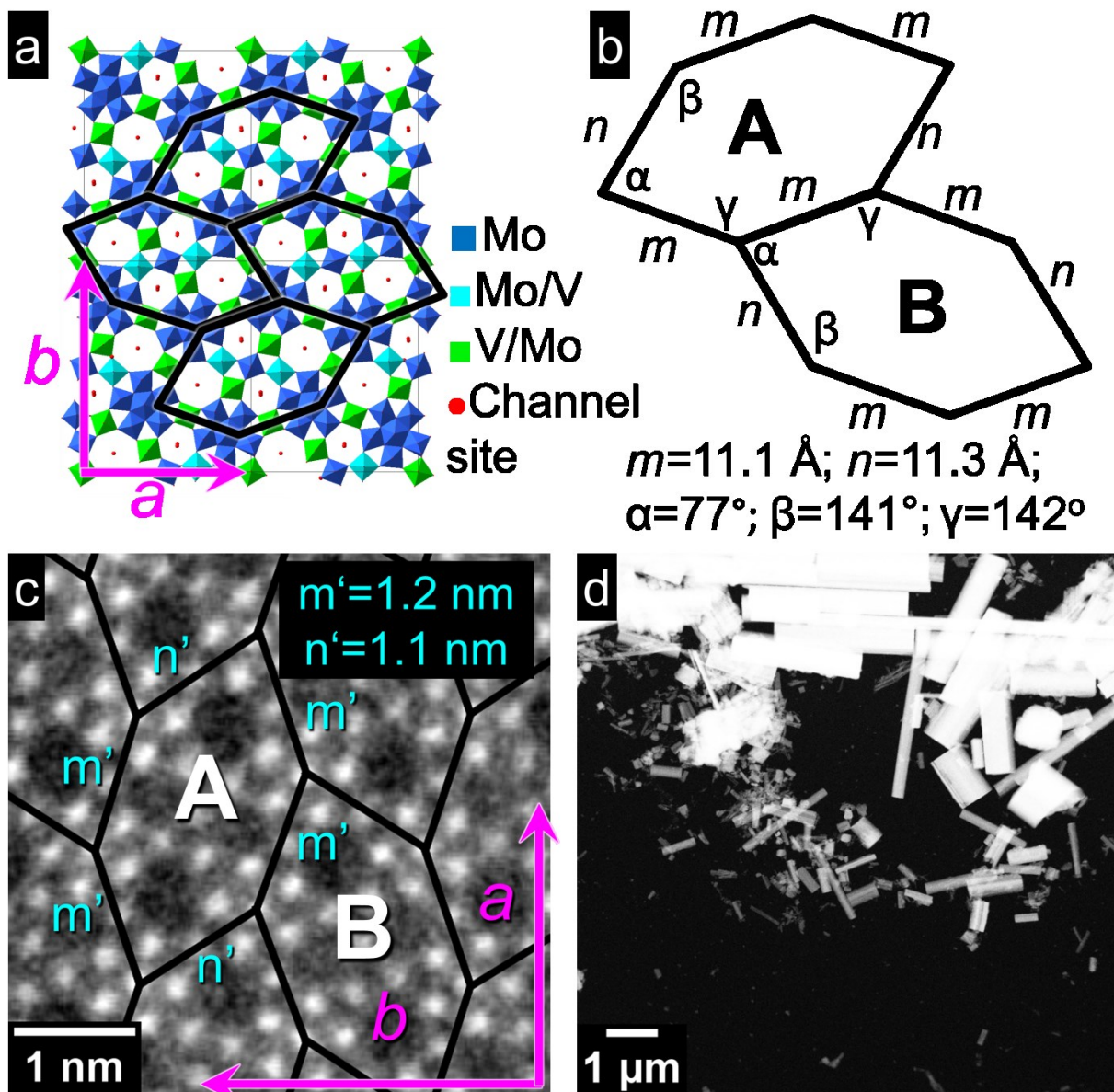

Figure 2-1: (a) Structural model of the M1 structure viewed along [001]. Black hexagons: standard tiling; Mo/V and V/Mo sites: preferred occupancy of Mo and V, respectively.21 (b) Schematic combination of A and B tiles (AB), their length (m, n) and angles (α, β) as obtained from the ideal crystal structure of the M1 phase.21 (c) HAADF-STEM image of the M1 structure viewed along [001] superimposed by the standard tiling. m´ and n´: lengths measured directly from the experimental image. (d) Overview HAADF-STEM image of M1 nanorods.

pentagonal channel arrangements are connected by the S1 and S2 site that act as inversion centers. The S1 and S2 cationic sites connect two adjacent heptagonal and hexagonal channels, respectively. In addition, the S2 site is located in the center of the tiling of the orthorhombic M1 phase. Distortions in the polyhedra of complex (Mo,V) mixed oxides are not uncommon and depend on the nature of the cations and their oxidation states.[12] The different oxidation states of the cations confined in the anionic configuration lead to different out-of-center distortions. For instance, fully oxidized molybdenum cations in an octahedral environment exhibit out-of-center displacements that are directed towards faces and edges, whereas V^{5+} cations are shifted towards the vertices.[22] Therefore, the complex microstructural arrangement of the orthorhombic M1 phase may be to some extent determined by the atomic displacements of the cations positioned in their individual anionic configuration. In addition, the orthorhombic symmetry of M1 forbids a long range 5-fold symmetry that is, for instance, observed in quasi-crystals.

For the above mentioned complex metal alloys the tiles can be transformed into each other by shifting and rotation, while for ternary $(Mo,V)O_x$ mixed oxide an additional mirror operation is needed.[15] An **AB** combination of tiles is required to describe the unit cell of orthorhombic $(Mo,V)O_x$ mixed oxide (Figure 2-1b). Figure 2-1c shows a HAADF-STEM image viewed along the [001] zone axis of complex $(Mo,V)O_x$ superimposed with combined **AB** tiles. Within the error of the measurement the measured angles and distances match the structural parameters obtained from the ideal crystal structure shown in Figure 2-1b. In addition, slight imperfections in the orientation of the $(Mo,V)O_x$ particle in the electron microscope may result in small variations of the tiling parameters. In this study the tiles were constructed individually for each particle. Further, the labels "ideal tiling" and "standard tiling" refer to the tiling taken from the ideal crystal structure and from specific $(Mo,V)O_x$ particles as obtained from HAADF-STEM imaging, respectively.[21] In agreement with other reports, the investigated orthorhombic $(Mo,V)O_x$ mixed oxide crystallizes in a rod-like structure (Figure 2-1d) that grow along the crystallographic *c*-axis.[8, 20-21] In addition, the measured particle size distribution presented in Figures S2-1 and S2-2 confirms an anisotropic particle shape.
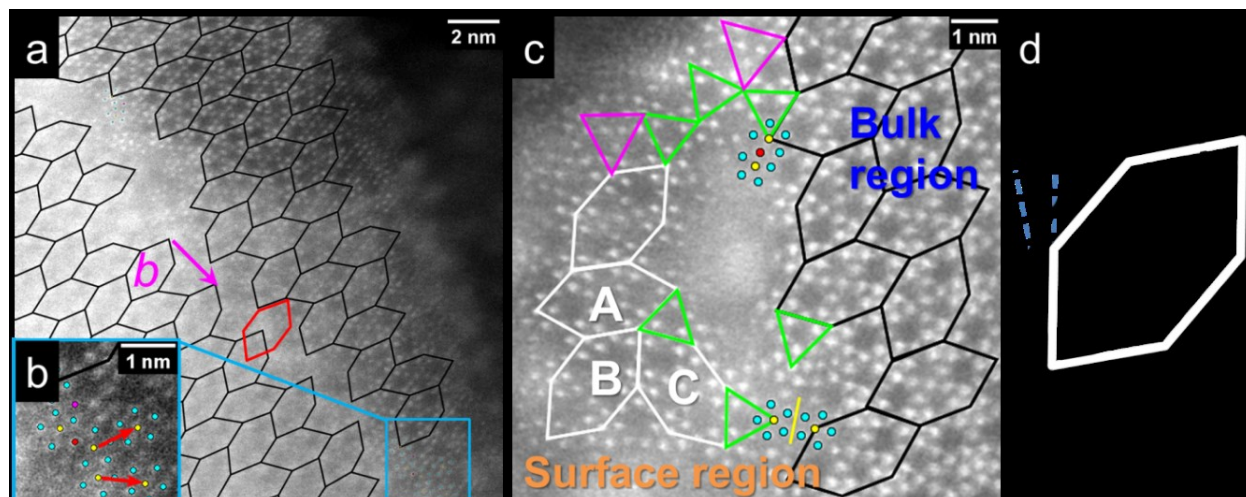
Figure 2-2: HAADF-STEM images of the M1 structure viewed along [001]. (a) Displacement of separated M1 phases. The red tile highlights this mismatch. (b) Magnified region showing re-connected {(Mo)Mo$_5$O$_{27}$} units. (c) M1 tiling at the surface region. (d) Schematic representation of the relative orientation of different tiles. Black hexagons: standard tiling; white tiles: rotated standard tiling; yellow and cyan circles: cations of the {(Mo)Mo$_5$O$_{27}$} units; red and pink circles: unusual positions of cations; red arrow: translation vector; yellow line: mirror plane.

X-ray diffraction analysis (XRD) (Figure S2-3) of the investigated M1 phase shows no indications for crystalline impurities or discernable defects in the orthorhombic structure. The observed deviations in the relative reflection intensities from the ideal theoretical values result from preferred crystal orientation effects caused by the crystallite morphology and sample preparation. Local TEM analyses of, altogether, 31 particles reveal the presence of new structural motifs, intergrowth, octagonal channels, interstitial regions, and inclinations. Based on local TEM investigations the average and median defect concentrations, considering all local and visible geometric modifications within orthorhombic (Mo,V)O$_x$ mixed oxide, amounts to 3.3 % and 1.6%, respectively (Table S2-1). Those defects interrupt the crystallographic bulk structure, form structurally decoupled, extended surface regions and/or appear individually at the particle surface. XRD is an averaging, integral bulk method, in which the coherently diffracting domains contribute to the mean with the weight of their respective volumes. Hence, the XRD pattern of the (Mo,V)O$_x$ mixed oxide (Figure S2-3) is dominated by the large domains of the orthorhombic structure and hardly influenced by the various defects visible in TEM.

Figure 2-2 may act as an example of how the local structural analysis benefits from the concept of tiling. The applied tiling indicates structurally decoupled regions. The HAADF-

STEM image in Figure 2-2a appears partially blurred. To identify the reason of blurring an additional image focusing on the initially blurred part was recorded (Figure S2-4). The comparison of both images indicates the presence of thickness differences of two structurally separated M1 parts. However, the contrast of Figure 2-2a is already high enough to identify the tiling. In addition, Figure 2-2a highlights a defect layer that discontinues the ideal M1 structure and proceeds along the crystallographic *b*-axis. The displacement vector (x,y) can be expressed by a linear combination of bulk lattice vectors projected onto a 2D plane with x and y yielding approximately 0.5*a* and 0.4*b*, respectively, where *a* and *b* correspond to the lattice parameters of the ideal crystal structure. The observed displacement in Figure 2-2a may result from strain relaxation induced by local changes in the connectivities of pentagonal $\{(Mo)Mo_5O_{27}\}$ (Figure 2-2b) units during synthesis. The tiling, highlighted in Figure 2-2, also simplifies the identification of surface regions with different connectivities and/or local alterations of the standard M1 structure that would otherwise be overlooked (Figure 2-2c). These regions partially cover the ideal orthorhombic $(Mo,V)O_x$ crystals and occur in 45 % of the investigated particles. Thus, the tiling can act as a measure to directly differentiate the standard bulk structure (black tiling) from local structural modifications observed in the structure of the surface region (white tiling and triangles in Figure 2-2c).

Both standard bulk and surface parts exhibit orthorhombic $(Mo,V)O_x$ motifs. The orthorhombic tiles in the surface region, however, display differences that are expressed by a slight rotation (tiles **A** and **B**) of 12° (Figure 2-2d) compared to the standard bulk tiling. Furthermore, tile **C** represents a mirrored or rotated image of tile **B**. These local geometric inconsistencies represent local structural re-arrangements that can be expressed by changes in the connectivity of the pentagonal $\{(Mo)Mo_5O_{27}\}$ building blocks and induce strain. In the transition region of bulk and surface structural strain may be relieved by the appearance of triangular motifs. Figure 2-2c underlines the occurrence of different structural defects that can co-exist close to the surface of complex $(Mo,V)O_x$ mixed oxide.

2.3.2 Structural motifs

Figures 2-2 and 2-3a,b suggest that the present structural fluctuations originate from different arrangements of the pentagonal building blocks where the local connectivity of the $\{(Mo)Mo_5O_{27}\}$ motifs does not reflect the structural arrangement expected for the orthorhombic M1 phase. This modified connectivity of the pentagonal building blocks can be observed in

various forms and occurs with different probability (Figure 2-3c,1-8, Figure S2-5). The new structural motifs that involve two or three neighboring $\{(Mo)Mo_5O_{27}\}$ building blocks can be grouped into two different categories: triangular (Figure 2-3c, motifs 2, 3) and linear. The linear motifs are divided into mirrored, translated, shared, twinned and rotated motifs (Figure 2-3c, motifs 4-8), respectively.
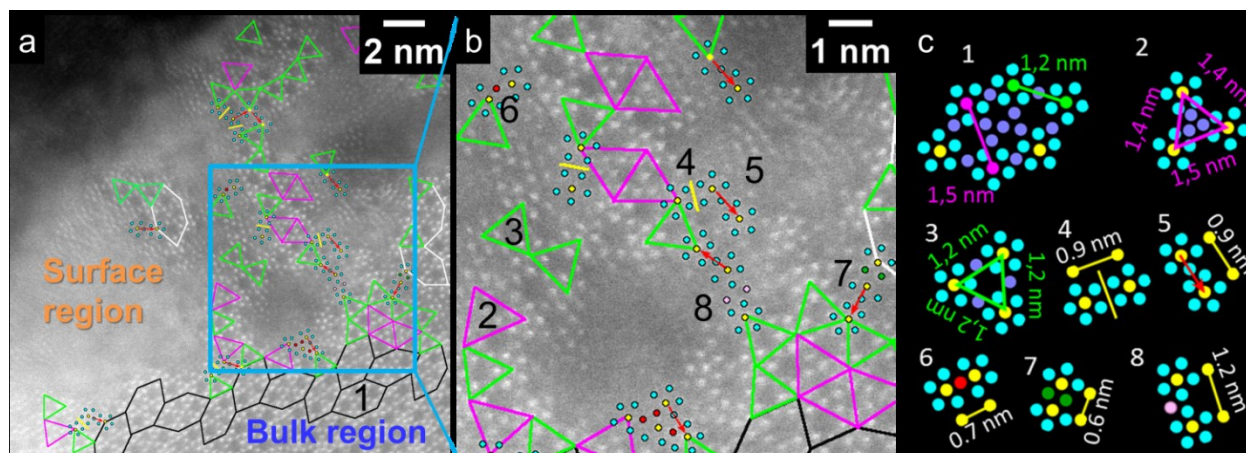
Figure 2-3: (a) HAADF-STEM image of the surface region and several defect types. (b) Magnified region with all kinds of local motifs (c) Schematic representation of structural motifs with average distances between central cations of the $\{(Mo)Mo_5O_{27}\}$ units: 1) standard M1 motif, 2) and 3) two types of the triangular motifs, 4) mirrored motif, 5) translated motif, 6) shared motif, 7) twinned motif, 8) rotated motif. Corresponding HAADF-STEM images of each motif are given in Figure S2-5.

In Figure 2-3c, motif 1 the standard motif for orthorhombic $(Mo,V)O_x$ that corresponds to a single tile is schematically presented. The triangular motifs (Figure 2-3c, motifs 2, 3) can be distinguished by two different connections of the $\{(Mo)Mo_5O_{27}\}$ units and exhibit structural features that have already been observed in the standard M1 tile.

— *The pentagonal units are connected by two cation sites.* The distance between the $\{(Mo)Mo_5O_{27}\}$ building block equals the width of the standard tiling (Figure 2-3c, motif 1). The triangular arrangement of the $\{(Mo)Mo_5O_{27}\}$ units results in an internal arrangement of cations that can also be found in the trigonal crystal structure (Figure 2-3c, motif 2).

— *The pentagonal $\{(Mo)Mo_5O_{27}\}$ units are connected by one cation site.* The length corresponds to the side of the standard M1 tiling (Figure 2-3c, motif 1). This

triangular motif exhibits a hexagonal channel and appears in the center of the trigonal unit cell (Figure 2-3c, motif 3).

The measured distances inside both triangular motifs match the respective length of the standard tiling of the orthorhombic phase. Therefore, it is expected that the mismatch strain between the triangular motifs and the M1 phase should be small. This might explain the significant enrichment of triangular motifs at the boundary of ordered bulk and surface regions compared to other defects (Figures 2-2c and 2-3). Furthermore, changes in the local geometric environment influence the distances and distortions of the pentameric units in the triangular motifs (Figure S2-6).

A mirrored motif is shown schematically in Figure 2-3c, motif 4 and can be described as a $\{(Mo)_2Mo_{10}O_{52}\}$ unit in which two octahedra of one $\{(Mo)Mo_5O_{27}\}$ cluster share corners with two octahedra of an adjacent $\{(Mo)Mo_5O_{27}\}$ cluster. Translated motifs are shifted $\{(Mo)Mo_5O_{27}\}$ motifs and form corner-shared $\{(Mo)_2Mo_{10}O_{52}\}$ units (Figure 2-3c, motif 5). In shared motifs (Figure 2-3c, motif 6), two $\{(Mo)Mo_5O_{27}\}$ units are connected sharing one MoO_6 octahedron providing edge-sharing $\{(Mo_2)Mo_9O_{48}\}$ linkers. The twinned motifs (Figure 2-3c, motif 7) are similar to the shared motifs but share two Mo cations. The rotated motif is presented in Figure 2-3c, motif 8. It is composed of two pentagonal units and one or two added cations (Mo,V) that are hosted in an anionic configuration. This motif has been observed only rarely.

The distances between the central Mo cations in neighboring $\{(Mo)Mo_5O_{27}\}$ units depend on the local environment (Figure 2-3 and Figure S2-6), but as a general trend the distances of the $\{(Mo)Mo_5O_{27}\}$ units decrease in the order: regular (~1.5 nm: $Mo_{central}$-$Mo_{central}$ distance along the width of the hexagonal tiling; ~1.2 nm: $Mo_{central}$-$Mo_{central}$ distance along the side of the hexagonal tiling) $\geq$ rotated (~1.2 nm: $Mo_{central}$-$Mo_{central}$ distance) > mirrored/translated (~0.9 nm: $Mo_{central}$-$Mo_{central}$ distance) > shared/twinned (~0.6 nm: $Mo_{central}$-$Mo_{central}$ distance). The influence of the local environment and connectivity on the $Mo_{central}$-$Mo_{central}$ distance is illustrated in Figure S2-6 for different triangular motifs (Figure S2-6a) and for a tetragonal arrangement of shared motifs (Figure S2-6b).

Complex orthorhombic $(Mo,V)O_x$ is a metastable compound in the phase space of extended oxide structures. The formation of this microstructure requires kinetic control and can be adjusted by the synthesis parameters: small (local) changes in temperature, pH value, concentration, autogeneous pressure, drying procedure or thermal treatment may cause structural

changes at the atomic scale that can be expressed by different connectivities of the pentagonal building blocks. The energy barriers between the different connectivities may be small, offering a variety of different structural motifs. Among the defective structural motifs of the pentameric units the translated motifs (Figure 2-3c, motif 5) are observed most frequently suggesting energetic preference of this structural motif. Rotated motifs (Figure 2-3c, motif 8) are relatively rare indicating a higher equilibrium energy and lower stability. The structural re-connected $\{(Mo)Mo_5O_{27}\}$ units within orthorhombic M1 structure might act as local structural defects. Subsequent energy and strain minimization due to the insertion of local defects may lead to structural discontinuities or bulk termination similar to the observations in complex alloys.[15]

2.3.3 Intergrowth phases

As mentioned in Figure 2-2a the ideal orthorhombic $(Mo,V)O_x$ structure can be discontinued. The intermediate region that separates ideal M1 crystal can contain any local motifs and tiles. Depending on their geometric arrangement three kinds of different intergrowth phases can be distinguished (Figure 2-4). The trigonal intergrowth is most common for this kind of ternary mixed oxide (Figure 2-4a).[9-12] We have further identified new intergrowth phases that we label aperiodic (Figure 2-4b,c) and zipper-like (Figure 2-4d,e) intergrowths. The orientation of the crystalline domains before and after the aperiodic intergrowth can differ (Figure 2-4b). The internal structure of the aperiodic phase can also vary (Figure 2-4c). The zipper-like intergrowth phase is the rarest and proceeds along the crystallographic *b-axis* (Figure 2-2a, 4d). The measured geometric displacement of two adjacent M1 domains as obtained from Figure 2-4d is 0.5a and 0.3b and corresponds within the error range to the displacement vector derived from Figure 2-2a. The zipper-like intergrowth contains twinned, shared and translated motifs (Figure 2-4e). Different kinds of intergrowth phases can simultaneously occur. Figure 2-4d, for instance, highlights the coexistence of zipper-like and trigonal intergrowth phases.
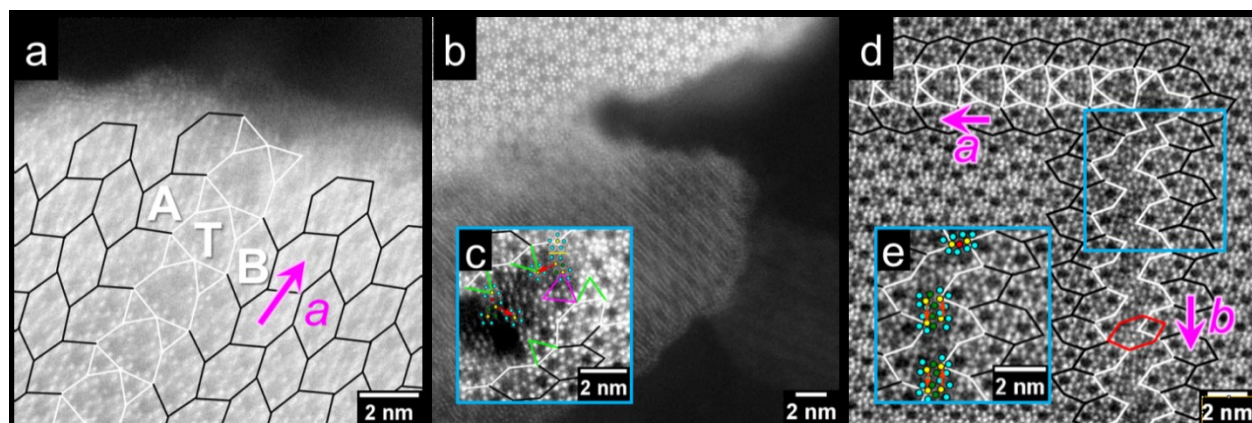
Figure 2-4: HAADF-STEM images of (a) trigonal, (b, c) aperiodic, and (d, e) zipper-like intergrowth, and their internal structure (c, e). Black hexagons: M1 phase; white arrowhead-shaped tiling: trigonal phase; magenta arrows: unit vectors; green and magenta triangles: triangular motifs; red arrows: translated motifs; yellow line: mirror motif; red circles: shared motifs; green circles: twinned motifs.

The occurrence of trigonal $(Mo,V)O_x$ inclusions in an orthorhombic grain may be attributed to similar synthesis conditions of both phases, which are most commonly obtained by a hydrothermal treatment at different pH values, and/or may originate from the condensation of individual $(Mo,V)O_x$ nanorods.[23-24] In addition to the structural relaxation mechanism proposed above, which may originate from the differently connected $\{(Mo)Mo_5O_{27}\}$ units, minute local chemical and/or surface potential fluctuations may cause the formation of trigonal phases. Orthorhombic and trigonal phases, however, exhibit different catalytic properties.[8]

For comparison, the crystal structure of the trigonal $(Mo,V)O_x$ phase is shown in Figure 2-5a.[23] It can be formed by the same $\{(Mo)Mo_5O_{27}\}$ pentagonal building blocks that characterize the orthorhombic structure.[25] Similar to the M1 phase the central Mo cations of the $\{(Mo)Mo_5O_{27}\}$ units are all located in the same plane perpendicular to the crystallographic *c*-axis. Therefore, these central Mo cations can act as vertices of a trigonal tiling. As opposed to the above mentioned localized structural motifs the trigonal intergrowth can be interpreted as a planar defect within the orthorhombic phase that lies parallel to the crystallographic *c*-axis and perturbs the orthorhombic structure. Hence, the trigonal tiling is depicted as arrowhead-shaped hexagons combined with equilateral triangles (Figure 2-5).
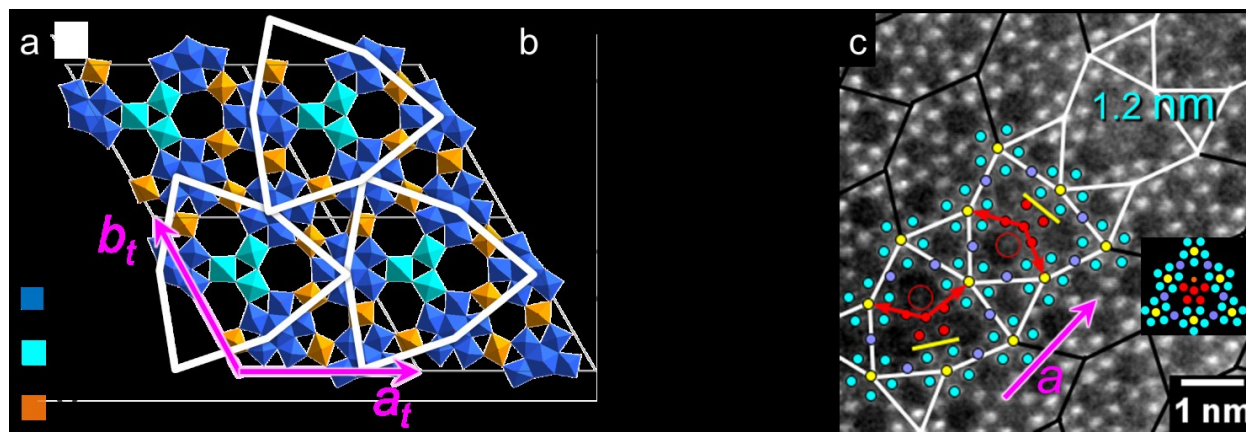
Figure 2-5: (a) Structural model of the trigonal $(Mo,V)O_x$ phase superimposed by tiling, V/Mo: preferred site occupancy of V.[23] (b) Schematic representation of the ideal trigonal tiling.[23] (c) HAADF-STEM image of the trigonal intergrowth viewed along [001], the inset in (c) schematically depicts the internal structure of the pseudo-trigonal tiling. Black hexagons: M1 phase; white arrowhead-shaped tiling: trigonal phase, red open circles: electron density in the channels; filled red circles: basis of the pentagonal building units; red arrows: translated motifs; yellow lines: mirrored motifs; yellow and cyan circles: cations of the $\{(Mo)Mo_5O_{27}\}$ units; violet circles: corner-sharing cations.

The combination of 2D tiles provides a comprehensive description of the involved phases. In contrast to the orthorhombic tiling of Figure 2-1b all edge lengths of the proposed trigonal tiles are equal (11.3 Å, Figure 2-5b). The HAADF-STEM image in Figure 2-4a and 5c highlights a trigonal intergrowth in-between an orthorhombic $(Mo,V)O_x$ crystal. The measured angles and distances match the geometric parameters obtained from the ideal crystal structure (Figure 2-5b) within experimental error bars. The trigonal intergrowth separates adjacent orthorhombic phases, but maintains the relative structural relationship. In addition, the periodicity and the direction of the trigonal intergrowth equal the length and direction of the crystallographic *a*-axis of the orthorhombic phase (Figure 2-4a).

As shown in Figure 2-1 the orthorhombic phase is represented by an **AB** combination of tiles. The trigonal intergrowth (**T**) breaks this tiling sequence and results in an **ATB** arrangement (Figure 2-4a). The individual **A** and **B** tiles contain boundary edges of two different lengths, 11.1 Å and 11.3 Å while the trigonal intergrowth (edge length 11.3 Å) connects only with the shorter edge of the **A/B** tile (11.1 Å). Due to this difference in edge length of **A/B** and **T** tiles the **ATB** arrangement of tiles is slightly strained. In addition, an **ATTB** tiling can also exist (Figure

S2-7). Other arrangements that include the intergrowth, such as **ATA** or **BTB**, or a connection of equally-distanced sides have not been observed.

High resolution HAADF-STEM imaging shows that the trigonal intergrowth (Figure 2-5c and Figure S2-8) does not always reflect the ideal trigonal structure (Figure 2-5a). For example, instead of exhibiting a central V rich triangle (Figure 2-5a) the $(Mo,V)O_x$ mixed oxide can be composed of a pseudo-pentagonal central unit that is built of four Mo or V cations with an additional column of lower contrast located in octagonal channels (Figure 2-5c). A quadrilateral arrangement of cations in the center of the trigonal intergrowth can also appear (Figure S2-8). Similar to previous report we consider this intergrowth as pseudo-trigonal.[10] The pseudo-trigonal structure in the present $(Mo,V)O_x$ mixed oxide with its central pentagonal unit usually exhibits two translated motifs and one mirror motif per trigonal tile (Figure 2-5c). Compared with the ideal $\{(Mo)Mo_5O_{27}\}$ unit the pseudo-pentagonal center of the pseudo-trigonal intergrowth is highly distorted with $M-M_{central}-M$ angles between 62° and 81° (with M denoting metal cations). In addition, the HAADF-STEM image in Figure 2-5c shows a rare case, in which neighboring units of an otherwise regular ordered pseudo-trigonal intergrowth are rotated by 115°. Furthermore, the pseudo-trigonal intergrowth proceeds through the whole bulk crystal and can also be found at the surface of orthorhombic $(Mo,V)O_x$ mixed oxide (Figure 2-4a). Similar to previous reports, crystalline trigonal phases at the edges of orthorhombic $(Mo,V)O_x$ mixed oxide have also been observed (Figure S2-9).[9-10]

2.3.4 Interstitial regions

The pseudo-trigonal intergrowth is occasionally interrupted by local structural modifications. These represent interstitial regions and cause a shift and/or a change of the direction of the intergrowth as highlighted by the arrowhead-shaped trigonal tiling in Figure 2-6, Figures S2-7 and S2-10-S2-14. Three different cases were observed as to how adjacent pseudo-trigonal intergrowths point at each other before and after the structural intersections (Figure 2-6) and are schematically summarized in Figure S2-10: back to back (type-1, Figure 2-6a), tip to tip (type-2, Figure 2-6b), and back to tip (type-3, Figure 2-6c).
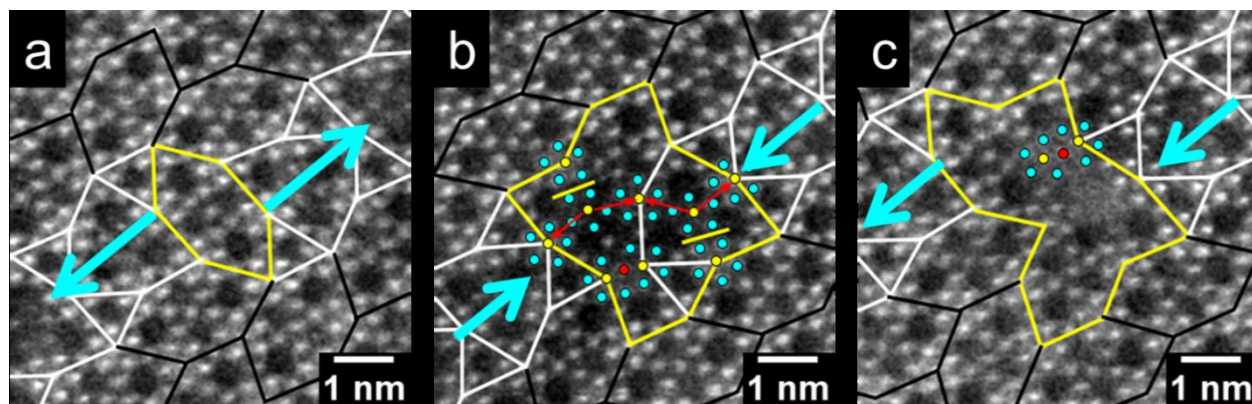
Figure 2-6: HAADF-STEM images of the most frequent interstitial regions. Cyan arrows: direction of the pseudo-trigonal intergrowth: a) type-1; b) type-2; c) type-3. Yellow polygons: interstitial regions; white tiling: trigonal intergrowth; black tiling: standard M1 structure; yellow and cyan circles: cations of the $\{(Mo)Mo_5O_{27}\}$ pentagonal units; yellow line: mirrored motifs; red arrows: translated motifs; red circles: shared motifs.

Interstitial regions with different shape were found in each pseudo-trigonal intergrowth and can appear in both bulk and surface regions (Figure 2-6 and Figures S2-10-S2-14). In Figure 2-6 the most frequent interstitial regions are highlighted. The interstitial region in Figure 2-6a and Figure S2-11 occurs most often and corresponds to a tile of the orthorhombic phase flipped along the long edge of the orthorhombic tile. It is further referred to as pristine interstitial region. This induces a two-fold rotation between tiles leading to the type-1 geometry. An interstitial region that induces a four-fold rotation between trigonal tiles is shown in Figure 2-6b and Figure S2-12 and causes the type-2 geometry of the pseudo-trigonal intergrowth. More complex interstitial regions with a type-3 arrangement of trigonal tiles are shown in Figure 2-6c and Figure S2-13.

Note that complex interstitial regions can contain all three types of geometrical arrangements (Figure S2-14). In general, the shift of the pseudo-trigonal intergrowth between the two sides of the local structural modification increases with increasing size of the interstitial region. In addition, any structural motifs and tiles mentioned above (Figure 2-1b, 2-3c, and 2-5b) can be observed in more complex interstitial regions, which differ from the pristine interstitial region introduced in Figure 2-6a. As for the pristine interstitial region only the outer local boundary can vary (Figure 2-6a and Figure S2-11), additional changes of the internal structure of more complex interstitial regions can be observed while the outer shape is preserved. For

example, the four-fold rotational interstitial region presented in Figure 2-6b is composed of four translated motifs, two mirrored motifs and one shared motif, whereas the similar interstitial region presented in Figure S2-12 is constructed of two translated motifs, one mirrored motif, one rotated motif, and two shared motifs. Both four-fold rotational interstitial regions host a trigonal tile. As indicated by their different contrast they may have different height with respect to the surrounding ideal orthorhombic structure. Furthermore, Figure S2-14 shows that the interstitial regions can be significantly larger and are characterized by a low contrast that indicates a higher degree of distortions. These regions frequently contain orthorhombic tiles with additional cation occupancies in the channels that can now be clearly observed in the HAADF-STEM image (Figure S2-14). In addition, a structure similar to the interstitial regions was observed, which is only surrounded by ideal bulk M1 (Figure S2-15). We further refer to this defect as an interstitial-like region, which can contain several motifs.

2.3.5 Combinations of different tiles

Figure 2-7a schematically displays all observed structural combinations of tiles where experimental evidence is given in Figures 2-1 to 2-6, Figures S2-11 and S2-16. The arrangements are grouped according to their occurrence and their mismatch of summed corner angles of joining tiles compared to 360°. Figure 2-7a,1 corresponds to the regular orthorhombic and trigonal tiles (for comparison see Figures 2-1 and 2-4). The combinations of tiles shown in Figure 2-7a,2 represent the pseudo-trigonal intergrowth (Figures 2-4 and 2-5). Both combinations appear with the same probability. Less frequent arrangements are shown in Figure 2-7a,3. They can be found at the surface region (Figure 2-2c and Figure S2-11) and at interstitial regions (Figure 2-6a and Figure S2-14). The rarest combinations of tiles are shown in Figure 2-7a,4, a,5, and a,6 and can be found in aperiodic intergrowths (Figure S2-16a) and at certain spots in the surface regions (Figure S2-16b,c), respectively. With the exception of 7a,4 and 7a,5 the occurrence decreases with an increasing mismatch of summed corner angles of joining tiles. Although the mismatch angle of the arrangement shown in Figure 2-7a,4 is 0°, this combination of tiles is rarely observed due to symmetry constrains of the M1 structure. The rare appearance of the arrangement of tiles displayed in Figure 2-7a,5 may be attributed to a lack of stabilization. In general, the strain induced by these mismatches is relieved by local inclinations or disinclinations that may induce a buckling of the surface. Inclinations may be present in the

pseudo-trigonal intergrowth (Figures 2-4a and 2-5c) and often cause the central pentagon to appear blurred.
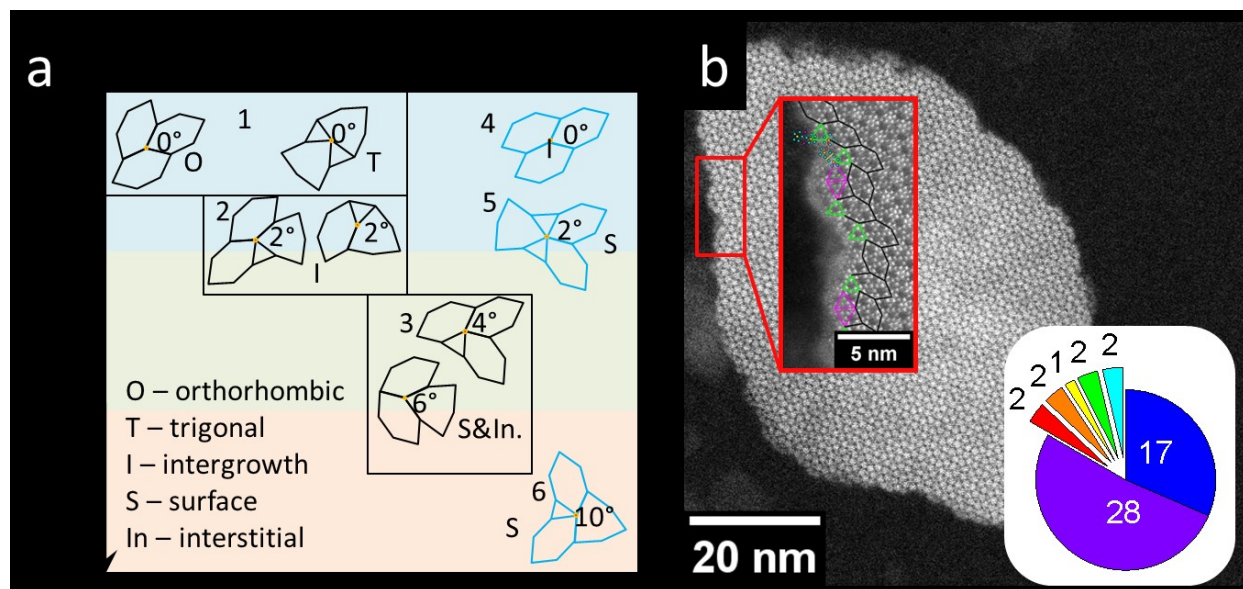
Figure 2-7: (a) Summary of observed combinations of tiles listed by their frequency of occurrence and mismatch of summed corner angles of joining tiles compared to 360°: orange circles: corner angles. Labels refer to their location of occurrence. The mismatch calculation is presented and explained in Table S-2-2. (b) HAADF-STEM image of one orthorhombic (Mo,V)O$_x$ particle (100x50 nm^2) viewed along [001]: The inset in (b) highlights the amount of different motifs that occur at the surface of this (Mo,V)O$_x$ particle: red: shared; orange: translated; yellow: rotated; green: mirrored; blue: triangular (Figure 2-3b, motif 2); violet: triangular (Figure 2-3b, motif 3); cyan: additional cation position (M).

In addition, the amount of extended and local defects that are embedded in an orthorhombic (Mo,V)O$_x$ crystal can vary noticeably (Table S2-1). As an example, Figure 2-7b shows an HAADF-STEM image of the M1 structure suggesting a defect-free bulk region. However, detailed analysis reveals the presence of at least 54 local defects of different types (Figure 2-7b, inset) close to the surface (Figure 2-7b).
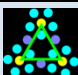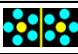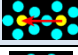
2.3.6 Catalog and composition of local structures
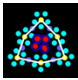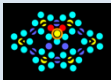
The observed local structures and extended defects and their individual compositions are summarized in the defect catalog for orthorhombic (Mo,V)O$_x$ mixed oxide (Table 2-1). In total, 19 different configurations were distinguished in different M1 crystals. While 16 configurations

vary in their structural composition, four of them are structurally identical, but were classified as a result of their appearance in different local environments. In addition, no evidence was found that these defective nano-structures could be formed during the exposure to the electron beam (Figure S2-17). These local deviations from the ideal M1 structure affect the local composition. The Mo/V ratio within the different defect structures varies (Table 2-1). For estimates of the defect composition the site occupancy of the different metal centers proposed for orthorhombic and trigonal structures was assumed.[21, 23] The preferred site occupancies in (Mo,V) based mixed oxides depend on the applied synthetic protocols.[18, 20-21, 26-28]

For instance, the particle presented in Figure 2-7b is characterized by a defect-free bulk structure, plus a plethora of different structural motifs, which were spotted at the surface of the *(a,b)* plane of the particle (Figure 2-7b). With regard to the composition of these local structures (Table 2-1) we find that the surface has a local composition of $(Mo_{610}V_{230}M_{70})O_x$, where M denotes metal sites of an uncertain composition (M= Mo and/or V). This composition can be converted into an M dependent vanadium content normalized to molybdenum, which ranges between 0.3 and 0.5. For comparison, the overall composition obtained from X-ray fluorescence (XRF) measurement is $(MoV_{0.4})O_x$, while the ideal bulk composition, which is derived from the local configuration (Table 2-1), is $(MoV_{0.27})O_x$. This result implies compositional differences between bulk and surface structure.

Table 2-1: Catalog of observed structures and their compositions.

Configuration	Schematics	Location[b]	Mo/V/M ratio crystal[b] (solely[c])	Normalized V content[d]	Total number of appearance[e]	Total area of extended defects /nm^2
			Local motifs			
Triangular motif (Figure 2-3c,2)		S	5.5/0.75 (19.25/0.75)	0.13	400	
Triangular motif (Figure 2-3c,3)[f]		S,I	4/3 (18/3)	0.75	690	
Mirrored motif		S,T,I,In	n.d.[g] (12/0)	0	210	
Translated motif		S,T,I,In	n.d. (12/0)	0	380	
Shared motif		S, In	n.d. (11/0)	0	120	
Twinned motif		S, In	n.d. (10/0)	0	20	

Rotated motif		S, In	n.d. (12/0/1-2)	0-0.17	80	
Tiling						
Orthorhombic M1		O	15.75/4.75 (40.5/6.5)	0.27	986000	Compare Table S-2-1
Orthorhombic rotated relatively to bulk		S	15.75/4.75 (40.5/6.5)	0.27	160	
Pseudo-trigonal		I, T	12/3.75 (37.5/6.75)	0.31	370	
		I, T	4/3 (18/3)	0.75	720	
Combined structures						
Quadrilateral arrangement		I	10.5/3/4 (36/6/4)	0.20-0.67	30	
Additional cation		S, In	15.75/4.25/1 (40.5/6.5/1)	0.25-0.33	70	
Intergrowth						
Pseudo-trigonal		along a-axis	n.d. (n.d)	n.d (n.d)	10	1229
Aperiodic	variable. higlighted with while outline		n.d (n.d)	n.d (n.d)	10	1861
Zipper-like		along b-axis	n.d. (n.d)	n.d (n.d)	2	27
Interstitial regions						
Pristine interstitial region		In	15.75/4.75 (40.5/6.5)	0.27	30	
Four-fold rotational interstitial region		In	53.63/10.50/2 (101/16.5/2)[i] ——— 53.54/14 (99.75/19.25)[j]	0.19-0.23 ——— 0.26	10	

Repetitive complex interstitial region		In	n.d (n.d.)	n.d	10	
Complex interstitial region	Yellow polygon with variable shape	In^k, $bulk^l$	n.d (n.d.)	n.d (n.d.)	10	200

[a] S: surface region, I: intergrowth, T: trigonal phase, In: interstitial region, O: orthorhombic phase

[b] nominal content of all cations in the structure, M corresponds to unidentified sites. Here, Mo, V are not distinguishable.

[c] nominal content taking the embedment of the local structure into the crystal into account, i.e. shared atoms at edges and vertexes. M corresponds to unidentified sites. Here, Mo, V are not distinguishable.

[d] V content normalized to Mo; the interval considers the borders between full occupancies of Mo or V of the unidentified sites.

[e] counted number of appearance. The rounded values account for the error of counting, and/or the uncertainty when the structure was not clear enough for counting.

[f] there is no difference between the triangular motif and the trigonal tile. Different coloring was only used to separate surface and intergrowth motifs.

[g] not distinguishable

[h] adjacent to both orthorhombic bulk tiles A and B.

[i] Figure 2-6b, [j] Figure S2-12

[k] discontinues the pseudo-trigonal intergrowth,

[l] interstitial-like region, surrounded only by bulk M1 structure and containing at least one motif.

2.4 Discussion and conclusions

2.4.1 Specific aspects on orthorhombic (Mo,V)Ox

The defects observed in orthorhombic $(Mo,V)O_x$ mixed oxide resemble those, which were found in complex metallic alloys. For instance, the orthorhombic metallic alloy phase T-Al-Pd-Mn has a local structure with 5-fold symmetry and can be described by a similar hexagon tiling.[15, 29] The structural similarity of the basic pentagonal units in complex metallic alloys promote a facile intermixing of structural units of different phases, which results in a facile

formation of planar defects, dislocations or phase boundaries.[30] The resulting low-strain connectivities form large and complex defect arrangements that consist of different phases. This behavior has been demonstrated for the intermixing of T- and R-phases or ε6- and ε28-phases in Al-Pd-Mn alloys.[15, 31-32] In addition, overlaps between atomic positions in neighboring pentagonal units reduce the distances between the centers of the units and can be considered as the origin of low strain defects and dislocations.[31] Similar intermixing and overlapping of structural units of different phases and pentagonal building blocks were also observed in orthorhombic $(Mo,V)O_x$ mixed oxide in the present study. Thus, the concept of structural intermixing, which causes the formation of different local and extended defects and/or nano-structures that are separated by a low energy barrier, can be transferred from complex alloys to complex mixed oxides with local 5-fold symmetry.

Triangular and linear motifs (mirrored, translated, shared, twinned, and rotated) as well as interstitial and interstitial-like regions described for orthorhombic $(Mo,V)O_x$ mixed oxide cataloged in the present work are in good agreement with the qualitative observations registered for $(Mo,V,Te,Nb)O_x$ M1 and M2 mixed oxides.[9, 19] The shared and twinned motifs are similar to structural defects reported for the pseudo-hexagonal M2 phase of multinary $(Mo,V,Nb,Te)O_x$ mixed oxide.[9] While in the defective M2 phase the shared and twinned motifs appear with large and small probability, respectively, our study shows that in orthorhombic $(Mo,V)O_x$ mixed oxide they occur only with a low probability compared to triangular, mirrored or translated motifs. The extended pseudo-trigonal intergrowth including the central pentagonal motif has already been reported before but important structural details, for example, the connectivity and orientation of the pentagonal center of the pseudo-trigonal intergrowth, were not analyzed.[10] Compared to the STEM images reported in the literature our investigation reveals important local atomistic differences in terms of participating pentagonal units.[10] Previous STEM images show that the pentagonal center of the pseudo-trigonal intergrowth is composed of two mirrored and one twinned motif. In our case the observed rotations result in the formation of one mirrored and two twinned motifs. Although this investigation does not focus on biasing factors for defects, it seems most likely that for this metastable complex oxide slight changes in the synthesis protocol, which involve crystallization temperature, time, and pH, may trigger the defect chemistry.

Details on the interplay of individual structures in these oxides can only be obtained by a three-step local analysis: First, the compositional modifications across individual crystals have to

be monitored and the effects of defects on the chemical bonding have to be understood. Second, the origin and pathways of vanadium surface migration have to be found and third, the relevant steady state motifs have to be assigned by theory to model their electronic structure and to sort local oxygen binding. The first cut in this long path has been successfully completed in the present work as far as $(Mo,V)O_x$ mixed oxide is concerned.

2.4.2 General impact on heterogeneous catalysis

The surface and bulk structure of model systems and relevant oxidation catalysts are different.[33-35] Owing to the absence of translational symmetry at the surface a direct determination of the surface structure is difficult. Surface science has developed techniques that allow the determination of atomic-scale properties of single crystal surfaces usually in ultrahigh vacuum (UHV) with high accuracy. Currently, increasing efforts have been devoted to surface structure and reactivity of metal oxides thin films.[36] Advancements in an atomistic description of the surface structure by thin film studies are limited by the inherent lack of surface-bulk (-support) interactions. Rare insights into the surface-bulk-interplay of relevant catalytic systems were obtained by TEM investigation, which revealed the presence of amorphous surface layers and spectroscopy, which demonstrated a structurally decoupled bulk and surface structure.[37-38] In addition, surface instabilities and dynamics complicate the reproduction of their structures.[21] The activity of a heterogeneous catalyst relies on the balanced interplay of compositional and structural parameters.[1, 8] Atomic differences in the bulk and surface structure of catalysts can be considered as geometric and electronic descriptors, which can discriminate their performance. Defects at the surface, for instance, can be considered as high energy centers. These high energy centers influence the surface termination and realize geometric and electronic surface structures, which can (i) regulate the electron-surface supply and (ii) response differently to the applied chemical potential.[21, 33] Our quantitative study shows that the defect concentration is particles dependent and it seems likely that each particle performs differently in a given catalytic reaction. It is worth noting that the activity of this class of material is expected to rely on synergistic surface effects of decoupled and defective surface structures, which can be considered as local nano-domains.[39-40] The unequal defect distribution and intermixing may render a macroscopically homogeneous sample locally heterogeneous. Our study can be considered as a general route of how such inter- and intra-structural complexity, far beyond translational-symmetry, can be analyzed. Complementary to the integral information provided by surface

spectroscopy our quantitative real space imaging approach directly pinpoints the positions and distribution of atoms, their distances and angles. The local structural modifications that are summarized in our defect catalog represent atomistic details that may be responsible for the activity of an oxidation catalyst. To elucidate the influence of the described defects on the catalytic performance, synthetic routines have to be developed to tailor individual local nano-structures at the surface. In addition, theoretical studies that consider the individual and/or a combination of defects are, therefore, of paramount importance.

2.5 Methods

Sample preparation.

The orthorhombic $(Mo,V)O_x$ mixed oxide (internal ID 20000) was prepared by hydrothermal synthesis. A specially built reactor (Premex Reactor AG, Lengnau, Switzerland) from corrosion resistant Hastelloy C-22 (2.4602) was utilized, which enables precise control of the reaction parameters. A mixture of 9.18 g $(NH_4)_6Mo_7O_{24}\cdot4H_2O$ (AHM, Merck, 52 mmol Mo) dissolved in 230 g water (Milli-Q, Merck) and 3.30 g $VOSO_4$ (Acros Organics, 12.9 mmol V) dissolved in 30 g water was loaded into a hydrothermal reactor at room temperature. Residual air was replaced by nitrogen. Subsequently the vessel was heated to 200°C at a rate of 1°C/min and hold at this temperature for 17 h. The reaction mixture is stirred during the whole experiment at a rate of 100 rpm. After cooling to room temperature, a black solid was isolated by filtration (pore 5 glass frit), washed twice with distilled water and dried at 80°C for 16 hours. To remove amorphous components in the hydrothermal product, 1 g of the powder was washed with 25 ml oxalic acid solution (0.25 M, Acros Organics) at 60°C for 30 min under stirring. The solid was centrifuged (5000 rpm, 30 min), washed twice with 25 ml water and dried at 80°C over night. Finally, a thermal treatment was performed in argon atmosphere at 400°C (heating rate 10°C/min) for 2 h in a rotary tube furnace (Xerion, Freiberg, Germany).

TEM.

Aberration-corrected scanning transmission electron microscopy (STEM) was performed on a JEM-ARM200F microscope with CEOS CESCOR and CEOS CETCOR hexapole aberration correctors for probe and image forming lenses, respectively, and a cold field emission gun (CFEG). STEM images were recorded with a JEOL high angle annular dark-field (HAADF) detector, respectively. Prior to the measurements, the powdered material was drop deposited on a

holey silica oxide coated gold TEM grid. Prior to the HAADF-STEM analysis each particle was oriented along the crystallographic *c*-axis.

XRD.

XRD measurements were performed in Bragg-Brentano geometry on a Bruker AXS D8 Advance II theta/theta diffractometer using Ni filtered Cu Kα radiation and a position sensitive energy dispersive LynxEye silicon strip detector. The sample powder was filled into the recess of a cup-shaped sample holder, the surface of the powder bed being flush with the sample holder edge (front loading).

XRF.

The XRF measurements were carried on with XRF X-ray Florescence Spectrometer Pioneer S4 (Bruker). The measurements were performed in vacuum using 100 mg of the sample, molten together with 8.9 g of di-Li-tetraborate, in a form of the glass disc with 40 mm diameter. The K-alpha lines were analyzed applying the calibration factors derived from the FHI-made appropriate standards.

2.6 References

1.   Taylor, H. S., A Theory of the Catalytic Surface. *Proc. R. Soc. London A* **1925,** *108* (745), 105-111.

2.   Qing-Hua, Z.; Dong-Dong, X.; Lin, G., Aberration-corrected scanning transmission electron microscopy for complex transition metal oxides. *Chin. Phys. B* **2016,** *25* (6), 066803.

3.   Yang, J. C.; Small, M. W.; Grieshaber, R. V.; Nuzzo, R. G., Recent developments and applications of electron microscopy to heterogeneous catalysis. *Chem. Soc. Rev.* **2012,** *41* (24), 8179-8194.

4.   Vendelbo, S. B.; Elkjær, C. F.; Falsig, H.; Puspitasari, I.; Dona, P.; Mele, L.; Morana, B.; Nelissen, B. J.; van Rijn, R.; Creemer, J. F.; Kooyman, P. J.; Helveg, S., Visualization of oscillatory behaviour of Pt nanoparticles catalysing CO oxidation. *Nat. Mater.* **2014,** *13* (9), 884-890.

5.   Lunkenbein, T.; Schumann, J.; Behrens, M.; Schlogl, R.; Willinger, M. G., Formation of a ZnO Overlayer in Industrial $Cu/ZnO/Al_2O_3$ Catalysts Induced by Strong Metal-Support Interactions. *Angew. Chem., Int. Ed.* **2015,** *54* (15), 4544-4548.

6.   Lunkenbein, T.; Girgsdies, F.; Kandemir, T.; Thomas, N.; Behrens, M.; Schlögl, R.; Frei, E., Bridging the Time Gap: A Copper/Zinc Oxide/Aluminum Oxide Catalyst for Methanol Synthesis Studied under Industrially Relevant Conditions and Time Scales. *Angew. Chem., Int. Ed.* **2016,** *55* (41), 12708-12712.

7.   Li, X.; Lunkenbein, T.; Pfeifer, V.; Jastak, M.; Nielsen, P. K.; Girgsdies, F.; Knop-Gericke, A.; Rosowski, F.; Schlogl, R.; Trunschke, A., Selective Alkane Oxidation by Manganese Oxide: Site Isolation of MnO_x Chains at the Surface of $MnWO_4$ Nanorods. *Angew. Chem., Int. Ed.* **2016,** *55* (12), 4092-4096.

8.   Konya, T.; Katou, T.; Murayama, T.; Ishikawa, S.; Sadakane, M.; Buttrey, D.; Ueda, W., An orthorhombic Mo_3VO_x catalyst most active for oxidative dehydrogenation of ethane among related complex metal oxides. *Catal. Sci. Technol.* **2013,** *3* (2), 380-387.

9.   Vogt, T.; Blom, D. A.; Jones, L.; Buttrey, D. J., ADF-STEM Imaging of Nascent Phases and Extended Disorder Within the Mo–V–Nb–Te–O Catalyst System. *Top. Catal.* **2016,** *59*, 1489–1495.

10.   Pyrz, W. D.; Blom, D. A.; Sadakane, M.; Kodato, K.; Ueda, W.; Vogt, T.; Buttrey, D. J., Atomic-level imaging of Mo-V-O complex oxide phase intergrowth, grain boundaries, and defects using HAADF-STEM. *P Natl Acad Sci USA* **2010,** *107* (14), 6152-6157.

11.   Pyrz, W. D.; Blom, D. A.; Sadakane, M.; Kodato, K.; Ueda, W.; Vogt, T.; Buttrey, D. J., Atomic-Scale Investigation of Two-Component MoVO Complex Oxide Catalysts Using Aberration-Corrected High-Angle Annular Dark-Field Imaging. *Chem. Mater.* **2010,** *22* (6), 2033-2040.

12.   Lunkenbein, T.; Girgsdies, F.; Wernbacher, A.; Noack, J.; Auffermann, G.; Yasuhara, A.; Klein-Hoffmann, A.; Ueda, W.; Eichelbaum, M.; Trunschke, A.; Schlogl, R.; Willinger, M. G., Direct Imaging of Octahedral Distortion in a Complex Molybdenum Vanadium Mixed Oxide. *Angew. Chem., Int. Ed.* **2015,** *54* (23), 6828-6831.

13.   Penrose, R., Pentaplexity A Class of Non-Periodic Tilings of the Plane. *The Mathematical Intelligencer* **1979,** *2* (1), 32-37.

14.   Hermann, K., Bulk Crystals: Three-Dimensional Lattices. In *Crystallography and Surface Structure: An Introduction for Surface Scientists and Nanoscientists*, Wiley-VCH Verlag GmbH & Co. KGaA: 2016; pp 7-89.

15.   Heggen, M.; Houben, L.; Feuerbacher, M., Plastic-deformation mechanism in complex solids. *Nat. Mater.* **2010,** *9* (4), 332-336.

16.   Sadakane, M.; Endo, K.; Kodato, K.; Ishikawa, S.; Murayama, T.; Ueda, W., Assembly of a Pentagonal Polyoxomolybdate Building Block, $[Mo_6O_{21}]^{6-}$, into Crystalline MoV Oxides. *Eur. J. Inorg. Chem.* **2013,** *2013* (10-11), 1731-1736.

17.   Sadakane, M.; Ueda, W., Building Block Synthesis of Crystalline Mo-V-based Oxides: Selective Oxidation Catalysts. *J. Jpn. Petrol. Inst.* **2012,** *55* (4), 229-235.

18.   Sadakane, M.; Yamagata, K.; Kodato, K.; Endo, K.; Toriumi, K.; Ozawa, Y.; Ozeki, T.; Nagai, T.; Matsui, Y.; Sakaguchi, N.; Pyrz, W. D.; Buttrey, D. J.; Blom, D. A.; Vogt, T.; Ueda, W., Synthesis of Orthorhombic Mo-V-Sb Oxide Species by Assembly of Pentagonal Mo_6O_{21} Polyoxometalate Building Blocks. *Angew. Chem., Int. Ed.* **2009,** *48* (21), 3782-3786.

19.   Blom, D. A.; Vogt, T.; Allard, L. F.; Buttrey, D. J., Observation of Sublattice Disordering of the Catalytic Sites in a Complex Mo-V-Nb-Te-O Oxidation Catalyst Using High Temperature STEM Imaging. *Top. Catal.* **2014,** *57* (14-16), 1138-1144.

20. Ishikawa, S.; Kobayashi, D.; Konya, T.; Ohmura, S.; Murayama, T.; Yasuda, N.; Sadakane, M.; Ueda, W., Redox Treatment of Orthorhombic $Mo_{29}V_{11}O_{112}$ and Relationships between Crystal Structure, Microporosity and Catalytic Performance for Selective Oxidation of Ethane. *J. Phys. Chem. C* **2015,** *119* (13), 7195-7206.

21. Trunschke, A.; Noack, J.; Trojanov, S.; Girgsdies, F.; Lunkenbein, T.; Pfeifer, V.; Hävecker, M.; Kube, P.; Sprung, C.; Rosowski, F.; Schlögl, R., The Impact of the Bulk Structure on Surface Dynamics of Complex Mo–V-based Oxide Catalysts. *ACS Catal.* **2017,** *7* (4), 3061-3071.

22. Ok, K. M.; Halasyamani, P. S.; Casanova, D.; Llunell, M.; Alemany, P.; Alvarez, S., Distortions in octahedrally coordinated d^0 transition metal oxides: A continuous symmetry measures approach. *Chem. Mater.* **2006,** *18* (14), 3176-3183.

23. Sadakane, M.; Watanabe, N.; Katou, T.; Nodasaka, Y.; Ueda, W., Crystalline Mo_3VO_x Mixed-Metal-Oxide Catalyst with Trigonal Symmetry. *Angew. Chem.* **2007,** *119* (9), 1515-1518.

24. Ishikawa, S.; Tashiro, M.; Murayama, T.; Ueda, W., Seed-assisted synthesis of crystalline Mo_3VO_x oxides and their crystal formation mechanism. *Cryst. Growth Des.* **2014,** *14* (9), 4553-4561.

25. Ishikawa, S.; Murayama, T.; Ohmura, S.; Sadakane, M.; Ueda, W., Synthesis of Novel Orthorhombic Mo and V Based Complex Oxides Coordinating Alkylammonium Cation in Its Heptagonal Channel and Their Application as a Catalyst. *Chem. Mater.* **2013,** *25* (11), 2211-2219.

26. DeSanto, P. j.; Buttrey, D. J.; Grasselli, R. K.; Lugmair, C. G.; Volpe, A. F. j.; Toby, B. H.; Vogt, T., Structural aspects of the M1 and M2 phases in Mo V Nb Te O propane ammoxidation catalysts. *Z. Kristallogr.* **2004,** *219*, 152-165.

27. DeSanto, P.; Buttrey, D. J.; Grasselli, R. K.; Pyrz, W. D.; Lugmair, C. G.; Volpe, A. F.; Vogt, T.; Toby, B. H., Comparison of MoVTaTeO and MoVNbTeO M1 crystal chemistry. *Top. Catal.* **2006,** *38* (1-3), 31-40.

28. Murayama, H.; Vitry, D.; Ueda, W.; Fuchs, G.; Anne, M.; Dubois, J. L., Structure characterization of orthorhombic phase in MoVTeNbO catalyst by powder X-ray diffraction and XANES. *Appl. Catal., A* **2007,** *318* (0), 137-142.

29.   Balanetskyy, S.; Meisterernst, G.; Heggen, M.; Feuerbacher, M., Reinvestigation of the Al–Mn–Pd alloy system in the vicinity of the T- and R-phases. *Intermetallics* **2008,** *16* (1), 71-87.

30.   Feuerbacher, M.; Heggen, M., Elastic energy of metadislocations in complex metallic alloys. *Acta Mater.* **2012,** *60* (4), 1703-1711.

31.   Heggen, M.; Feuerbacher, M., Metadislocation core structure and atomic model for metadislocation motion. *Acta Mater.* **2013,** *61* (10), 3851-3857.

32.   Feuerbacher, M.; Heggen, M., Metadislocations. In *Dislocations in Solids*, Hirth, J. P.; Kubin, L., Eds. Elsevier: 2010; Vol. 16, pp 109-170.

33.   Schlögl, R., Selective Oxidation: From a Still Immature Technology to the Roots of Catalysis Science. *Top. Catal.* **2016,** *59* (17), 1461-1476.

34.   Freund, H. J.; Kuhlenbeck, H.; Staemmler, V., Oxide surfaces. *Rep. Prog. Phys.* **1996,** *59* (3), 283-347.

35.   Sterrer, M.; Freund, H.-J., Properties of Oxide Surfaces. In *Surface and Interface Science*, Wiley-VCH Verlag GmbH & Co. KGaA: 2013; pp 229-278.

36.   Kuhlenbeck, H.; Shaikhutdinov, S.; Freund, H.-J., Well-Ordered Transition Metal Oxide Layers in Model Catalysis – A Series of Case Studies. *Chem. Rev.* **2013,** *113* (6), 3986-4034.

37.   Guliants, V. V.; Benziger, J. B.; Sundaresan, S.; Yao, N.; Wachs, I. E., Evolution of the active surface of the vanadyl pyrophosphate catalysts. *Catal. Lett.* **1995,** *32* (3), 379-386.

38.   Heine, C.; Hävecker, M.; Sanchez-Sanchez, M.; Trunschke, A.; Schlögl, R.; Eichelbaum, M., Work function, band bending, and microwave conductivity studies on the selective alkane oxidation catalyst MoVTeNb oxide (orthorhombic M1 phase) under operation conditions. *J. Phys. Chem. C* **2013,** *117* (51), 26988-26997.

39.   He, Q.; Woo, J.; Belianinov, A.; Guliants, V. V.; Borisevich, A. Y., Better Catalysts through Microscopy: Mesoscale M1/M2 Intergrowth in Molybdenum–Vanadium Based Complex Oxide Catalysts for Propane Ammoxidation. *ACS Nano* **2015,** *9* (4), 3470-3478.

40.   Bordes, E., Synergistic effects in selective oxidation catalysis: does phase cooperation result in site isolation? *Topics in Catalysis* **2001,** *15* (2), 131-137.

2.7 Supporting information
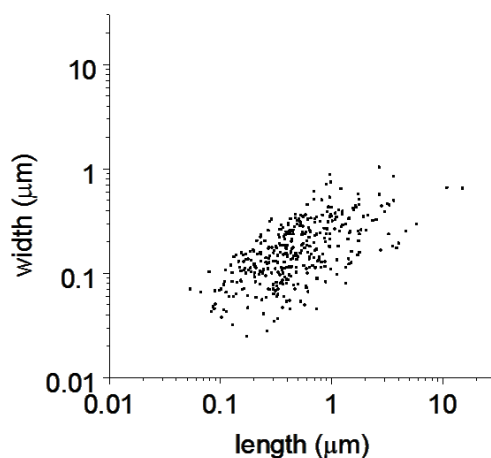
Figure S2-1: Size distribution of lengths and widths of (Mo,V)O$_x$ particles based on TEM images. The total analysis included the evaluation of 365 individual particles. The distribution highlights the presence of mainly rod-like particles.
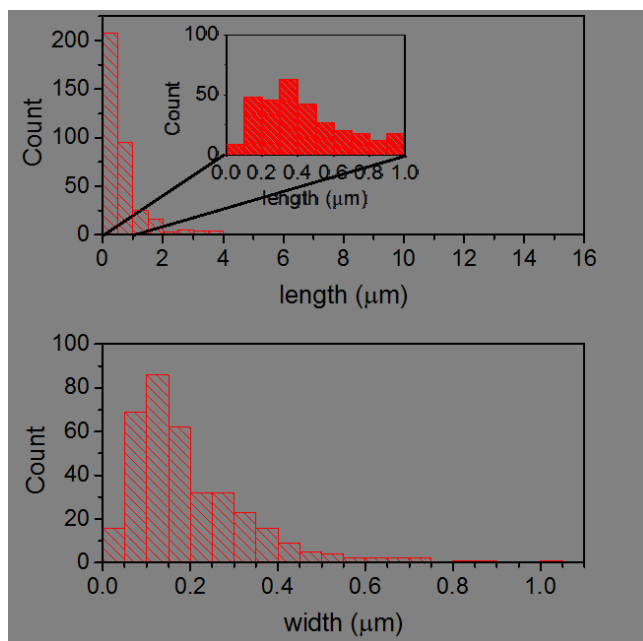
Figure S2-2: Occurrence of different sized particles represented as a function of their lengths (top) and widths (bottom). Data were taken from Figure S2-1.
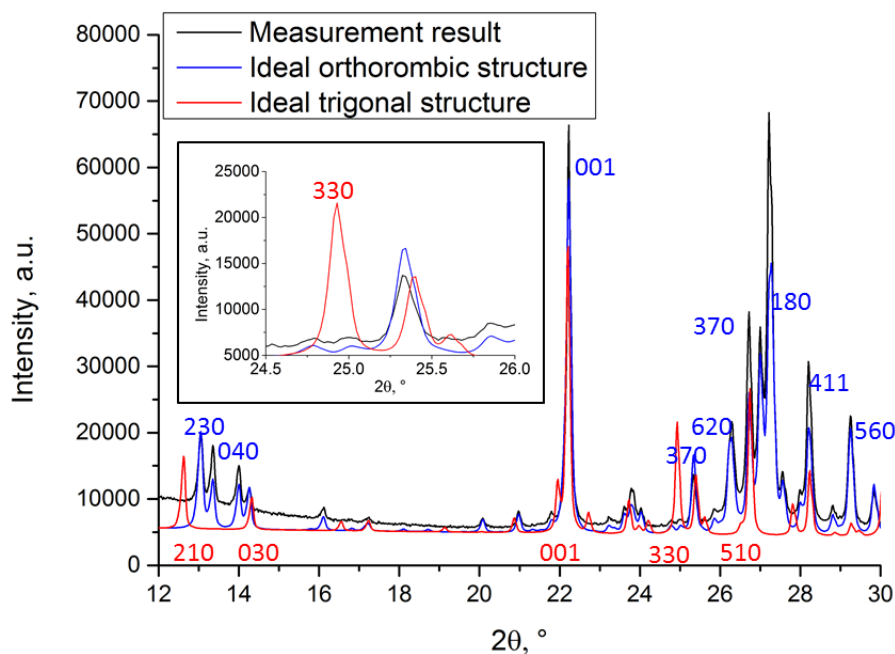
Figure S2-3: Comparison of the measured XRD pattern (black) of the investigated (Mo,V)Ox with different complex molybdenum vanadium oxide reference pattern obtained from the literature: orthorhombic (blue) and trigonal (red) structures.[1,2] The obtained data do not show any peak, which is not attributable to the orthorhombic structure. Unique reflections of the trigonal phase are missing (inset). This indicates that the domains of the trigonal defects observed by TEM are too small or too rare to be observable by XRD. Due to the rod-like growth of the M1 crystals along the *c*-axis, the measured pattern exhibits a pronounced preferred orientation effect. Especially the 00l reflections are reduced in intensity due to the measurement geometry (reflection mode, front loading). The intensity differences between the black and blue curve result from shortcomings of the preferred orientation model used in the Rietveld simulation. The observed peak widths appear isotropic and indicate domain sizes larger than 100 nm for all crystal directions.

Table S2-1 Defect analysis for individual particles.

Particle number	Total area/ 1000 nm$^{2\,a}$	Defect area/ 1000 nm$^{2\,b}$ (%)
1	27	0.19 (0.7)
2	6.1	0.16 (2.6)
3	23	0.67 (2.8)
4	6.6	0.20 (3.0)
5	15	< 0.08 (<0.5)
6	5.4	< 0.03 (<0.5)
7	9.7	0.17 (1.8)
8	14	0.12 (0.8)
9	2.8	0.14 (5.1)
10	1.3	0.07 (5.3)
11	52	6.4 (12.2)
12	15	0.78 (5.3)
13	10	< 0.05 (<0.5)
14	27	< 0.14 (<0.5)
15	36	0.65 (1.8)
16	5.4	0.08 (1.6)
17	3.5	< 0.02 (<0.5)
18	8.5	< 0.04 (<0.5)
19	30	0.62 (2.1)
20	11	< 0.06 (<0.5)
21	3.3	1.1 (33)
22	3.0	0.28 (9.3)
23	12	<0.06 (<0.5)
24	230	1.4 (0.6)
25	40	1.0 (2.5)
26	22	<0.1 (<0.5)
27	53	0.67 (1.3)
28	36	0.68 (1.8)
29	22	0.30 (1.4)
30	30	0.15 (0.5)
31	1.3	0.045 (3.3)

[a] Total area of the individual particle as obtained from HAADF-STEM images.

[b] Defect area as obtained from HAADF-STEM images for the same particle.
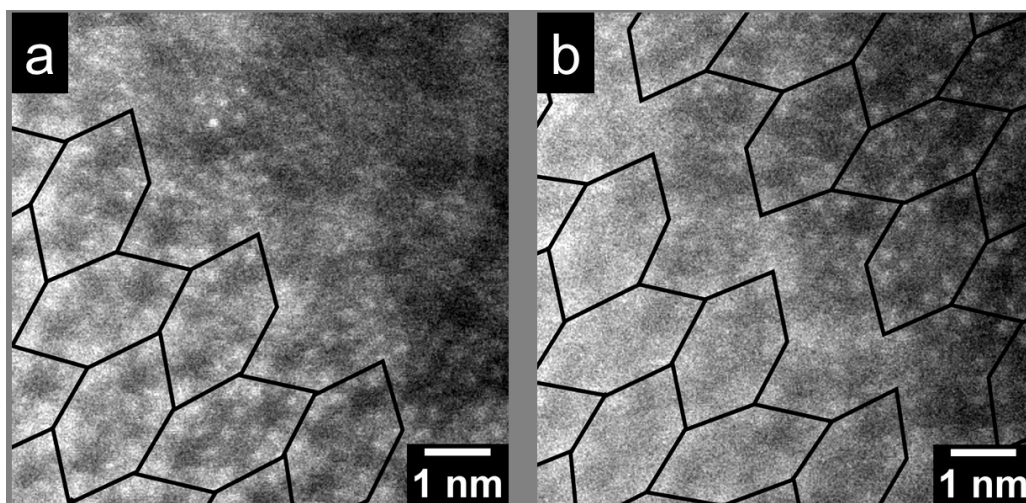
Figure S2-4: HAADF-STEM images of the same regions recorded at different focus of a) crystallite 1 and b) crystallite 2: black hexagons: the M1 structure.
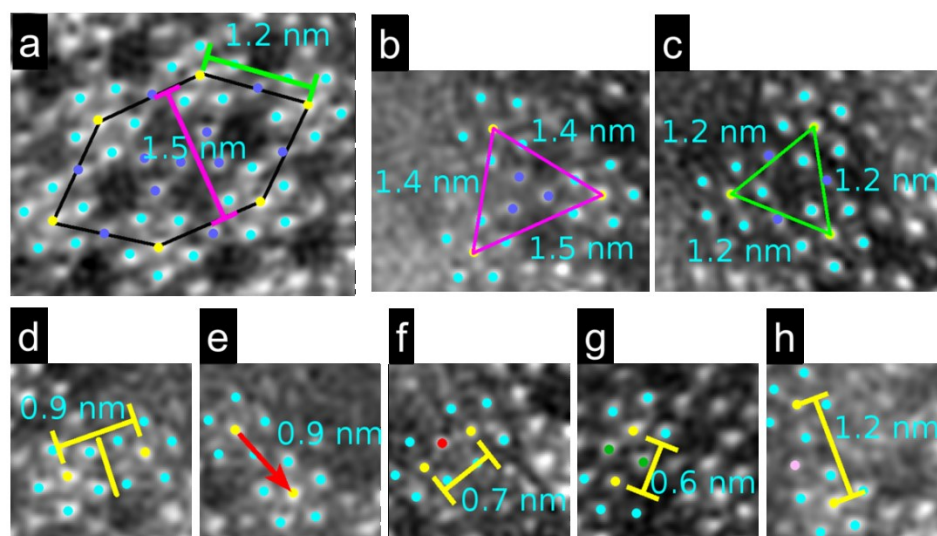
Figure S2-5: HAADF-STEM images of the observed structural motifs that correspond to the scheme representation presented in Figure 2-3c: a) the orthorhombic M1 tile (black hexagon), b) and c) different triangular motifs (magenta and green triangles), d) mirrored motif (yellow line: mirror plane), e) translated motif (red arrow: translation vector), f) shared motif (red circle: shared cation between two $\{(Mo)Mo_5O_{27}\}$ pentagonal units, g) twinned motif (green circles: two cations that are shared between two $\{(Mo)Mo_5O_{27}\}$ pentagonal units), h) rotated motif (pink circle(s): Mo or V cation(s), which does not belong to the $\{(Mo)Mo_5O_{27}\}$ pentagonal unit, but required for the stabilization of this motif). Yellow and cyan circles: cations of $\{(Mo)Mo_5O_{27}\}$ units; blue circles: cations mandatory for the orthorhombic structures and triangular motifs.
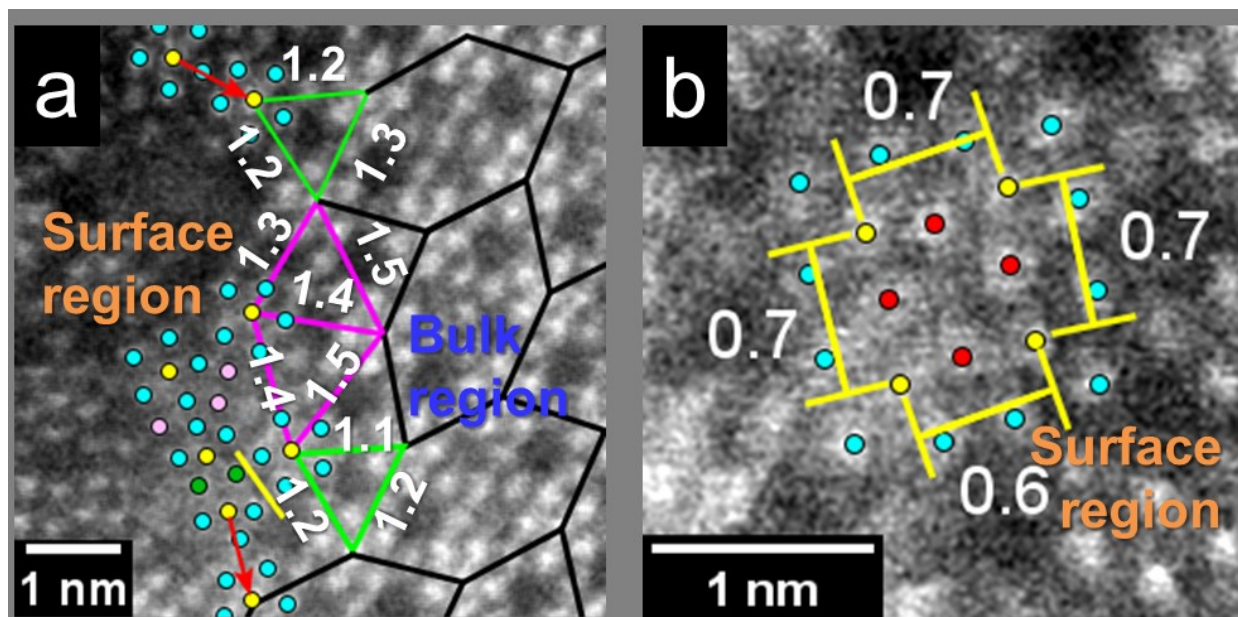
Figure S2-6: HAADF-STEM images of a) the interface between bulk and surface regions highlighting the influence of the local environment on the triangular motifs and b) a surface region that contains an unusual tetragon configuration of shared motifs. The distances are given in nm. Black hexagons: bulk M1 structure; magenta and green triangles: triangular motifs; yellow and cyan circles: cations of the $\{(Mo)Mo_5O_{27}\}$ pentagonal units; yellow line: mirror plane between two $\{(Mo)Mo_5O_{27}\}$ pentagonal units; red arrow: translated motif; red circles: shared cations between two $\{(Mo)Mo_5O_{27}\}$ pentagons; green circles: twinned motif; pink circles: rotated motifs.
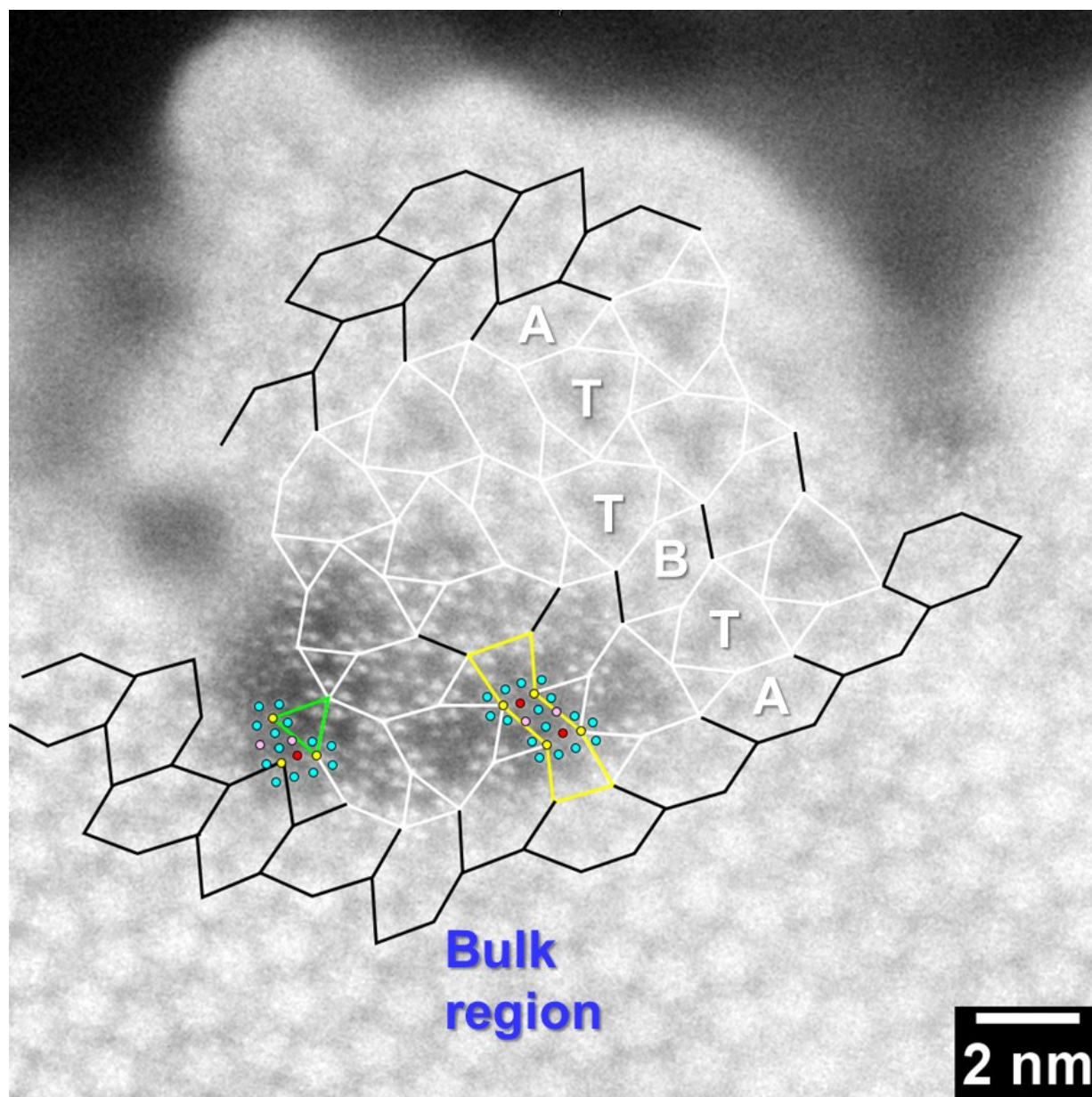
Figure S2-7: HAADF-STEM image of a ATTBTA tiling arrangement: Yellow polygon: termination of orthorhombic and trigonal structures. Black hexagons: bulk M1 structure; white standard hexagons: orthorhombic tiles that are rotated relatively to the bulk tiling; white arrowhead-shaped hexagons and triangles: trigonal tiling; green triangle: triangular motif; yellow and cyan circles: pentagonal {(Mo)Mo$_5$O$_{27}$} units; red circles: shared motifs; and pink circles: rotated motifs.
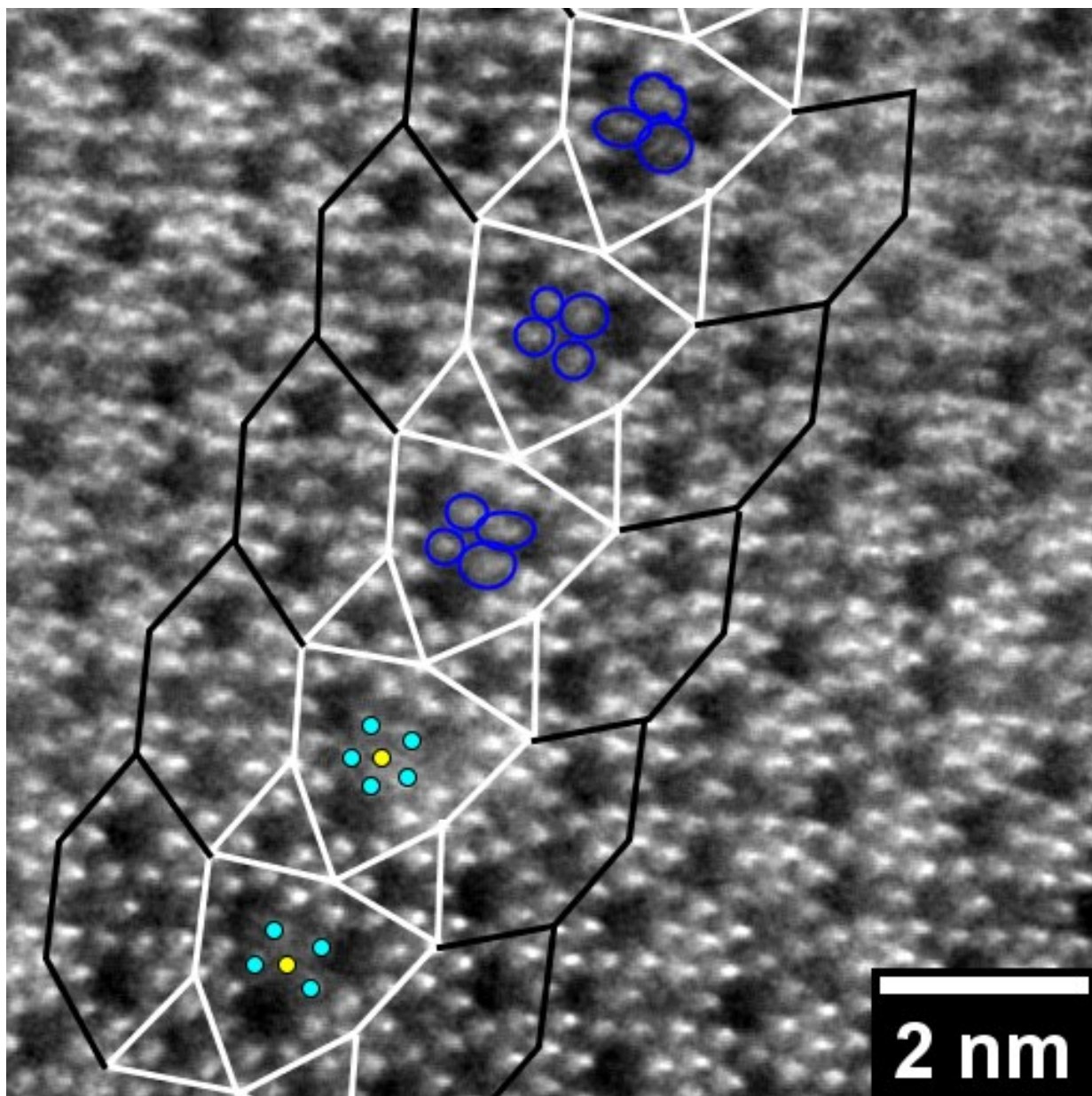
Figure S2-8: The HAADF-STEM image of a (Mo,V)O$_x$ crystal viewed along [001] focusing on the pseudo-trigonal intergrowth. Black hexagons: bulk M1 structure; white arrowhead-shaped hexagons and triangles: trigonal tiling of the pseudo-trigonal intergrowth; blue ovals: metal cations arranged in a quadrilateral configuration; yellow and cyan circles: cations of the {(Mo)Mo$_5$O$_{27}$} pentagonal units.
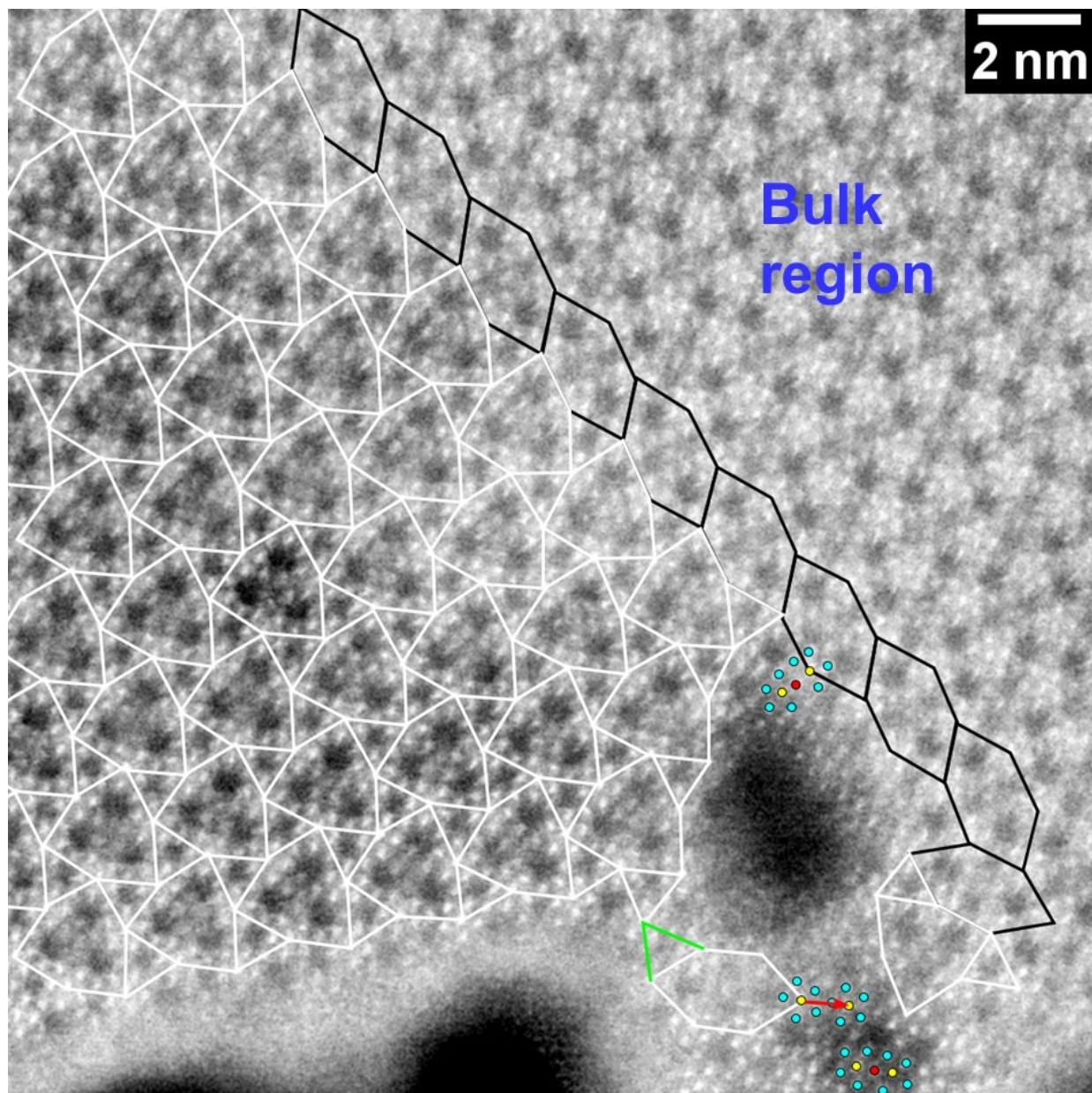
Figure S2-9: HAADF-STEM image of a trigonal add-phase connected to the orthorhombic bulk structure. Similar to the pseudo-trigonal intergrowth the connection proceeds along the crystallographic *a-axis* of the orthorhombic phase. Black hexagons: bulk M1 structure; white standard hexagons: orthorhombic tiles that are rotated relatively to the bulk tiling; white arrowhead-shaped hexagons and triangles: trigonal tiling; green triangle: triangular motif not connected to the trigonal phase; red arrow: translated motif; red circles: shared motifs; yellow and cyan circles: cations of the $\{(Mo)Mo_5O_{27}\}$ pentagonal unit.
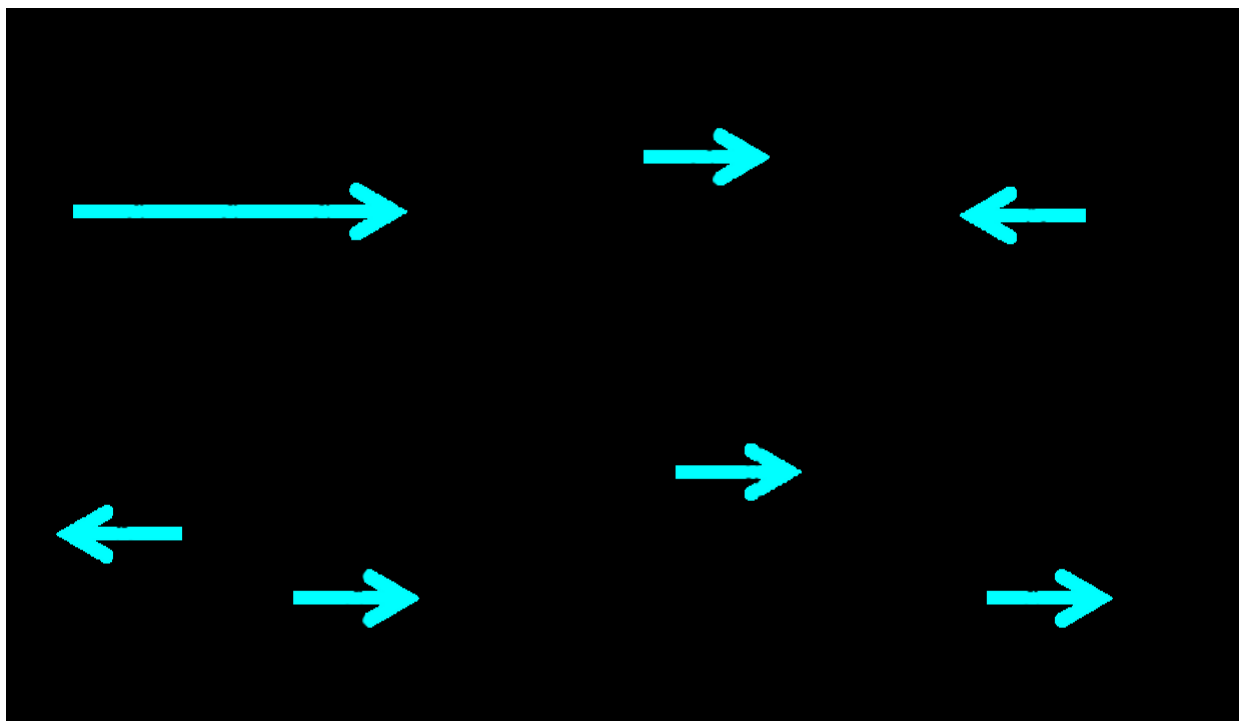
Figure S2-10: Schemes representing (a) the trigonal intergrowth and the most common geometries of the interstitial regions that influence the intergrowth directions: (b) type-1, (c) type-2 and (d) type-3. Cyan arrows: intergrowth direction.
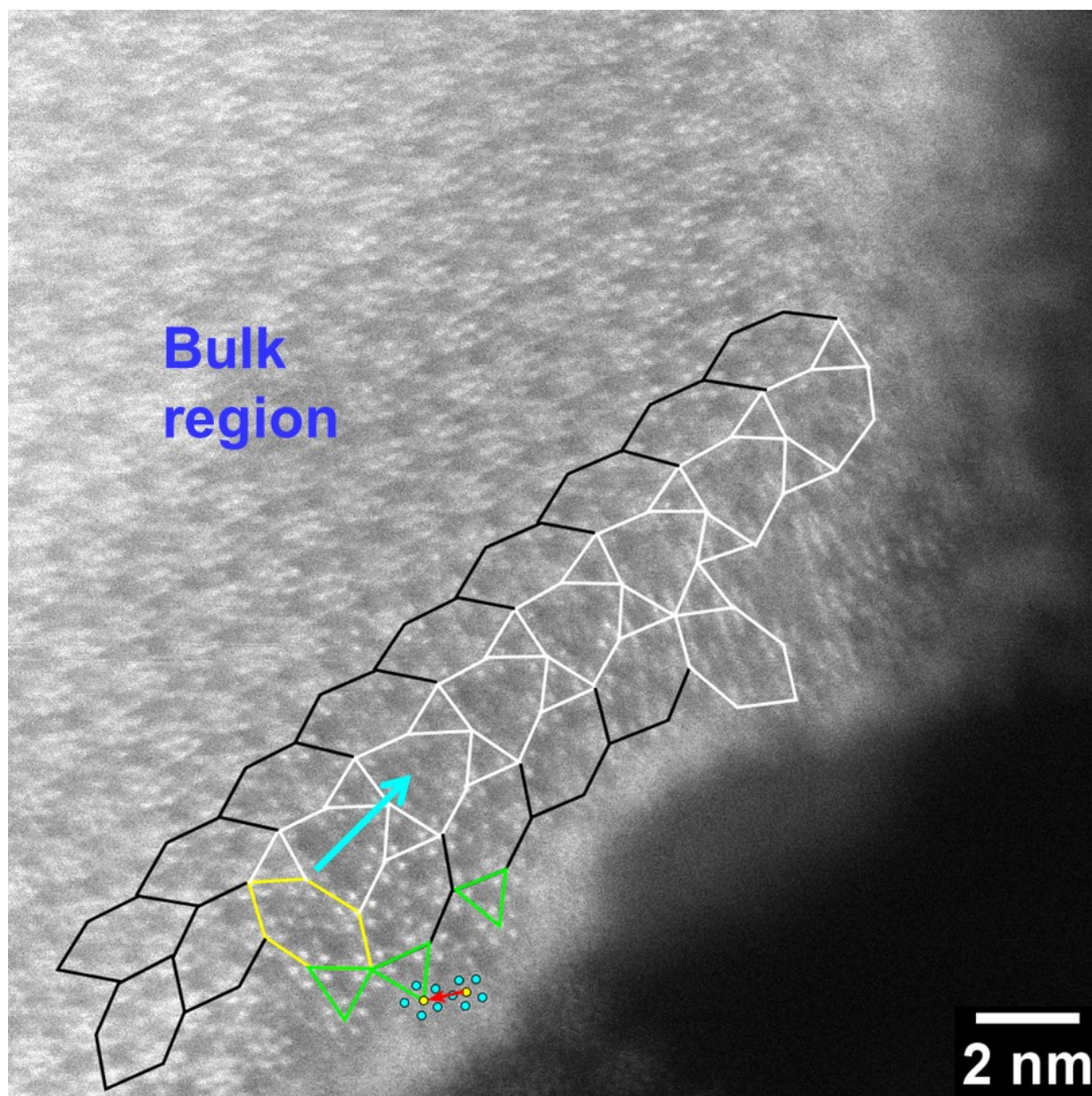
Figure S2-11: HAADF-STEM image of the pseudo-trigonal intergrowth starting from a pristine interstitial region (yellow hexagon). Black hexagons: bulk M1 structure; white arrowhead-shaped hexagons and triangles: trigonal tiling; cyan arrow: intergrowth direction; green triangles: triangular motifs; red arrow: translated motif; yellow and cyan circles: cations of the $\{(Mo)Mo_5O_{27}\}$ pentagonal units.
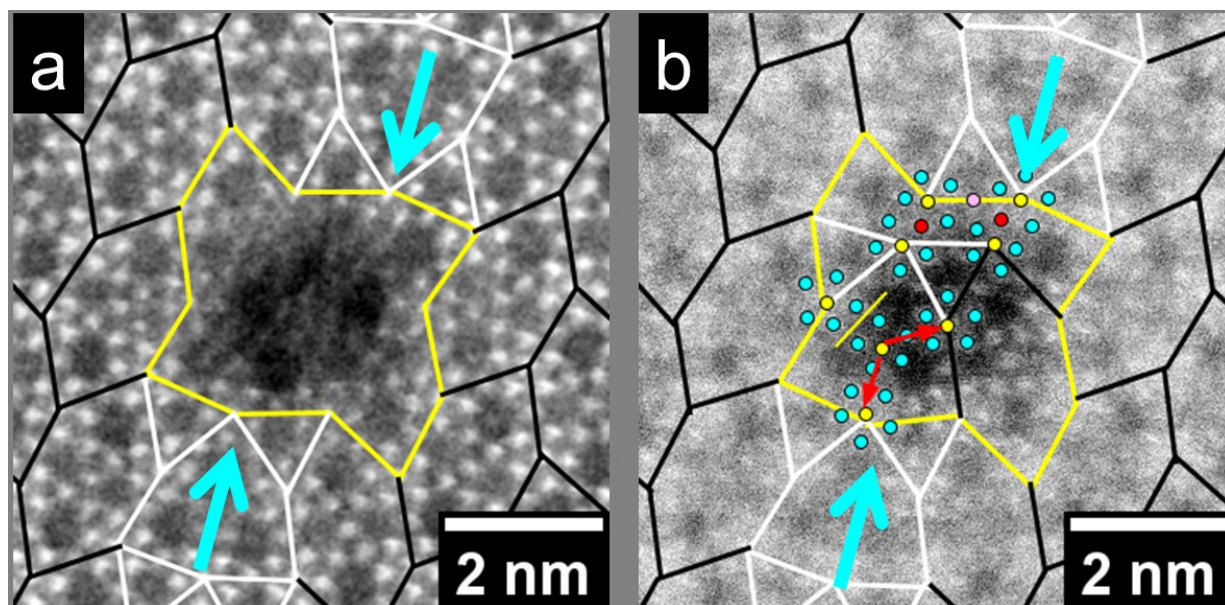
Figure S2-12: HAADF-STEM images of the same location focusing on a) the orthorhombic (black hexagons) and the pseudo-trigonal intergrowth (white arrowhead-shaped hexagon and triangle) surrounding an interstitial region (yellow) and b) the interstitial region. Furthermore, in b) the orthorhombic tile (black) and trigonal tile (white) can be observed within the interstitial region, leading to a structural arrangement similar to the one shown in Figure S2-7. The interstitial region contains two translated motifs (red arrows), one mirror motif (yellow line), two shared motifs (red circles) and one rotated motif (pink circle): cyan arrows: intergrowth direction, yellow and cyan circles: cations of the $\{(Mo)Mo_5O_{27}\}$ pentagonal units.
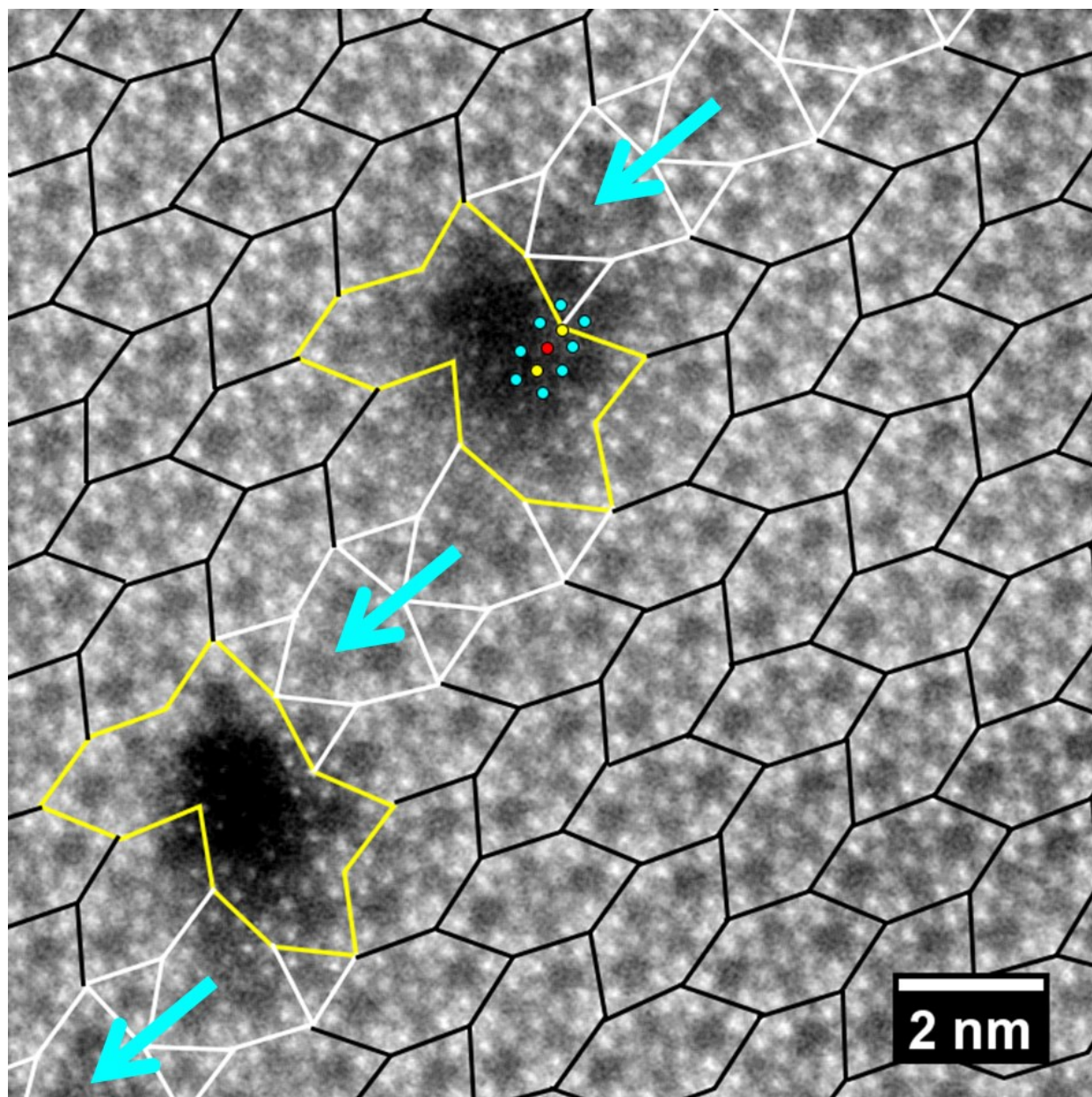
Figure S2-13: HAADF-STEM image of two complex interstitial regions (yellow polygons). Black hexagons: bulk M1 structure; white arrowhead-shaped hexagons and triangles: trigonal tiling; cyan arrows: intergrowth direction; red circle: shared motif; yellow and cyan circles: central and side cations of the $\{(Mo)Mo_5O_{27}\}$ pentagonal units.
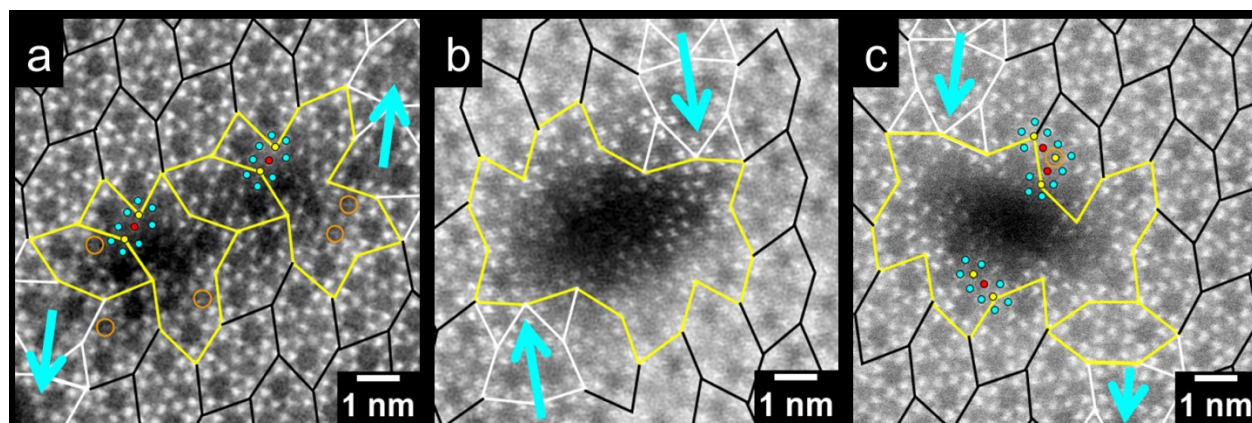
Figure S2-14: HAADF-STEM images of different complex interstitial regions (yellow polygons) with different directions (cyan arrows) of the pseudo-trigonal intergrowth (white arrowhead shaped tiling): (a) type-1, (b) type-2 and (c) type-3. Despite of its complexity the interstitial region shown in Figure S2-14b has a two-fold rotation symmetry of its outline. Tiles similar to the pristine interstitial region (Figure 2-6a, yellow hexagon) can sometimes be separated. Black hexagons: bulk M1 structure; white arrowhead-shaped hexagons and triangles: trigonal tiling; orange circles: electron density in the center of the channels that cannot be observed by HAADF-STEM imaging in the standard bulk structure; cyan arrows: intergrowth directions; red circles: shared motifs; yellow and cyan circles: cations of the $\{(Mo)Mo_5O_{27}\}$ pentagonal units.
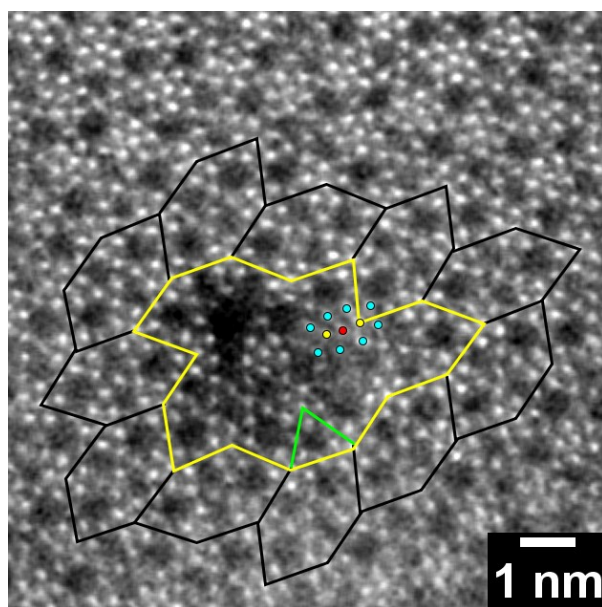
Figure S2-15: HAADF-STEM image of the interstitial-like region (yellow polygon). Black hexagons: bulk M1 structure; green triangle: triangular motif; red circle: shared motif.
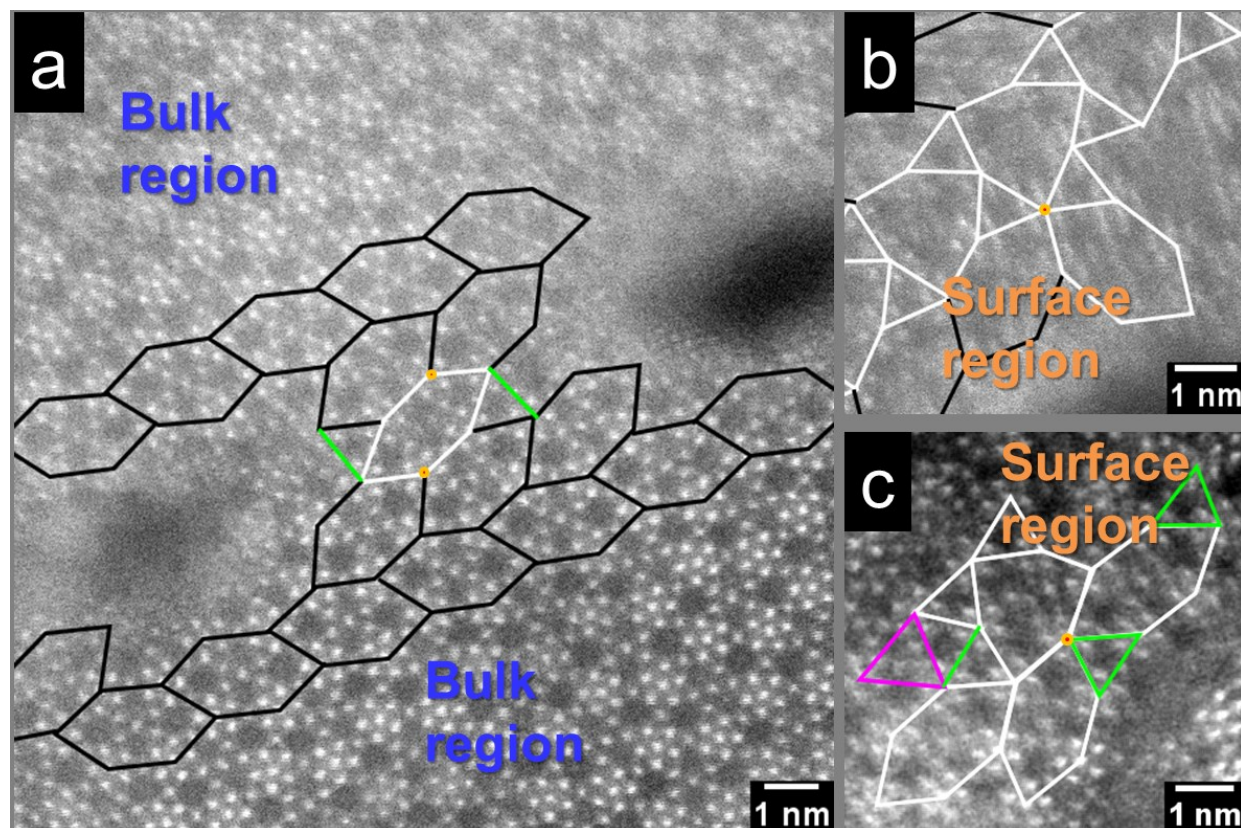
Figure S2-16: HAADF-STEM images of the rarest combination of tiles: (a) corresponds to Figure 2-7a-4; (b) is depicted in Figure 2-7a-5 and (c) is highlighted in Figure 2-7a-6. Black hexagons: bulk M1 structure; white standard hexagons: orthorhombic tiles that are rotated relatively to the bulk tiling; white arrowhead-shaped hexagons and triangles: trigonal tiling; orange circles: corner angles (compare Figure 2-7); pink and green triangles: triangular motifs.

Table S2-2: Evaluation of the combinations of different orthorhombic and trigonal tiles listed by their occurrence and mismatch of summed corner angles of joining tiles to 360°.

Occurrence group (Figure 2-7A)	Structure type	Structural angles combination[a]						Sum angle, °	Corner angle mismatch, °[b]
		α, 77°	β, 141°	γ, 142°	δ, 60°	ε, 84°	ζ, 156°		
1,4	Orthorhombic structure, intergrowth	1	1	1				360	0
		1	2					359	1
		1		2				361	1
1	Trigonal structure				2	1	1	360	0
2	Trigonal intergrowth	1	1		1	1		362	2
		1		1	1	1		363	3
				1	1		1	358	2
			1		1		1	357	3
3	Surface, boundary regions		2			1		367	6
			1	1		1		366	7
				2		1		368	8
		2		1	1			355	4
		2	1		1			356	5
5	Surface	2			2	1		358	2
6		2			1		1	370	10
	Non-observed[c]	1	1				1	374	14
			1			1	1	381	21

[a] The angles correspond to the ideal tiling (crystal structure) and are labeled according to Figures 2-1b and 2-4b.

[b] The exact match of the sum angle to 360° indicates a planar configuration of the contacting tiles. Other angles suggest the presence of disclinations or inclinations.

[c] Further possible and not observed configuration. Theoretically a large number of configurations far from the planar arrangement can also exist.

In order to check whether the observed nano-structures could be formed during imaging, we induced beam damage to the sample (Figure S2-17). We found that at a magnification higher than 12000000x holes start to appear, which could be related to thickness changes of an otherwise ideal M1 microstructure (Figure S2-17a). In addition after prolonged exposure of selected spots (Figure S2-17b) or area (Figure S2-17c,d) holes are formed, which exhibit a blurred surrounding. In none of the beam induced scenarios any of the described nano-structures were formed.
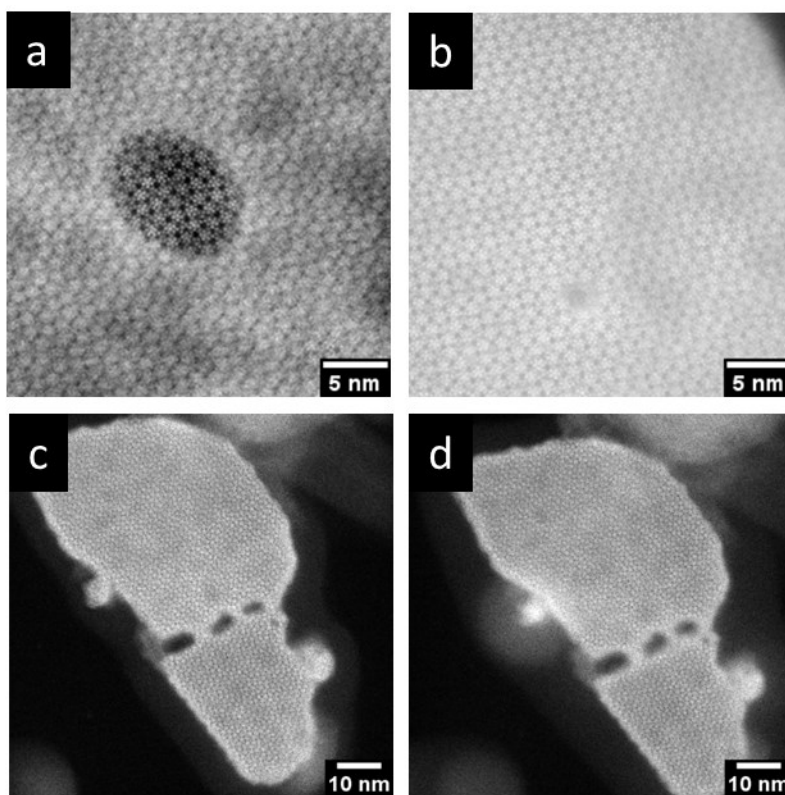
Figure S2-17: HAADF-STEM images of (Mo,V)O$_x$ after induction of beam damage.

1.   Trunschke, A.; Noack, J.; Trojanov, S.; Girgsdies, F.; Lunkenbein, T.; Pfeifer, V.; Hävecker, M.; Kube, P.; Sprung, C.; Rosowski, F., et al. The Impact of the Bulk Structure on Surface Dynamics of Complex Mo–V-Based Oxide Catalysts. *ACS Catal.* **2017**, *7*, 3061-3071.

2.   Sadakane, M.; Watanabe, N.; Katou, T.; Nodasaka, Y.; Ueda, W. Crystalline Mo$_3$VO$_x$ Mixed-Metal-Oxide Catalyst with Trigonal Symmetry. *Angew. Chem.* **2007,** *119*, 1515-1518.

3 Towards the metal distribution in complex mixed metal oxide catalysts

3.1 Abstract

The real structure and composition of a heterogeneous catalyst can locally deviate from their idealized bulk and surface analogues. However, their determination is difficult due to their appearance on the nanoscale and statistic distribution. Here, we present a qualitative investigation of the local fluctuations of the composition on the atomic level of orthorhombic $(Mo,V)O_x$ exploiting scanning transmission electron microscopy coupled with electron energy loss spectroscopy (STEM-EELS). The compositional variations, which occur within the bulk, are related to the local inhomogeneities of the unit cell and reflect different site occupancies as well as to differences between bulk and extended defects. Our results further suggest a preferential Mo enrichment of the surface, while partially V-rich surface facets can also be exposed to the environment. The interplay of the local compositional inhomogeneities, in particular at the surface, may lead to atomic scale fluctuations of adsorption, redox and/or acidity/basicity properties as well as to surface strain, which can tune the conversion and product selectivity distribution in heterogeneous catalysis. The gained knowledge of the local composition may be beneficial in order to prospectively establish new nanoscale activity-composition correlations, which would push forward the understanding in heterogeneous catalysis.

3.2 Introduction

Heterogeneous catalysis is a crucial technology for a variety of chemical processes in industry. These chemical transformations take part on the surface of mostly complex catalysts and involve even more complex reaction mechanisms. The evolution of heterogeneous catalysis from an early empiricism over its establishment in industry to a prospective technology for energy storage has powered research in this field with the aim to understand and to tailor catalyst systems for any desired applications.[1]

The realization of the dream of tailoring heterogeneous catalysts requires unprecedented atomistic view on every part of the applied functional material (bulk and surface) and their

delicate interplay during the prevailing time of a catalytic reaction. However, catalytic systems are highly sophisticated, which allows, for instance, to combine active centers for different reaction steps in one structure. This renders any detailed analysis difficult, which can be referred to as complexity challenge. This complexity challenge can be attributed to the presence of geometric and electronic features beyond the ideal crystal. They also include surface terminations, local compositional fluctuations and other defects. Those parameters describe the real structure of a catalyst and the interplay of their individual determines the performance of the working structure.

The interplay of surface and bulk structure of a catalyst is crucial and it may modulate stabilization and regeneration of the active phases.[2-3] It has been shown for semiconducting oxides that, for instance, the electron migration from the bulk to the surface is controlled by band bending, which already implies that the electronic structure and/or composition of surface and bulk are different.[4-5] These differences have already been addressed by the combination of surface averaging X-ray photoelectron spectroscopy (XPS) with chemical analysis, such as X-ray fluorescence (XRF), and could be locally visualized by high angle annular dark-field scanning transmission electron microscopy (HAADF-STEM).[6,7]

In particular, local structural analysis using modern aberration corrected STEM is powerful enough to unravel differences of the bulk and surface structure of a catalyst.[7-9] The interpretative depth of the images can be enhanced by coupling STEM with chemical analytical techniques, such as energy dispersive X-ray spectroscopy (EDX) and electron energy loss spectroscopy (EELS).[10-12] These techniques are sensitive to the element composition and EELS allows also for tracking the electronic and structural states of the involved elements.[13] In addition, modern aberration corrected TEMs can provide elemental analysis down to atomic resolution.[10, 14-15]

Here we use ternary orthorhombic $(Mo,V)O_x$ catalyst, which is active and selective in the oxidative dehydrogenation of ethane (ODE), as an structural example to unravel compositional differences between bulk, defects and surface.[16-19] This mixed molybdenum-vanadium oxide has been subject of a multitude of structural studies, which included, for instance, disclosing local geometric differences of the bulk and the surface structures.[8, 18, 20] However, mixed occupation of the cationic sites as well as thickness differences, structural defects and/or ill-defined morphology presence hardly allow for detailed and direct conclusion of the surface concentration

by common Z-contrast imaging. To overcome this dilemma we focus on a local STEM-EELS analysis of bulk, surface, and defects to determine the variations of the chemical composition in the real structure of orthorhombic $(Mo,V)O_x$. As we will show the surface is preferentially enriched in molybdenum, while the composition of extended defective inclusions depends on the internal structure and can be vanadium or molybdenum rich compared to the bulk composition. The results are in line with the composition obtained by XRF analysis and surface sensitive XPS measurements.

3.3 Results

3.3.1 Bulk composition

Orthorhombic mixed (Mo,V) oxides are composed of pentagonal building blocks, which are connected by corner-sharing MO_6 octahedra (M= Mo, V) such that structural hexagonal and heptagonal channels are formed (Figure 3-1a). Sample averaging XRD measurements suggest that the base metal of the pentagonal building blocks is Mo solely composed of, while the linker sites are composed by a mixed Mo and V ratio.[6, 18, 21] These individual metal sites are preferentially enriched by of one these elements.[6, 9, 18, 21-22] However, local modifications of the elemental composition to the ideal structure have not being elucidated. Chemical analysis of the structure by XRF analysis shows a V/Mo ratio of 0.4.

We have recently shown that HAADF-STEM images of orthorhombic $(Mo,V)O_x$ similar to those presented in Figure 3-1b can provide the local geometric information for different parts of the same crystallites.[8] In particular, at the surface or for defect sites, where the particle thickness and/or connectivity of the pentagonal building blocks can vary, conclusions on the elemental composition solely based on Z-contrast imaging are difficult. However, the delicate combination of a focused electron beam with the element sensitivity of inelastic scattered electrons can provide this information with atomic resolution.[14] Corresponding STEM-EELS line scans along the a-axis of $(Mo,V)O_x$ viewed along the c-axis were recorded at different positions of the b-axis (Figure 3-1b). As orthorhombic $(Mo,V)O_x$ is electron beam sensitive, we carefully adjusted beam dose and acquisition time, in order to avoid beam induced artefacts (Figure S3-1). Individual spectra of one pixel suffer from a low signal to noise ratio. Thus, we accumulated and averaged over complete line scans to obtain EELS spectra, which can be used for further qualitative interpretation.
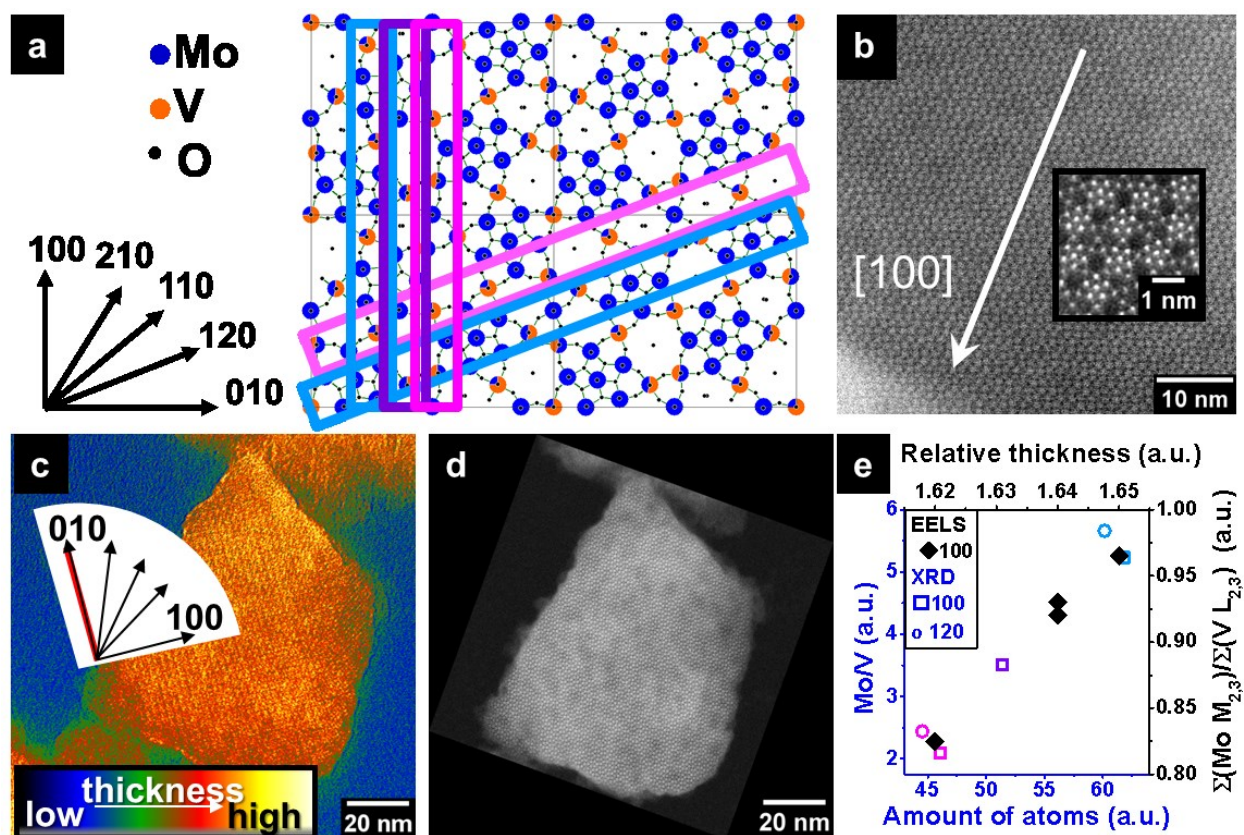
Figure 3-1: a) Structural representation of orthorhombic (Mo,V)Ox viewed along [001] and main crystallographic axes (blue: Mo; orange: V; sector sizes denote metal site occupancies). Magenta, violet and blue rectangles: regions with low, medium and high Mo/V ratio, respectively. b) HAADF-STEM image of (Mo,V)O$_x$ particle viewed along [001]. Inset: high resolution HAADF-STEM image. White arrow: scan direction and length (see Figure S3-3 for exact positions). c) EFTEM contrast enhanced thickness map of (Mo,V)O$_x$ particle viewed along [001] (see Figure S3-2 for corresponding zero-loss and unfiltered images) and d) corresponding identical location ADF-STEM image, rotated to the same orientation viewed along [001]. Black arrows: main crystallographic directions; red line: slight misorientation of the sample, under the assumption that [100] is perfectly aligned. e) Relative elemental Mo/V ratio derived from the averaged crystallographic structure (colored) and qualitative STEM-EELS (black) evaluation.

Thickness inhomogeneities along the microstructure of orthorhombic (Mo,V)O$_x$ viewed along [001] were tracked by energy filtered TEM (EFTEM) imaging, which allows for thickness mapping (Figure 3-1c; for details, see also Figure S3-2) and corresponds to the ADF-STEM image of the identical orthorhombic (Mo,V)O$_x$ crystal (Figure 3-1d). As opposed to the [010] direction where thickness fluctuations can be attributed to the alternating stacking of channel

sites (thin) and pentagonal building blocks (thick), this thickness pattern can due to signal broadening as result of the presence of chromatic aberration not be observed for the [100] direction.[23-24]

Corresponding background corrected, and mass thickness deconvoluted EELS spectra of Mo $M_{2,3}$-, V $L_{2,3}$-, and O K- edges are shown in Figure S3-3. As suggested previously we used the Mo $M_{2,3}$- edge for the qualitative estimation of the Mo/V ratio.[25] However, in order to avoid misinterpretation due to mixed Mo $M_{4,5}$ and C K edges, background subtraction was performed via the second difference approach.[23, 26] Qualitative expressions of the Mo/V ratio of bulk STEM-EELS measurements can be derived from the sum ratio of the integrated Mo $M_{2,3}$- to the V $L_{2,3}$- edges. Figure 3-1e summarizes the Mo/V ratio, which was recorded at different positions of the b-axis and scanned along [100] (see Figure S3-3). The Mo/V ratio derived from the STEM-EELS measurements discloses local compositional differences (Figure 3-1e, black), which resembles the Mo/V ratio distribution obtained from the averaged crystal structure (Figure 3-1e, colored). The XRD suggests that the highest Mo content can be observed for measurement along the pentagonal building blocks, where only a minor fraction of connective vanadium containing octahedra are present (Figure 3-1a, e; blue). The lowest Mo/V ratio (in agreement with [6]) was estimated for structural channels and corner sharing, V-rich octahedra, which connect the pentagonal building blocks (Figure 3-1a, e; magenta). Following these trends the analyzed crystal structure can be used to calibrate the qualitative STEM-EELS evaluation. The low Mo/V ratio can, thus, be tentatively assigned to scans along structural channels, which partially occupy V moieties, and linking V rich octahedra (Figure 3-1e, black). The high Mo/V sum ratio may correspond to a line scan which was measured along Mo rich pentagonal building blocks (Figure 3-1e, black). An intermediate Mo/V sum ratio suggest scan positions in-between both extrema. The STEM-EELS measurements also indicate slight relative thickness differences (Figure 3-1e), which are in line with the observations made by EFTEM thickness mapping (Figure 3-1c) and the amount of atoms, which were used to derive the composition from the averaged crystallographic structure. It further indicates that in the structural channels less scattering occurs compared to the pentagonal building blocks and supports the experimental assignment of the Mo/V sum ratios with different channel and pentagonal sites. Thus, qualitatively an intimate match of the Mo/V composition derived from averaging crystallographic data and local STEM-EELS measurements exists, which suggests that the

qualitative determination of the Mo/V ratio by STEM-EELS experiments can be extended to derive the composition of different local structures.

3.3.2 Intergrowth composition

Extended local structure, such as intergrown phases are common for ternary orthorhombic $(Mo,V)O_x$. Amongst others the pseudo-trigonal intergrowth has been identified as the most frequent structural building block of the extended defect family. The pseudo-trigonal intergrowth (Figure 3-2a) proceeds along [100] and is composed of Mo containing pentagonal building blocks connected by linking Mo/V mixed sites along the intergrowth borders (Figure 3-2b). The intergrowth central area is usually characterized by a lower contrast compared to the surrounding structure, which renders the determination of the central elemental composition solely by Z-contrast imaging due to thickness differences, difficult. These thickness variations in the intergrowth area are highlighted by the EFTEM thickness map, which is presented in Figure 3-2c. The combined evaluation of the EFTEM thickness map with the ADF-STEM image (Figure 3-2d) of the identical orthorhombic $(Mo,V)O_x$ crystal demonstrates the presence of a thinner intergrown region. These extended defects can exhibit pentagonal (Figure 3-2b) or quadrilateral arrangements (Figure 3-2e) with unknown elemental distribution, as major differences to the ideal triangular arrangements spotted in the trigonal phase of $(Mo,V)O_x$ (Figure 3-2f). The qualitative STEM-EELS evaluations (Figure 3-2g, black) confirm the occurrence of thickness inhomogeneities from the center of the pseudo-trigonal intergrowth to the bulk $(Mo,V)O_x$ structure and demonstrate a Mo enrichment in the thinner central areas of the intergrowth. Spectra of the bulk area scanned along the crystallographic a-axis are given for comparison (Figure 3-2g, blue). The exact scan positions are presented in the Figure S3-4.

Based on the structural similarities between the central part of the intergrowth presented in Figure 3-2b (red) and the pentagonal building blocks (Figure 3-1a, blue) it is reasonable to assume, that these structural motifs have the same chemical origin and composition. These pentagonal structures can originate from early steps of the synthesis and have been described in early studies as $\{(Mo)Mo_5O_{21}(H_2O)_6\}$ units, in which the water molecules are necessary to extent the coordination sphere.[27-29] However, the Mo enrichment would also fit to the quadrilateral arrangement described in Figure 3-2e. Here, the central structure of the intergrowth is neither related to the orthorhombic bulk nor to the trigonal structure, but appears to be similar to the bridging metal sites of two pentagonal motifs (see for instance Figure 3-2b, black circle).
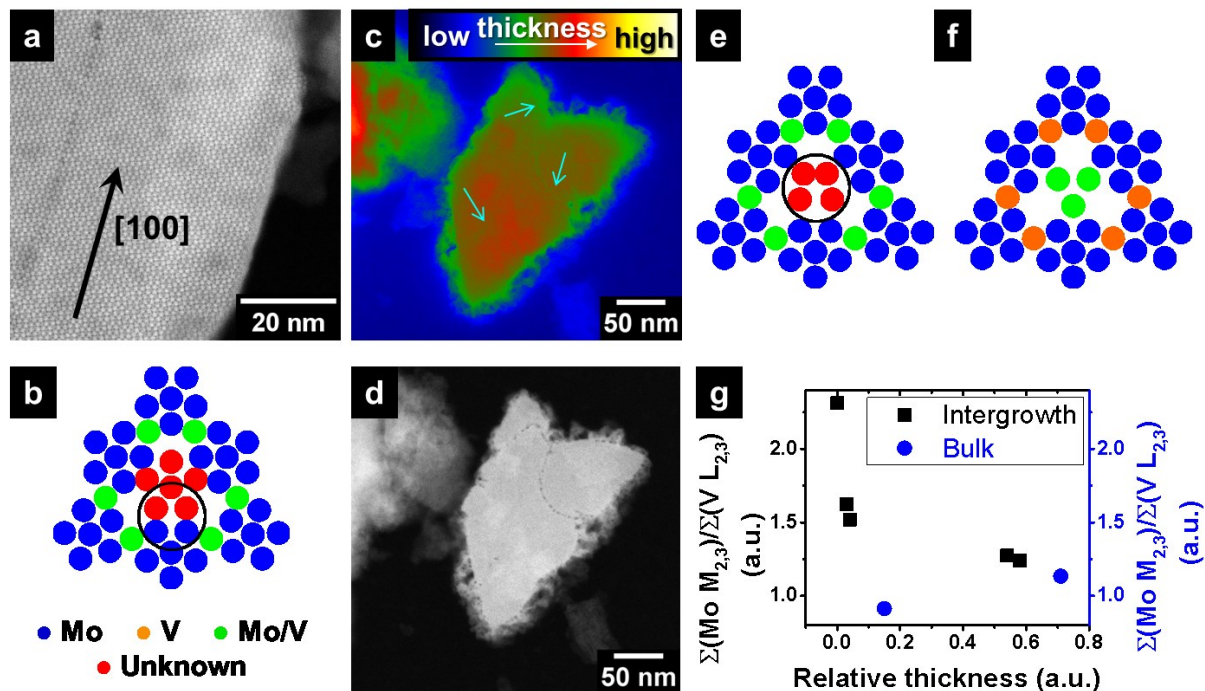
Figure 3-2: a) HAADF-STEM image of (Mo,V)O$_x$ with pseudo-trigonal intergrowth. Black arrow:line scans direction length (Figure S3-4 for exact positions). b) Scheme of the pseudo-trigonal intergrowth with internal pentagonal building block. c) EFTEM contrast enhanced thickness map (see Figure S3-5 for corresponding zero-loss and unfiltered images). Cyan arrows: thinner intergrowth regions. d) Corresponding identical location ADF-STEM image, rotated to the same orientation and viewed along [001]. e) Schematic representation of pseudo-trigonal intergrowth with quadrilateral arrangement. Black circles in b) and e) highlight structural similarities. f) Internal structure of the trigonal phase. g) Qualitative Mo/V ratio estimation based on STEM-EELS analysis.

Extended defect structures are not exclusively enriched in Mo. Other intergrown phases can also exhibit a different composition. An example is shown in Figure 3-3. Figure 3-3a displays a HAADF-STEM image of a rare star-like defect, which proceeds chevron-like through the microstructure of orthorhombic (Mo,V)O$_x$. The central six-fold channels of this defect appear dark. Higher magnified HAADF-STEM images indicate the presence of a microstructure inside these channels (Figure 3-3a, inset). Here, STEM-EELS line scans on this structure were conducted in [-110] direction (Figure 3-3a, Figure S3-6). The qualitative evaluation of the Mo/V ratio is presented in Figure 3-3b. These results indicate an V-enriched, thin interior of the defect structure compared to the bulk composition of orthorhombic (Mo,V)O$_x$.
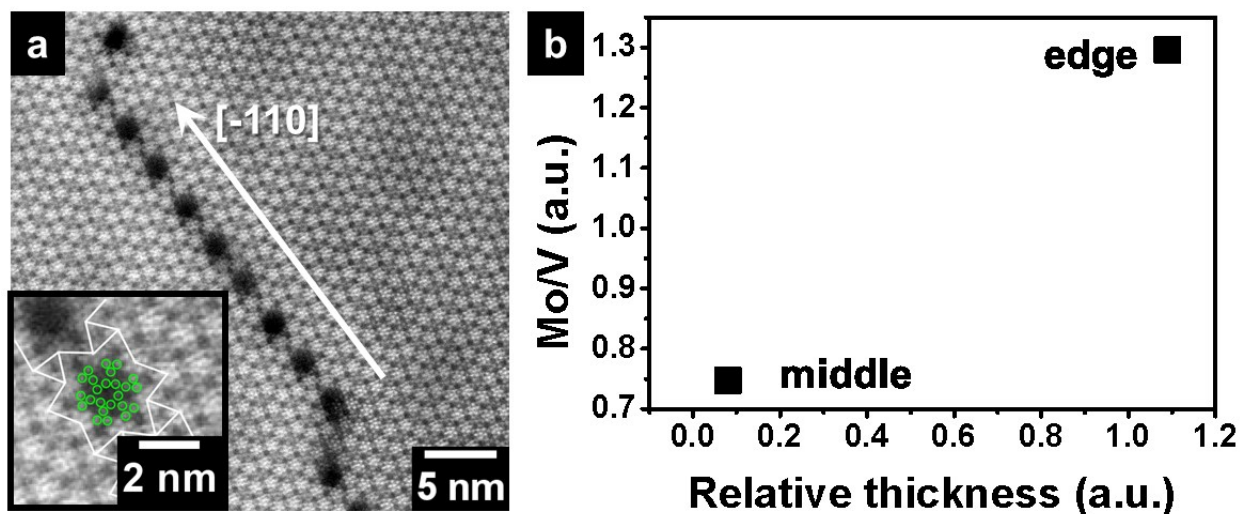
Figure 3-3: a) HAADF-STEM image of a star-like intergrowth in the microstructure of orthorhombic (Mo,V)Ox. White arrow: scans direction and length (see Figure S3-6 for exact positions). The inset represents a magnified region of the highlighted area. White polygons: intergrowth structural units, green circles: internal structure sites. b) Corresponding qualitative Mo/V ratio estimation based on STEM-EELS analysis.

3.3.3 Surface composition

The surface represents the largest defect in any material. It has been previously shown by complementary TEM and XPS studies that the surface structure can be decoupled from the bulk structure, which may imply structural and compositional differences.[6, 8] STEM-EELS measurements allow for tracking compositional inhomogeneities at the microscale, nanoscale (i.e. dimension of the unit cell) and atomic scale. The intensity distribution of the HAADF-STEM image (Figure 3-4a) also represent thickness information (Figure 3-4b), which can be correlated to the relative thickness information obtained from the zero-loss spectra (Figure 3-4c). Here, the surface is characterized by lower relative thickness values compared to the bulk. This observation is backed up by the EFTEM thickness maps, which are presented in Figure 3-1c and Figure 3-2c. The HAADF-STEM image in Figure 3-4a displays the characteristic rod-like structure of orthorhombic (Mo,V)O$_x$ with a preferential growth direction along the crystallographic c-axis. In addition, local contrast fluctuations along the nanorod indicate the presence of a plethora of different open or closed pores along [001] with variable size. The HAADF-STEM intensity (Figure 3-4b) was measured along the yellow highlighted area of Figure 3-4a. The intensity scan (Figure 3-4b) shows two steep intensity ascents at around 20 nm

and 40 nm, which correspond to the onset of the particle and to surface sites, which are almost parallel to the electron beam, respectively. The qualitative estimation of the STEM-EELS measurements in Figure 3-4c indicate a Mo enrichment of the thinner surface region of the particle compared to the thicker bulk part. The observation of a Mo rich surface is in line with surface averaging XPS measurements, which give a surface V/Mo ratio of 0.23. The observation of a Mo rich surface was also confirmed for different $(Mo,V)O_x$ rods (Figure S3-7). The color code of Figure 3-4c reflects the relative time (red – early; violet – late), at which individual STEM-EELS line scans were recorded to account for possible beam damage. For multiple STEM-EELS line scans at different relative times at similar/same positions the estimated qualitative Mo/V ratios are reproducible within the error range. However, the highlighted data point in Figure 3-4c, resembles an exception to the outlined thickness-composition behavior. As opposed to the described thickness-composition correlation, the highlighted region exhibits a too high relative thickness as expected for the Mo/V ratio. The scan region corresponds to the second ascent of the HAADF intensity distribution presented in Figure 3-4b, which is characterized by a surface site almost parallel to the electron beam. This can result in thicker surface regions where more inelastic scattering events lead to an initial higher Mo/V ratio. Subsequent traversing of the electron beam with the underlying Mo poorer bulk structure may adjust the final Mo/V ratio to an intermediate value.
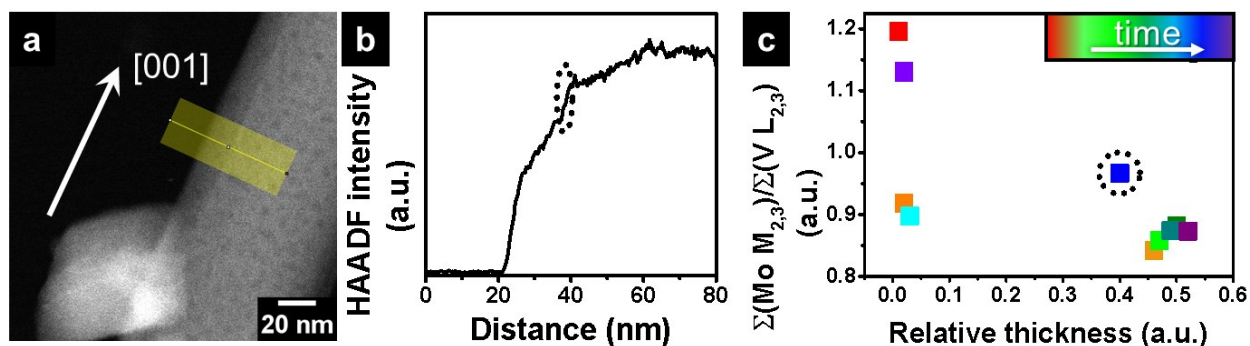
Figure 3-4: a) HAADF-STEM image of orthorhombic $(Mo,V)Ox$. Yellow line: area, in which the HAADF-STEM intensity profile was measured; white arrow: STEM-EELS scan direction and length (exact positions: Figure S3-8). b) Corresponding intensity profile and c) relative elemental content to thickness relation based on STEM-EELS measurements. The color highlights the temporal order of scans.

A further example of local compositional surface differences in an oriented orthorhombic $(Mo,V)O_x$ is presented in Figure 3-5. The HAADF-STEM image of the particle viewed along [001] is presented in Figure 3-5a. STEM-EELS measurements of oriented particles at this magnification sometimes reveal too low scattering intensity in order to obtain measurable relative thickness values. However, similar to imaging geometric structural details of the central part of the intergrowth or surface structure a variation of the focus suggests the existence of thickness differences.[8] For relative thickness differences below 0.3, multiple scattering can be neglected.[30] Thus, in this thickness regime the intensity of the core loss edges and the thickness can be directly correlated. The total area of the Mo $M_{2,3}$- and V $L_{2,3}$- edges is used as a measure of the different thicknesses.

Qualitative descriptions of the Mo/V ratio at higher magnifications were conducted on [2-10] and [010] terminated surfaces and are presented in Figure 3-5b. The [2-10] terminated surface is characterized by a Mo enrichment followed by a Mo depletion into the bulk, while the [010] terminated surface is V-rich accompanied by a Mo enrichment towards the bulk structure. For the [010] terminated surface the probe size is already small enough to observe unit cell inhomogeneities in the STEM-EELS line scans, which would allow to distinguish between Mo-rich pentagonal building blocks and V-rich channel sites (see also Figure 3-1). Although the observed V enrichment of the [010] terminated surface, which may correspond to channel and linker sites, mixed site occupancies may also allow the presence of some Mo moieties at the surface. For higher order planes, interplanar spacing is much smaller than for [010], which can result in non-resolvable structural and compositional inhomogeneities of the unit cell for the same probe size. Thus, for the [2-10] terminated surfaces the composition can be averaged, which results in a loss of compositional sensitivity. The observed Mo enrichment can be strengthened by contributions of the above described Mo rich overlayer (see also Figure 3-4). Additional STEM-EELS line scans at high resolution at the surface of the particle shown in Figure S3-9 also suggest a Mo enrichment at the surface.
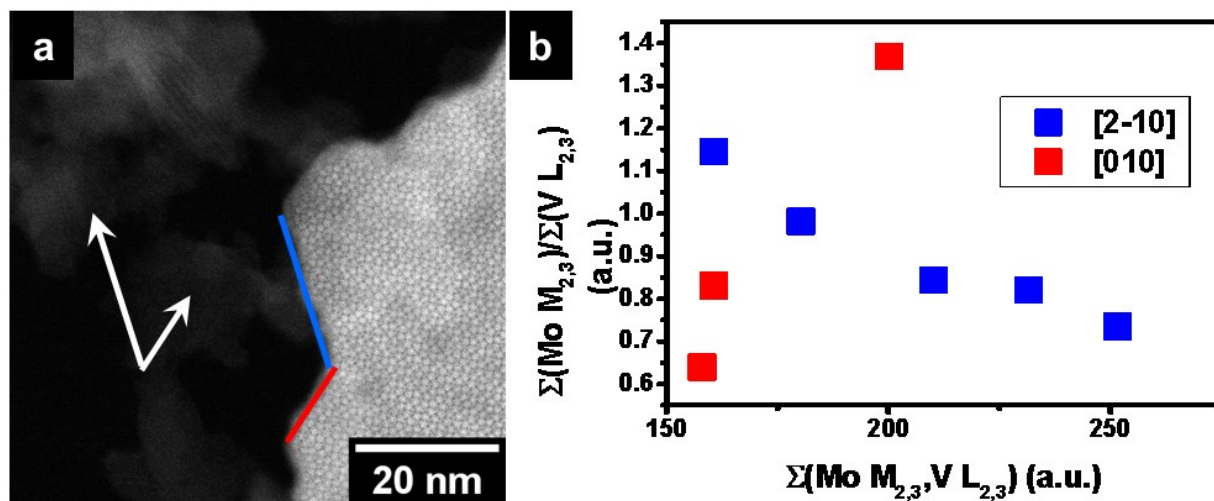
Figure 3-5: a) High resolution HAADF-STEM image of the surface of (Mo,V)Ox viewed along [001]. White arrows: direction and length of line scans, blue and red lines: [2-10] and [010] crystallographic terminations, respectively (see Figure S3-10 for exact positions). b) Qualitative elemental content as determined from STEM-EELS measurements.

3.4 Discussion

A visual expression of how a surface layer can embed the bulk structure of orthorhombic $(Mo,V)O_x$, is presented in Scheme 3-1. Scheme 3-1.I represents a 3-dimensional (3D) representation of a rod-like orthorhombic $(Mo,V)O_x$ particle, which is elongated in the preferred growth direction (crystallographic c-axis) similar to the particle shown in Figure 3-4. The Scheme 3-1.II, which displays a cut through the crystallographic (a,b), can explain the observed deviation of the highlighted point in Figure 3-4c from the otherwise regular content-thickness correlation. The surface Mo enrichment can be expressed by the line scan ratio l'/l (Scheme 3-1.II). As can be seen from Scheme 3-1.II a low l'/l ratio corresponds to a high amount of Mo surface species. Thus, the line scan 1 in Scheme 3-1.II will show significant Mo enrichment, which is accompanied by a low thickness, line scan 2 (Scheme 3-1.II) displays a significant Mo enrichment despite the high thickness. The line scan 3 (Scheme 3-1.II) is characterized by the highest thickness and lowest Mo content. A similar effect might also occur for the oriented orthorhombic $(Mo,V)O_x$ viewed along the crystallographic c-axis. Here, the probe size of the electron beam affects the STEM-EELS line scan and local inhomogeneities on the nanoscale can become important. Scheme 3-1.III denotes a scan through the (b,c) plane, which mimics the scan situation described in Figure 3-1, in which the electron beam travels along the crystallographic c-

axis. Line scans 4 and 5 (Scheme 3-1.III) represent such STEM-EELS line scans, which were shifted along the crystallographic b-axis with a scan direction along the crystallographic a-axis. The l' and l values for this STEM-EELS line scans differ only slightly, which might influence the thickness and composition. However, at higher magnification (Scheme 3-1.IV) the electron beam can independently pass through Mo rich pentagonal building blocks or V rich channel and linking sites. As a result a higher difference in the thickness and composition can be observed compared to particle shape related effect.
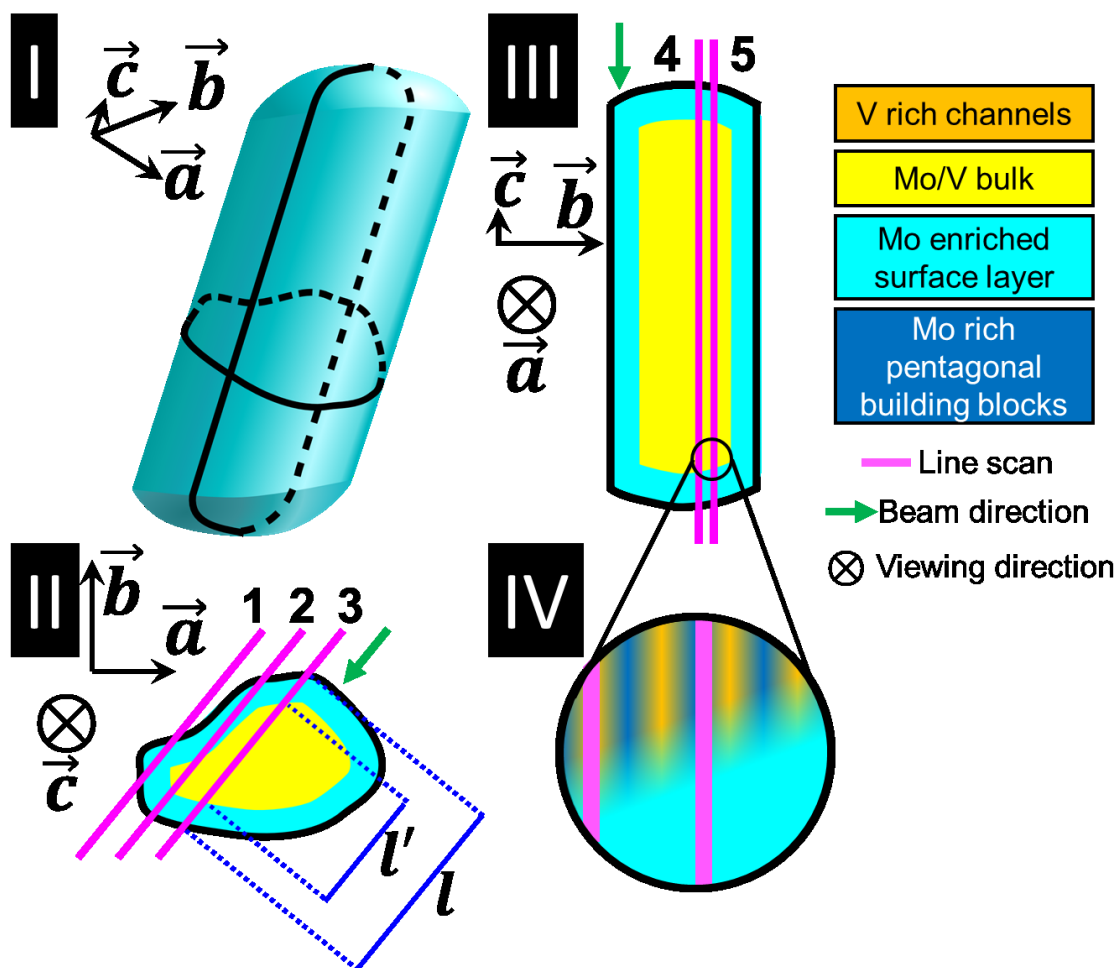
Scheme 3-1: Schematic model of the of orthorhombic (Mo,V)O$_x$ particle. I) 3-dimensional view, black shapes: cuts along (a,b) and (a,c) crystallographic planes. II, III) cuts along (a,b) and (a,c) crystallographic planes viewed perpendicular to the cut planes. Magenta lines: line scans and cut planes intersections. IV) magnified area from Scheme 3-1.III

Our spatially resolved STEM-EELS studies has unraveled the real composition of complex orthorhombic $(Mo,V)O_x$. The structure exhibits intrinsic compositional inhomogenities of the mixed $(Mo,V)O_x$ at different scales, which were observed in the bulk, in extended defects and at the surface and can be expressed by local Mo- or V- enrichment. The observations are in line with XRF and XPS studies. Detailed local analyses of the surface and of defects with different internal structures show that the composition can vary and suggest the presence of compositionally decoupled surfaces.

Compared to the ideal trigonal structure, the pseudo-trigonal intergrowth is enriched by Mo. In addition, at the intergrowth-bulk border slight distortion occur, which may allow for a better fit of the relatively large pentagonal or quadrilateral molybdenum blocks into the central part of the pseudo-trigonal intergrowth compared to the smaller triangular V-rich arrangements of the ideal trigonal phase. The Mo enrichment inside the intergrowth may result from the lack of available vanadium moieities in the current synthesis protocol and/or may be forced by structural distortions between the pseudo-trigonal intergrowth and the bulk, which can be observed by the formation of larger octagonal channels that cannot be build up by V triangles.

The surface enrichment may be determined by excess molybdenum moieties, which remain until the end of the hydrothermal synthesis. The pentagonal building blocks are already formed in the beginning of the synthesis.[28-29] If there is lack of linking cations, Mo rich structural defects, such as mirror motif, translated motif or shared motifs, can be formed at the surface region. The homogeneity and thickness of the enriched surface layer is supposed to be in the nanometer or even Angstrom range, which is based on the observed Mo enrichment-thickness dependency. Further quantitative studies of the surface layer would require a comprehensive 3D particle reconstruction.

To our knowledge, the real composition of individual parts (bulk, defects, and surface) of a complex mixed oxide catalyst has not been unraveled before. However, the knowledge of these local differences on the nano (atomic) scale may be important, as they may tune strain, adsorption affinities, redox and semiconducting properties. As the ionic radii of $V^{4+/5+}$ and Mo^{6+} in an octahedral environment are similar, strain may not be induced solely by the occurrence of mixed metal sites and is rather a result of their differences in the polyhedral distortion.[9, 31] Preferential Mo surface enrichment may result from different Mo-rich structural motifs, which can terminate the crystal.[8] They are characterized by rearranged pentagonal building block in a

strained local confinement. This may lead to surface strain and frustrated Mo surface sites, which are active in alkane conversion.[32] The existence of vicinal surfaces with different composition (Mo- or V- rich) within a few nanometers may not only locally vary the redox properties of a catalyst, but also modulate the adsorption of reactants. The sudden change of adsorption energies for different Mo- or V- rich surfaces in the sub-nanometer regime can crucially influence conversion, selectivity and/or oxygen activation.

The structural and compositional inhomogeneities of the surface and intergrowth lead also to complicated electronic effects, which can modulate the band bending of the catalyst. Single filling of the linker sites with Mo instead of V can be treated as anti-site defect, which results in the appearance of a single energy level inside the forbidden zone.[33] According to the Pauli exclusion principle this energy level splits up to the impurity band formation if multiple, coupling defects of such kind are present in the structure.[33-34] Extended defects, such as the pseudo-trigonal or star-like intergrowth can be treated as heterostructures, which can give rise to presence of quantum wells or the formation of electron barriers.[35] The outcome depends on the relationship between the energy levels of the intergrowth and orthorhombic structure. The extent of the mentioned effects alters the catalytic conversion and depends strongly on the chemical composition. The knowledge of the real structure and composition may prospectively allow of how additional charge carrier and/or recombination effects involve the electron transfer to the reactants, lead to selective reactions or create deep level traps.

3.5 Conclusions

In summary, this study demonstrates that the local, real metal distribution of an oxide may vary from the averaged ideal composition. In particular, surface compositional alterations may crucially influence the catalytic performance as they will tune local redox, acid/base, migration and adsorption/desorption behavior. The interphase where different surface composition and structures meet can be of particular importance and must be considered in the interpretation of prospective experimental and theoretical work on heterogeneous catalysts. The complex microstructure of orthorhombic $(Mo,V)O_x$ combined with its complex microcomposition can act as an example of how important it is to understand the real structure of a catalyst and highlights the difficulties, which chemists have to suffer, in order to tailor active and selective catalyst.

3.6 Methods

Synthesis

Hydrothermal synthesis of the orthorhombic $(Mo,V)O_x$ mixed oxide (internal ID 20000) was curried in specially built reactor (Premex Reactor AG, Lengnau, Switzerland) from corrosion resistant Hastelloy C-22 (2.4602). A mixture of 9.18 g $(NH_4)_6Mo_7O_{24} \cdot 4H_2O$ (AHM, Merck, 52 mmol Mo) dissolved in 230 g water (Milli-Q, Merck) and 3.30 g $VOSO_4$ (Acros Organics, 12.9 mmol V) dissolved in 30 g water was loaded into a reactor at room temperature. Residual air was replaced by nitrogen. Subsequently the vessel was heated to 200°C at a rate of 1°C/min and hold at this temperature for 17 h. The reaction mixture was stirred during the whole experiment at a rate of 100 rpm. After cooling to room temperature, a black solid was isolated by filtration (pore 5 glass frit), washed twice with distilled water and dried at 80°C for 16 hours. To remove amorphous components in the hydrothermal product, 1 g of the powder was washed with 25 ml oxalic acid solution (0.25 M, Acros Organics) at 60°C for 30 min under stirring. The solid was centrifuged (5000 rpm, 30 min), washed twice with 25 ml water and dried at 80°C over night. Finally, a thermal treatment was performed in 100 ml/min argon flow at 400°C (heating rate 10°C/min) for 2 h in a rotary tube furnace (Xerion, Freiberg, Germany).

XPS

The sample was investigated as pressed pellet. Spectra were recorded at room temperature, using non-monochromatized Al Kα (1486.6 eV) excitation and a hemispherical analyzer (Phoibos 150, SPECS). The binding energy scale was calibrated by the standard Au4f7/2 and Cu2p3/2 procedure. To calculate the elemental composition, theoretical cross sections from Yeh and Lindau were used.[36]

XRF

The XRF measurements were carried on with XRF X-ray Florescence Spectrometer Pioneer S4 (Bruker). The measurements were performed in vacuum using 100 mg of the sample, molten together with 8.9 g of di-Li-tetraborate, in a form of the glass disc with 40 mm diameter. The K-alpha lines were analyzed applying the calibration factors derived from the FHI-made appropriate standards.

(S)TEM

TEM investigations were performed on a JEM-ARM200F microscope with CEOS CESCOR and CEOS CETCOR hexapole aberration correctors for probe and image forming lenses, respectively, and a cold field emission gun (CFEG). Prior to the measurements, the powdered material was drop deposited on a holey silica oxide coated gold TEM grid or carbon coated copper TEM grid. Some particles were oriented along the crystallographic *c*-axis in the TEM mode. STEM-EELS images were recorded with a GATAN high angle annular dark-field (HAADF) detector. STEM images corresponding to EFTEM mapping – JEOL ADF detector.

EFTEM

EFTEM data were collected with Gatan Imaging Filter (Quantum) CCD camera with applying a monochromator slit of 10eV width for zero-loss collection. Thickness maps were obtained from the ratio of unfiltered and zero-loss maps and further color enhanced for clarity.

EELS

EELS spectra were collected with Gatan Imaging Filter (Quantum) in dual-EELS mode, with 0.25 eV window, with the pixel time lower or equal 0.5s (except the beam damage probes), emission current lower or equal 8μA, pixel size higher or equal 3Å. Low and high loss spectra were recorded simultaneously using dual-EELS mode in Gatan DigitalMicrograph software. The drift correction was applied after each 10 pixels. HAADF-STEM images of the examined area were collected before and after each scan and drift correction area was further used as a reference to confirm beam damage absence.

EELS Evaluation

To minimize beam artefacts, STEM-EELS line scans where recorded with intermediate resolution, which renders it difficult to determine the exact position. Qualitative calibration of the scan position was obtained by taking the different thicknesses/atomic densities of the porous structure of orthorhombic (Mo,V)Ox into account, which results in different inelastic scattering events. This factor is reflected by the so-called relative thickness value, which was evaluated from the low-loss spectra measured at each point of the line scan. In case if relative thickness was lower than 0.1 multiple scattering was neglected.[30] In these cases summed up peak intensities of Mo $M_{2,3}$ and V $L_{2,3}$ edges were used for referring the position.

All the collected spectra were dark corrected, aligned by zero-loss peak, summed up along the scan line, than the background of the high loss prior the C K edge was subtracted and

the plural scattering was removed via the Fourier-ratio method. The peak intensities were evaluated using the "Measure peak intensities" tool from the EELS Tools plugin for a Digital Micrograph.[26]

3.7 References

1.   Fechete, I.; Wang, Y.; Védrine, J. C., The past, present and future of heterogeneous catalysis. *Catal. Today* **2012,** *189* (1), 2-27.

2.   Guliants, V. V.; Benziger, J. B.; Sundaresan, S.; Yao, N.; Wachs, I. E., Evolution of the active surface of the vanadyl pyrophosphate catalysts. *Catal. Lett.* **1995,** *32* (3), 379-386.

3.   Heine, C.; Hävecker, M.; Sanchez-Sanchez, M.; Trunschke, A.; Schlögl, R.; Eichelbaum, M., Work function, band bending, and microwave conductivity studies on the selective alkane oxidation catalyst MoVTeNb oxide (orthorhombic M1 phase) under operation conditions. *J. Phys. Chem. C* **2013,** *117* (51), 26988-26997.

4.   Eichelbaum, M.; Hävecker, M.; Heine, C.; Wernbacher, A. M.; Rosowski, F.; Trunschke, A.; Schlögl, R., The Electronic Factor in Alkane Oxidation Catalysis. *Angew. Chem., Int. Ed.* **2015,** *54* (10), 2922-2926.

5.   Zhang, Z.; Yates, J. T., Band Bending in Semiconductors: Chemical and Physical Consequences at Surfaces and Interfaces. *Chem. Rev.* **2012,** *112* (10), 5520-5551.

6.   Trunschke, A.; Noack, J.; Trojanov, S.; Girgsdies, F.; Lunkenbein, T.; Pfeifer, V.; Hävecker, M.; Kube, P.; Sprung, C.; Rosowski, F.; Schlögl, R., The Impact of the Bulk Structure on Surface Dynamics of Complex Mo–V-based Oxide Catalysts. *ACS Catal.* **2017,** *7* (4), 3061-3071.

7.   Li, X.; Lunkenbein, T.; Pfeifer, V.; Jastak, M.; Nielsen, P. K.; Girgsdies, F.; Knop-Gericke, A.; Rosowski, F.; Schlogl, R.; Trunschke, A., Selective Alkane Oxidation by Manganese Oxide: Site Isolation of MnOx Chains at the Surface of MnWO$_4$ Nanorods. *Angew. Chem., Int. Ed.* **2016,** *55* (12), 4092-4096.

8.   Masliuk, L.; Heggen, M.; Noack, J.; Girgsdies, F.; Trunschke, A.; Hermann, K. E.; Willinger, M.-G.; Schloegl, R.; Lunkenbein, T., Structural Complexity in Heterogeneous Catalysis: Cataloging Local Nano-Structures. *The Journal of Physical Chemistry C* **2017,** *121* (43), 24093-24103.

9.   Lunkenbein, T.; Girgsdies, F.; Wernbacher, A.; Noack, J.; Auffermann, G.; Yasuhara, A.; Klein-Hoffmann, A.; Ueda, W.; Eichelbaum, M.; Trunschke, A.; Schlogl, R.; Willinger, M. G., Direct Imaging of Octahedral Distortion in a Complex Molybdenum Vanadium Mixed Oxide. *Angew. Chem., Int. Ed.* **2015,** *54* (23), 6828-6831.

10. Batson, P. E., Simultaneous Stem Imaging and Electron-Energy-Loss Spectroscopy with Atomic-Column Sensitivity. *Nature* **1993,** *366* (6457), 727-728.

11. Williams, D. B.; Carter, C. B., X-ray Spectrometry. In *Transmission Electron Microscopy: A Textbook for Materials Science*, Williams, D. B.; Carter, C. B., Eds. Springer US: Boston, MA, 2009; pp 581-603.

12. Egerton, R. F., TEM Applications of EELS. In *Electron Energy-Loss Spectroscopy in the Electron Microscope*, Egerton, R. F., Ed. Springer US: Boston, MA, 2011; pp 293-397.

13. Su, D. S., Analytical Tem Characterisation of Catalytic Materials. In *Low-Dimensional Systems: Theory, Preparation, and Some Applications*, Liz-Marzán, L. M.; Giersig, M., Eds. Springer Netherlands: Dordrecht, 2003; pp 241-252.

14. Bosman, M.; Keast, V. J.; García-Muñoz, J. L.; D'Alfonso, A. J.; Findlay, S. D.; Allen, L. J., Two-Dimensional Mapping of Chemical Information at Atomic Resolution. *Physical Review Letters* **2007,** *99* (8), 086102.

15. Allen, L. J.; D'Alfonso, A. J.; Freitag, B.; Klenov, D. O., Chemical mapping at atomic resolution using energy-dispersive x-ray spectroscopy. *MRS Bulletin* **2012,** *37* (1), 47-52.

16. Ishikawa, S.; Yi, X.; Murayama, T.; Ueda, W., Catalysis field in orthorhombic Mo3VOx oxide catalyst for the selective oxidation of ethane, propane and acrolein. *Catal. Today* **2014**.

17. Ueda, W., Establishment of Crystalline Complex Mo-V-Oxides as Selective Oxidation Catalysts. *J. Jpn. Petrol. Inst.* **2013,** *56* (3), 122-132.

18. Konya, T.; Katou, T.; Murayama, T.; Ishikawa, S.; Sadakane, M.; Buttrey, D.; Ueda, W., An orthorhombic Mo_3VO_x catalyst most active for oxidative dehydrogenation of ethane among related complex metal oxides. *Catal. Sci. Technol.* **2013,** *3* (2), 380-387.

19. Katou, T.; Vitry, D.; Ueda, W., Structure dependency of Mo-V-O-based complex oxide catalysts in the oxidations of hydrocarbons. *Catal. Today* **2004,** *91-2*, 237-240.

20. Wagner, J. B.; Timpe, O.; Hamid, F. A.; Trunschke, A.; Wild, U.; Su, D. S.; Widi, R. K.; Abd Hamid, S. B.; Schlogl, R., Surface texturing of Mo-V-Te-Nb-O-x selective oxidation catalysts. *Top. Catal.* **2006,** *38* (1-3), 51-58.

21. Ishikawa, S.; Kobayashi, D.; Konya, T.; Ohmura, S.; Murayama, T.; Yasuda, N.; Sadakane, M.; Ueda, W., Redox Treatment of Orthorhombic $Mo_{29}V_{11}O_{112}$ and Relationships between Crystal Structure, Microporosity and Catalytic Performance for Selective Oxidation of Ethane. *J. Phys. Chem. C* **2015,** *119* (13), 7195-7206.

22.   Pyrz, W. D.; Blom, D. A.; Sadakane, M.; Kodato, K.; Ueda, W.; Vogt, T.; Buttrey, D. J., Atomic-Scale Investigation of Two-Component MoVO Complex Oxide Catalysts Using Aberration-Corrected High-Angle Annular Dark-Field Imaging. *Chem. Mater.* **2010,** *22* (6), 2033-2040.

23.   Egerton, R. F., Instrumentation for Energy-Loss Spectroscopy. In *Electron Energy-Loss Spectroscopy in the Electron Microscope*, Egerton, R. F., Ed. Springer US: Boston, MA, 1996; pp 31-129.

24.   Egerton, R., Limits to the spatial, energy and momentum resolution of electron energy-loss spectroscopy. *Ultramicroscopy* **2007,** *107* (8), 575-86.

25.   Lajaunie, L.; Boucher, F.; Dessapt, R.; Moreau, P., Quantitative use of electron energy-loss spectroscopy Mo-M2,3 edges for the study of molybdenum oxides. *Ultramicroscopy* **2015,** *149* (Supplement C), 1-8.

26.   Mitchell, D. R. G.; Schaffer, B., Scripting-customised microscopy tools for Digital Micrograph™. *Ultramicroscopy* **2005,** *103* (4), 319-332.

27.   Ishikawa, S.; Tashiro, M.; Murayama, T.; Ueda, W., Seed-assisted synthesis of crystalline Mo_3VO_x oxides and their crystal formation mechanism. *Cryst. Growth Des.* **2014,** *14* (9), 4553-4561.

28.   Sadakane, M.; Ueda, W., Building Block Synthesis of Crystalline Mo-V-based Oxides: Selective Oxidation Catalysts. *J. Jpn. Petrol. Inst.* **2012,** *55* (4), 229-235.

29.   Sanchez, M. S.; Girgsdies, F.; Jastak, M.; Kube, P.; Schlogl, R.; Trunschke, A., Aiding the Self-Assembly of Supramolecular Polyoxometalates under Hydrothermal Conditions To Give Precursors of Complex Functional Oxides. *Angewandte Chemie-International Edition* **2012,** *51* (29), 7194-7197.

30.   Egerton, R. F., Physics of Electron Scattering. In *Electron Energy-Loss Spectroscopy in the Electron Microscope*, Egerton, R. F., Ed. Springer US: Boston, MA, 2011; pp 111-229.

31.   Shannon, R., Revised effective ionic radii and systematic studies of interatomic distances in halides and chalcogenides. *Acta Crystallographica Section A* **1976,** *32* (5), 751-767.

32.   Amakawa, K.; Sun, L. L.; Guo, C. S.; Havecker, M.; Kube, P.; Wachs, I. E.; Lwin, S.; Frenkel, A. I.; Patlolla, A.; Hermann, K.; Schlogl, R.; Trunschke, A., How Strain Affects the Reactivity of Surface Metal Oxide Catalysts. *Angewandte Chemie-International Edition* **2013,** *52* (51), 13553-13557.

33.   Electronic Defect States. In *The Physics of Semiconductors: An Introduction Including Devices and Nanophysics*, Grundmann, M., Ed. Springer Berlin Heidelberg: Berlin, Heidelberg, 2006; pp 149-187.

34.   Hamaguchi, C., Energy Band Structures of Semiconductors. In *Basic Semiconductor Physics*, Hamaguchi, C., Ed. Springer Berlin Heidelberg: Berlin, Heidelberg, 2010; pp 1-27.

35.   Heterostructures. In *The Physics of Semiconductors: An Introduction Including Devices and Nanophysics*, Grundmann, M., Ed. Springer Berlin Heidelberg: Berlin, Heidelberg, 2006; pp 277-301.

36.   Yeh, J. J.; Lindau, I., Atomic subshell photoionization cross sections and asymmetry parameters: $1 \leqslant Z \leqslant 103$. *Atomic Data and Nuclear Data Tables* **1985,** *32* (1), 1-155.

3.8 Supporting information
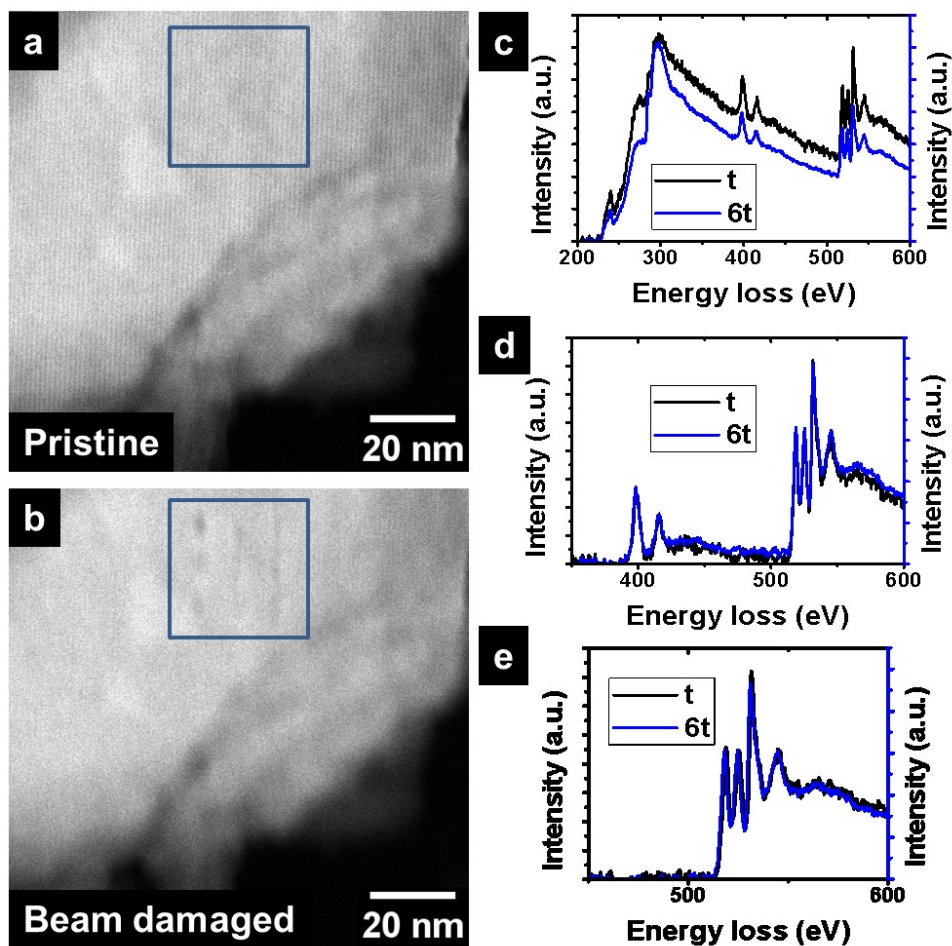
Figure S3-1: **HAADF-STEM images of (Mo,V)O$_x$ particle viewed along [001] a) before and b) after spectra collection indicating morphological changes in the overexposed area (blue square). c) EELS spectra background corrected prior to the C K edge, indicating carbon contamination accumulation, d) and e) EELS spectra background corrected prior to the Mo M$_{2,3}$ edges and V L$_{2,3}$ edges indicating absence of the target edges change. The observations suggest morphological changes as reliable beam damage marker.**
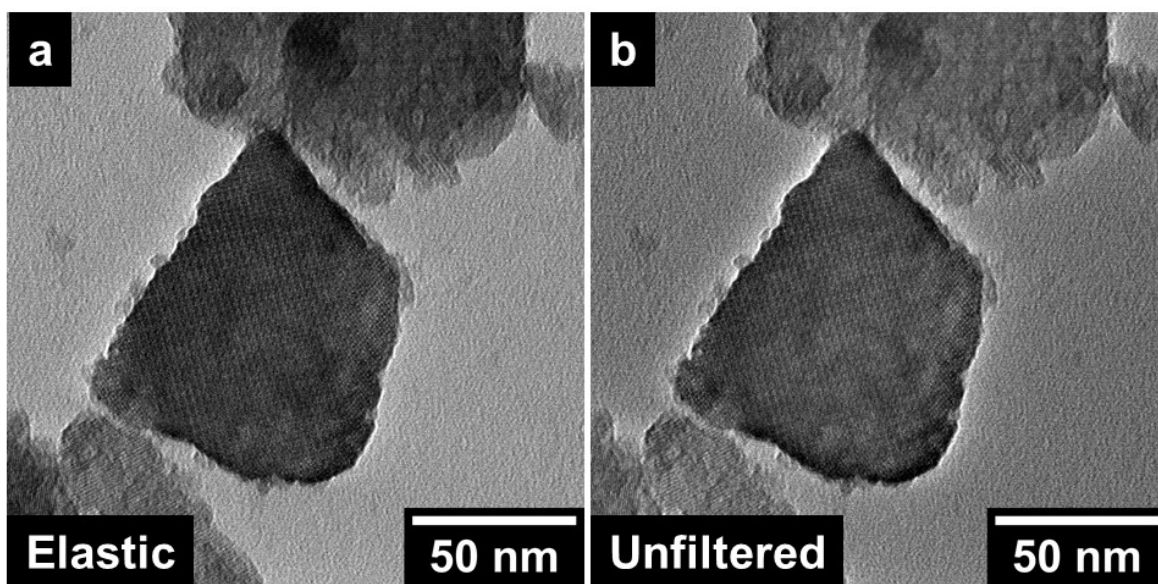
Figure S3-2: Energy filtered around zero-loss peak with 10eV window (a) and unfiltered EFTEM images of (Mo,V)O$_x$ particle viewed along [001]. The resulting map (Figure 3-1c) is obtained by Gatan DigitalMicrograph software.
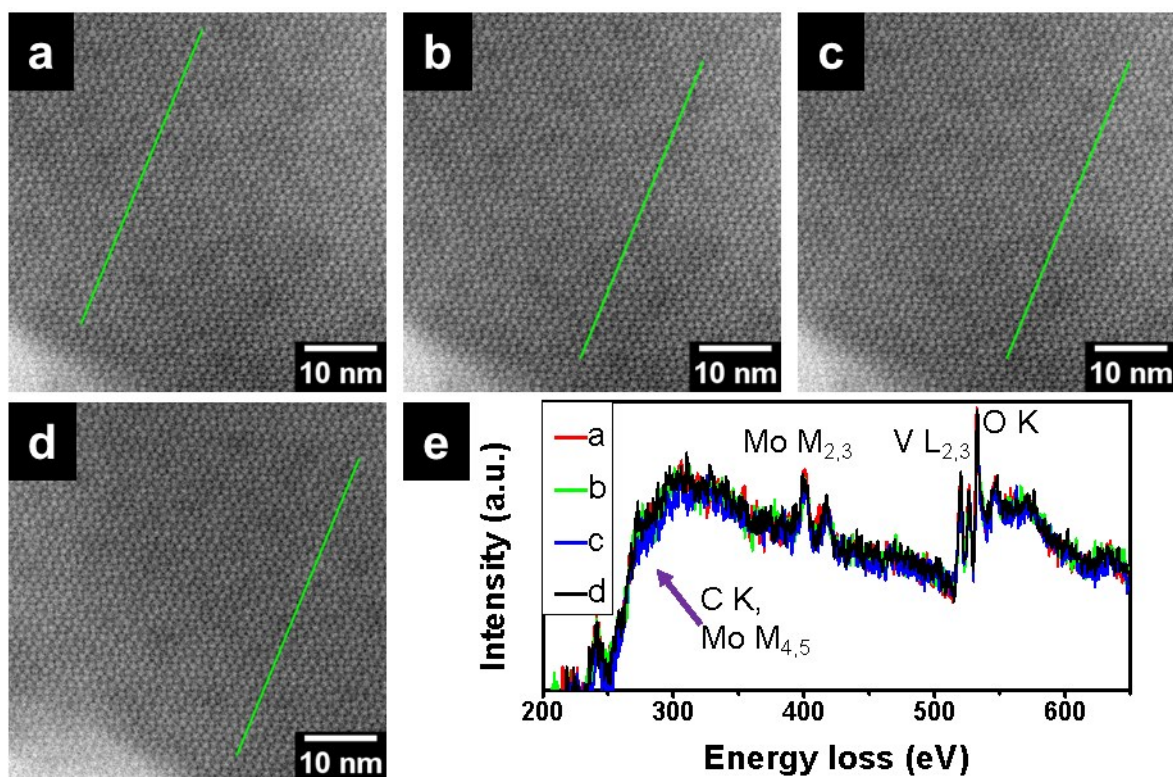
Figure S3-3: a-d) HAADF-STEM images of (Mo,V)O$_x$ particle viewed along [001] indicating the scan positions (green lines). e) corresponding background corrected prior to C K edge and deconvoluted EELS spectra. Green line: spectrum collection position.
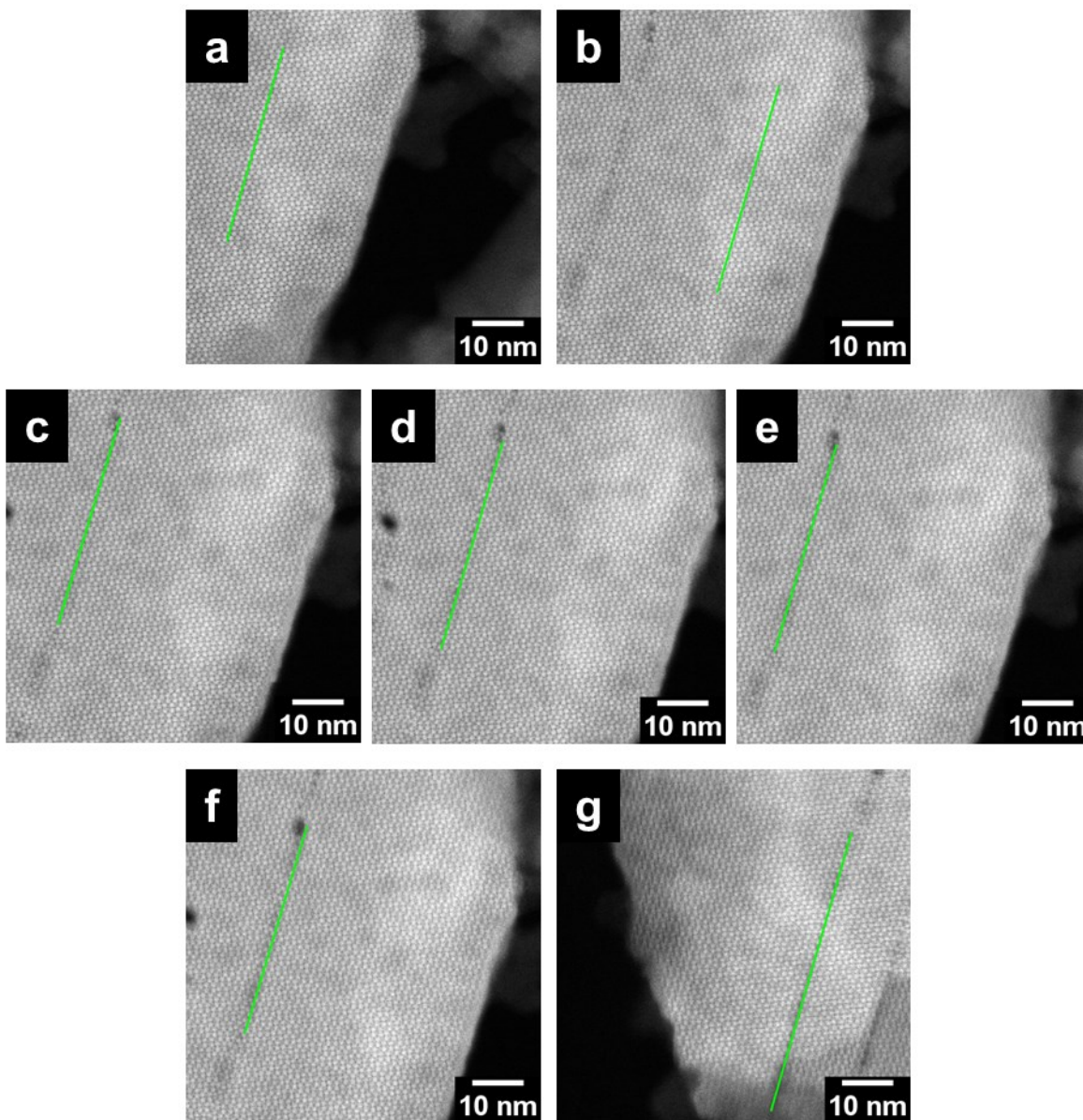
Figure S3-4: HAADF-STEM images of (Mo,V)O$_x$ particle viewed along [001] indicating the scan positions (green lines) in bulk region (a,b) and along pseudo-trigonal intergrowth (c-g).
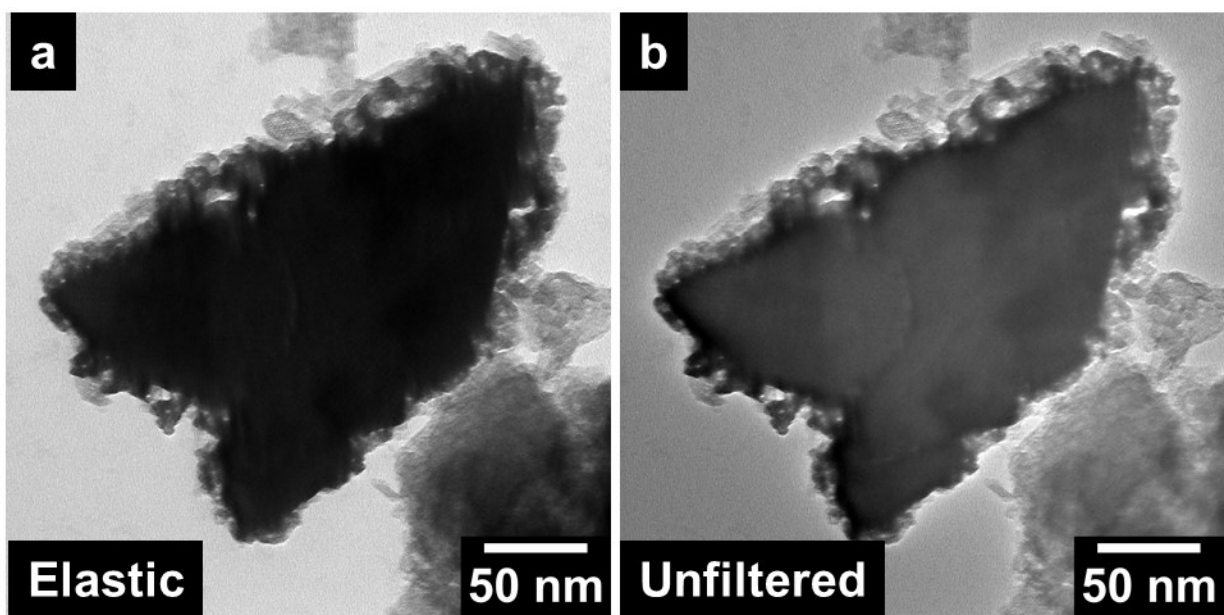
Figure S3-5: Energy filtered around zero-loss peak with 10eV window (a) and unfiltered EFTEM images of (Mo,V)O$_x$ particle viewed along [001]. The resulting map (Figure 3-2c) is obtained by Gatan DigitalMicrograph software.
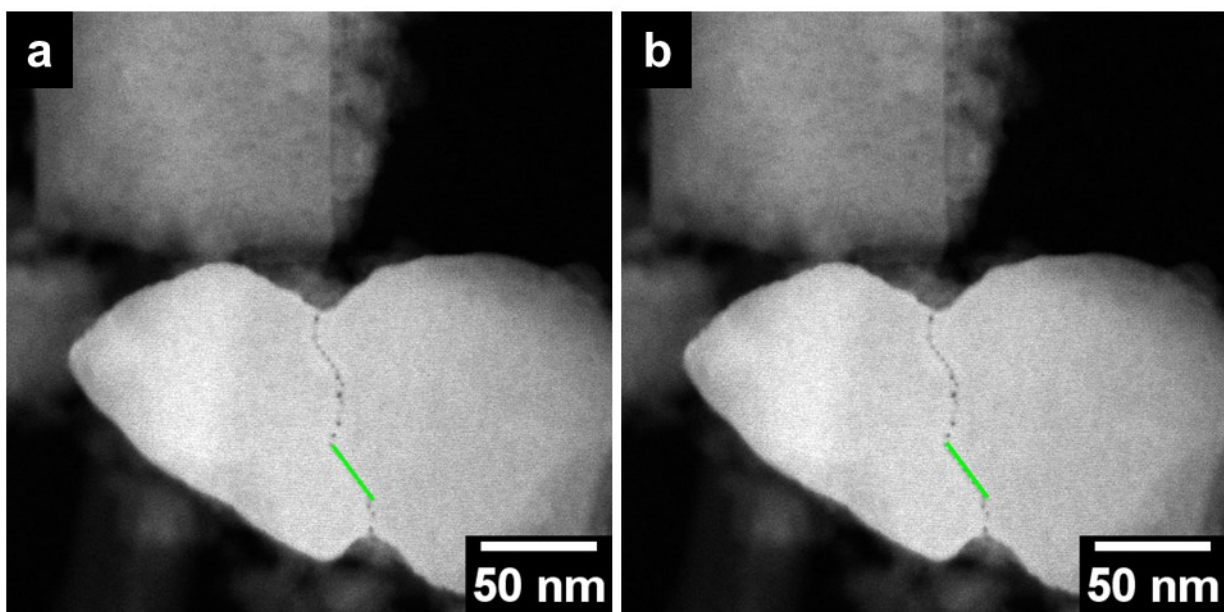
Figure S3-6: HAADF-STEM images of (Mo,V)O$_x$ particle viewed along [001] indicating the scan positions along the intergrowth region (green lines).
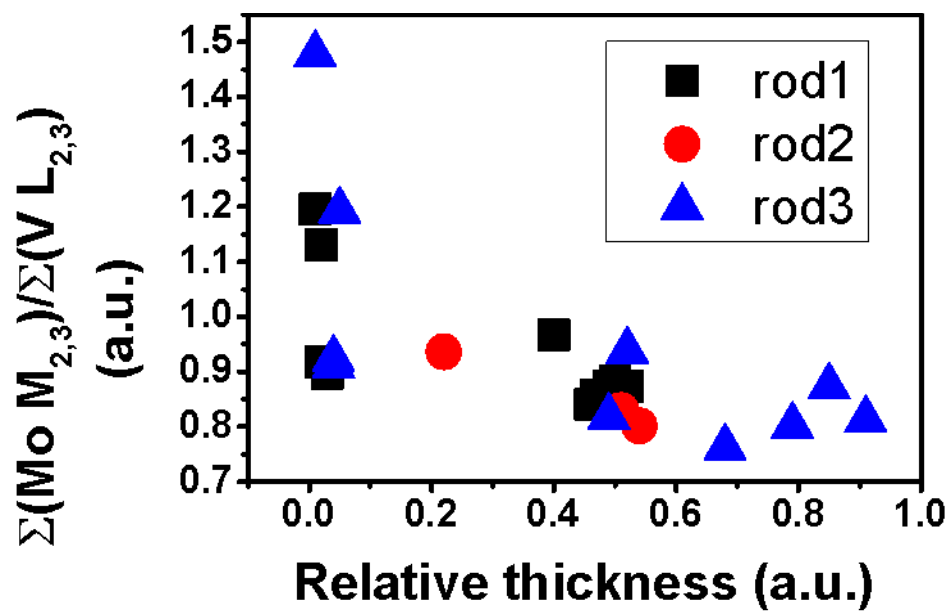
Figure S3-7: Qualitative Mo/V ratio estimation based on STEM-EELS analysis of three different rod-shaped of (Mo,V)O$_x$ particles viewed perpendicular to [001].
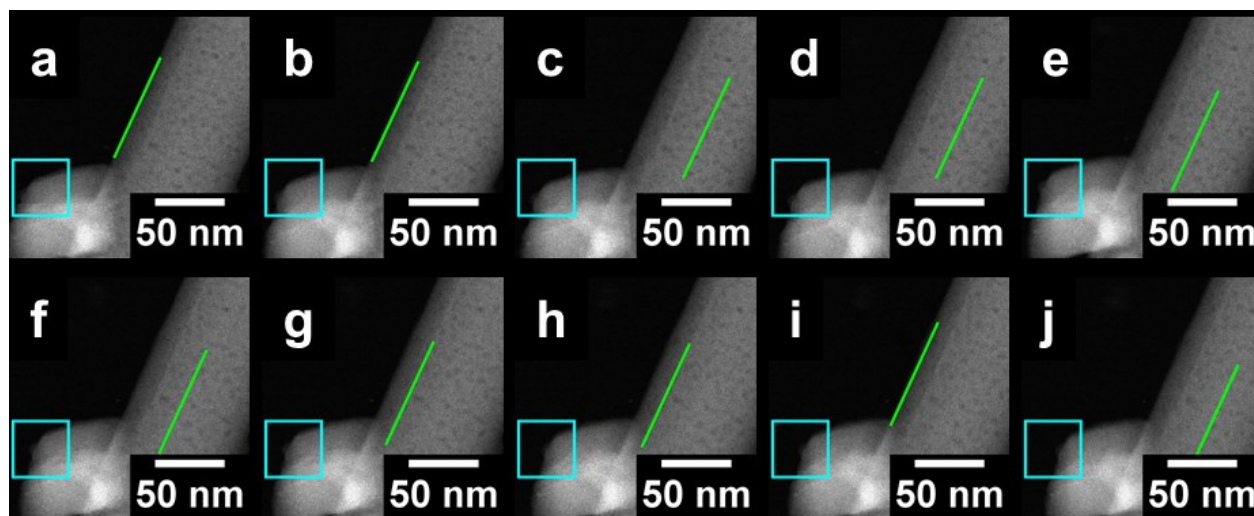
Figure S3-8: HAADF-STEM images of (Mo,V)O$_x$ rod viewed perpendicular to [001] indicating the scan positions along [001] (green lines). Cyan square: reference region used for drift correction.
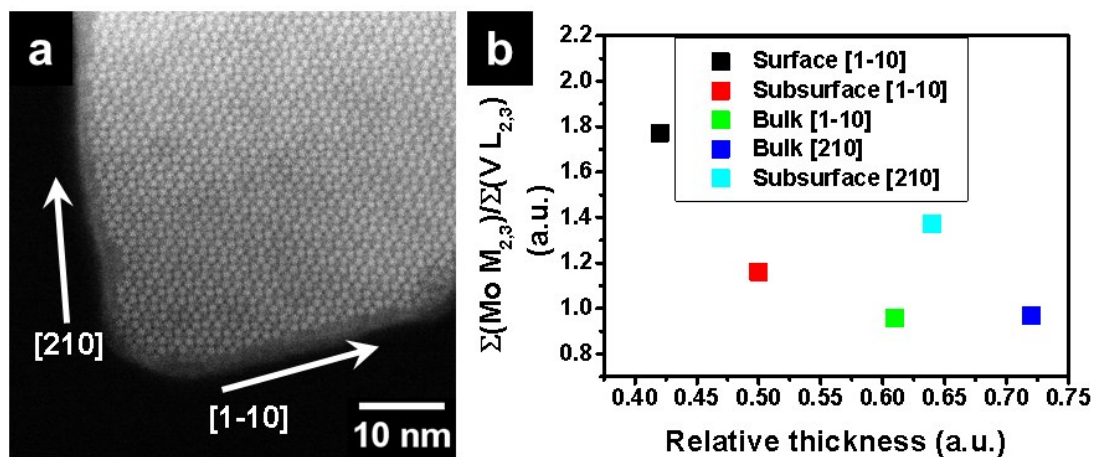
Figure S3-9: a) HAADF-STEM image of (Mo,V)O$_x$ particle viewed along [001] indicating the scan direction and length (white arrows) b) corresponding qualitative Mo/V ratio estimation based on STEM-EELS analysis.
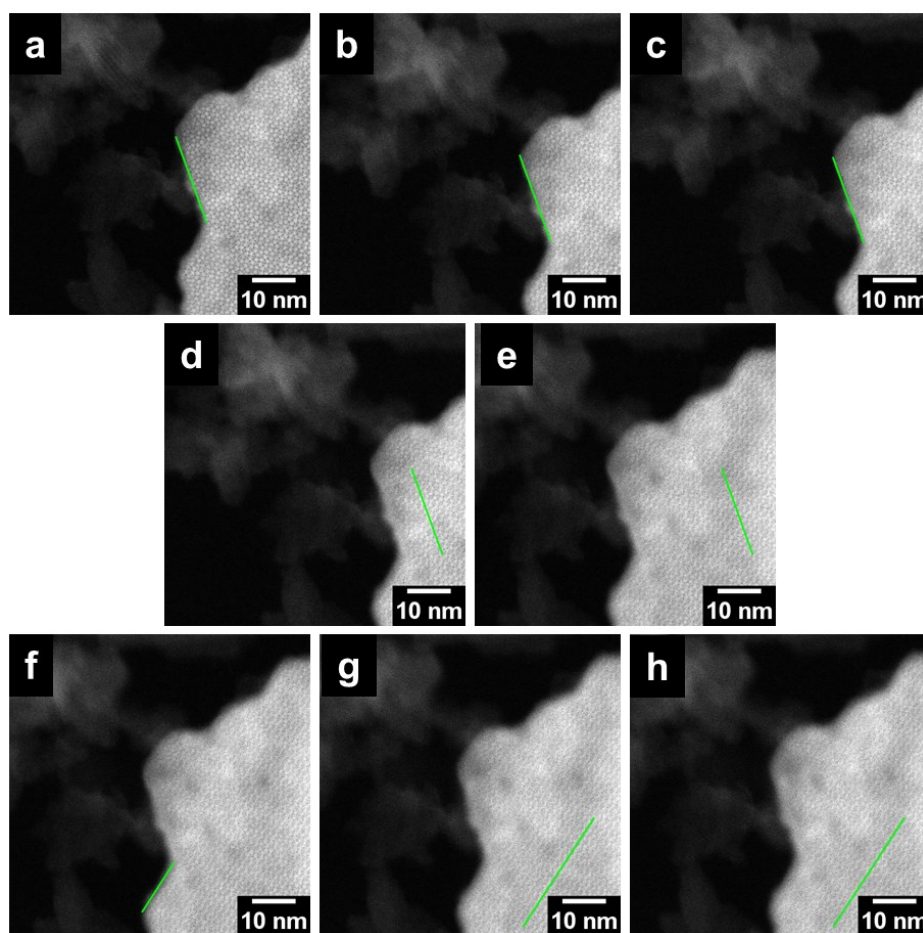
Figure S3-10: HAADF-STEM images of (Mo,V)O$_x$ particle viewed along [001] indicating the scan positions (green lines).

4 A *quasi in-situ* TEM reactor for decoupling catalytic gas phase reactions and analysis

4.1 Abstract

We present a versatile transmission electron microscopy (TEM) grid reactor setup, which is based on the concept of decoupling catalytic gas-phase reactions and structural analysis. The system exhibits superior properties in terms of image resolution, long-term measurements and gas analytics compared to conventional *in-situ* TEM analysis and allows for monitoring catalytic conversions on a TEM grid by proton-transfer reaction mass spectrometry. Using Pt and Cu/ZnO/Al$_2$O$_3$ as an example we show that structural changes of identical particles before and after reactive experiments can be tracked. In addition, identical location imaging benefits from a secure transfer of the sample between TEM and the reactor system by vacuum transfer holders. During catalytic testing the samples are exposed to homogeneous reaction conditions. The concept minimizes electron-sample and electron-atmosphere interactions and can prospectively be considered as complementary tool to *in-situ* TEM analysis.

4.2 Introduction

Heterogeneous catalysis is considered to be one of the most promising technologies for prospective energy storage.[1-2] To tailor catalyst systems for such specific applications the evolution of the active phases under a given chemical potential and their impact on catalytic conversion has to be understood. A pre-requisite for harvesting details on relevant structural dynamics is the investigation of catalytic systems at relevant reaction conditions (i.e. gaseous environment, temperature, pressure), which also includes the detection of catalytic conversion. These requirements can be met by spectroscopic and electron microscopic techniques.[3-7] Gas-phase induced changes can for instance be tracked by *in-situ* spectroscopic analysis, such as infra-red (IR), Raman or X-ray photoelectron spectroscopy (XPS).[8-10] In combination with theoretical modelling, these techniques can deliver integral information of compositional alterations, surface species and oxidation states.[11-12] Those analytical methods, however, average

over the whole sample and, thus, local alterations and/or important defects, and surface states may be overlooked.

Local geometric and electronic information can be obtained by *ex-situ* and *in-situ* transmission electron microscopy (TEM), respectively.[13-18] In *ex-situ* TEM experiments, samples are analyzed after removal from the catalytic reactor using the optimal TEM resolution and are compared with the structure of as-synthesized samples. This *ex-situ* approach neglects the position of the investigated catalyst particles in the reactor, whose surface structures may be biased by location-dependent modifications of the gas composition and/or temperature gradients.[19-20] Due to these inhomogeneities, extrapolation of the observed local surface structure to the whole catalyst system may not reflect the state of the complete catalyst batch inside the reactor. In addition, during exposure to ambient air, hydration phenomena may occur that alter the structure of the surface.

The concept of *in-situ* TEM is long-rooted in electron microscopic science.[21-23] Currently, two kinds of *in-situ* TEM set-ups are commonly used: (1) environmental and (2) gas-cell holders.[6, 15, 18, 24-25] In the former set-up, gas is introduced directly into the octagon region of the TEM. Owing to electron scattering events at the gaseous atmosphere the pressure is limited to approximately 1 mbar. For the latter set-up, the sample is sandwiched between two microelectromechanical system (MEMS) chips, which are equipped with electron transparent windows. Those systems can be applied in a broad research field, which ranges from heterogeneous catalysis, electrocatalysis, to biochemistry, inorganic chemistry and engineering.[6, 26-31] *In-situ* TEM delivers valuable insights into sample-gas and sample-liquid interactions, or mechanical stabilities. Gas cell holders can be operated at ambient pressure. However, data interpretation of *in-situ* experiments may be limited by lower resolution and electron-matter interactions.

To link the advantages of *ex-situ* with *in-situ* TEM analysis, the *quasi in-situ* approach was developed.[32-33] *Quasi in-situ* TEM is defined as the repeated exposure of the same specific sample to the TEM and to relevant as well as homogeneous reaction conditions outside the TEM.[34] The concept of *quasi in-situ* TEM has already been exploited, for instance, in the electrochemical degradation of Pt/C systems and in corrosion studies of AA2024-T3 alloys.[34-35] Changes of the particles were monitored by identical location imaging (ILI).[35-36] In addition, a

controlled environment TEM holder has been recently introduced, which allows for sample transfer between different analytical tools under the same environment.[33]

Here, we present a *quasi in-situ* set-up as general tool to study catalytic gas-phase reactions on a TEM grid under relevant and homogeneous conditions. The reactor setup decouples catalysis and analysis. The system operates at elevated temperatures and allows the detection of catalytic conversion. A sophisticated transfer procedure is established to transport the TEM grid without exposure to ambient air. The proof of working principle is demonstrated here with CO oxidation over different Pt compounds and the reductive activation of Cu/ZnO/Al$_2$O$_3$ catalyst for methanol synthesis.

4.3 Materials and methods

The setup of the *quasi in-situ* TEM grid reactor is presented in Figure 4-1. It is composed of three CF-16 parts that are sealed by inert Au coated Cu gaskets and can be operated at ambient pressure. The reactor was passivated by silylation (Silkotec). The top part of the reactor that is shown in Figure 4-1A resembles a schematic drawing of the modified CF-16 blind flange that hosts gas in- and outlet, and Reynold´s number calculations imply a laminar gas flow to the sample. The middle CF-16 flange exhibits a sealable feed-through for one thermocouple (type K). The thermocouple is mounted in an electrically conductive Si-infiltrated SiC (Si/SiC) sample holder and touches the bottom of the TEM grid. The TEM grid is fixed in the cavity of the Si/SiC sample holder by Au coated Cu clamp rings (Figure 4-1C). The Si/SiC sample holder is screwed on an Au coated stainless steel holder, which is placed on top of a CF-16 fused-silica window (MDC Vacuum Ltd.). The fused-silica window exhibits high transparency for red and infrared (IR) light. Passive heating of the TEM grid is accomplished by the Si/SiC holder, which is exposed to an IR laser light (λ= 800 nm, Limo) from the bottom. The laser light ensures temperatures up to 500°C. Owing to the small sample (<60 µg) and high power of the laser a fast heating and rapid cooling (quenching) can be realized. As shown in Figure 4-1B the gas in- and outlet are composed of Swagelok tubes and nuts (1/8", 1/16"). The reactor is connected via Swagelok quick connectors of the QM series to the gas feeding line (inlet).

At the outlet, a proton-transfer mass spectrometer (PTR-MS, Ionicon) is placed to detect the conversion of the catalytic reaction. TEM images were recorded on a Cs corrected FEI Titan 80-300 and on a double corrected JEOL ARM 200F, respectively. GATAN vacuum transfer

holders (single tilt 648 and VTST4006) were used for sample transfer. Energy dispersive X-ray (EDX) spectrometry was recorded on a Philipps CM FEG 200 equipped with a Genesis 4000 EDX detector.

250 µm thick Pt foils (99.9999, Goodfellow) were purchased from Goodfellow. A round, self-supporting sample with 3 mm diameter, which matches the diameter of the TEM grid holder, was stamped out the foil before catalytic testing. Pt nanoparticles were prepared by vapor deposition onto silica coated Si_3N_4 windows (15 nm, Norcada). $Cu/ZnO/Al_2O_3$ catalysts were synthesized as reported previously.[37]
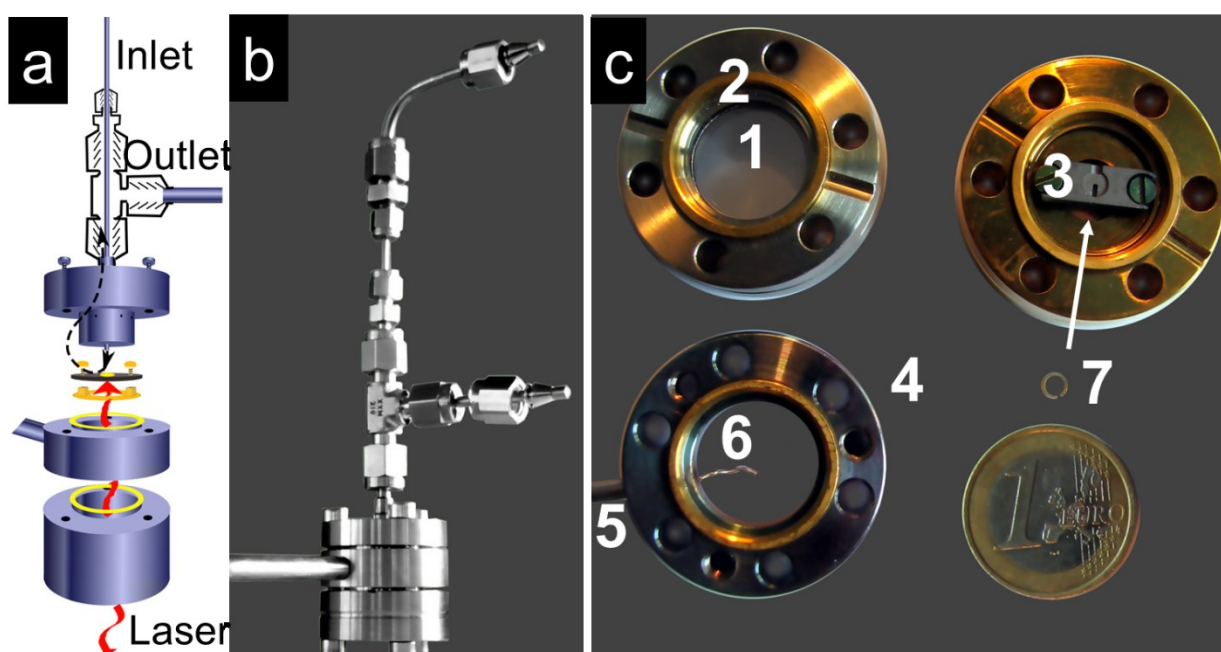
Figure 4-1: The quasi in-situ TEM grid reactor. (a) Schematic drawing and (b) photograph of the TEM grid reactor, highlighting gas in- and outlet, and laser light supply. (c) Detailed photographs of the bottom and center flanges of the TEM grid reactor: (1) Au coated CF- 16 flange with fused silica window, (2) Au coated Cu gasket, (3) Si/SiC crucible with TEM grid cavity and slot for the thermocouple (white arrow) mounted on an annular Au coated stainless steel holding device, which is placed on top of the fused silica window sample, (4) modified center CF-16 flange, (5) feedthrough for thermocouple, (6) thermocouple, and (7) clamp ring to mount the TEM grid in the Si/SiC crucible.

4.4 Results

4.4.1 Conversion detection

For catalytic reactions, which happen on a TEM grid, very low conversions can be expected. To overcome this detection limitation a PTR-MS is used. The PTR-MS is very sensitive and allows the detection of volatile species in the low parts per trillion (pptv) regime.[38-39] The absence of electron ionization is the key for its selectivity. Ionization is usually accompanied by a high-energy impact on the analyte, which subsequently leads to undesired fragmentation, which lowers the sensitivity. In PTR-MS, the ionization is initiated by energetic soft proton transfer from *in-situ* generated hydronium cations to the analyte. A prerequisite for the detection of the volatile molecule is usually a higher proton affinity (PA) of the analyte compared to water (PA= 7.2 eV). However, if gases have to be detected that have a lower proton affinity than water, for instance CO_2 (PA= 5.6 eV), an additional energy of 1.6 eV can be applied to shift the reaction towards protonated CO_2 (CO_2H^+). The energetic boost can be obtained by fine tuning the voltages at the end of the drift tube.[40] Note, the PA of CO (PA= 6.2 eV) is higher than the one for CO_2.

4.4.2 Temperature calibration and wall reactivity

The temperature of the TEM grid reactor was calibrated by thermal decomposition of carbonates (Figure 4-2A). Lead carbonate (PbCO3) was used as carbonate source. PbCO3 decomposes in three distinct steps at temperatures below 400°C to PbO.[41] These three steps which arise at 248 °C, 293 °C, and 343 °C can also be observed in thermogravimetric reference measurements (TGA, Figure 4-2a, top and middle), which were conducted in Ar atmosphere. During the thermal decomposition of PbCO3 using the TEM grid reactor setup the CO2 traces of the PTR-MS (Figure 4-2a, bottom) reveal a shoulder at lower temperatures and two sharp peaks at 310°C and 360°C. The shift to higher temperatures in the PTR-MS CO2 traces may be attributed to the cooling of the low amount of sample by a relatively high flow of N2 and/or an increased response time of the PTR-MS as a consequence of a large reactor-MS distance.

CO oxidation was chosen as a catalytic test reaction since this reaction requires very clean and inert reactors. This is of particular importance due to the low amount of catalysts, which is usually deposited on the TEM grid. The presence of hydrocarbons, dust impurities and/or reactive walls can increase the CO2 signal. In addition, CO forms volatile carbonyl

species with Ni (Mond Process) and Fe (Carbonyl Iron) even at room temperature. These volatile carbonyls decompose at temperatures above 200 °C at the sample as evidenced by the blue interference pattern and the energy dispersive X-ray spectra, which are presented in Figure 4-2b, top. To avoid the formation and deposition of volatile Ni and/or Fe carbonyls a carbonyl trap filled with SiC particles was placed in front of the reactor and heated to 250 °C. After the carbonyl trap Cu tubes were used and all reactive stainless steel parts, including the thermocouple, inside the reactor were coated with a macroscopic Au layer, which is inactive in the CO oxidation.[42] After this passivation step, no Ni and/or Fe species were identified on the sample as indicated by EDX measurements (Figure 4-2b, bottom).
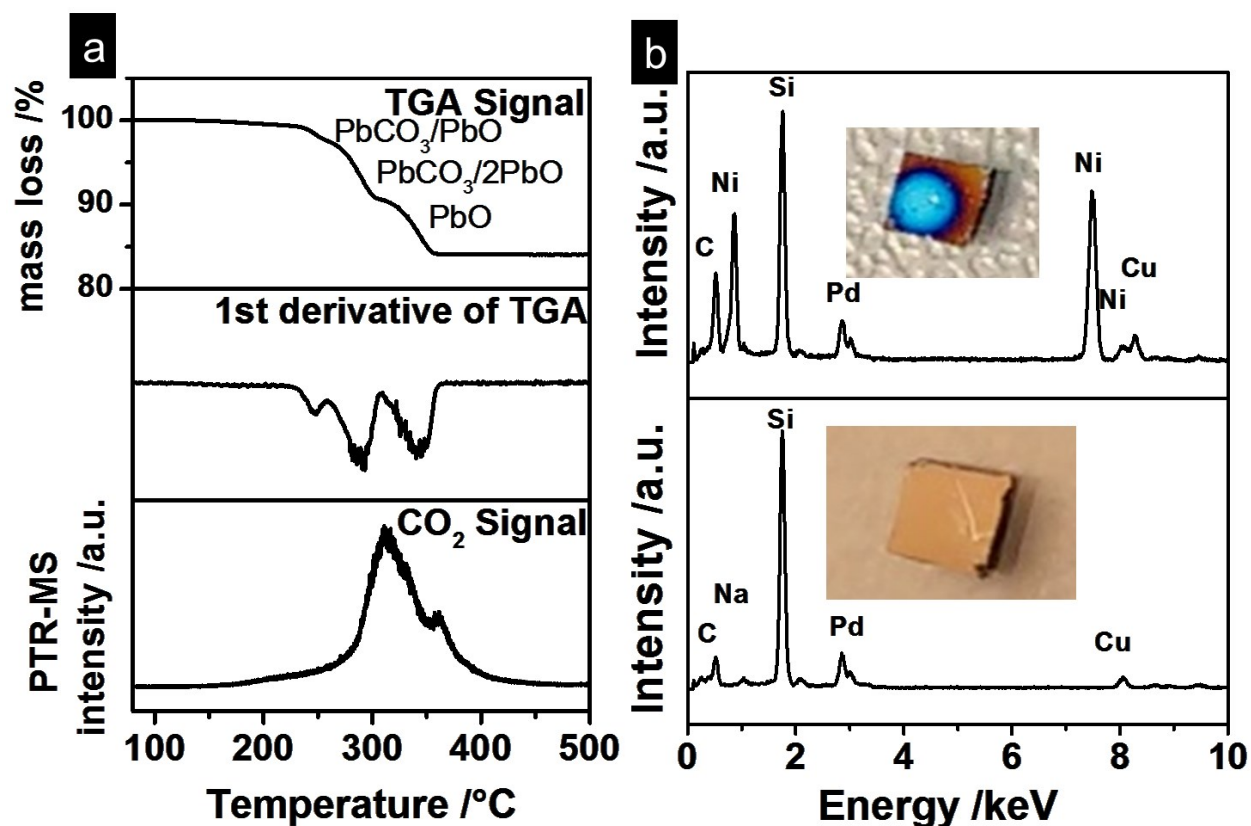
Figure 4-2. (a) Temperature calibration of the TEM grid reactor: TGA signal (top), 1st derivative of the TGA signal (middle) and PTR-MS signal (bottom) as obtained from the thermal decomposition of $PbCO_3$ in inert atmosphere recorded with a heating rate of 10 °C/min. (b) EDX measurements of Pd@Si wavers, which were placed in the TEM grid reactor during CO oxidation: (top) before and (bottom) after inertization. The Cu signal can be attributed to the TEM holder.

4.4.3   Catalytic Oscillations

Figure 4-3a shows PTR-MS CO and CO_2 traces of a polycrystalline Pt foil (diameter: 3mm), which was exposed to CO oxidation conditions ($CO:O_2$=1:5) in the TEM grid reactor. The reaction of CO and O_2 over Pt foils has a long history in heterogeneous catalysis research[43] and was tracked in the temperature regime up to 450 °C using heating and cooling rates of 10 and 2 °C/min, respectively. Above 250 °C the formation of CO_2 was detected, while the CO signal decreased. The relatively high onset temperature might be attributed to the low sensitivity of the PTR-MS for CO_2 (approx. 100 ppm). During fast heating (10 °C/min) weak oscillations were observed in the temperature regime between 290 °C and 310 °C (Figure 4-3b). Upon slow cooling (2 °C/min) strong oscillations were detected in the temperature interval between 320 °C and 290 °C (Figure 4-3c). In addition, an exponential correlation of the oscillation periodicity and temperature was found (Figure 4-3d). Such oscillations are common for platinoids in CO oxidation and may originate at pressures above 1 mbar from an interchanging between metallic and oxidic surfaces states.[44] CO exhibits high adsorption energy for metal surfaces, which generates smoothed surfaces states. After conversion of CO to CO_2, the CO partial pressure decreases and the excess oxygen initiates the formation of rough oxidic surfaces. This may enhance the reaction velocity. Roughening, however, energetically favors metallic surfaces, which are less active. The decrease of the reaction rate ensures an accumulation of CO on smoothed surfaces. This model[44] theoretically predicted a strong temperature dependency of the oscillations. As opposed to previous measurements[45], the temperature dependency of our data underlines an exponential increase of the periodicity of oscillations with decreasing temperature.
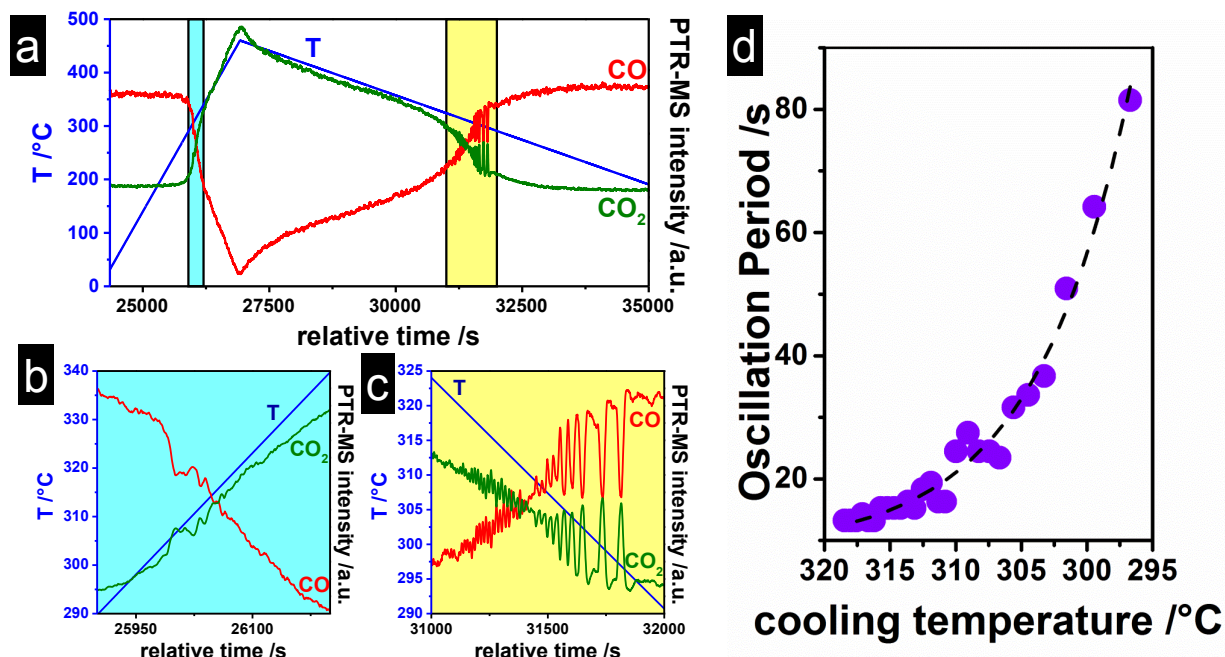
Figure 4-3: CO Oxidation of a Pt foil in the TEM grid reactor: (a) PTR-MS traces of CO and CO_2; (b) magnified excerpt of the heating curve taken from the cyan region in (a); (c) close up of yellow region from the cooling curve; (d) oscillation period versus cooling temperature. The inset in (d) represents and SEM image of the Pt foil, which was thinned by ion milling to obtain electron transparent parts. Conditions: N2: 13.62 ml/min, O2: 1.15 ml/min, CO: 0.23 ml/min, heating rate: 10°C/min, cooling rate: 2°C/min.

4.4.4   Identical location imaging (ILI)

The morphological changes accompanying CO oxidation were investigated (Figure 4-4) using Pt nanoparticles. The corresponding light-off curve of Pt nanoparticles is presented in Figure 4-4a. The exposure of pristine Si_3N_4 TEM grids to CO oxidation conditions evidences no catalytic conversion (Figure 4-4a, bottom) in the measured temperature regime, which demonstrates the inertness and cleanliness of the reactor setup. After the deposition of Pt nanoparticles on the TEM grid an increase of the CO_2 traces (Figure 4-4a, middle), which is accompanied by a decrease of the CO signal (Figure 4-4a, top), is detected by the PTR-MS at temperatures above 200°C. After quenching the reaction, identical Pt nanoparticles were reinvestigated in the TEM. A detailed particle size distribution analysis (Figure 4-4b) indicates the transformation of spherical to more anisotropic particles. Figure 4-4c displays TEM images recorded at identical locations before (top) and after (bottom) the catalytic reaction. The images

demonstrate the mobility of individual nanoparticles during the prevailing time of the catalytic reaction, which can be expressed by rotation, migration or reshaping.
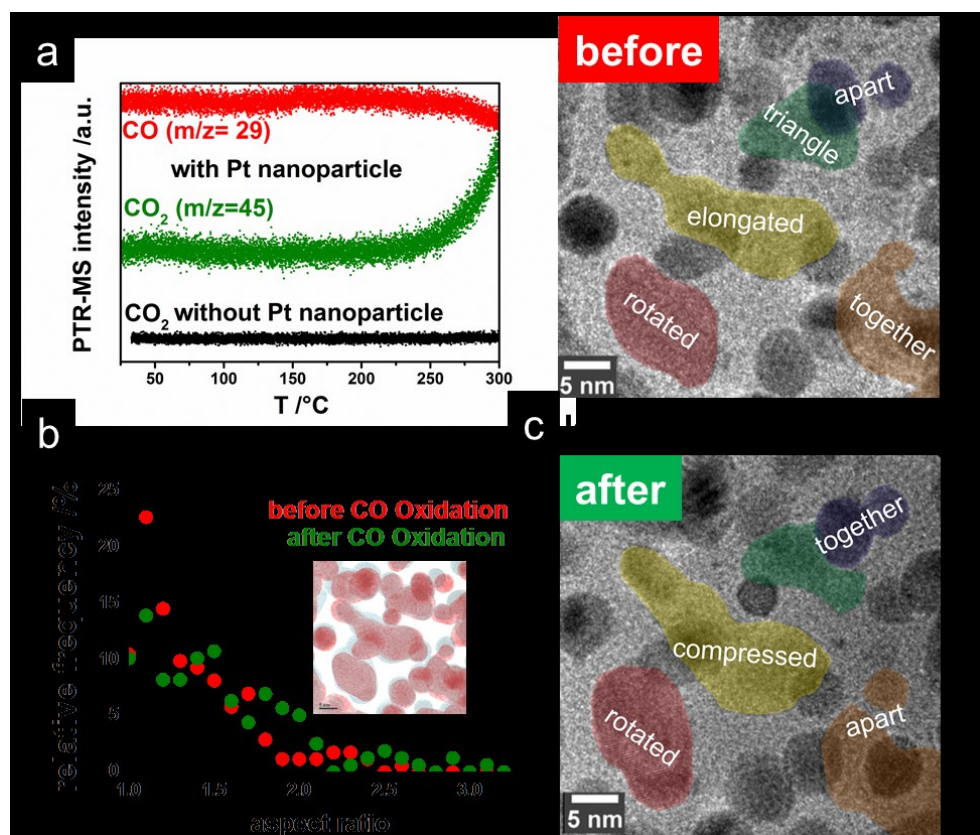
Figure 4-4: Identical location imaging of Pt nanoparticle in CO Oxidation: (a) PTR-MS traces and (b) statistical analysis of morphological changes of Pt nanoparticles before (red) and after (green) CO Oxidation. (c) Identical location imaging of Pt nanoparticles before (top) and after (bottom) CO Oxidation. Conditions: $CO:O_2:N_2=1:5:60$, ramp: 10°C/min, flow: 15 ml/min.

4.4.5   Sample transfer and high resolution imaging

As shown in Figure 4-5a,b the *quasi in-situ* TEM approach allows to track catalysis induced changes at atomic resolution. In addition, often post-catalytic contact to ambient air may cause changes to the samples, which can be expressed by oxidation, hydration and/or electronic structure alterations. Therefore, a secure transfer system was established to avoid exposure to ambient air during transport of the sample from the TEM grid reactor to the TEM and back. The transfer system involves the use of automatic and hermetical sealed quick connectors mounted at the inlet and outlet of the reactor, the transient storage and transfer into an Ar-containing inert glove box and the use of vacuum transfer holders[32]. Imaging the $Cu/ZnO/Al_2O_3$ catalyst for

methanol synthesis after reductive activation in hydrogen atmosphere at ambient pressure may act as an example. During this activation period the Cu^{2+} moieties, which are homogeneously distributed in the solid zincian malachite solution start to form individual, metallic Cu nanoparticles. Those *in-situ* generated Cu nanoparticles are supported and, due to the occurrence of strong metal support interaction (SMSI), embedded by a ZnO overlayer.[46] Cu, however, is very sensitive to oxygen and immediately oxidizes even at room temperature at oxygen partial pressure above 10^{-9} mbar. Figure 4-5c shows a high resolution TEM image of zinchian malachite reduced in the TEM grid reactor at 350 °C. The sample was securely transferred via the outlined transfer system. Fast Fourier Transform (FFT) analysis evidences the presence of metallic Cu nanoparticle, which is embedded by an amorphous ZnO layer. The absence of the graphite-like structure of the ZnO overlayer can be attributed to the higher reduction temperature.
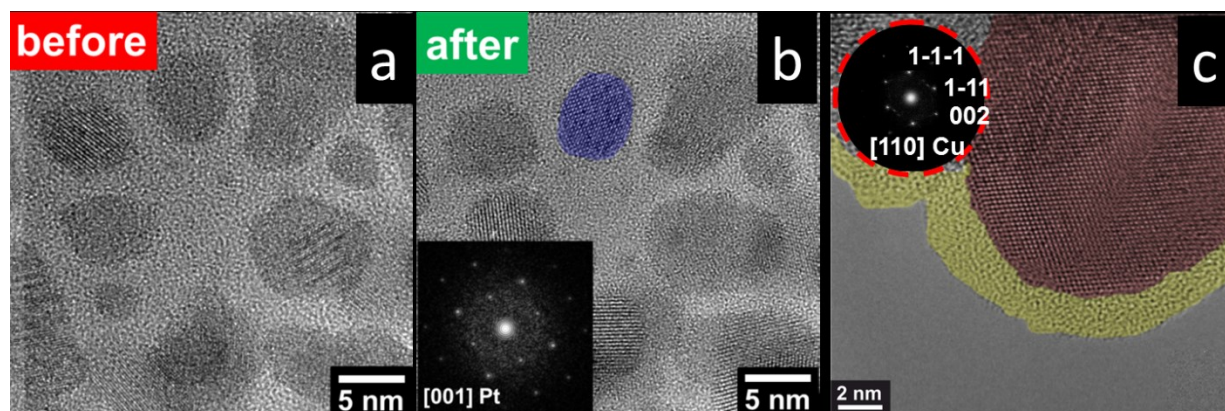
Figure 4-5: High resolution TEM images of Pt nanoparticles before (a) and after (b) CO oxidation (Conditions: CO:O$_2$:N$_2$=2:1:60, ramp: 10°C/min, flow: 15 ml/min). The Fast Fourier analysis (FFT, inset (b, bottom) was recorded from the blue highlighted Pt nanoparticle (c) Inert sample transfer: High resolution TEM image of reduced Cu/ZnO/Al$_2$O$_3$ activated in hydrogen atmosphere at 350°C (conditions: H$_2$/N$_2$ =10/90, heating rate: 10°C/min, dwell time: 2 h); red: Cu and yellow: ZnO.

4.5 Discussion and conclusions

As shown above, the presented TEM grid reactor allows the visual investigation of morphological changes of identical catalyst particles under *quasi in-situ* conditions, i.e. decoupling the catalytic gas-phase reaction and TEM analysis. The system allows the detection of conversion of TEM amounts of sample and is robust to withstand different conditions and gas mixtures, ranging from reductive to oxidative. In addition, the different samples, which were

investigated, display the broad versatility of this concept. The possibility to detect oscillation phenomena further indicates the fast response and read out time of the PTR-MS and shows the capability of our system to track kinetic phenomena.

Quasi in-situ TEM characterization features relevant, homogeneous reaction, and well-defined flow conditions for all catalyst particles and high-resolution TEM imaging. The introduced transfer system (reactor ↔ glove box ↔ vacuum transfer holder ↔ TEM) allows a secure sample transfer and the avoidance of moisture and air-induced surface changes. In addition, the impact of the electron beam during the catalytic reaction, which is expressed by electron-sample and/or electron-gas interactions, can be minimalized by this concept. The minimization of the electron impact is of particular importance in heterogeneous catalysis. Usually, solid catalyst systems are highly energetic, metastable materials, which geometrically and/or electronically transform even by small external energy stimuli. In addition, gases may form reactive radical species while interacting with the electron beam and may, therefore, contribute to irrelevant catalytic conversion and/or structural changes. The TEM grid reactor concept does not deliver any real-time information and may be prone to cooling and transfer artifacts, as well as wall reactions. As we have shown above, the latter can be avoided by careful passivating the inner parts of the reactor.

Prospectively, the *quasi in-situ* approach may complement *ex-situ* and *in-situ* TEM analysis in heterogeneous catalysis linking relevant reaction conditions, high resolution imaging, and detectable conversion with real time imaging. A relevant, overall and visual picture of structural alterations during heterogeneous catalysis can only be obtained, if *quasi in-situ* and *in-situ* TEM are applied on the same sample and the same conditions in a comprehensive fashion. Heterogeneous catalyst can be best compared, when they operate under steady state conditions. Thus, in particular for catalytic systems, for which the development of the steady state regime is a long-lasting process, the TEM grid reactor setup will be beneficial.

4.6 References

1. Olah, G. A.; Goeppert, A.; Prakash, G. K. S., *Beyond Oil and Gas: The Methanol Economy*. Wiley: 2009.

2. Schlögl, R., *Chemical Energy Storage*. De Gruyter: 2013.

3. Hävecker, M.; Mayer, R. W.; Knop-Gericke, A.; Bluhm, H.; Kleimenov, E.; Liskowski, A.; Su, D.; Follath, R.; Requejo, F. G.; Ogletree, D. F.; Salmeron, M.; Lopez-Sanchez, J. A.; Bartley, J. K.; Hutchings, G. J.; Schlögl, R., In Situ Investigation of the Nature of the Active Surface of a Vanadyl Pyrophosphate Catalyst during n-Butane Oxidation to Maleic Anhydride. *The Journal of Physical Chemistry B* **2003,** *107* (19), 4587-4596.

4. Hävecker, M.; Wrabetz, S.; Kröhnert, J.; Csepei, L.-I.; Naumann d'Alnoncourt, R.; Kolen'ko, Y. V.; Girgsdies, F.; Schlögl, R.; Trunschke, A., Surface chemistry of phase-pure M1 MoVTeNb oxide during operation in selective oxidation of propane to acrylic acid. *J. Catal.* **2012,** *285* (1), 48-60.

5. Trunschke, A.; Noack, J.; Trojanov, S.; Girgsdies, F.; Lunkenbein, T.; Pfeifer, V.; Hävecker, M.; Kube, P.; Sprung, C.; Rosowski, F.; Schlögl, R., The Impact of the Bulk Structure on Surface Dynamics of Complex Mo–V-based Oxide Catalysts. *ACS Catal.* **2017,** *7* (4), 3061-3071.

6. Vendelbo, S. B.; Elkjær, C. F.; Falsig, H.; Puspitasari, I.; Dona, P.; Mele, L.; Morana, B.; Nelissen, B. J.; van Rijn, R.; Creemer, J. F.; Kooyman, P. J.; Helveg, S., Visualization of oscillatory behaviour of Pt nanoparticles catalysing CO oxidation. *Nat Mater* **2014,** *13* (9), 884-890.

7. Bremmer, G. M.; Zacharaki, E.; Sjastad, A. O.; Navarro, V.; Frenken, J. W. M.; Kooyman, P. J., In situ TEM observation of the Boudouard reaction: multi-layered graphene formation from CO on cobalt nanoparticles at atmospheric pressure. *Faraday Discussions* **2017,** *197* (0), 337-351.

8. Eren, B.; Heine, C.; Bluhm, H.; Somorjai, G. A.; Salmeron, M., Catalyst Chemical State during CO Oxidation Reaction on Cu(111) Studied with Ambient-Pressure X-ray Photoelectron Spectroscopy and Near Edge X-ray Adsorption Fine Structure Spectroscopy. *Journal of the American Chemical Society* **2015,** *137* (34), 11186-11190.

9.   Velasco-Velez, J. J.; Pfeifer, V.; Hävecker, M.; Weatherup, R. S.; Arrigo, R.; Chuang, C.-H.; Stotz, E.; Weinberg, G.; Salmeron, M.; Schlögl, R.; Knop-Gericke, A., Photoelectron Spectroscopy at the Graphene–Liquid Interface Reveals the Electronic Structure of an Electrodeposited Cobalt/Graphene Electrocatalyst. *Angewandte Chemie International Edition* **2015,** *54* (48), 14554-14558.

10.   Burcham, L. J.; Deo, G.; Gao, X.; Wachs, I. E., In situ IR, Raman, and UV-Vis DRS spectroscopy of supported vanadium oxide catalysts during methanol oxidation. *Topics in Catalysis* **2000,** *11* (1), 85-100.

11.   Pfeifer, V.; Jones, T. E.; Velasco Velez, J. J.; Massue, C.; Greiner, M. T.; Arrigo, R.; Teschner, D.; Girgsdies, F.; Scherzer, M.; Allan, J.; Hashagen, M.; Weinberg, G.; Piccinin, S.; Havecker, M.; Knop-Gericke, A.; Schlogl, R., The electronic structure of iridium oxide electrodes active in water splitting. *Physical Chemistry Chemical Physics* **2016,** *18* (4), 2292-2296.

12.   Pfeifer, V.; Jones, T. E.; Wrabetz, S.; Massue, C.; Velasco Velez, J. J.; Arrigo, R.; Scherzer, M.; Piccinin, S.; Havecker, M.; Knop-Gericke, A.; Schlogl, R., Reactive oxygen species in iridium-based OER catalysts. *Chemical Science* **2016,** *7* (11), 6791-6795.

13.   Freakley, S. J.; He, Q.; Harrhy, J. H.; Lu, L.; Crole, D. A.; Morgan, D. J.; Ntainjua, E. N.; Edwards, J. K.; Carley, A. F.; Borisevich, A. Y.; Kiely, C. J.; Hutchings, G. J., Palladium-tin catalysts for the direct synthesis of H_2O_2 with high selectivity. *Science* **2016,** *351* (6276), 965-968.

14.   Nguyen, L.; Tao, F., Development of a reaction cell for in-situ/operando studies of surface of a catalyst under a reaction condition and during catalysis. *Review of Scientific Instruments* **2016,** *87* (6), 064101.

15.   de Jonge, N.; Bigelow, W. C.; Veith, G. M., Atmospheric Pressure Scanning Transmission Electron Microscopy. *Nano Letters* **2010,** *10* (3), 1028-1031.

16.   Lunkenbein, T.; Girgsdies, F.; Kandemir, T.; Thomas, N.; Behrens, M.; Schlögl, R.; Frei, E., Bridging the Time Gap: A Copper/Zinc Oxide/Aluminum Oxide Catalyst for Methanol Synthesis Studied under Industrially Relevant Conditions and Time Scales. *Angewandte Chemie International Edition* **2016,** *55* (41), 12708-12712.

17.   Lunkenbein, T.; Schumann, J.; Behrens, M.; Schlögl, R.; Willinger, M. G., Formation of a ZnO Overlayer in Industrial Cu/ZnO/Al2O3 Catalysts Induced by Strong Metal–Support Interactions. *Angewandte Chemie International Edition* **2015,** *54* (15), 4544-4548.

18.   Wang, Z.; Santhanagopalan, D.; Zhang, W.; Wang, F.; Xin, H. L.; He, K.; Li, J.; Dudney, N.; Meng, Y. S., In Situ STEM-EELS Observation of Nanoscale Interfacial Phenomena in All-Solid-State Batteries. *Nano Letters* **2016,** *16* (6), 3760-3767.

19.   Korup, O.; Goldsmith, C. F.; Weinberg, G.; Geske, M.; Kandemir, T.; Schlögl, R.; Horn, R., Catalytic partial oxidation of methane on platinum investigated by spatial reactor profiles, spatially resolved spectroscopy, and microkinetic modeling. *Journal of Catalysis* **2013,** *297*, 1-16.

20.   Korup, O.; Mavlyankariev, S.; Geske, M.; Goldsmith, C. F.; Horn, R., Measurement and analysis of spatial reactor profiles in high temperature catalysis research. *Chemical Engineering and Processing: Process Intensification* **2011,** *50* (10), 998-1009.

21.   Ruska, E., Beitrag zur übermikroskopischen Abbildung bei höheren Drucken. *Kolloid-Zeitschrift* **1942,** *100* (2), 212-219.

22.   Marton, L., Electron Microscopy of Biological Objects. *Physical Review* **1934,** *46* (6), 527-528.

23.   Marton, L., La microscope electronique des objects biologiques. *Acad. R. Belg. Bull. Cl. Sci.* **1934,** *5* (20), 439-446.

24.   Hansen, T. W.; Wagner, J. B., Environmental Transmission Electron Microscopy in an Aberration-Corrected Environment. *Microscopy and Microanalysis* **2012,** *18* (4), 684-690.

25.   Helveg, S.; Lopez-Cartes, C.; Sehested, J.; Hansen, P. L.; Clausen, B. S.; Rostrup-Nielsen, J. R.; Abild-Pedersen, F.; Norskov, J. K., Atomic-scale imaging of carbon nanofibre growth. *Nature* **2004,** *427* (6973), 426-429.

26.   Roiban, L.; Li, S.; Aouine, M.; Tuel, A.; Farrusseng, D.; Epicier, T., Fast 'Operando' electron nanotomography. *Journal of Microscopy* **2017**, n/a-n/a.

27.   de Jonge, N.; Ross, F. M., Electron microscopy of specimens in liquid. *Nat Nano* **2011,** *6* (11), 695-704.

28.   Hermannsdörfer, J.; de Jonge, N., Studying Dynamic Processes of Nano-sized Objects in Liquid using Scanning Transmission Electron Microscopy. *Journal of Visualized Experiments : JoVE* **2017,** (120), 54943.

29.   Elgrabli, D.; Dachraoui, W.; Ménard-Moyon, C.; Liu, X. J.; Bégin, D.; Bégin-Colin, S.; Bianco, A.; Gazeau, F.; Alloyeau, D., Carbon Nanotube Degradation in Macrophages: Live Nanoscale Monitoring and Understanding of Biological Pathway. *ACS Nano* **2015,** *9* (10), 10113-10124.

30.   Raabe, S.; Mierwaldt, D.; Ciston, J.; Uijttewaal, M.; Stein, H.; Hoffmann, J.; Zhu, Y.; Blöchl, P.; Jooss, C., In Situ Electrochemical Electron Microscopy Study of Oxygen Evolution Activity of Doped Manganite Perovskites. *Advanced Functional Materials* **2012,** *22* (16), 3378-3388.

31.   Hansen, P. L.; Wagner, J. B.; Helveg, S.; Rostrup-Nielsen, J. R.; Clausen, B. S.; Topsøe, H., Atom-Resolved Imaging of Dynamic Shape Changes in Supported Copper Nanocrystals. *Science* **2002,** *295* (5562), 2053-2055.

32.   Kooyman, P. J.; Hensen, E. J. M.; de Jong, A. M.; Niemantsverdriet, J. W.; van Veen, J. A. R., The observation of nanometer-sized entities in sulphided Mo-based catalysts on various supports. *Catalysis Letters* **2001,** *74* (1), 49-53.

33.   Damsgaard, C. D.; Zandbergen, H.; W. Hansen, T.; Chorkendorff, I.; B. Wagner, J., Controlled Environment Specimen Transfer. *Microscopy and Microanalysis* **2014,** *20* (4), 1038-1045.

34.   Malladi, S. R. K.; Tichelaar, F. D.; Xu, Q.; Wu, M. Y.; Terryn, H.; Mol, J. M. C.; Hannour, F.; Zandbergen, H. W., Quasi in situ analytical TEM to investigate electrochemically induced microstructural changes in alloys: AA2024-T3 as an example. *Corrosion Science* **2013,** *69*, 221-225.

35.   Mayrhofer, K. J. J.; Ashton, S. J.; Meier, J. C.; Wiberg, G. K. H.; Hanzlik, M.; Arenz, M., Non-destructive transmission electron microscopy study of catalyst degradation under electrochemical treatment. *Journal of Power Sources* **2008,** *185* (2), 734-739.

36.   Hodnik, N.; Zorko, M.; Bele, M.; Hočevar, S.; Gaberšček, M., Identical Location Scanning Electron Microscopy: A Case Study of Electrochemical Degradation of PtNi Nanoparticles Using a New Nondestructive Method. *The Journal of Physical Chemistry C* **2012,** *116* (40), 21326-21333.

37.   Schumann, J.; Lunkenbein, T.; Tarasov, A.; Thomas, N.; Schlögl, R.; Behrens, M., Synthesis and Characterisation of a Highly Active Cu/ZnO:Al Catalyst. *ChemCatChem* **2014,** *6* (10), 2889-2897.

38.   Lindinger, W.; Hansel, A.; Jordan, A., On-line monitoring of volatile organic compounds at pptv levels by means of proton-transfer-reaction mass spectrometry (PTR-MS) medical applications, food control and environmental research. *International Journal of Mass Spectrometry and Ion Processes* **1998,** *173* (3), 191-241.

39.   Ellis, A. M.; Mayhew, C. A., *Proton Transfer Reaction Mass Spectrometry: Principles and Applications*. Wiley: 2013.

40.   Beauchamp, J.; Herbig, J.; Dunkl, J.; Singer, W.; Hansel, A., On the performance of proton-transfer-reaction mass spectrometry for breath-relevant gas matrices. *Measurement Science and Technology* **2013,** *24* (12), 125003.

41.   Sarig, S.; Kahana, F., Thermal decomposition of basic lead carbonate. *Thermochimica Acta* **1976,** *14* (3), 263-268.

42.   Klyushin, A. Y.; Greiner, M. T.; Huang, X.; Lunkenbein, T.; Li, X.; Timpe, O.; Friedrich, M.; Hävecker, M.; Knop-Gericke, A.; Schlögl, R., Is Nanostructuring Sufficient To Get Catalytically Active Au? *ACS Catalysis* **2016,** *6* (5), 3372-3380.

43.   Langmuir, I., The mechanism of the catalytic action of platinum in the reactions 2Co + O2= 2Co2 and 2H2+ O2= 2H2O. *Transactions of the Faraday Society* **1922,** *17* (0), 621-654.

44.   Hendriksen, B. L. M.; Ackermann, M. D.; van Rijn, R.; Stoltz, D.; Popa, I.; Balmes, O.; Resta, A.; Wermeille, D.; Felici, R.; Ferrer, S.; FrenkenJoost, W. M., The role of steps in surface catalysis and reaction oscillations. *Nat Chem* **2010,** *2* (9), 730-734.

45.   Jensen, R.; Andersen, T.; Nierhoff, A.; Pedersen, T.; Hansen, O.; Dahl, S.; Chorkendorff, I., Self-sustained carbon monoxide oxidation oscillations on size-selected platinum nanoparticles at atmospheric pressure. *Physical Chemistry Chemical Physics* **2013,** *15* (8), 2698-2702.

46.   Lunkenbein, T.; Schumann, J.; Behrens, M.; Schlögl, R.; Willinger, M. G., Formation of a ZnO Overlayer in Industrial Cu/ZnO/Al2O3 Catalysts Induced by Strong Metal–Support Interactions. *Angewandte Chemie* **2015,** *127* (15), 4627-4631.

5 Complex orthorhombic mixed $(Mo,V)O_x$ – an example of a living catalyst

5.1 Abstract

Complexity describes not only the composition and structure of industrially tuned and relevant catalyst systems, but also their ability for structural adaption to the chemical potential of the gaseous surrounding. Here, we explore the structural adaptability of identical orthorhombic $(Mo,V)O_x$ particles by combining scanning transmission electron microscopy (STEM) with a TEM grid reactor at ultimate resolution. The applied conditions mimic relevant conditions of thermal activation (N_2) and catalytic reaction, which is the oxidative dehydrogenation of ethane (ODE). The results, which were obtained by this *quasi in-situ* TEM approach, suggest a reshaping and restructuring of the orthorhombic $(Mo,V)O_x$ particles, which depends on the reaction media and can be expressed by mass transport, restructuring of defect rich- and surface areas and the migration of individual cation columns into surface-near hexagonal channels, while the crystalline bulk of open-framework orthorhombic $(Mo,V)O_x$ remains rather unaffected. The *quasi in-situ* technique was compared to *in-situ* heating in high vacuum conditions. The observed structural reorganization represents an example of an open-framework functional material with a living defect and surface character.

5.2 Introduction

The selective conversion of small alkanes, such as methane, ethane, or propane into more reactive building blocks is one of the key processes in chemical industry.[1-2] To enhance the economic outcome these transformations usually happen on the surface of heterogeneous catalysts.[3-4] However, effective heterogeneous catalysts are quite sophisticated and were often found by empirical rather than by knowledge-based optimization. This knowledge limitation of the working structure of the catalysts restricts any attempts to tailor heterogeneous catalysts for specific applications. These limitations also arise from a dynamical response of heterogeneous catalysts to the chemical potential of the gaseous surrounding, which is difficult to track with often applied *ex-situ* techniques.[5-6]

Therefore, *in-situ* methods for X-ray photoelectron spectroscopy (XPS) or transmission electron microscopy (TEM) measurements have been developed and became a common technique to investigate the working structure of heterogeneous catalysts under operation conditions.[5, 7-11] Heterogeneous catalysis research has benefited from *ex-situ* and *in-situ* TEM investigation as it provides local and visual information of compositional, geometric and electronic inhomogeneities in the bulk and at the surface, which reflects the real structure of a catalyst. However, *in-situ* or *ex-situ* results have to be treated carefully as pressure gap, resolution limitation, electron beam, or uncertain catalysts position in the reactor may affect the interpretation.[7, 12-15]

To overcome these interpretation barriers the *quasi in-situ* TEM approach was developed.[16-19] This technique allows for decoupling, for instance, catalysis at relevant operation conditions and imaging. Catalysis induced geometric and electronic changes can, then, be tracked by comparing identical locations of the same particles with ultimate resolution. This approach is beneficial for following changes of heterogeneous catalysts with nanoscale inhomogenities, which may be otherwise overseen or misinterpreted by common surface and bulk averaging methods.

Such inhomogenities on the nanoscale exists in complex (Mo,V)-based oxide ((Mo,V)O$_x$), which crystallizes in an orthorhombic structure and is sometimes referred to as M1 phase.[20-21] The microstructure is composed of pentagonal {(Mo)Mo$_5$O$_{27}$} building blocks, which are linked by corner sharing MO$_6$ (M=Mo and/or V) octahedra forming hexagonal and heptagonal channels. The hexagonal channels are partially occupied by V moieties.[11] Orthorhombic (Mo,V)O$_x$ is highly active and selective for the oxidative dehydrogenation of ethane (ODE).[22-25] Local and extended defects as well as polyhedra distortions, which can be present in this structure, have recently been catalogued and quantified.[21, 26] In addition to the reported structural inhomogenities, these complex oxides dynamically responses to the reaction media, which can be expressed by structural and compositional surface modifications.[11] The role of the intrinsic geometric defects in the catalytic reaction is still unknown.

A plethora of different (Mo,V) based oxides with different compositions have been subject of a multitude of different catalytic reactions studies aiming to unravel their working structure.[11, 27-29] However, detailed structural studies of their calcination and activation processes are scarce as small structural changes during thermal activation might be overseen by the applied averaging

techniques and/or decomposition of the structure due to overheating or overreducing.[22, 30-36] However, the proper activation of catalysts crucial in order to obtain optimized activity and selectivity distributions.[37] It has been shown, for instance, for quaternary and quinary analogues that the resulting catalytic performance depends on the temperature and atmosphere during calcination as well as on an additional post-treatment, while almost nothing is known for its impact on the microstructure and how it influence the activity of ternary orthorhombic $(Mo,V)O_x$.[22, 38-41]

Here we present a *quasi in-situ* scanning (S)TEM study mimicking calcination (nitrogen) and catalytic reaction (ODE conditions: ethane:oxygen=1:2) at ambient pressure and relevant temperatures to disclose the structure responses of orthorhombic $(Mo,V)O_x$ in different environments with atomic resolution. The outcome of the *quasi in-situ* study is further compared to *in-situ* heating of orthorhombic $(Mo,V)O_x$ in high vacuum. As we will show structural changes are pressure dependent and are most pronounced at the surface, in surface-near region and intergrowth, while the bulk structure remains almost unaffected.

5.3 Results

5.3.1 Quasi in-situ TEM

Quasi in-situ TEM was used to study morphological changes of identical $(Mo,V)O_x$ particles before and after stepwise heat treatments at different temperatures as well as inert and reactive atmospheres at ambient pressure in order to mimic relevant conditions of activation and catalytic conversion. If not explicitly mentioned all (Mo,V)Ox particles were imaged along [001]. Overview annular dark-field (ADF)-STEM images of identical $(Mo,V)O_x$ particles in their pristine, heat treated (2h, 400°C, N_2) and reacted state (2h, 300°C, ethane:oxygen=1:2) are presented in Figure 5-1a, b and c, which represent the starting, intermediate and end point of this study, respectively. Details of the real geometric structure of pristine orthorhombic $(Mo,V)O_x$ are presented elsewhere and form the sound basis of this study.[42]
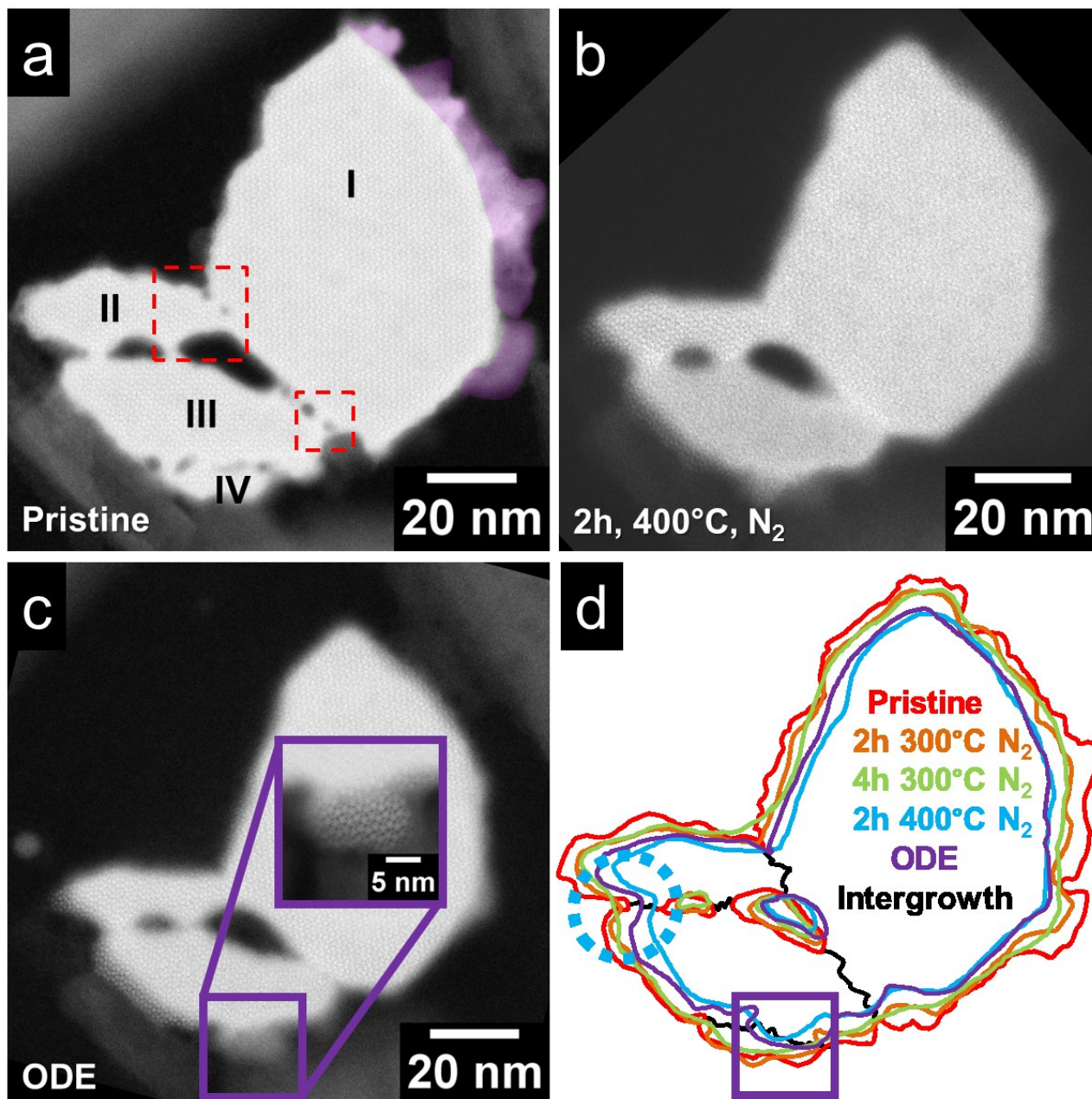
Figure 5-1 ADF-STEM images of oriented (Mo,V)Ox particle viewed along the crystallographic c-axis a) pristine b) after the complete set of heat treatments in N2 atmosphere, c) after ODE and d) the particle surface contours after each heating step. Dashed red squares: areas, which are further examined in Figures 5-3 and 5-4; violet squares and inset: re-oriented grain; black lines: intergrowth positions; dotted cyan circle: region with pronounced change of the surface.

The $(Mo,V)O_x$ particle highlighted in Figure 5-1a,b,c is composed of four crystals, which are interconnected by intergrown regions. In addition, the pristine particle exhibits regions of extended surface defects, which partially embed the bulk of the structure grain I in the array of condensed $(Mo,V)O_x$ crystals (Figure 5-1a, magenta). The surface contours after each step of the thermal treatment for the identical particle are schematically presented in Figure 5-1d. During thermal treatments at different temperatures and atmosphere the surface contours are modified, while the overall bulk microstructure remains. In addition, after thermal activation in nitrogen a stepwise decrease of the surface area of the basal plane (Table 5-1) can be observed. This decrease of the surface area of the basal plane during thermal activation in nitrogen involves mostly the lateral boundaries of the crystals and is accompanied by misorientation of different grains (Table S5-1), a decrease and/or depletion of intergranular pores, which are highlighted by dashed red boxes at the Figure 5-1a, the degradation of extended surface regions (Figure 5-1a, magenta outline) and surface smoothing (Figure 5-1d, blue circle). The ADF-STEM images of orthorhombic $(Mo,V)O_x$ recorded after heat treatment in different atmospheres (Figure 5-1) demonstrate that the $(Mo,V)O_x$ crystal is influenced by the chemical potential of the gaseous environment. As opposed to the ADF-STEM images of the nitrogen treated sample, the $(Mo,V)O_x$ crystal slightly expands after thermal exposure to the ethane/oxygen reaction mixture, which is schematically expressed by the contour plot in Figure 5-1d and the slightly increased surface area is depicted in Table 5-1. This behavior can be explained by a reorientation of small ant thin crystallites, which are clearly resolvable after ODE (Figure 5-1c, inset), and further suggests a reorganization of the intergrowth regions between the individual crystallites.

Table 5-1: Influence of *quasi in-situ* heat treatment in N_2 atmosphere on the observed surface area obtained from identical location ADF-STEM images of the oriented $(Mo,V)O_x$ particle.

Treatment	Normalized Total Area $(10^2$ a.u.$)^a$
Pristine	11.5
2h 300°C N_2	11.3
4h 300°C N_2	11.0
2h 400°C N_2	8.5
ODE	8.8

[a] misorientation corrected.

The origin of the disappearance of the extended defects at the surface during the heat treatment in nitrogen can be versatile and can be expressed by (I) a misorientation and a subsequent abolishment of channeling conditions, (II) a decrease of the thickness of the defect, which renders it unresolvable in the vicinity of a large and heavy scattering particle; (III) the complete loss of the defect by loosening the defect-bulk interphase during heat treatment. For defects, which re-appear as microstructured orthorhombic $(Mo,V)O_x$ grains after heat treatment in an ODE reaction mixture (Figure 5-1c, inset) the degradation mechanism (I) and (II) can be assumed. The disappearance of the outer extended surface defects (Figure 5-1a, magenta area) can be of chemical origin. The occurrence of mass transport may also explain surface smoothening, which is highlighted in Figure 5-1d (see cyan dashed circle).

The microgram amounts of catalyst on the TEM grid, which is required to obtain a beam transparent sample for vicinal STEM investigation leads to high weight hourly space velocity (WHSV) in range of 10^4 ml*g/min in the *quasi in-situ* setup, which can not be reduced by current state-of-the-art mass-flow controllers (Figure S5-1). Despite the expected low conversion the sensitive proton transfer reaction mass spectrometer (PTR-MS) allows for detecting the main reaction product ethylene (black squares in Figure 5-3a, which exhibits proton affinity similar to water. Due to the much lower proton affinity and low conversion, changes of the mass traces that correspond to ethane cannot be observed. CO_2 (blue squares in Figure 5-3a) was also detected. The signal increases with temperature. With the applied PTR-MS settings the sensitivity of this device to CO_2 is approximately 100 ppm (Figure S5-2).[43] Thus, due to the low conversion it seems likely that the majority of detected CO2 originates from the decomposition of organic impurities, which could have lined the walls of the reactor rather than reaction products. The exact quantification at these conditions is difficult due to the occurrence of the back transfer of protons from $CO_2 \cdot H^+$ to ethylene and/or water.[44-45] For comparison, the selectivity-conversion, which was measured in a fixed bed reactor with WHSV of 10^3 ml*g/min is presented in Figure 5-3b, indicating that in the analyzed temperature range 100% selectivity is obtained, which is in a good qualitative agreement with resulting PTR-MS traces, for which the ethylene signal remains constant in the temperature regime.
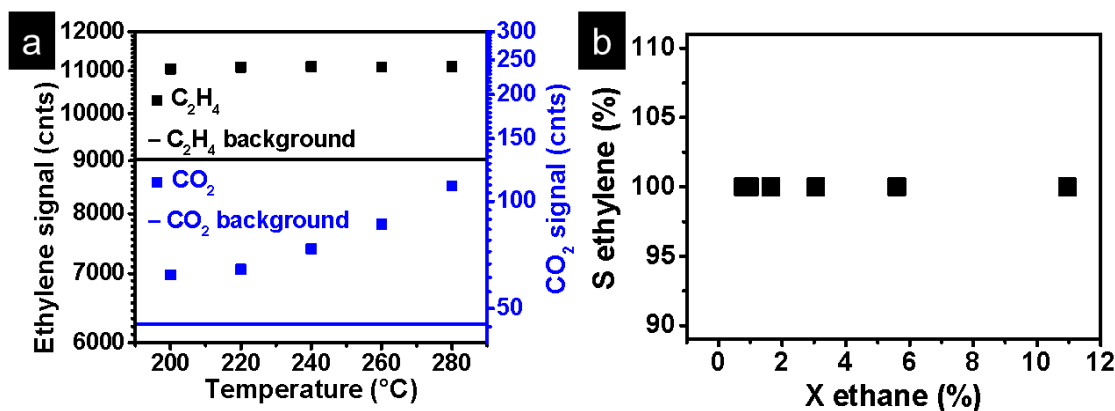
Figure 5-2: a) PTR-MS data confirming conversion presence at around 10^4 ml*g/min WHSV, see Figure S5-2 for details b) comparative selectivity/conversion plot for 10^3 ml*g/min WHSV, total flow 45 ml/min. $C_2H_6:O_2:N_2$ 3:6:91, dwell time at each temperature 4h, heating rate 2°C/min.

5.3.1.1 *Atomic level investigation*

High resolution (HR) ADF-STEM images before and after heat treatment in different atmospheres are shown in Figures 5-3 and 5-4. These ADF-STEM images represent magnified analogues of the region of interests of the crystals presented in Figure 5-1a and highlight two rotated M1 grains, which share an intergrowth interface. In their pristine state, they are also characterized by intergranular pores at their intersection (Figure 5-3a, 4a). As we have shown recently, the extension of the ideal M1 microstructure in orthorhombic $(Mo,V)O_x$ can be tracked by superimposing the image with hexagonal tiles.[42] A superposition of structural tiles, which correspond to the orthorhombic M1 phase, before (black) and after (blue) heat treatment in nitrogen, is presented in Figure 5-3a and indicates a partial depletion of the ideal M1 surface layer upon heat treatment in N_2 atmosphere. As opposed to the pristine grains, where only a few triangular motifs (Figure 5-3a, green and pink triangles) can be observed close to the surface, a complex array of different surface motifs can be observed after heat treatment in N_2 atmosphere (Figure 5-3b). These local surface defects are supposed to be molybdenum and can be identified as shared, twinned, mirrored, and translated motifs.[42] These structural motifs are suggested to be oxygen deficient compared to the ideal bulk motif of orthorhombic $(Mo,V)O_x$. In addition, the number of triangular motifs increases. The intragranular pore, which is situated at the grain boundary of two M1 grains in the pristine sample, is replenished by atoms, which arrange such that they form mirrored and translated structural motifs. Additional contrast can be spotted at the topmost and the bottom parts of the surface region, which may further indicate a high degree of

mass transport during heat treatment in nitrogen atmosphere. The heat treatment process has also partially filled of surface-near hexagonal pores. The filling of hexagonal channels was recently attributed to the migration of V cations on empty channel sites during heat treatment.[11] The ADF-STEM micrograph recorded after the exposure of orthorhombic $(Mo,V)O_x$ to relevant ODE conditions demonstrates that additional structural channels are filled, including both hexagonal and heptagonal (Figure 5-3c, orange and red circles). The filling of the channels involves not only the surface, but also the bulk part. The same ADF-STEM picture further displays that structural motifs at the surface, which have formed during nitrogen treatment, degrade. In addition, no contrast can be observed in the central topmost part of the particle, while the shape of the inter-granular pore in the bottom has changed to become more elliptical. These two phenomena suggest the occurrence of mass transport, which happens at the surface region, while the bulk with its comparable stable and crystalline M1 remains almost unaffected. In addition, the structural arrangement similar to the pristine interstitial region (orange dashed tiling) retains the exposure to different gaseous atmospheres (Figure 5-3, yellow tile). This pristine interstitial like region may, thus, act as rigid, structural anchor, which keeps the orientation and rotation relationship between the two grains even after thermal treatments in different atmospheres.
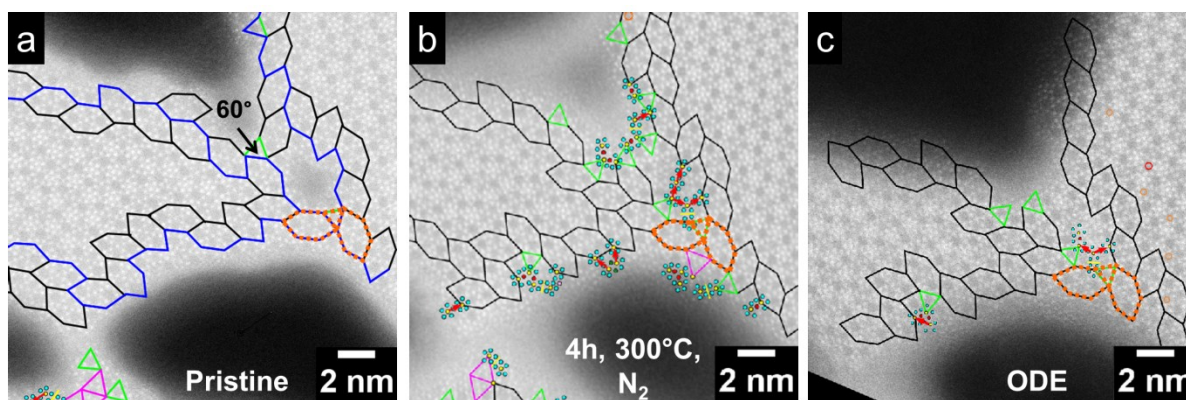
Figure 5-3: High resolution identical location ADF-STEM images of oriented $(Mo,V)O_x$ particle viewed along the crystallographic c-axis a) before, b) after heat treatment in N_2 and c) after exposure to conditions relevant for ODE reaction (ethane:oxygen=1:2): Black hexagons: M1 phase; blue line: M1 surface contour after heat treatment in N_2; green and magenta triangles: triangular motifs; red arrows: translated motifs; yellow lines: mirrored motifs; red circles: shared motifs; green circles: twinned motifs; orange circles: filled hexagonal channels; red circle: filled heptagonal channel.

The ADF-STEM micrographs in Figure 5-3 show the boundary region between two condensed orthorhombic (Mo,V)O$_x$ grains, which are fixed to each other and can keep the phase relationship upon heating. Although the crystals are rotated in the (a,b) crystallographic plane, their crystallographic c-axis point in the same direction even after heat treatment. Heat treatment can also loosen the contact points between two adjacent grains, which leads to an orientation mismatch as presented, for instance, in Figure 5-4. While the pristine interface of the grain boundary of two condensed orthorhombic (Mo,V)O$_x$ crystals can also be composed by an array of different structural motifs and pores (Figure 5-4a), heating induced mass transfer induces the disappearance and/or rotation along the c-axis of parts of the triangular motifs close to the surface. Simultaneously, modifications of the structural motifs transform the grain boundary into an ill-defined interphase (Figure 5-4b-d, compare grain I and III). The transformation into an ill-defined interphase softens the connectivity of the involved grains and the orientation relationship starts to disappear, which can be observed by the elongation of individual atomic columns (Figure 5-4c, grain III), which corresponds to a total heating time of 4h at 300°C in N$_2$ atmosphere. More severe temperature treatment at 400°C (2h, N$_2$) cause a higher loss in the contrast of grain III, which can be interpreted as an enhanced misorientation of grain III and is most likely accompanied by an amorphization of the intergrown region (Figure 5-4d). After changing the chemical potential of the gaseous environment to conditions that are relevant for the ODE reaction (feed: ethane:oxygen=1:2) the initial orientation relation between grain I and grain III has retained, which is accompanied by restoring the short range order in the intergrown region has restored (Figure 5-4e). Furthermore, additional cations on hexagonal channel sites can be observed in the bulk part of grain I. Figure 5-4f schematically depicts a possible mechanism of the appearance and disappearance of the misorientation in different atmosphere, which involves the flattening (N$_2$) and dimpling (ethane:oxygen=1:2) of the intergrown region.

Anionic vacancies can take part in catalytic processes via activating oxygen from the reaction media and further transferring it to the target reactant molecule.[33] Heating in inert gas atmosphere induces a smooth surface reduction, which leads to the formation of oxygen vacancies and subsequently to further structural rearrangement in favor of oxygen-deficient motifs, while ODE in oxygen excess conditions can lead to an immediate refilling of the oxygen vacancies and even subsequent back-structuring of the motifs.
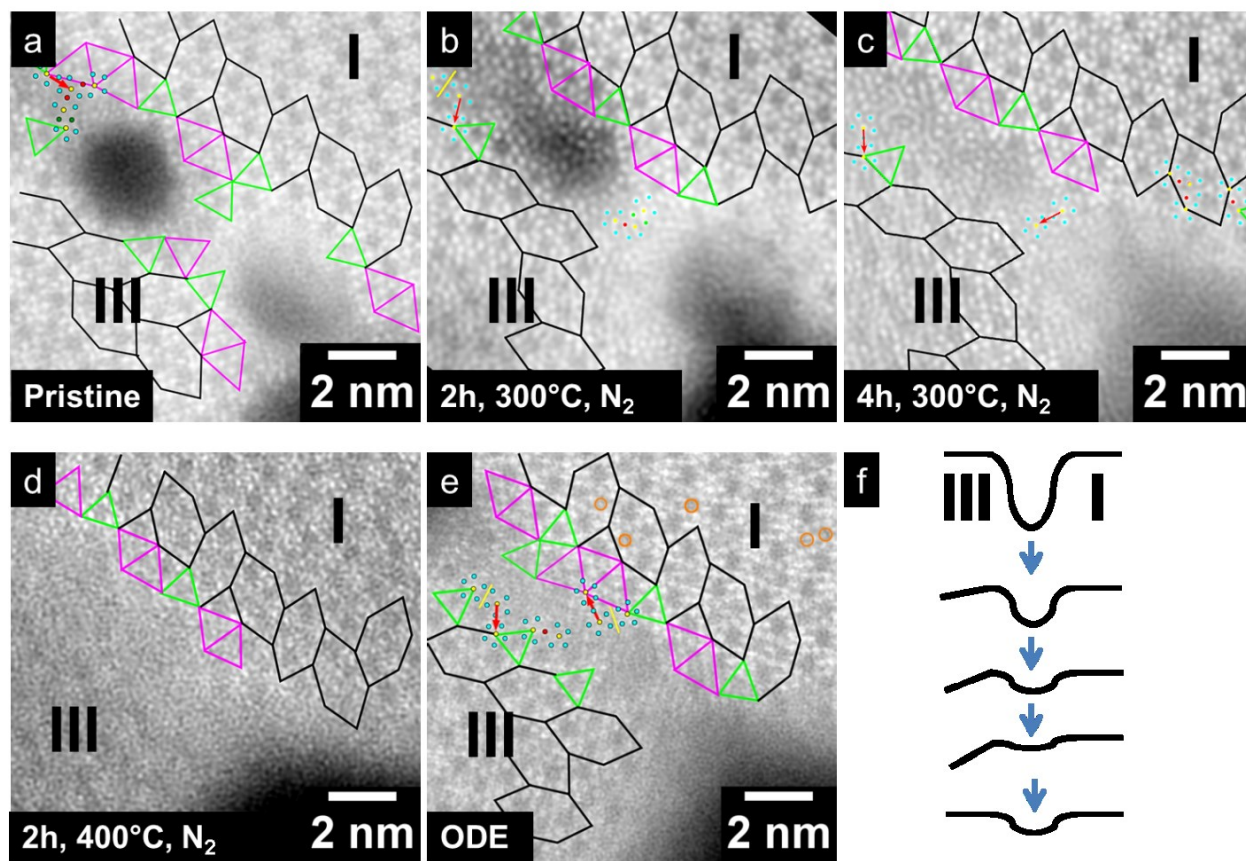
Figure 5-4: Identical location ADF-STEM images of oriented (Mo,V)O$_x$ particle viewed along the crystallographic c-axis before (a) and after (b,c) different times of heat treatment at 300°C, d) after heat treatment at 400°C e) after exposure to ODE (ethane:oxygen 1:2) mixture. f) Schematic representation of the structural evolution along the crystallographic c-axis. Black hexagons: M1 phase; green and magenta triangles: triangular motifs; red arrows: translated motifs; red circles: shared motifs; green circles: twinned motifs; orange circles: filled channel.

Mass transport may also be the dominating mechanism for morphological changes at places where crystals of different orientations meet (Figure 5-5). After heat treatment to 300°C the phase, which surrounded the ideal orthorhombic M1 phase has completely disappeared (compare Figures5 a and b). Similar to the observation mentioned in Figure 5-3, structural motifs, i.e. shared and triangular, which can be interpreted as local defects can be observed after this heat treatment (Figure 5-5b). After heat treatment in nitrogen atmosphere, additional contrast in some structural channels, preferable in the hexagonal cavities, in the surface near region brightens up (Figure 5-5b, orange arrows). Based on the initial structural model, which was derived from single X-ray measurements the occupancy of hexagonal channel sites with V

cations is low.[11] This low site occupation leads to a scattering cross section, which is comparable to light elements. Thus, in ADF-STEM experiments the occupancy of the hexagonal channels is usually overwhelmed by the signal of the surrounding heavy scatters. Based on the ADF-STEM images, we assign the contrast in the hexagonal channels to a filling of the cavities by Mo and/or V moieties, which migrate to the channel sites during heat treatment.
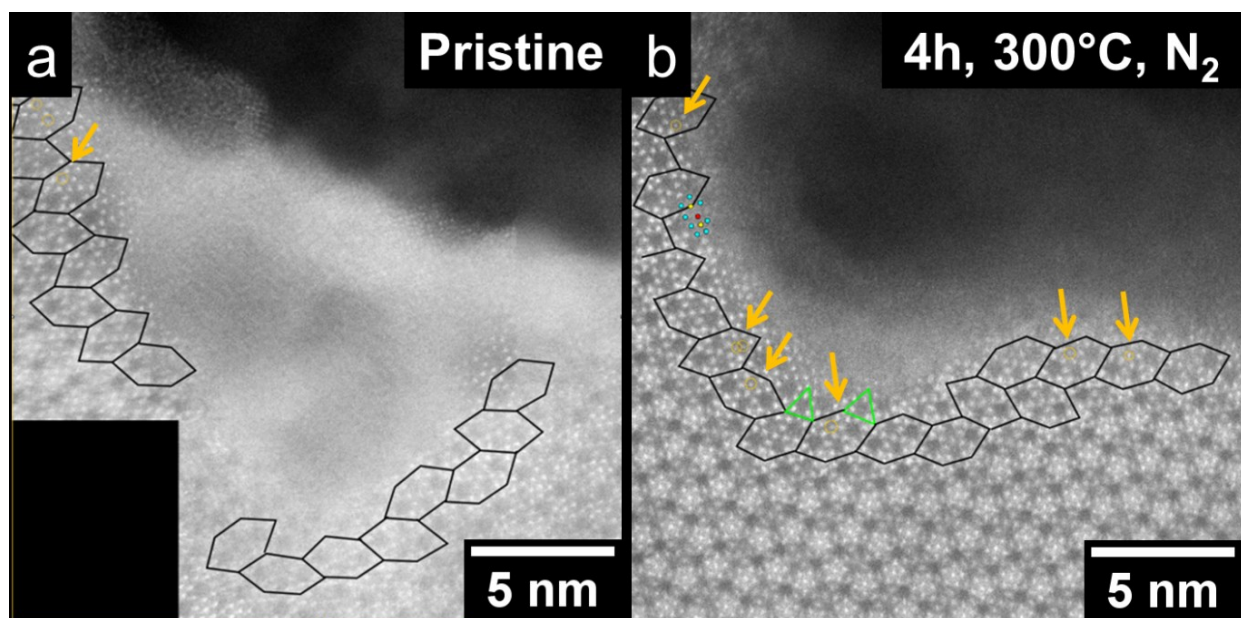
Figure 5-5: Identical location ADF-STEM images before (a) and (b) after the heat treatment. The ADF-STEM image in (a) was reconstructed from two raw images. Black hexagons: M1 phase; green triangles: triangular motifs; red circles: shared motifs; orange circles/arrows: filled channels.

The appearance of additional cations in the hexagonal channels during the heat treatment can further be considered as an intermediate step for restructuring of the orthorhombic M1 phase towards shared or triangular motifs (Scheme 5-1), which are frequently observed after heat treatment in nitrogen atmosphere. A schematic drawing of an ideal orthorhombic tile is presented in Scheme 5-1a, with "open" channel structure as derived from the ADF-STEM images. Upon heating cations may migrate to the hexagonal channel sites (Scheme 5-1b). The "filled" channel sites interact with vicinal pentagonal building blocks, which can lead to intra-channular distortions. These distortions can cause a pentagonal surrounding of the displaced central cation in the hexagonal channels and result in the formation of triangular and shared motifs (Scheme 5-1c). This local restructuring may induce strain, which can be relieved by eliminating

or rotating out of c-axis one (Scheme 5-1d) or two (Scheme 5-1e) pentagonal building blocks from the unsaturated surface.
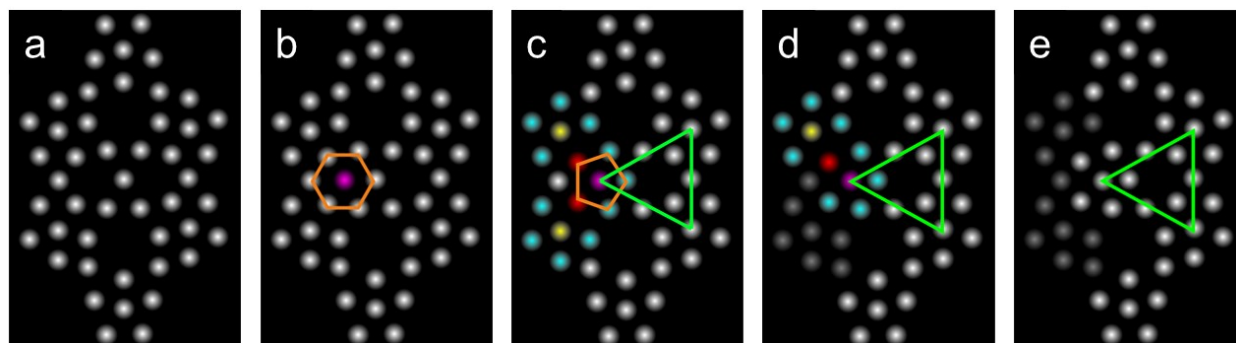
Scheme 5-1: M1 restructuring: (a) ideal orthorhombic structure b) inclusion of additional cations in one hexagonal channel, c) pentagonal rearrangement of surrounding atoms, forming two shared motifs and one triangular motif, d) first distortion of one pentagonal building block (shared + triangular motif), e) second distortion of one pentagonal building block (triangular motif). Red circles: shared cations; magenta: the channel atom; yellow and blue circles: central and side cations of pentagonal motifs; grey circles: distorted pentagonal blocks; orange hexagon and pentagon: channel configuration; green triangle: triangular motif.

5.3.1.2 *Pseudo-trigonal intergrowth*

Figure 5-6a shows an ADF-STEM image of a pseudo-trigonal intergrowth, which penetrates the pristine orthorhombic bulk structure of $(Mo,V)O_x$. As previously described the pseudo-trigonal intergrowth is composed of different structural motifs and is interrupted by different kind of pristine and complex interstitial regions.[21] While the main part of the intergrowth can be stabilized by the surrounding bulk, the terminations of the intergrowth (white arrows in Figure 5-6) and large interstitial regions lack this stabilization and are consumed. This significant structural degradation can be observed even at medium resolution and is independent of the kind of the atmosphere (Figure 5-6, overview images a to d). The smaller interstitial regions and the pseudo-trigonal arrowhead-shaped structural units demonstrate structural flexibilities, which can be expressed by structural reorganization of the defects and structural flattening or roughening. However, the internal structure response can differ. For instance, while the intergrown region marked with magenta arrow initially shows the tendency toward flattening and structural simplification in nitrogen atmosphere, it roughens or degrades, which can be identified by the decrease of internal contrast, after the ODE treatment. The situation changes

for the intergrown region, which is marked by the yellow arrow. This defect is characterized by a switch between two different shaped interstitial regions in nitrogen atmosphere, but appears to be stable in the ODE reaction. The internal structure of the pseudo-trigonal intergrowth, which is highlighted by the arrowhead-shaped hexagons structural units exhibit switching between the full range of the observed possible fillings, including no contrast and such defects as quadrilateral formation, missing cation in the central pentagonal unit and a full pentagonal building block inside with one mirror and two translation motifs formation in the order of thermal treatment. The identical location ADF-STEM images suggest that the formation of internal structure in orthorhombic $(Mo,V)O_x$ depends on thermodynamics.

The pseudo-trigonal intergrowth resembles an example, in which the kinetically stabilized internal structure of a defect is thermally rearranged in order to minimize geometrical strain. A size dependency of a restructuring of the interstitial region can be assumed. While smaller complex interstitial regions simplify their structural arrangement during heat treatment, larger member of this defect family can behave similar to the surface of orthorhombic $(Mo,V)O_x$ during heat treatment.
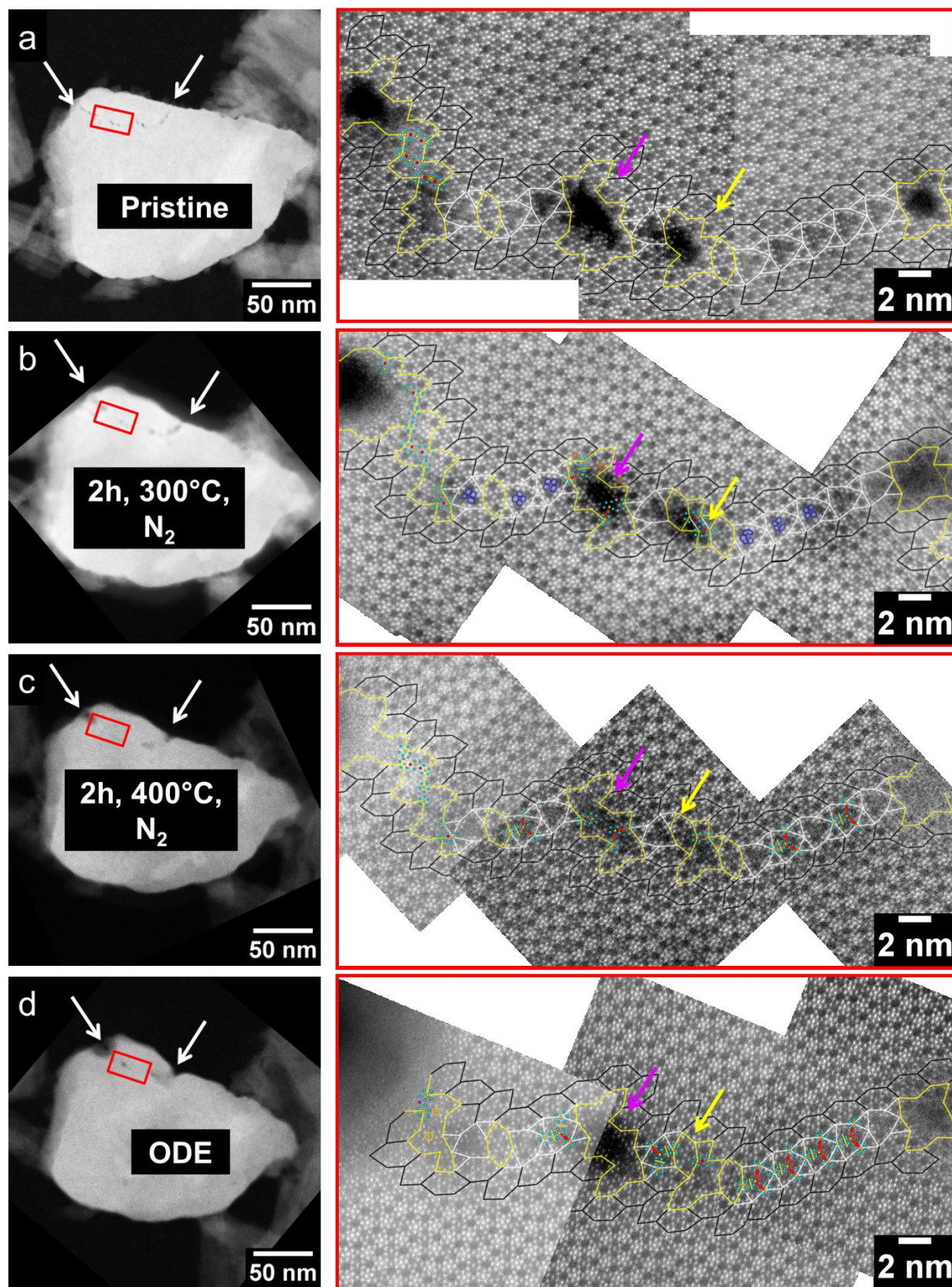
Figure 5-6: Panoramic ADF-STEM images of the identical location of a pseudo-trigonal intergrowth before (a), after first (b) and last (c) heat treatment in nitrogen and after ODE (d). Red polygon: inset; white arrows: intergrowth terminations; black hexagons: M1 phase; white hexagons and triangles: pseudo-trigonal intergrowth; yellow polygons: interstitial regions; green triangles: triangular motifs; red arrows: translated motifs; yellow lines: mirrored motifs; red circles: shared motifs; green circles: twinned motifs; pink circles: rotated motifs; orange circles: additional cations; blue ovals: quadrilateral arrangements.

In order to conclude on the influence of post-modification of the geometric surface structure during exposure to ambient air after exposure the sample after heat treatment and ODE reaction, the TEM grid was first securely transferred from the TEM grid reactor, via glove box and a double tilt vacuum transfer to the TEM. Figure 5-7a shows the corresponding high angle (HA) ADF-STEM image of orthorhombic $(Mo,V)O_x$ after exposure to oxidative dehydrogenation of ethane conditions, which was transferred without exposure to ambient air. Subsequent exposure of the sample to ambient for 60 min and identical location imaging displays the absence of structural modifications (Figure 5-5b). This would allow for a simpler, direct transfer of the sample after heat treatment to the TEM as long as morphological changes will be addressed. However, to study electronic changes on the surface the exposure to air has to be carefully omitted, as carbon dioxide, oxygen and water may lead to partial and immediate hydrolization and/or carbonization of the surface, which will post-catalytically induce changes in the electronic fingerprint of the surface oxygen species and/or changes to the oxidation state of exposed metal sites.
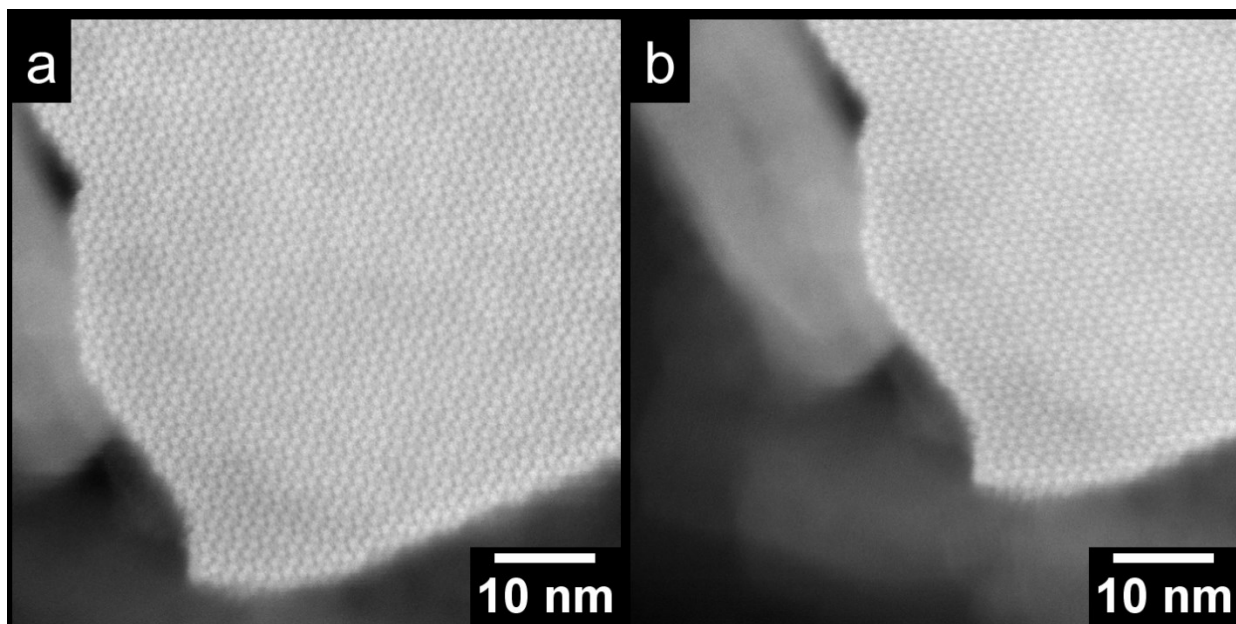
Figure 5-7: Identical location HAADF-STEM images of oriented (Mo,V)O$_x$ particle viewed along the crystallographic c-axis a) without exposure to air (transferred by vacuum transfer holder) and b) subsequent 1h exposure to the ambient air.

5.3.2   In-situ TEM

Orthorhombic (Mo,V)O$_x$ crystals were further heated in vacuum inside the TEM to 300°C. During temperature ramping the electron beam was switched off, in order to avoid a severe impact of the electron beam on the structure. Representative *in-situ* ADF-STEM images are shown in Figure 5-8a,b. In contrary to the *quasi in-situ* TEM approach, the images, which were recorded at 300 °C, show a roughening of the surface. This surface roughening is not uncommon for reducible complex oxides and is usually induced by the electron beam, while one of the cations migrates to the surface. Heating in vacuum partially reduces the cationic moieties of orthorhombic (Mo,V)O$_X$, which is strengthened by the energy impact of the electron beam.
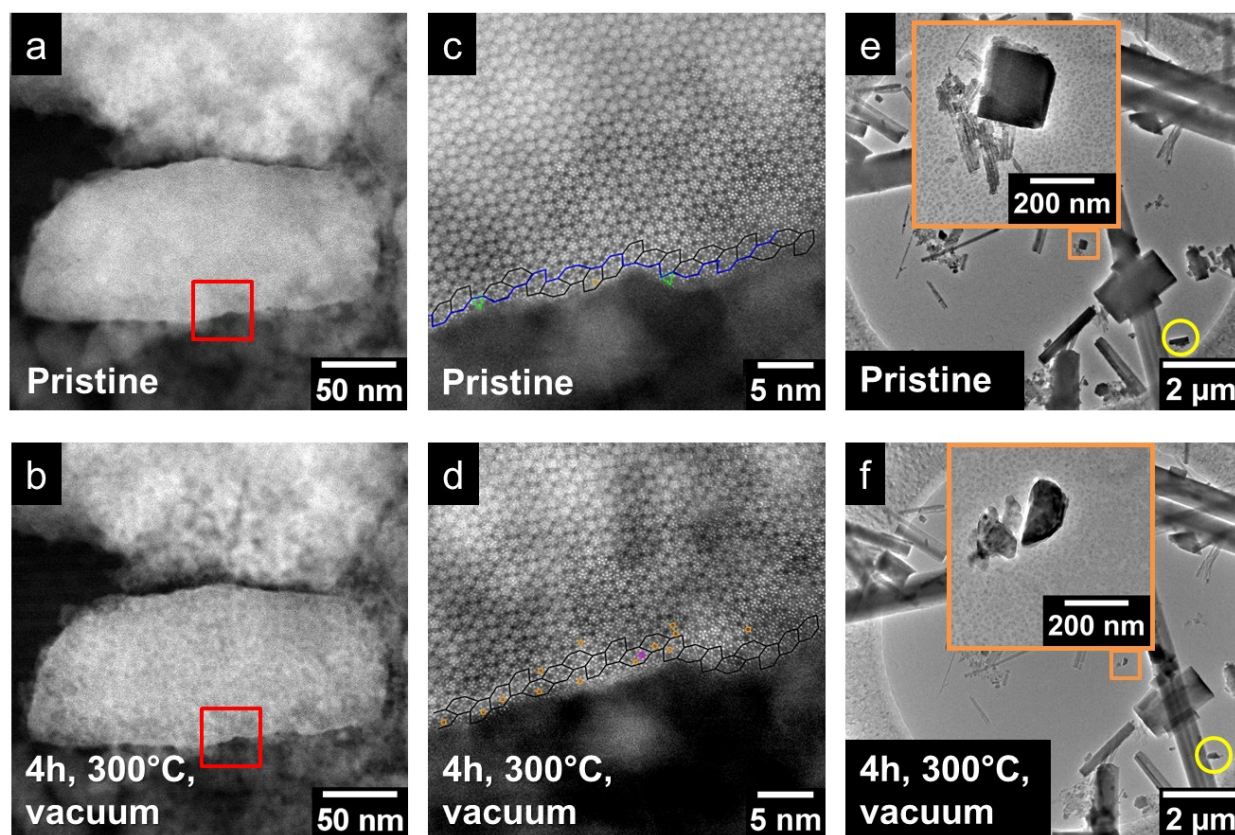
Figure 5-8: ADF-STEM images before (top row) and after (bottom row) heat treatment in vacuum, a) b) overview images of oriented in the ab plane catalyst particle, red squares: areas imaged at high resolution c), d) high resolution images of the identical locations. Black hexagons: orthorhombic tiling; blue line: outline of the tiling after the complete heat treatment; orange circles: additional cations in the hexagonal channels; green triangles: triangular motifs; magenta circle: cation in a heptagonal channel. e), f) low magnification overview images, demonstrating rods ruining; orange square: area shown at the inset; yellow circle: catalyst rod exposed to the beam only before and after heat treatment.

Despite this difference, the total M1 area decreases and the surface is partially depleted. (Figure 5-8c,d). Furthermore, additional cations situated in hexagonal and even heptagonal channel sites (Figure 5-8d) appear. The density and the extension of these additional cations into the bulk has increased as compared to the observations made by *quasi in-situ* imaging. Other kinds of defects have not been observed in this area. The ill-defined surrounding of the oriented particle displays a change of the contrast, which again points to the occurrence of mass transport. In addition, Figure 5-8e,f demonstrates that some of the catalyst particles, completely lose their rod-like structure during heating in vacuum. As only one of the rods was imaged at medium

magnification (Figures 5-8e,f, inset) and the second one was only exposed to the electron beam during the prevailing time when the overview images were collected before and after heating (marked by a yellow circle), this effect might rather be related to the pressure-gap.

5.4 Discussion

The effects, which we have observed for different *in-situ* and *quasi in-situ* conditions are summarized in the Table 5-2 and show similarities as well as significant differences. The table shows the benefit of *quasi in-situ* TEM, which is not influenced by pressure gap related effects, as heating and exposure to the electron beam in high vacuum are separated in time.

Table 5-2: Comparison of the in-, ex- and *quasi in-situ* TEM imaging

Effect	In-situ	Quasi in-situ
Motifs surface enrichment (channels filling)	✓	✓
Shape smoothing	✗[b]	✓
Top surface roughening	✓[b]	✗
Rods ruining	✓[b]	✗
Extended surface defects breaking	?	✓

✓ – the effect is detected,

✗ – the effect was not detected but the method allows to detect the phenomena if it really happens

? – the effect might occur but was not detected due to the method limitations

[b] difference might be related to pressure gap

The visualized nanoscale structure response of orthorhombic $(Mo,V)O_x$ to the different atmospheres is in good agreement with *in-situ* XPS data, which have already suggested surface modifications under relevant catalytic conditions.[11] As the changes happen on the nanoscale, it explains the difficulties to track these modifications solely by X-ray diffraction (XRD) in earlier studies.[21-22, 30]

This *quasi in-situ* study demonstrates that as opposed to the defect and surface structure the open-framework structure of orthorhombic $(Mo,V)O_x$ remains rather unaffected. During heat treatment and catalytic reaction neither breakage of the bulk structure nor cracks were formed. However, restructuring of defects and the surface may induce strain into the crystalline bulk structure. The key for its bulk stability may be the open-framework channnular structure of

orthorhombic $(Mo,V)O_x$, which allows for reliving and/or storing the strain in the structural channels.

At the atomic level our *quasi in-situ* ADF-STEM study clearly demonstrates the occurrence of structural rearrangements and filling of hexagonal pores during different heat treatments. The structure response further depends on the chemical potential of the gas phase. The occurrence of these morphological rearrangements may result from mass transport phenomena, which occurs from ill-defined surface regions and can explain the appearance of new surface motifs and/or the flattening of the structure. This mass transport phenomena uncovers surface states, which may be required for catalytic turnovers. In addition, the open-framework bulk structure of orthorhombic $(Mo,V)O_x$ may be a pre-requiste to stabilize surface structures which can efficiently activate small hydrocarbons and/or oxygen. In this regard, thermal activation in inert atmosphere can be important as it may form an oxygen deficient surface layer, which may act as precursor and can be transformed under conditions relevant for ODE into the active phase. The formation of the active phase depends on the local chemical potential around individual atoms in their respective polyhedral coordination.

As we have proposed in Scheme 5-1 restructuring into structural motifs can also be possible by filling the hexagonal channels. On the one hand, if the hexagonal channels are filled with Mo and vicinal linker sites are Mo rich a restructuring to the pentagonal building block can be favorable and may lead to the appearance of structural motifs, which we have observed after nitrogen treatment. On the other hand, if the hexagonal channel site is occupied by V and/or the linking sites are V rich the pentagonal configuration may be less favorable and additional motifs may not be formed and may explain the absence of restructuring at the surface after the treatment in ODE conditions. This V enrichment in the hexagonal channels after ODE may also induce strain, which is low enough to avoid bond cleavage, but can activate Mo-O bonds. For instance, the strain may elongate vincinal. Mo-O bonds, which can be localized at the S2 metal site and connects two hexagonal channels. The activation by strain is not uncommon for Mo-O bonds, which are transferred into a frustrated state. Thus, in $(Mo,V)O_x$ V cations may be the inductors of strain and the structural channels may be the reservoir for activating elements. Our ADF-STEM suggest that the catalytic activity of orthorhombic $(Mo,V)O_x$ depends on strain and local disorder.

The mechanism that leads to the visual appearance of defects during heat treatment in nitrogen may be explained by the slightly reducing potential of the atmosphere, which leads to the formation of oxygen surface vacancies and a subsequent restructuring to the observed thermodynamically more stable oxygen deficient structural motifs with different surface potentials.[46] Local fluctuations of the surface potential in defect rich areas may influence the stability of anion vacancies, which may lead to the formation energetically different extended defects.

The observed structural dynamics and morphological changes are to a certain point irreversible and render the definition of a heterogeneous catalyst being part of a catalytic reaction without being changed as too strict.[47] Even if the structural defects are not directly participating in the reaction as active sites, they play a significant role in stabilizing the structure. This will further lead to additional restructuring related band bending effects, which may differ from the already described chemical band bending that results from the adsorption of reactant molecules on the surface.[48] Band bending at the surface of a semiconductor can originate from a plethora of phenomena, from which the most important one for orthorhombic $(Mo,V)O_x$ in a gaseous environment is charge redistribution at the surface area. This effect can result from anisotropic terminations of the bulk and play a significant role in n and p-type semiconductors.[49] In addition, charge redistribiution can occur due to adsorption of the reactant molecules.[49] The latter can affect band bending in different directions and depends on whether oxygen molecules (acceptors) or ethane molecules (donors) are adsorbed.[49] Furthermore, surface defects and their rearrangements can strongly influence the band structure and its response to the reaction media. However, complex combinations of defects render any exact prediction difficult. For instance, while a single cation on channel sites cannot interact with other defects, it can be interpreted as inclusion and may lead to the formation of a single energy level inside the forbidden zone. The reaction induced migration of atoms from the bulk to the surface channel sites can be referred as Schottky defects.[50] The breaking of bonds during this migration can be treated as the appearance of electron vacancies, which would further lead to an acceptor-like behavior in order to fill the vacancies and several energy levels. Following the Pauli exclusion principle, the interaction of two defects of the same kind will lead to a splitting of the energy level, which correspond to the individual defects.[51-52] Different combinations of defects in an intimate vicinity would lead to the coexistence of multiple energy levels.

Thus, it remains unclear how the restructuring band bending effect modulates the catalytic performance. This effect can either occur at low time scales, which is needed to form an energetically favorable defect layer for the selected conditions and may result in the formation of a steady state. It can also be cumulative in time if the reaction media continuously creates anionic vacancies, which requires further structure response and may lead to the degradation of the complete catalyst. This may render a heterogeneous catalytic system into a "living" system that self protects the bulk from the surrounding environment.

5.5 Conclusions

In conclusion, we have examined the living character of orthorhombic $(Mo,V)O_x$ after heat treatment in different atmospheres via identical location STEM imaging with ultimate resolution. Nanoscale structural rearrangements in defect-rich areas, such as surface and intergrowth were pinpointed in all the cases. Differences in the structure responses can be linked to the nature of the media and, in case of *in-situ* imaging, to the pressure-gap related effects.

Mass transfer phenomena can combine the structure response and the reactive media, as surface band bending can be due to the interaction with the reaction environment and restructuring. Further conclusions on the mechanisms underlying structural rearrangements can be obtained by measuring the stability influence of different reaction media. Thus, it seems likely that for the forthcoming of heterogeneous catalysis research and to understand individual details of the living character of such functional materials the chemical potential influence and catalytic activity of one atom in different anionic environments and their cooperative interaction with a 2D and/or 3D solid has to be studied.

5.6 Methods

Synthesis

Hydrothermal synthesis of the orthorhombic $(Mo,V)O_x$ mixed oxide (internal ID 20000) was curried in specially built reactor (Premex Reactor AG, Lengnau, Switzerland) from corrosion resistant Hastelloy C-22 (2.4602). A mixture of 9.18 g $(NH_4)_6Mo_7O_{24} \cdot 4H_2O$ (AHM, Merck, 52 mmol Mo) dissolved in 230 g water (Milli-Q, Merck) and 3.30 g $VOSO_4$ (Acros Organics, 12.9 mmol V) dissolved in 30 g water was loaded into a reactor at room temperature. Residual air was replaced by nitrogen. Subsequently the vessel was heated to 200°C at a rate of

1°C/min and hold at this temperature for 17 h. The reaction mixture was stirred during the whole experiment at a rate of 100 rpm. After cooling to room temperature, a black solid was isolated by filtration (pore 5 glass frit), washed twice with distilled water and dried at 80°C for 16 hours. To remove amorphous components in the hydrothermal product, 1 g of the powder was washed with 25 ml oxalic acid solution (0.25 M, Acros Organics) at 60°C for 30 min under stirring. The solid was centrifuged (5000 rpm, 30 min), washed twice with 25 ml water and dried at 80°C over night. Finally, a thermal treatment was performed in 100 ml/min argon flow at 400°C (heating rate 10°C/min) for 2 h in a rotary tube furnace (Xerion, Freiberg, Germany).

TEM

STEM measurements, which involved secure sample transfer, were carried out using 648 Double tilt vacuum transfer holder from Gatan and FEI Talos F200X operated at 200keV. The rest of the experiments were performed on a JEM-ARM200F microscope with CEOS CESCOR and CEOS CETCOR hexapole aberration correctors for probe and image forming lenses, respectively, and a cold field emission gun (CFEG). STEM images were recorded with a JEOL annular dark-field (ADF) detector. Prior to the measurements, the powdered material was drop deposited on a silica oxide coated gold TEM grid. Prior to the ADF-STEM analysis some particles were oriented along the crystallographic c-axis.

In-situ

The *in-situ* heat treatment was performed directly inside the double corrected Jeol ARM 200F microscope using Protochips Fusion holder with a SiN_3 heating chip up to 300°C with a dwell time of 4 h total. One oriented particle was imaged during the heating with pausing the temperature increase during imaging and at selected times during the dwell time, while one used as a reference was imaged only prior the experiment, after 2 h heating and after the experiment. Additionally several catalyst rods were imaged before heating and after cooling the sample.

***Quasi in-situ* TEM**

The *quasi in-situ* heating in neutral atmosphere was carried on in a TEM grid reactor with mimicking the *in-situ* experiment conditions, except the imaging was only performed after 2 h and 4h total exposure to 300 °C in N_2. As the morphology changes happened only at a low scale during the experiment additional treatment in 400 °C was carried on for comparison.

The reaction gas treatment was carried on in a way to assure detectable conversion, in the temperature range from 220 to 280°C at about 2h exposure to each temperature and 2 K/min

temperature ramp, at the flow below 1 ml/min with total ratios C_2H_6:O_2:N_2 3:6:91 in the ambient pressure range. Catalytic conversion was detected by PTR-MS Ionicon Analytic with a quadrupole mass filter QMG 422 under artificially enhanced nose cone voltage in order to increase the sensitivity to CO_2.

Image analysis

The catalyst bulk was used as a reference for tracking the changes in the direction parallel to the electron beam, which appearance depend on the focus depth (Figure S5-3). In order to confirm the absence of the cumulative beam and temperature effect over several measurements additional catalyst particles not imaged before were selected after each measurement as well as some of the previously examined particles were studied again only after several reaction steps, creating the relevant references for each experiment step, as schematically shown at Table S5-2.

Test catalysis

The catalytic tests were carried in the Taniwha reactor described elsewhere.[53] Catalyst load and total flow were selected to provide 10^3 ml*g/min WHSW in the same gas mixture as used for *quasi in-situ* ODE (C_2H_6:O_2:N_2 3:6:91). The signal at each temperature was collected at least for 6h in order to confirm steady state. Additional measurement at 220 °C was carried on after the main treatment in order to confirm deactivation absence.

The conversion X_{R_i} in the catalytic reaction was calculated product-based:

$$X_R = \frac{\sum_j (\Delta C_{P_j})}{C_{R_0}} \tag{1}$$

$$S_{P_j} = \frac{\Delta C_{P_j}}{\sum_j \Delta C_{P_j}} \tag{2}$$

where R_i and P_j are reactants and products, C_x is the amount of carbon in mol corresponding to the compound x, 0 corresponds to the reactants mixture and Δ marks the difference between products and reactants mixture.

5.7 References

1.   Amghizar, I.; Vandewalle, L. A.; Van Geem, K. M.; Marin, G. B., New Trends in Olefin Production. *Engineering* **2017,** *3* (2), 171-178.

2.   Maddox, R. N.; Cannon, R. E., Natural Gas. In *Riegel's Handbook of Industrial Chemistry*, Kent, J. A., Ed. Springer US: Boston, MA, 1992; pp 510-526.

3.   Fechete, I.; Wang, Y.; Védrine, J. C., The past, present and future of heterogeneous catalysis. *Catal. Today* **2012,** *189* (1), 2-27.

4.   Koleske, J. V., Economic Aspects of the Chemical Industry. In *Kent and Riegel's Handbook of Industrial Chemistry and Biotechnology*, Kent, J. A., Ed. Springer US: Boston, MA, 2007; pp 63-82.

5.   Vendelbo, S. B.; Elkjær, C. F.; Falsig, H.; Puspitasari, I.; Dona, P.; Mele, L.; Morana, B.; Nelissen, B. J.; van Rijn, R.; Creemer, J. F.; Kooyman, P. J.; Helveg, S., Visualization of oscillatory behaviour of Pt nanoparticles catalysing CO oxidation. *Nat. Mater.* **2014,** *13* (9), 884-890.

6.   Schlögl, R., Heterogeneous Catalysis. *Angew. Chem., Int. Ed.* **2015,** *54* (11), 3465-3520.

7.   A. Crozier, P., *Nanocharacterization of Heterogeneous Catalysts by Ex Situ and In Situ STEM*. 2011; p 537-582.

8.   Ek, M.; Ramasse, Q. M.; Arnarson, L.; Georg Moses, P.; Helveg, S., Visualizing atomic-scale redox dynamics in vanadium oxide-based catalysts. *Nature Communications* **2017,** *8* (1), 305.

9.   Zhu, Y.; Sushko, P. V.; Melzer, D.; Jensen, E.; Kovarik, L.; Ophus, C.; Sanchez-Sanchez, M.; Lercher, J. A.; Browning, N. D., Formation of Oxygen Radical Sites on MoVNbTeOx by Cooperative Electron Redistribution. *J Am Chem Soc* **2017,** *139* (36), 12342-12345.

10.   Sharma, R., Observing Chemical Reactions Using Transmission Electron Microscopy. In *In-Situ Electron Microscopy*, Wiley-VCH Verlag GmbH & Co. KGaA: 2012; pp 145-170.

11.   Trunschke, A.; Noack, J.; Trojanov, S.; Girgsdies, F.; Lunkenbein, T.; Pfeifer, V.; Hävecker, M.; Kube, P.; Sprung, C.; Rosowski, F.; Schlögl, R., The Impact of the Bulk Structure on Surface Dynamics of Complex Mo–V-based Oxide Catalysts. *ACS Catal.* **2017,** *7* (4), 3061-3071.

12.   Heine, C.; Hävecker, M.; Stotz, E.; Rosowski, F.; Knop-Gericke, A.; Trunschke, A.; Eichelbaum, M.; Schlögl, R., Ambient-Pressure Soft X-ray Absorption Spectroscopy of a Catalyst Surface in Action: Closing the Pressure Gap in the Selective n-Butane Oxidation over Vanadyl Pyrophosphate. *The Journal of Physical Chemistry C* **2014,** *118* (35), 20405-20412.

13.   Ross, F. M., In Situ Transmission Electron Microscopy. In *Science of Microscopy*, Hawkes, P. W.; Spence, J. C. H., Eds. Springer New York: New York, NY, 2007; pp 445-534.

14.   Stoltze, P.; Nørskov, J. K., Bridging the "Pressure Gap" between Ultrahigh-Vacuum Surface Physics and High-Pressure Catalysis. *Physical Review Letters* **1985,** *55* (22), 2502-2505.

15.   Korup, O.; Goldsmith, C. F.; Weinberg, G.; Geske, M.; Kandemir, T.; Schlogl, R.; Horn, R., Catalytic partial oxidation of methane on platinum investigated by spatial reactor profiles, spatially resolved spectroscopy, and microkinetic modeling. *J. Catal.* **2013,** *297*, 1-16.

16.   Malladi, S. R. K.; Tichelaar, F. D.; Xu, Q.; Wu, M. Y.; Terryn, H.; Mol, J. M. C.; Hannour, F.; Zandbergen, H. W., Quasi in situ analytical TEM to investigate electrochemically induced microstructural changes in alloys: AA2024-T3 as an example. *Corrosion Science* **2013,** *69* (0), 221-225.

17.   Janbroers, S.; Louwen, J. N.; Zandbergen, H. W.; Kooyman, P. J., Insights into the nature of iron-based Fischer–Tropsch catalysts from quasi in situ TEM-EELS and XRD. *J. Catal.* **2009,** *268* (2), 235-242.

18.   Vogelaar, B. M.; Steiner, P.; Dick van Langeveld, A.; Eijsbouts, S.; Moulijn, J. A., Deactivation of Mo/Al2O3 and NiMo/Al2O3 catalysts during hydrodesulfurization of thiophene. *Appl. Catal., A* **2003,** *251* (1), 85-92.

19.   Kuhrs, C.; Swoboda, M.; Weiss, W., Single crystal flow reactor for studying reactivities on metal oxide model catalysts at atmospheric pressure to bridge the pressure gap to the adsorption properties determined under UHV conditions. *Top. Catal.* **2001,** *15* (1), 13-18.

20.   Pyrz, W. D.; Blom, D. A.; Sadakane, M.; Kodato, K.; Ueda, W.; Vogt, T.; Buttrey, D. J., Atomic-level imaging of Mo-V-O complex oxide phase intergrowth, grain boundaries, and defects using HAADF-STEM. *P Natl Acad Sci USA* **2010,** *107* (14), 6152-6157.

21.   Masliuk, L.; Heggen, M.; Noack, J.; Girgsdies, F.; Trunschke, A.; Hermann, K. E.; Willinger, M.-G.; Schloegl, R.; Lunkenbein, T., Structural Complexity in Heterogeneous Catalysis: Cataloging Local Nano-Structures. *The Journal of Physical Chemistry C* **2017,** *121* (43), 24093-24103.

22.   Ishikawa, S.; Ueda, W., Microporous crystalline Mo-V mixed oxides for selective oxidations. *Catalysis Science and Technology* **2016,** *6* (3), 617-629.

23.   Ueda, W., Establishment of Crystalline Complex Mo-V-Oxides as Selective Oxidation Catalysts. *J. Jpn. Petrol. Inst.* **2013,** *56* (3), 122-132.

24.   Ishikawa, S.; Yi, X.; Murayama, T.; Ueda, W., Catalysis field in orthorhombic Mo3VOx oxide catalyst for the selective oxidation of ethane, propane and acrolein. *Catal. Today* **2014**.

25.   Thorsteinson, E. M.; Wilson, T. P.; Young, F. G.; Kasai, P. H., The oxidative dehydrogenation of ethane over catalysts containing mixed oxides of molybdenum and vanadium. *J. Catal.* **1978,** *52* (1), 116-132.

26.   Lunkenbein, T.; Girgsdies, F.; Wernbacher, A.; Noack, J.; Auffermann, G.; Yasuhara, A.; Klein-Hoffmann, A.; Ueda, W.; Eichelbaum, M.; Trunschke, A.; Schlogl, R.; Willinger, M. G., Direct Imaging of Octahedral Distortion in a Complex Molybdenum Vanadium Mixed Oxide. *Angew. Chem., Int. Ed.* **2015,** *54* (23), 6828-6831.

27.   Aouine, M.; Epicier, T.; Millet, J. M. M., In Situ Environmental STEM Study of the MoVTe Oxide M1 Phase Catalysts for Ethane Oxidative Dehydrogenation. *ACS Catal.* **2016,** *6* (7), 4775-4781.

28.   Hävecker, M.; Wrabetz, S.; Kröhnert, J.; Csepei, L.-I.; Naumann d'Alnoncourt, R.; Kolen'ko, Y. V.; Girgsdies, F.; Schlögl, R.; Trunschke, A., Surface chemistry of phase-pure M1 MoVTeNb oxide during operation in selective oxidation of propane to acrylic acid. *J. Catal.* **2012,** *285* (1), 48-60.

29.   Botella, P.; García-González, E.; Dejoz, A.; López Nieto, J. M.; Vázquez, M. I.; González-Calbet, J., Selective oxidative dehydrogenation of ethane on MoVTeNbO mixed metal oxide catalysts. *J. Catal.* **2004,** *225* (2), 428-438.

30.   Fang Chen, N.; Ueda, W.; Oshihara, K., Hydrothermal synthesis of Mo-V-M-O complex metal oxide catalysts active for partial oxidation of ethane. *Chem Commun* **1999,** (6), 517-518.

31.   Suppiah, D. D.; Komar, A.; Abd Hamid, S. B., Structural dynamics of molybdenum vanadium oxide (MoVOx) Influence of activation condition. *Journal of Thermal Analysis and Calorimetry* **2017,** *129* (3), 1367-1376.

32.   Blom, D. A.; Vogt, T.; Allard, L. F.; Buttrey, D. J., Observation of Sublattice Disordering of the Catalytic Sites in a Complex Mo-V-Nb-Te-O Oxidation Catalyst Using High Temperature STEM Imaging. *Top. Catal.* **2014,** *57* (14-16), 1138-1144.

33.   Pacchioni, G., Numerical Simulations of Defective Structures: The Nature of Oxygen Vacancy in Non-reducible (MgO, SiO2, ZrO2) and Reducible (TiO2, NiO, WO3) Oxides. In *Defects at Oxide Surfaces*, Jupille, J.; Thornton, G., Eds. Springer International Publishing: Cham, 2015; pp 1-28.

34.   Valente, J. S.; Armendáriz-Herrera, H.; Quintana-Solórzano, R.; Del Ángel, P.; Nava, N.; Massó, A.; López Nieto, J. M., Chemical, structural, and morphological changes of a MoVTeNb catalyst during oxidative dehydrogenation of ethane. *ACS Catal.* **2014,** *4* (5), 1292-1301.

35.   Nguyen, T. T.; Deniau, B.; Baca, M.; Millet, J. M. M., Influence of Nb Content on the Structure, Cationic and Valence Distribution and Catalytic Properties of MoVTe(Sb)NbO M1 Phase Used as Catalysts for the Oxidation of Light Alkanes. *Top. Catal.* **2016,** *59* (17-18), 1496-1505.

36.   Ishikawa, S.; Kobayashi, D.; Konya, T.; Ohmura, S.; Murayama, T.; Yasuda, N.; Sadakane, M.; Ueda, W., Redox Treatment of Orthorhombic $Mo_{29}V_{11}O_{112}$ and Relationships between Crystal Structure, Microporosity and Catalytic Performance for Selective Oxidation of Ethane. *J. Phys. Chem. C* **2015,** *119* (13), 7195-7206.

37.   Delmon, B., Reactions During Catalyst Activation. In *Handbook of Heterogeneous Catalysis*, Wiley-VCH Verlag GmbH & Co. KGaA: 2008.

38.   Concepción, P.; Hernández, S.; Nieto, J. M. L., On the nature of active sites in MoVTeO and MoVTeNbO catalysts: The influence of catalyst activation temperature. *Appl. Catal., A* **2011,** *391* (1-2), 92-101.

39.   Ueda, W.; Oshihara, K., Selective oxidation of light alkanes over hydrothermally synthesized Mo-V-M-O (M=Al, Ga, Bi, Sb, and Te) oxide catalysts. *Appl. Catal., A* **2000,** *200* (1–2), 135-143.

40.   Lin, M. M., Complex metal oxide catalysts for selective oxidation of propane and derivatives: II. The relationship among catalyst preparation, structure and catalytic properties. *Appl. Catal., A* **2003,** *250* (2), 287-303.

41.   Oshihara, K.; Hisano, T.; Ueda, W., Catalytic oxidative activation of light alkanes over Mo–V-based oxides having controlled surface. *Top. Catal.* **2001,** *15* (2), 153-160.

42.   Masliuk, L.; Heggen, M.; Noack, J.; Girgsdies, F.; Trunschke, A.; Hermann, K. E.; Willinger, M. G.; Schlögl, R.; Lunkenbein, T., Structural Complexity in Heterogeneous

Catalysis: Cataloging Local Nanostructures. *The Journal of Physical Chemistry C* **2017,** *121* (43), 24093-24103.

43.   Beauchamp, J.; Herbig, J.; Dunkl, J.; Singer, W.; Hansel, A., On the performance of proton-transfer-reaction mass spectrometry for breath-relevant gas matrices. *Measurement Science and Technology* **2013,** *24* (12), 125003.

44.   Ellis, A. M.; Mayhew, C. A., PTR-MS in the Food Sciences. In *Proton Transfer Reaction Mass Spectrometry*, John Wiley & Sons, Ltd: 2014; pp 221-265.

45.   Keck, L.; Hoeschen, C.; Oeh, U., Effects of carbon dioxide in breath gas on proton transfer reaction-mass spectrometry (PTR-MS) measurements. *International Journal of Mass Spectrometry* **2008,** *270* (3), 156-165.

46.   Gai-Boyes, P. L., Defects in Oxide Catalysts: Fundamental Studies of Catalysis in Action. *Catal. Rev.* **1992,** *34* (1-2), 1-54.

47.   Dictionary, O. E., *"catalyst, n.".* Oxford University Press.

48.   Heine, C.; Hävecker, M.; Sanchez-Sanchez, M.; Trunschke, A.; Schlögl, R.; Eichelbaum, M., Work function, band bending, and microwave conductivity studies on the selective alkane oxidation catalyst MoVTeNb oxide (orthorhombic M1 phase) under operation conditions. *J. Phys. Chem. C* **2013,** *117* (51), 26988-26997.

49.   Zhang, Z.; Yates, J. T., Band Bending in Semiconductors: Chemical and Physical Consequences at Surfaces and Interfaces. *Chem. Rev.* **2012,** *112* (10), 5520-5551.

50.   Mahajan, S., Defects in semiconductors and their effects on devices. *Acta Mater.* **2000,** *48* (1), 137-149.
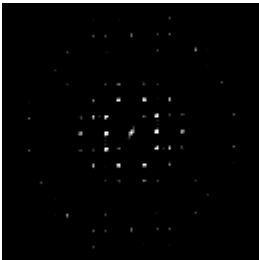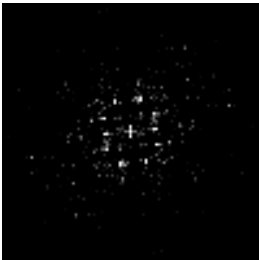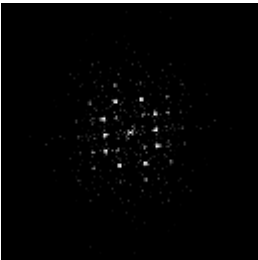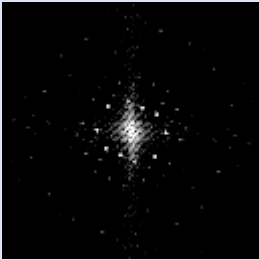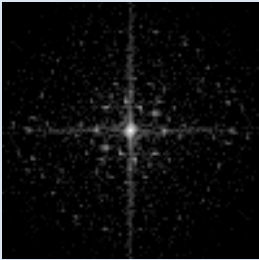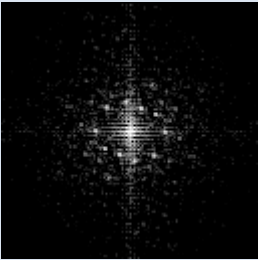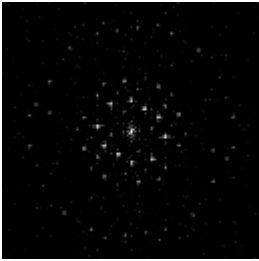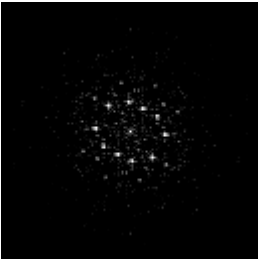
51.   Electronic Defect States. In *The Physics of Semiconductors: An Introduction Including Devices and Nanophysics*, Grundmann, M., Ed. Springer Berlin Heidelberg: Berlin, Heidelberg, 2006; pp 149-187.

52.   Hamaguchi, C., Energy Band Structures of Semiconductors. In *Basic Semiconductor Physics*, Hamaguchi, C., Ed. Springer Berlin Heidelberg: Berlin, Heidelberg, 2010; pp 1-27.

53.   Cotter, T. P.; referee: Thomas, A.; referee: Schomäcker, R.; referee: Schlögl, R.; referee: Christmann, K. The reducibility of mixed Mo/V oxide materials to carbides and their reactivity in the activation of propane. phd, Technische Universität, Berlin, 2011.

5.8 Supporting information

Table S5-1: Fast Fourier transform (FFT) of the different grains of the oriented along z-axis catalyst particle obtained from ADF-STEM images corresponding to Figure 5-1a to c. The contrast is artificially enhanced in order to obtain the highest clarity.

Grain\step	Pristine	2h, 400C, N$_2$	ODE
I			
II			
III			
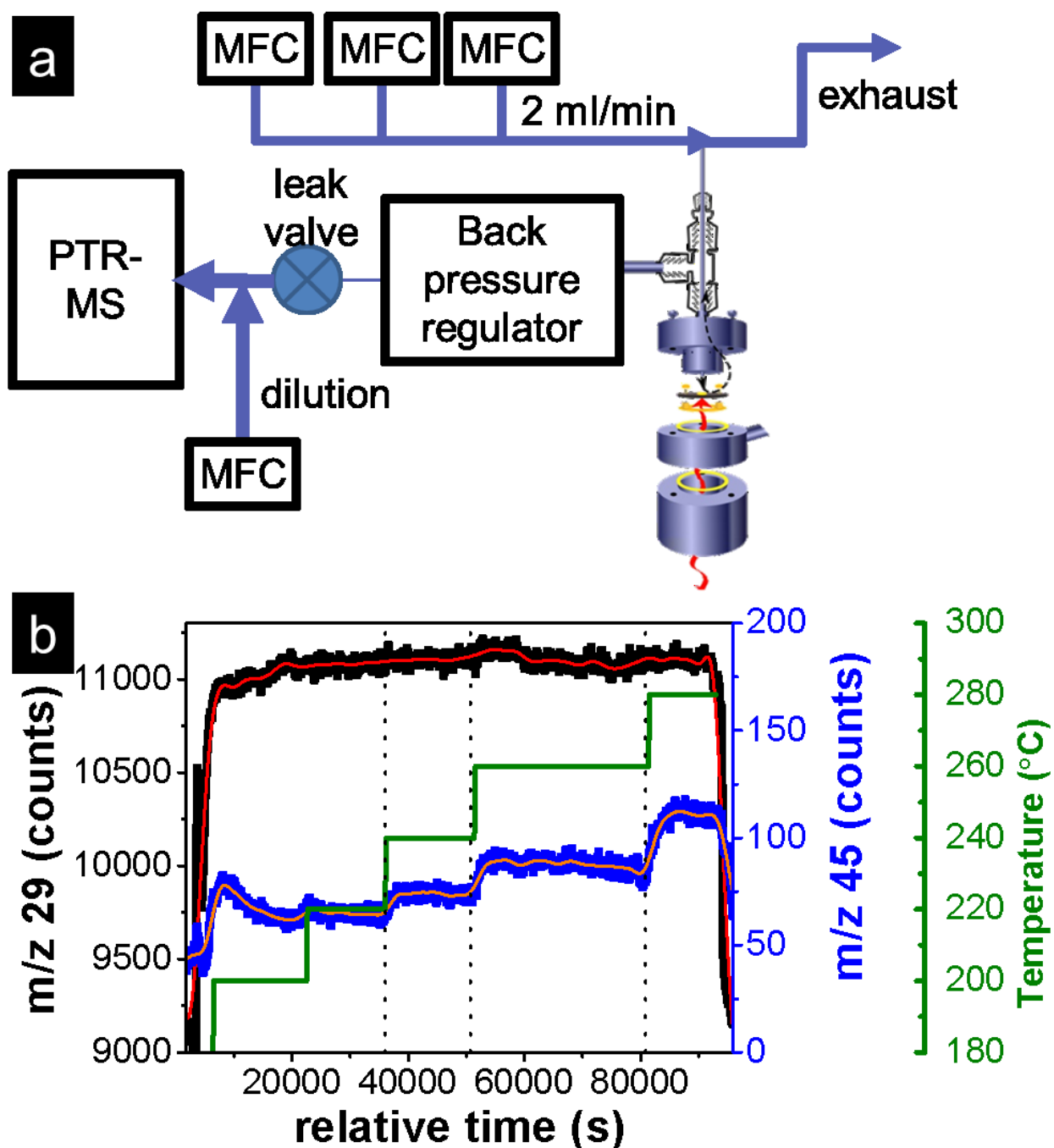
Figure S5-1: a) *Quasi in-situ* **TEM setup for 10^4 ml*g/min flow range. b) Raw PTR-TOF signals demonstrating the detectable conversion, the signals at each temperature were collected until steady state. The points demonstrated at the Figure 5-2a are each average of 500s under steady state conditions.**
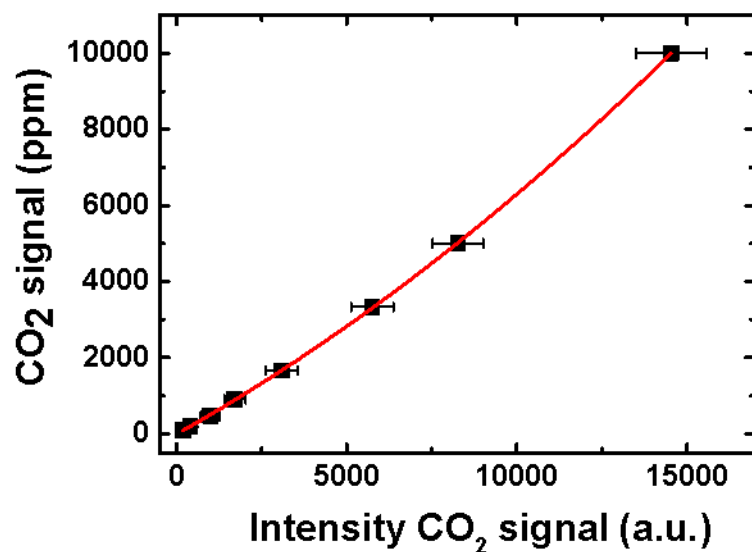
Figure S5-2: PTR-MS sensitivity to CO₂ dependence on the gas concentration.
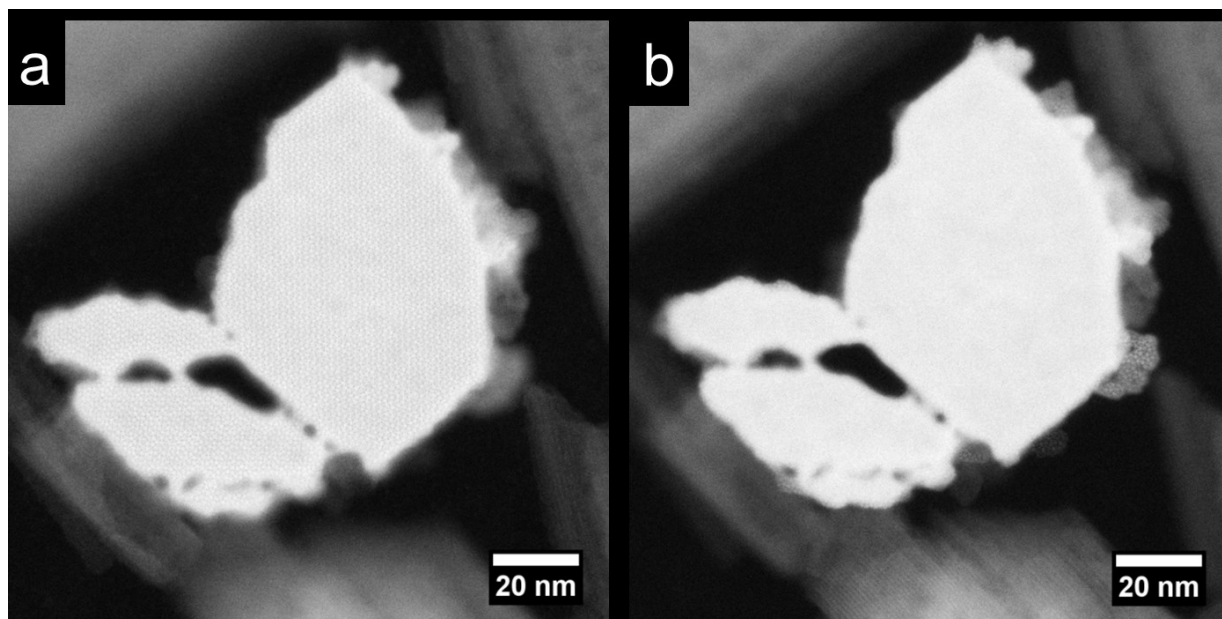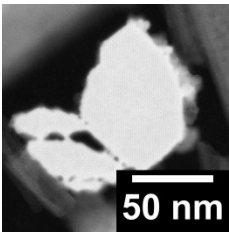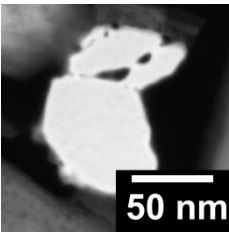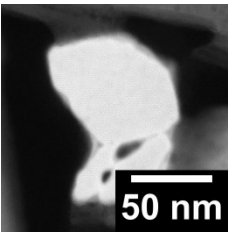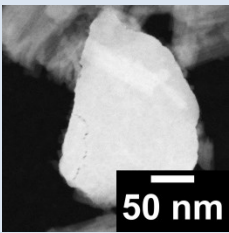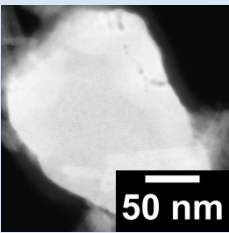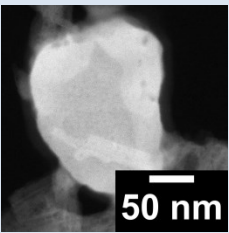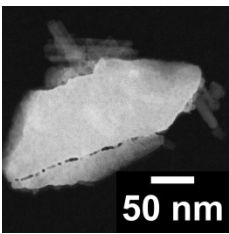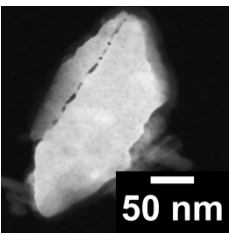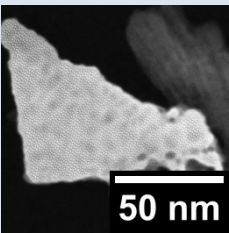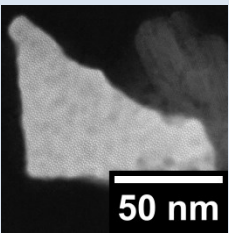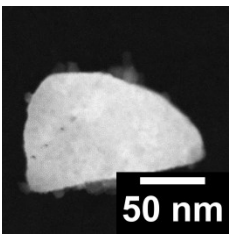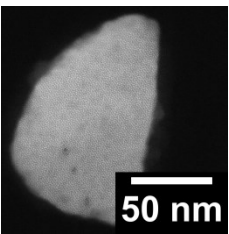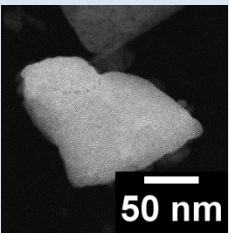
Figure S5-3: Identical location ADF-STEM images of the pristine oriented along z-axis catalyst particle with a) focus at the bulk area and b) focus at the surface region at the right side of the particle.

Table S 5-2: Raw ADF-STEM identical location images of the catalyt particles viewed along [001] crystallographic direction used as references for first three steps of the heat treatment treatment.

Pristine	2h, 300°C, N$_2$	4h, 300°C, N$_2$

6 Structural adaptability of isostructural complex mixed oxides in selective oxidation

6.1 Abstract

Amongst others, the local surface potential of heterogeneous catalysts depends on its geometric and electronic structure as well as composition. Using two different molybdenum and vanadium containing mixed oxides, which crystallize in the same orthorhombic structure, as an example, we present a comparative *quasi in-situ* transmission electron microscopy (TEM) study focusing on the structural adaptability of isostructural surfaces in the oxidative dehydrogenation of ethane (ODE). Orthorhombic $(Mo,V)O_x$ and M1-type $(Mo,V,Te,Nb)O_x$ are highly active and selective in the ODE reaction. The two complex oxides differ in their defect chemistry and composition. In addition, identical location imaging (ILI) of the same catalyst particles of $(Mo,V)O_x$ and $(Mo,V,Te,Nb)O_x$ at the relevant catalytic conversion disclose reaction induced surface changes, which depend on the kind of molybdenum and vanadium containing mixed oxide. While for orthorhombic $(Mo,V)O_x$, which is already highly active below 300 °C, the surface visually adapts to the gaseous environment by filling of surface-near hexagonal channels and the reconnection of surface motifs, almost no changes can be observed for M1-type $(Mo,V,Te,Nb)O_x$, which is activated in the temperature regime above 350 °C. The present study shows how different local surface potentials of heterogeneous catalysts define the adaption potential of a functional material to the local environment and can tune the activity or energy barriers of a catalytic reaction.

6.2 Introduction

Catalysts are widely used in modern chemical industry in order to reduce the energy demand and to enhance the selectivity towards favorable products in the target process.[1-2] This application benefit arises from the creation of different intermediate states, which lower the overall activation barrier for the reaction.[2] Due to their structural complexity heterogeneous catalysts can host different intermediates of multistep reactions.[3-4] Moreover, catalysts dynamically respond to the reaction conditions. Thus, the nature of the active site state under

reaction conditions can differ from the equilibrium state.[3, 5-7] This response not only includes electron or oxygen transfer between the catalyst and the reactants, but also energy transfer in the frame of surface energy minimization, which can lead to structural and electronic reorganization and/or transformation of the catalyst structure.[8]

One of the most energy consuming industrial chemical processes is the production of ethylene by steam cracking.[9] Alternative catalytic processes, such as oxidative dehydrogenation of ethane (ODE) could reduce the energy demand and may decrease the operation cost by 20%. [9-10] Modern catalysts already produce high enough ethylene yield at sufficiently low temperatures to economically compete with the established steam cracking.[11] However, further investigations of the working structure of the catalyst are required in order to tailor these complex systems towards their lifetime enhancement.

Examples of efficient ODE catalysts are mixed molybdenum and vanadium based oxides, which can crystallize in an orthorhombic phase that is also referred to as M1-type.[11-14] Despite of the structural similarities within this family of catalysts, selectivity and conversion can differ under the same reaction conditions and depends on the composition and pre-treatment of the catalyst.[15-17] Differences in the performance can be explained by the concept of "seven pillars" of selective heterogeneous oxidation catalysis.[18] Some of these pillars, such as metal-oxygen bond strength and phase cooperation, highlight the importance of studying the real catalyst structure, which includes structural defects and differences of surface states. This mixed molybdenum and vanadium based oxides can exhibit a plethora of structural defects and co-existing phases.[19-22] However, investigations of the structures response in catalytic reactions of this catalyst family mostly relies on X-ray diffraction (XRD) measurements, which can be powerful to detect the bulk response to the reaction media such as the size modifications of structural channels or phase transformations, but is unable to provide nanoscale structural details on the local modifications of the surface layer. [16-17, 23-25] *In-situ* transmission electron microscopy (TEM) investigations, which can detect local structural modifications at the atomic scale, carried out for M1-type $(Mo,V,Te)O_x$ and $(Mo, V, Te, Nb)O_x$ have demonstrated a depletion of Te moieties from the structural channels. These observation have to be questioned as this effect can be caused by the presence of impurity phases and/or can be attributed to the low pressure conditions (<10mbar), at which the experiments were conducted, which can potentially result in pressure gap related effects.[24, 26] Other methods, such as *in-situ* XPS pinpoint compositional changes, such as feed

dependent surface enrichment by V cations. The extent of surface enrichment depends on the composition of these classes of oxides. However, these measurements can not directly reproduce the structure.[27-28]

Nanoscale structural changes caused by relevant reaction conditions can be detected by *quasi in-situ* TEM (see chapters 4 and 5), which includes imaging of a pristine sample deposited on the TEM grid, exposure of the sample to the reaction environment under relevant and operando conditions and imaging of identical locations after the reaction.[29] Similar to conventional TEM this method provides the reproduction of structural details down to the atomic level. As opposed to *in-situ* TEM the electron beam does not influence the catalytic reaction. Structural changes of identical locations particles can be imaged before and after the catalytic reaction.[29-31]

Here, we present a comparative high resolution *quasi in-situ* scanning transmission electron microscopy (STEM) investigation of orthorhombic $(Mo,V)O_x$ and M1-type $(Mo,V,Te,Nb)O_x$. We will demonstrate the differences of their pristine structures, which include the description of structural defects, and their structure responses to the reaction media at the relevant conversion in the ODE reaction.

6.3 Results

6.3.1 Structural comparison of $(Mo,V)O_x$ and $(Mo,V,Te,Nb)O_x$

Molybdenum and vanadium form the basis of compositional flexible, complex mixed oxides, which can crystallize in the same orthorhombic crystal structure, but slightly different microstructures, which can be expressed by the different metal sites occupancies. For instance, ternary $(Mo,V)O_x$ and quinary $(Mo,V,Te,Nb)O_x$ are isostructural and can appear in the same orthorhombic phase (Figure 6-1a), Differences can be found in, for instance, the occupancy of the structural channels. For ternary $(Mo,V)O_x$ the hexagonal channel sites are partially (4% and/or 20 %) occupied by V moieties.[17, 28] In annular dark-field scanning transmission electron microscopy (ADF-STEM) experiments, the scattering intensity of this channel sites is overwhelmed by fully occupied vicinal metal sites. Thus, these channel sites appear empty or blurred (Figure 6-1b). For quinary $(Mo,V,Te,Nb)O_x$ the hexagonal channels are filled by Te (69% or 74%).[32-33] Due the higher occupancies of the channel sites and its higher element number electrons are scattered stronger. Thus, the in ADF-STEM image presented in Figure 6-1c

the Te moieties in the hexagonal channels can clearly be observed. In addition, the composition of the center of the pentagonal $\{(M)Mo_5\}$ (M= Mo or Nb) unit, which is the main building block of both oxides, varies. While this building block is completely composed of Mo cations for ternary orthorhombic $(Mo,V)O_x$, M1-type $(Mo,V,Te,Nb)O_x$ the center of the pentagonal building block is composed of a pentagonal NbO_7 bipyramid.[13, 17, 28, 34-35] As Nb and Mo are neighboring elements in the periodic table a discrimination based on the intensity distribution of the ADF-STEM micrograph is impossible.

Although these differences do not affect the space group, these outlined compositional alterations between the two oxides can moderate activity and selectivity in partial oxidation of light alkanes and can tune the appearance of geometric bulk and surface defects.[36-37] For instance, both catalysts can exhibit trigonal and amorphous inclusions, but the inclusions of the M2 phase were reported only for M1-type $(Mo,V,Te,Nb)O_x$.[19-22]
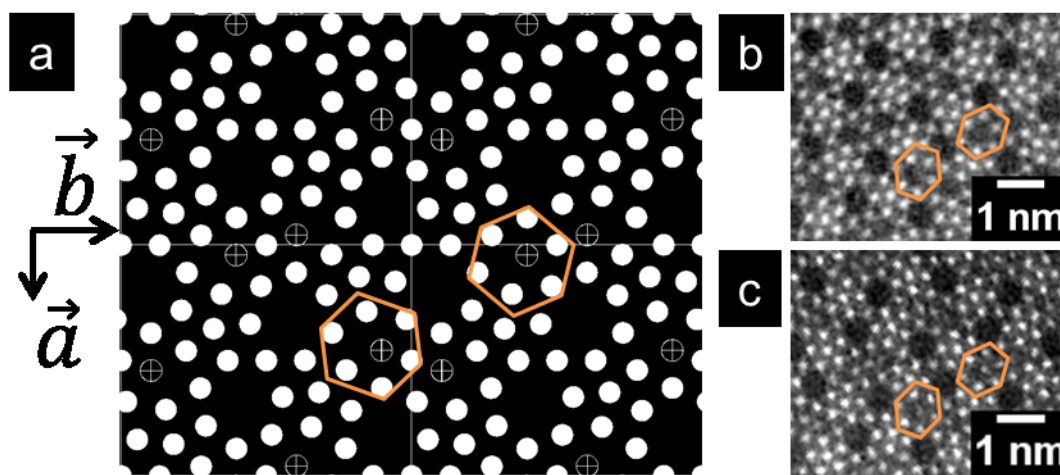
Figure 6-1: a) Structural model of orthorhombic and M1-type mixed molybdenum and vanadium oxides, which corresponds to a quadruple unit cell of M1-type $(Mo,V,Te,Nb)O_x$ (ICSD: 55097) viewed along the crystallographic c-axis; white filled circles: common sites for $(Mo,V)O_x$ and $(Mo,V,Te,Nb)O_x$, crossed circles: channel sites with different elemental composition and site occupancies. b) and c) ADF-STEM images of identical structural regions of ternary $(Mo,V)O_X$ (b) and quinary $(Mo,V,Te,Nb)O_x$ (c). Orange hexagons: hexagonal channels with pronounced differences of the occupation.

The morphological differences of orthorhombic $(Mo,V)O_x$ and M1-type $(Mo,V,Te,Nb)O_x$ can be further spotted by the termination of the surface at medium magnification (Figure 6-2), The surface of M1-type $(Mo,V,Te,Nb)O_x$ (Figure 6-2a) is composed of large facets and appears

much smoother than the rough and defective surface of orthorhombic $(Mo,V)O_x$ (Figure 6-2b). The surface of the quinary oxide is mainly characterized by (210), (110), (100), and (010) facets. In addition, the representative ADF-STEM image of the M1-type $(Mo,V,Te,Nb)O_x$ particle, which is shown in Figure 6-2a, is characterized by the absence of any surface defects, while the surface of presented orthorhombic $(Mo,V)O_x$ crystal hosts in total 54 structural motifs, from which 45 are triangular (see chapter 2). Due to the observed surface roughness and the presence of surface defects a clear assignment of the crystallographic surface terminations is unfeasible for orthorhombic $(Mo,V)O_x$ mixed oxide..
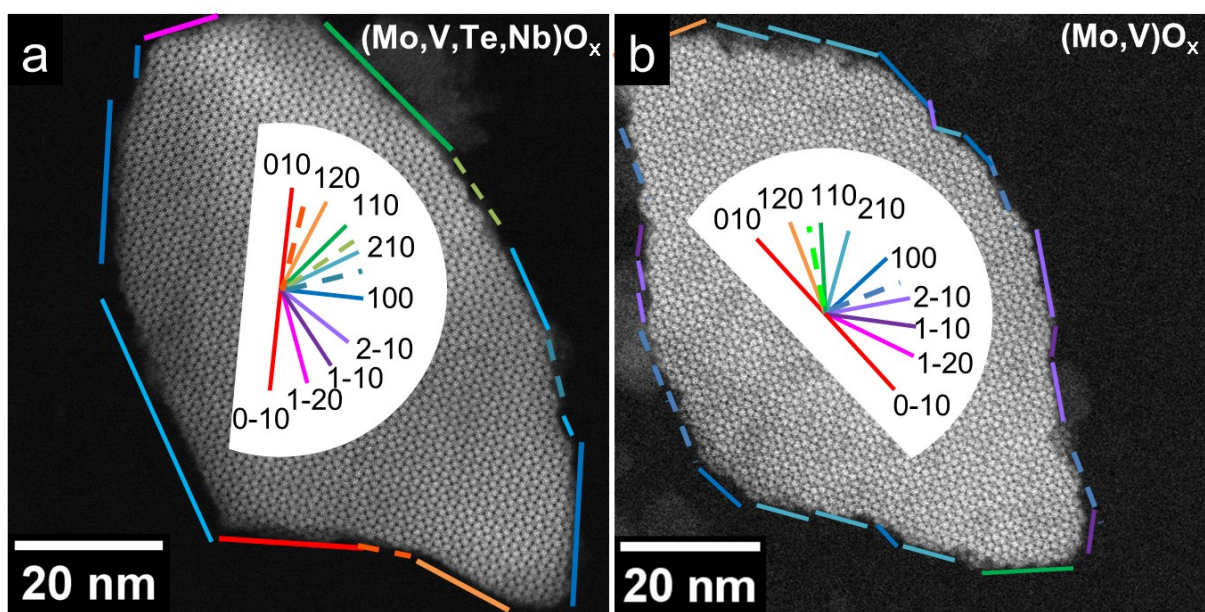
Figure 6-2: ADF-STEM images of a) quinary $(Mo,V,Te,Nb)O_x$ and b) ternary $(Mo,V)O_x$ crystals viewed along the crystallographic c-axis. Solid lines: low order crystallographic planes and terminations, dashed lines: higher order lattice planes.

We have previously shown that intergrown phases, which represent extended defects, can appear in ternary $(Mo,V)O_x$.[21] The STEM and EFTEM images in Figure 6-3 indicate that this kind of extended defects can also occur in quinary $(Mo,V,Te,Nb)O_x$. For orthorhombic $(Mo,V)O_x$ extended defects such as pseudo-trigonal and aperiodic intergrowth can be clearly separated and classified. The pseudo-trigonal intergrowth can be interrupted by non-periodic regions, which were identified as interstitial regions. The majority of the pseudo-trigonal intergrowth can still be highlighted by the corresponding structural tiling.[20-21] Figure 6-3a shows a contrast enhanced overview bright-field (BF)- STEM micrograph of an M1-type

$(Mo,V,Te,Nb)O_x$ particle viewed along the crystallographic c-axis. The particle is composed of three individual crystallites, which are separated by intergrown regions. This intergrown regions are mostly aperiodic in nature, but can exhibit some pseudo-trigonal inclusions (Figure 6-3b). In total the pseudo-trigonal moieties cover only about 5% of the total intergrowth length. The intermixing of different types of intergrowths is a general structural feature for extended defects in M1-type $(Mo,V,Te,Nb)O_x$.

As opposed to the intergrowth structure in orthorhombic $(Mo,V)O_x$ (chapter 3), the intergrowth in M1-type $(Mo,V,Te,Nb)O_x$ hardly exhibits significant internal thickness variations or thickness differences in its surrounding bulk structure (Figure 6-3a to c). In addition, large structural channels inside the intergrown regions were not detected by both STEM imaging and EFTEM mapping.

Additionally to the structural diversity, which occurs in orthorhombic $(Mo,V)O_x$, dislocation cores inside the bulk of M1-type $(Mo,V,Te,Nb)O_x$ were spotted (Figures 6-3d and e).[20-21] This defect differs from the intergrown region, which were observed in quinary $(Mo,V,Te,Nb)O_x$ such that it is characterized by a decrease of thickness, while traversing from the bulk to the surface of the particle (see thickness map in Figure 6-3d). It is difficult to extract the exact starting point of the defect due to a slight but cumulative translational and rotational discrepancy of the structure within the defect (Figure 6-3e). As indicated by the red marked high resolution image of Figure 6-3e the interior of the defect area exhibits a distorted crystals structure, in which the atomic columns are 8-shaped rather than distinct localized spots. This observation can be explained by the presence of turbostratic disorder within M1-type $(Mo,V,Te,Nb)O_x$. Usually turbostratic disorder occurs in two-dimensional (2D) layered materials, which would imply a layer-like character of M1-type $(Mo,V,Te,Nb)O_x$ with a preferential stacking direction along the crystallographic c-axis.[38]
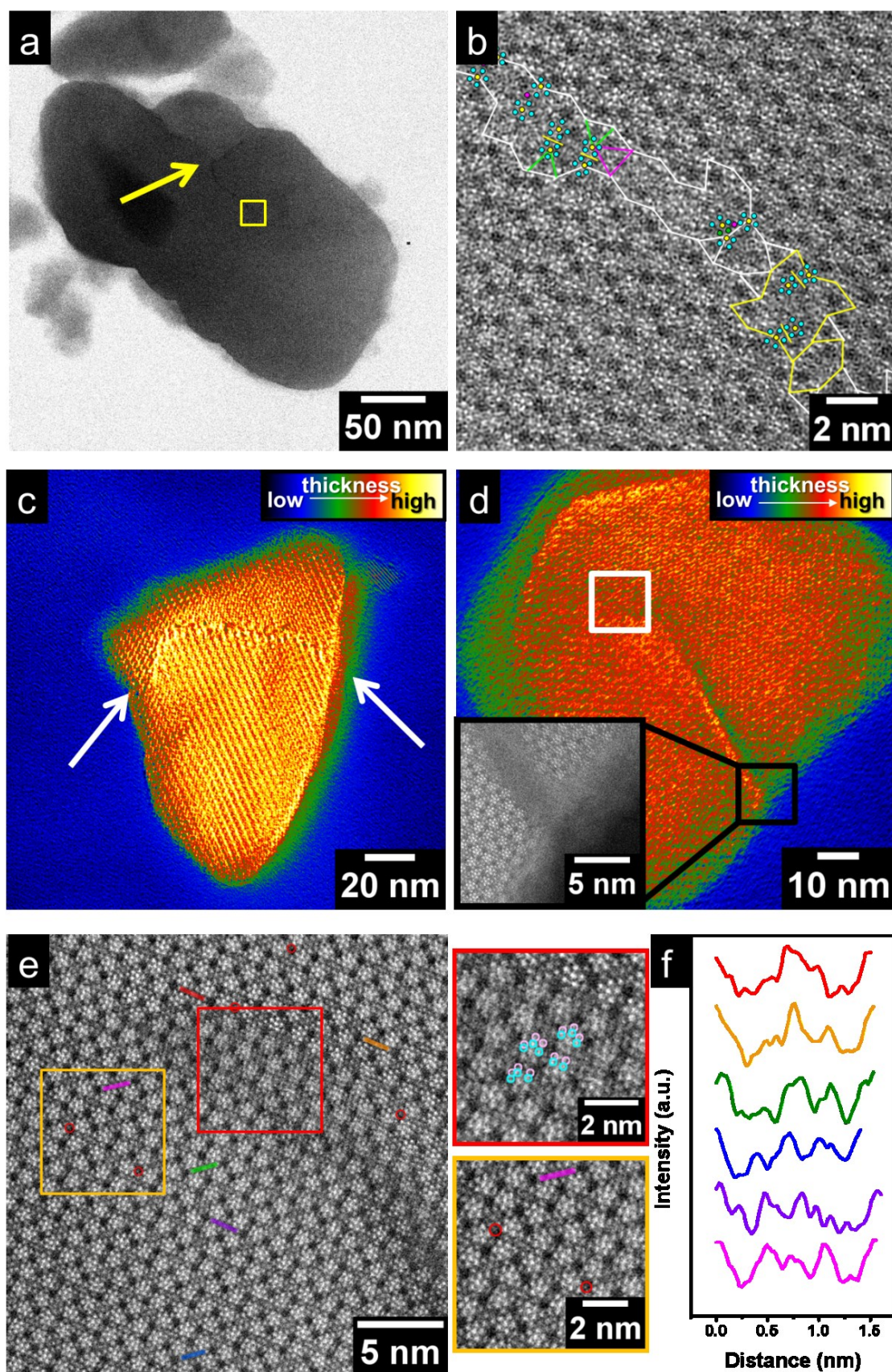
Figure 6-3 a) Contrast enhanced BF-STEM image of the of M1-type (Mo,V,Te,Nb)O$_x$ particle viewed along the crystallographic c-axis. The original image is presented in Figure S6-1. Yellow arrow: point where individual crystals merge. (b) High resolution ADF-STEM image of the intergrown region with a pseudo-trigonal inclusion, taken from the area highlighted by the yellow square in Figure 6-3a. White lines: intergrowth outline; yellow polygons: interstitial regions; arrow-shaped hexagons: trigonal intergrowth area; pink and magenta triangles: triangular motifs; yellow lines: mirrored motifs; green circles: twinned motif; magenta circles: rotated motifs; yellow and cyan circles: central and side cations of the pentagonal building blocks. (c), (d) EFTEM thickness maps of the M1-type (Mo,V,Te,Nb)O$_x$ particles viewed along the crystallographic c-axis, which highlights an intergrowth (c) and a dislocation (d), respectively. The inset in (d) represents high resolution ADF-STEM image of the dislocation termination viewed along the crystallographic c-axis. (e) High resolution ADF-STEM image of the dislocation core, which correspond to the white square in Figure 6-3d. Red square: dislocation area with pronounced re-shaping of atoms position; cyan and pink circles: two overlapping atomic positions leading to 8-shaped arrangements; red circles: cations inside the heptagonal channels. f) Intensity line profiles of selected channel areas. The color code reflects the colored lines in Figure 6-3e.

6.3.2 Comparison of the structure responses of (Mo,V)O$_x$ and (Mo,V,Te,Nb)O$_x$ in the oxidative dehydrogenation of ethane (ODE)

Catalytic tests of the mixed molubdenum and vanadium based oxides were initially carried in the fixed bed reactor, which is described elsewhere, in order to determine conversion dependence on the temperature for (Mo,V)O$_x$ and (Mo,V,Te,Nb)O$_x$ (Figure 6-4, filled squares and circles).[39] Afterwards, for the ILI the TEM grid reactor, which is described in the chapter 3, was connected between the outlet of the fixed bad reactor and gas chromatograph (GC) (Scheme S6-1) in order to study the response of structure biased by the products distribution (C$_2$H$_4$, H$_2$O, CO$_x$). The catalytic data, which was obtained by the TEM grid reactor implemented in the system is highlighted in the Figure 6-4 (open squares and circles) and follow the trend observed in the fixed bed reactor., The reaction media inside the TEM grid reactor is determined by the conversion inside the fixed bed reactor.
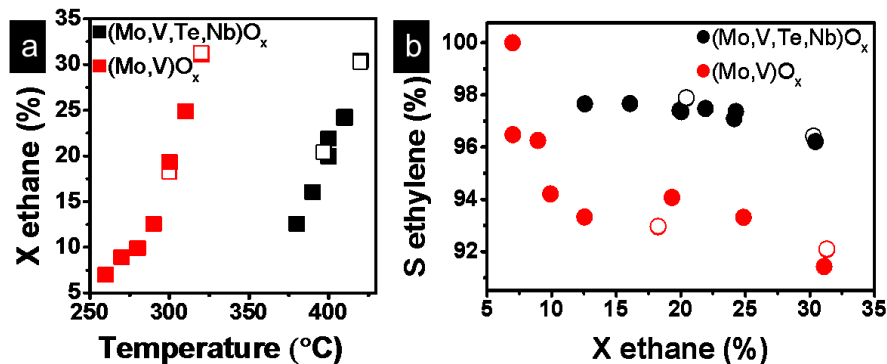
Figure 6-4: a) Ethane conversion as a function of temperature in the ODE reaction for orthorhombic (Mo,V)Ox and M1-type (Mo,V,Te,Nb)Ox. b) Dependence of the selectivity of ethylene on the ethane. Filled circles and squares: data obtained using only a fixed bed reactor, opened circles and squares: data obtained using the TEM Grid reactor and the fixed bed reactor. Flow 7 ml/min, $C_2H_6:O_2:N_2$ 3:6:91.

In the ODE reaction orthorhombic $(Mo,V)O_x$ is more active than M1-type $(Mo,V,Te,Nb)O_x$ as it reaches similar conversion at much lower temperature (Figure 6-4a).[40] M1-type $(Mo,V,Te,Nb)O_x$ demonstrates higher selectivity to ethylene at higher conversion ranges (Figure 6-4b), while both catalysts are highly selective at low conversion. In addition, the selectivity of ethylene for orthorhombic $(Mo,V)O_x$ continuously decays for higher conversion. This decay is very pronounced in the conversion range of 5-12%. A steady selectivity plateau can be observed for quinary $(Mo,V,Te,Nb)O_x$ up to 25% conversion.

Although orthorhombic $(Mo,V)O_x$ is more active at lower reaction temperatures in the ODE reaction significantly more pronounced structural changes compared to M1-type $(Mo,V,Te,Nb)O_x$ can be observed.

The changes of ternary $(Mo,V)O_x$ at 20% conversion of ethane can be observed by comparing ADF-STEM images of identical particles before and after ODE reaction at low magnification (Figure 6-5a,b) and at high magnification (Figure 6-5c,d). Already at low magnification changes of the surface structure can be estimated and can be interpreted as, partial disappearance of defective surface parts, which leads to a smoothing of the surface. The main structural rearrangements of orthorhombic $(Mo,V)O_x$ further include the appearance of additional cations in the hexagonal channels near the surface. In the pristine sample, some of the structural channels already had a higher metal occupancy than the average hexagonal channel sites in the bulk (orange circles in Figure 6-5c). After ODE reaction, the occupancy of some of

these channels has changed, as revealed by ILI, while other hexagonal channels, which were not cation enriched before have gained contrast (Figure 6-5d, orange circles). The contrast enhancement after catalysis can be attributed to the filling of these holes as a result of migration of individual metal cations or complete metal columns due the thermal and/or chemical stimulus during catalytic reaction.

Owing to the unknown composition of the rearranged surface motifs the reorganization process can be attributed to the filling of structural channels and subsequent reorganization of the microstructure of orthorhombic $(Mo,V)O_x$ or to the formation of hexagonal-shaped motifs, which, for instance, can be observed in the so-called M2 phase.[34] The boundary between two catalyst particles at the bottom of Figures 6-5c and d (white ovals, see also Figure S6-2 for overview images) almost vanishes. Although both images were collected with exactly the same gain and intensity level values of the ADF-STEM detectors, the absence of contrast after the ODE reaction indicates the occurrence of significant mass transfer.

The applied conditions lead to much less changes than observed previously for orthorhombic $(Mo,V)O_x$ (see chapter 5). This can be referred to a lower weight hourly space velocity (WHSV), the additional pre-treatment in nitrogen atmosphere or to the differences in the gas mixtures. The defect rich (surface) regions exhibit higher structural changes than the orthorhombic bulk, which remains almost unaffected.
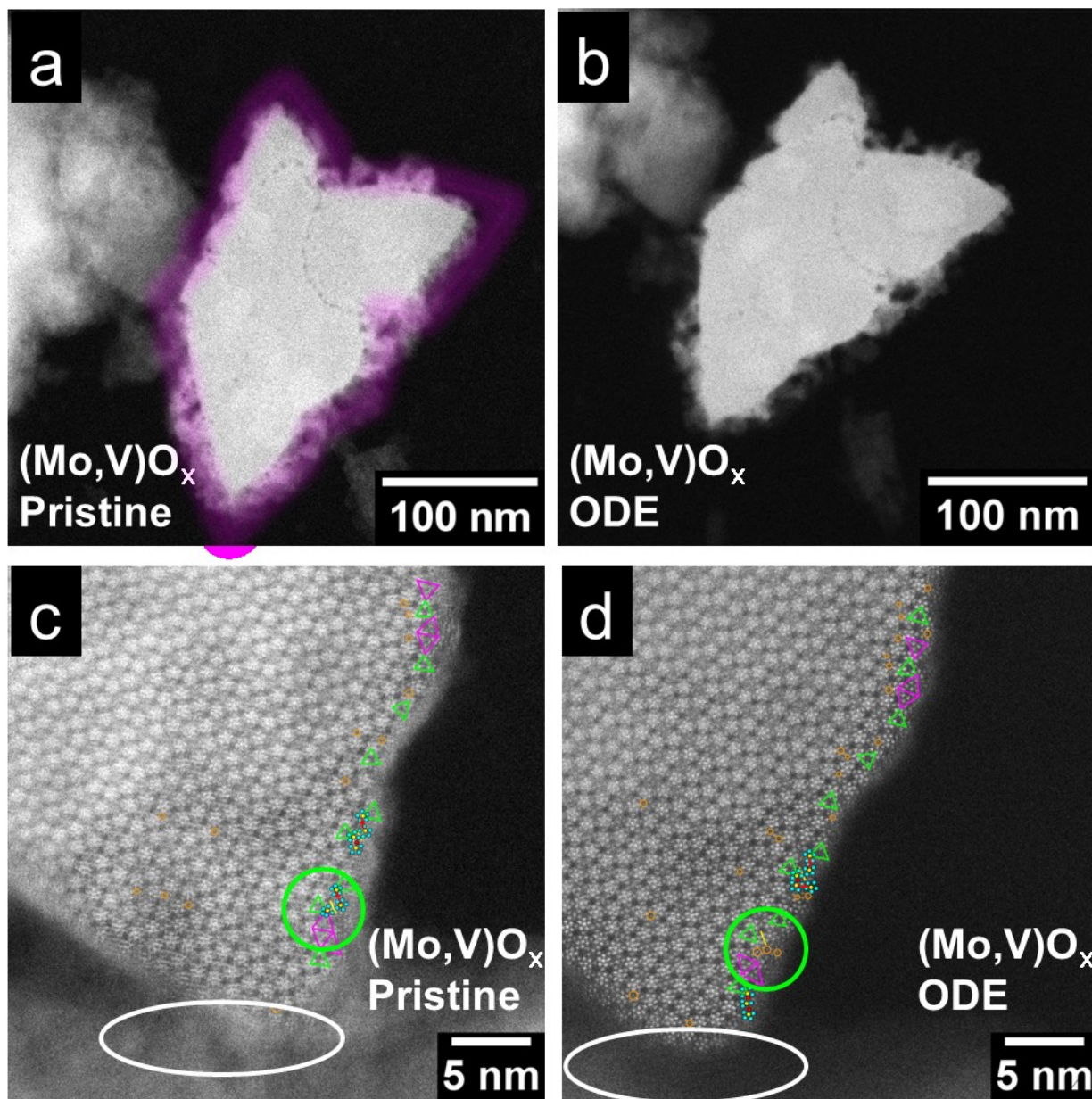
Figure 6-5: Identical location ADF-STEM images of orthorhombic (Mo,V)O$_x$ particles before (a,c) and after (b,d) ODE at 20% conversion of ethane. a), b) Overview images, which indicate the modification of a defective surface layer (highlighted magenta). c), d) high resolution STEM images, which highlight changes of the occupation of surface and channel sites. Magenta outline: surface layer; green and magenta triangles: triangular motifs; red arrows: translated motifs; yellow lines: mirror motifs; red cirlces: shared cations; cyan and yellow circles: corner and central cations of the pentagonal building blocks of the motifs; orange circles: filled channels; green circles: defects rearrangement area; white ovals: boundary between two catalyst particles.

While pronounced structural changes can be observed for orthorhombic $(Mo,V)O_x$ M1-type $(Mo,V,Te,Nb)O_x$ exhibits almost no geometric, reaction induced reconstructions at 30% conversion of ethane. ADF-STEM images of identical locations before and after ODE reaction of quinary $(Mo,V,Te,Nb)O_x$ demonstrate the absence of structural modifications even for metastable regions of the oxide such as defect-rich terminations of the intergrown phases (Figure 6-6a,b). The most pronounced changes in the examined particles include shrinkage of the surface contours by approximately 0.5 nm and the occurrence of a single pair of mirrored and shared motifs at one particle (Figure 6-6c,d), which was not resolved in the pristine sample, while others remained unaffected (see Figure 6-5a,b). This motif can result from a structural rearrangement towards a more stable configuration or a structural flattening, which resulted in more optimized imaging conditions of the edge of the M1-type $(Mo,V,Te,Nb)O_x$ particle.
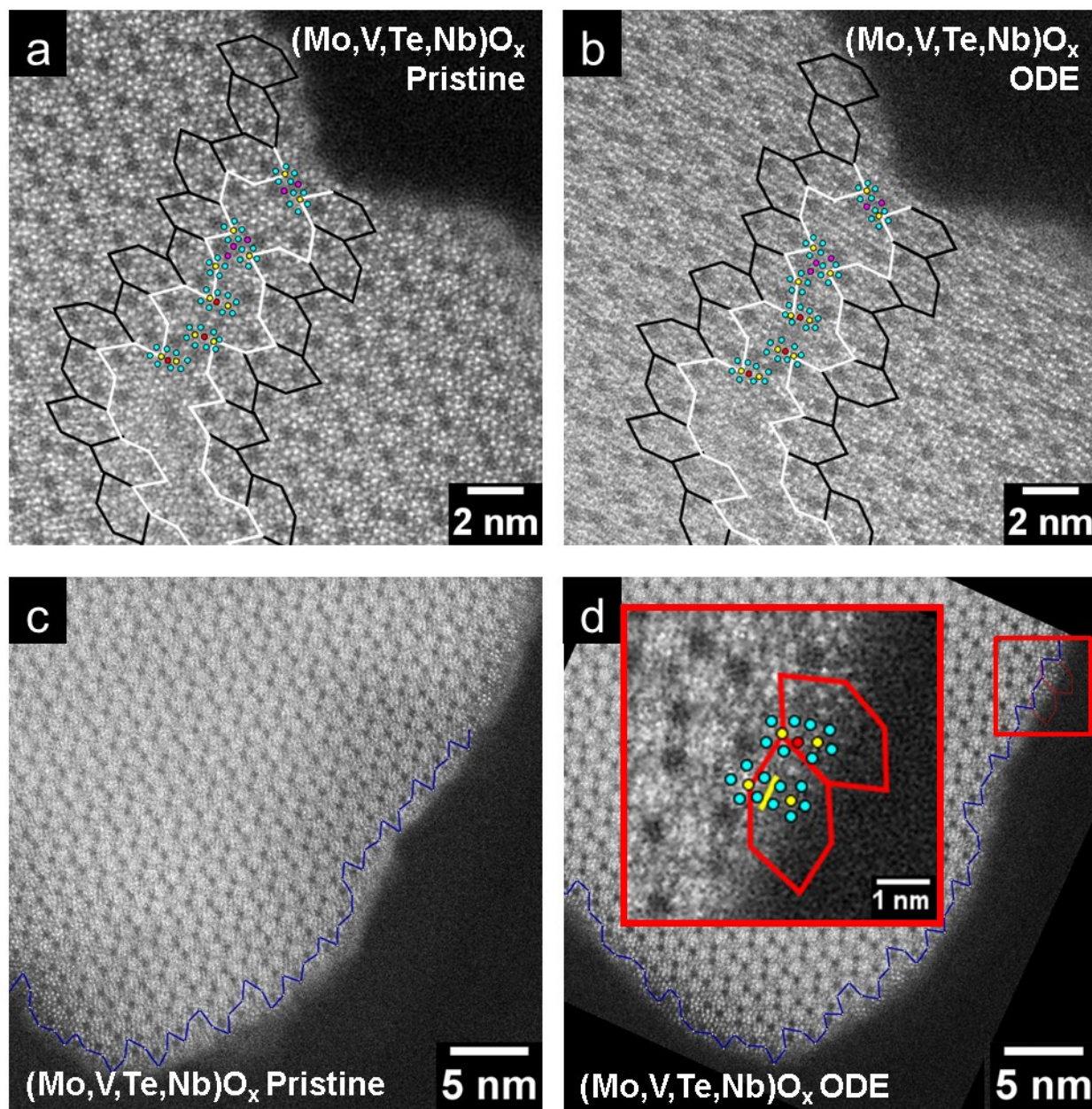
Figure 6-6: Identical location ADF-STEM images of M1-type (Mo,V,Te,Nb)O$_x$ catalyst particles viewed along the crystallographic c-axis in the pristine state (a, c) and after exposure to the ODE reactions at 30% conversion of ethane (b, d). a), b) An intergrown region and c), d) surface region. White lines: aperiodic intergrowth black tiles: M1 structure; blue segmented line: outline of the surface contours before and after reaction; red hexagons: expected tiling; yellow line: translated motif, red circles: shared motifs; magenta circles: rotated motifs; cyan and yellow circles: side and central cations of the motifs.

Contradictory to the previous studies disappearance of the Te from the structural channels was neither suggested by high resolution ADF-STEM images (Figure 6-6b,d) nor by energy dispersive X-ray spectroscopy (EDX) mapping (Figure 6-7a).[24-26] This difference probably is caused by the absence or reversibility of Te reduction under selected conditions due to a high excess of oxygen in the feed. In order to examine potential atmosphere induced effect additional TEM grid reactor tests with a secure transfer were carried out, which also confirmed high channel occupancies even after prolonged reaction times for 10 days (Figure 6-7b).
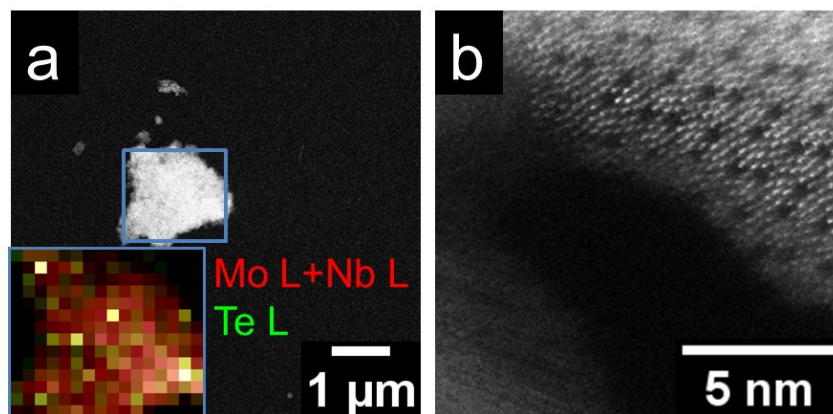
Figure 6-7: a) ADF-STEM image and STEM-EDX map (inset) of an agglomeration of a M1-type (Mo,V,Te,Nb)O$_x$ particle. b) HAADF-STEM image of the M1-type (Mo,V,Te,Nb)O$_x$ particle, which was exposed to the ODE reaction mixture C$_2$H$_6$:O$_2$:N$_2$ 3:6:91 at 400°C for 10 days in the TEM grid reactor setup described in chapter 5, viewed in the direction close to the crystallographic c-axis.

6.4 Discussion

The observed differences of their pristine structures and their defect chemistry of the examined complex molybdenum and vanadium oxides can arise from differences in the synthesis protocols, but also from compositional differences between orthorhombic (Mo,V)O$_x$ and M1-type (Mo,V,Te,Nb)O$_x$.[13, 19-20, 23, 41] In particular, the presence of Nb may stabilize the structure and prevent the oxide from overreduction or overoxidation, which may, therefore, limit the formation of oxygen vacancies in M1-type (Mo,V,Te,Nb)O$_x$.[23, 42] Thus, further recombination to oxygen deficient structural motifs during the activation of the catalyst and under reaction conditions is omitted. In addition, the ionic radii of the metal cations, which are present in the structural channels can strongly differ for V and Te cations and depend on the coordination number and charge.[43] These size flexibility can lead to differences in the strength of induced

strain into the surrounding bulk structure. In particular, for Mo-containing oxides, it has previously been shown that structural strain can lead to frustrated MoO_x species, which are able to transform reactants.[44] Thus, the difference of the ionic radii of the channel site cannot only tune the induced strain, but modulate the catalytic activity. It seems reasonable to assume that different selective oxidation reactions may require different magnitudes of strain as additional source of surface energy, which may also depend on the geometric structure, structural surface motifs and composition. The adjusted surface potential can moderate energy barriers and/or the activation of small molecules, such as the transformations of molecular oxygen into different electrophilic oxygen species. Thus, additional studies shall focus on the influence of the strain and composition on adjusting the oxygen philicity. Additionally, the initial high occupancy of structural channels by Te for M1-type $(Mo,V,Te,Nb)O_x$ reduces the probability of V transfer into the channels.[23]

The dislocation core spotted in the M1-type $(Mo,V,Te,Nb)O_x$ can be interpreted as structural anisotropy, which occurs in this mixed oxide. The crystallographic structure of the examined oxides can be described as a set of pentagonal bipyramids and octahedra with metal cations in the center, which are surrounded by oxygen anions.[45] These polyhedra are arranged to a crystalline framework via corner and edge sharing octahedra. While both corner and edge sharing octahedra are observed in the crystallographic (ab) plane, only corner sharing octahedra exist along the crystallographic c-axis, which allows for the occurrence of a facile possibility of a rotational mismatch for single pairs of polyhedra. This can lead to the formation of structures, which resemble those that can be observed in turbostratic disordered layered materials, and/or to local strain, which can be referred to as surface inclination or disinclination.[21, 38]

The potential energy of the active site of a catalyst changes during the catalytic transformation due to the interaction with the reactands.[46] These interaction reduces the energy barrier for the reaction compared to the non-catalyzed reaction, but requires still a certain energy for activation. This can lead to an activity of the oxidation catalysts, which depend on the strength of the metal-oxide bonds in the catalyst framework.[2, 18] If the surface site was not in its equilibrium position the introduced external energy can lead to structural reorganization, which creates lower potential energy states.[25, 47] Therefore, the sites, which demonstrate transformations under lower temperatures and/or less reductive/oxidative conditions, can be considered less stable towards the applied media (see also chapter 5).[17, 23, 26, 28, 42] Based on the observed

structure responses to different media for orthrorhombic $(Mo,V)O_x$ and M1-type $(Mo,V,Te,Nb)O_x$ we can derive the following stability of structural units: pentagonal Nb containing building blocks> pentagonal Mo building blocks>bulk framework composed of linker octahedra sites > channel sites with Te cations> channel sites with V cations and structural defects. Moreover, the Te depletion from the structural channels of M1-type $(Mo,V,Te,Nb)O_x$, which was described previously, was detected in a more reductive atmosphere.[24-26] The oxygen-rich non-stoichiometric mixture, which was applied in the current study, allows for avoiding the reduction of Te, or renders the Te reduction due to the interaction with ethane reversible, which limits the loss of Te from the structure. As opposed to the empty channels of orthorhombic $(Mo,V)O_x$ the Te interaction with the surrounding atoms, which form the channel, restricts a possible compression of the structural pores and stabilizes the voids of M1-type $(Mo,V,Te,Nb)O_x$.

The structural stabilization, which is provided by the presence of Nb and Te, also influences surface and extended defects. Moreover, despite the high concentration of potentially oxygen-deficient structural motifs, the examined aperiodic intergrown regions inside the M1-type $(Mo, V, Te,Nb)O_x$ hardly exhibit structural changes. This effect can come from the lack of large intergrown regions, which can be stabilized by two surrounding bulk crystals.

Our study suggests that structural channels in open-framework, microporous molybdenum and vanadium containing oxides may act as reservoirs for active atoms. In this respect the term active atoms is defined as reactive surface-near channel site, which induces strain to vicinal Mo-O bonds that may act as active centers for the oxidative transformation of small alkanes. Strained Mo-O bonds can be an intrinsic property, for instance for $(Mo,V,Te,Nb)O_x$, or require thermal activation, in which cation migration to the hexagonal channels is involved (see $(Mo,V)O_x$). For the latter the interplay of intrinsic structural motifs and thermal induced activation may lead to the formation of surface overpotentials, which render any control on the activation of molecular oxygen into electrophilic species difficult. The surface overpotentials can be translated to the lower active temperature regime of $(Mo,V)O_x$. Tt may complicate the incorporation of defined oxygen species into hydrocarbon, which is often expressed by overoxidation of the functionalized hydrocarbon to CO_x.

6.5 Conclusions

In summary we have demonstrated a correlation between activity of the catalyst and the adaptability of the catalyst structure. Defects-rich surfaces of orthorhombic $(Mo,V)O_x$ catalyst, supported on a relative flexible empty-channels structure, clearly display a structure response to the ODE reaction at 300°C temperature, while non-defective surface of M1-type $(Mo,V,Te,Nb)O_x$, which is further stabilized by the bulk structure with restricted flexibility due to the presence of Te in the channels, remains rather unaffected even at 420°C. Orthorhombic $(Mo,V)O_x$ exhibits high activity at much lower temperatures compared to M1-type $(Mo,V,Te,Nb)O_x$. Further studies of the catalysts responses to the reaction media with extended time-on-stream and/or temperature range would allow to separate the reversible structure response towards surface energy minimization under the applied chemical potential and irreversible processes, which may lead to the deactivation of the catalyst.

6.6 Methods

Synthesis

$(Mo,V)O_x$

Hydrothermal synthesis of the orthorhombic $(Mo,V)O_x$ mixed oxide (internal ID 20000) was curried in specially built reactor (Premex Reactor AG, Lengnau, Switzerland) from corrosion resistant Hastelloy C-22 (2.4602). A mixture of 9.18 g $(NH_4)_6Mo_7O_{24}\cdot4H_2O$ (AHM, Merck, 52 mmol Mo) dissolved in 230 g water (Milli-Q, Merck) and 3.30 g $VOSO_4$ (Acros Organics, 12.9 mmol V) dissolved in 30 g water was loaded into a reactor at room temperature. Residual air was replaced by nitrogen. Subsequently the vessel was heated to 200°C at a rate of 1°C/min and hold at this temperature for 17 h. The reaction mixture was stirred during the whole experiment at a rate of 100 rpm. After cooling to room temperature, a black solid was isolated by filtration (pore 5 glass frit), washed twice with distilled water and dried at 80°C for 16 hours. To remove amorphous components in the hydrothermal product, 1 g of the powder was washed with 25 ml oxalic acid solution (0.25 M, Acros Organics) at 60°C for 30 min under stirring. The solid was centrifuged (5000 rpm, 30 min), washed twice with 25 ml water and dried at 80°C over night. Finally, a thermal treatment was performed in 100 ml/min argon flow at 400°C (heating rate 10°C/min) for 2 h in a rotary tube furnace (Xerion, Freiberg, Germany).

(Mo,V,Te,Nb)O$_x$

(Mo,V,Te,Nb)O$_x$ was synthesized by first adding a solution of 11.75 g (NH$_4$)$_6$Mo$_7$O$_{24}$ · 4 H$_2$O (56.1 mmol Mo, MERCK, Lot# A758482 622)) in 140 mL distilled water to a solution of 3.80 g niobium oxalate (H.C. Starck) in 30 mL dist. water and stirring the mixture in an autoclave setup (Premex Switzerland) for 30 minutes. The solution was heated to 175 °C under continuous stirring. After 145 minutes at 175 °C, a 30 mL solution containing 3.86 g of VOSO$_4$ · 5 H$_2$O (16.6 mmol V, Sigma Aldrich, Lot# MKBX1043V) was pumped into the autoclave at 20 ml/min. After further 145 minutes, a solution of 30 mL with 3.52 g telluric acid Te(OH)$_6$ (15. 3 mmol Te, Süd-Chemie, Lot# LCB 5478 D) was pumped at 20 ml/min as well. The reaction mixture was kept at 175 °C for 14 hours under constant stirring and then cooled down to room temperature. After the hydrothermal treatment, the resulting black-violet suspension was centrifuged and washed with dist. water thrice. The remaining solid was dried at 80 °C in air.The black solid was activated in a rotary tube furnace under a constant argon flow of 100 ml/min at 650 °C for 2 hours.

TEM imaging

Aberration-corrected scanning transmission electron microscopy (STEM) was performed on a JEM-ARM200F microscope with CEOS CESCOR and CEOS CETCOR hexapole aberration correctors for probe and image forming lenses, respectively, and a cold field emission gun (CFEG). STEM images were recorded with a JEOL annular dark-field (ADF) detector. Prior to the measurements, the powdered material was drop deposited on a silica oxide coated gold TEM grid. Prior to the ADF-STEM analysis some particles were oriented along the crystallographic c-axis. In case of secure transfer imaging Gatan single tilt vacuum transfer holder VTST4006 was used.

EFTEM mapping

EFTEM data were collected with Gatan Imaging Filter (Quantum) CCD camera with applying a monochromator slit of 10eV width for zero-loss collection. Thickness maps were obtained from the ratio of unfiltered and zero-loss maps and further color enhanced for clarity.

EDX

The elemental analysis was performed using a high angle silicon drift EDX detector with the solid angle up to 0.98 steradians from a detection area of 100mm^2. EDX maps and spectra were collected using Gatan Digital Micrograph software.

ODE

The catalytic tests were carried on using the Taniwha reactor described elsewhere.[39] Initial reaction gas mixture was (C_2H_6:O_2:N_2 3:6:91) with the total flow of 7 ml/min and 40 mg catalyst loading (diluted with SiC in order to avoid local overheating, as described in [39]). The reaction products were finally detected by Agilent 6890 gas chromatograph. Firstly the model reaction was carried on to determine the conversion of ethane dependence on the reaction temperature. After the temperature determination the outlet of the Taniwha reactor was coupled with the inlet of the microreactor in order to expose the catalyst loaded on the TEM grid to the reactants and products mixture (See Scheme S6-1). For the ILI $(Mo,V)O_x$ was deposited on the amorphous SiO_2 covered gold grid, while M1-type $(Mo,V,Te,Nb)O_x$ on the amorphous SiN_3 TEM window.

The ODE reaction for structure response measurements was carried for 12h for 2 different ethane conversions - first 20% and then 30% for both orthorhombic $(Mo,V)O_x$ and M1-type $(Mo,V,Te,Nb)O_x$. Structural changes were monitored after each treatment.

The conversion X_{R_i} in the catalytic reaction was calculated product-based:

$$X_R = \frac{\sum_j (\Delta C_{P_j})}{C_{R_0}} \tag{1}$$

$$S_{P_j} = \frac{\Delta C_{P_j}}{\sum_j \Delta C_{P_j}} \tag{2}$$

where R_i and P_j are reactants and products, C_x is the amount of carbon in mol corresponding to the compound x, 0 corresponds to the reactants mixture and Δ marks the difference between products and reactants mixture.

6.7 References

1.   Heterogeneous Catalysis. In *Modern Heterogeneous Catalysis*, Wiley-VCH Verlag GmbH & Co. KGaA: 2017; pp 1-13.

2.   Davis, B. H., Development of the Science of Catalysis. In *Handbook of Heterogeneous Catalysis*, Wiley-VCH Verlag GmbH & Co. KGaA: 2008.

3.   Dumesic, J. A.; Huber, G. W.; Boudart, M., Principles of Heterogeneous Catalysis. In *Handbook of Heterogeneous Catalysis*, Wiley-VCH Verlag GmbH & Co. KGaA: 2008.

4.   Amakawa, K.; Kolen'ko, Y. V.; Villa, A.; Schuster, M. E.; Csepei, L.-I.; Weinberg, G.; Wrabetz, S.; Naumann d'Alnoncourt, R.; Girgsdies, F.; Prati, L.; Schlögl, R.; Trunschke, A., Multifunctionality of Crystalline MoV(TeNb) M1 Oxide Catalysts in Selective Oxidation of Propane and Benzyl Alcohol. *ACS Catal.* **2013,** *3* (6), 1103-1113.

5.   Vendelbo, S. B.; Elkjær, C. F.; Falsig, H.; Puspitasari, I.; Dona, P.; Mele, L.; Morana, B.; Nelissen, B. J.; van Rijn, R.; Creemer, J. F.; Kooyman, P. J.; Helveg, S., Visualization of oscillatory behaviour of Pt nanoparticles catalysing CO oxidation. *Nat. Mater.* **2014,** *13* (9), 884-890.

6.   Ek, M.; Ramasse, Q. M.; Arnarson, L.; Georg Moses, P.; Helveg, S., Visualizing atomic-scale redox dynamics in vanadium oxide-based catalysts. *Nature Communications* **2017,** *8* (1), 305.

7.   Schlögl, R., Heterogeneous Catalysis. *Angew. Chem., Int. Ed.* **2015,** *54* (11), 3465-3520.

8.   Equilibrium Thermodynamics. In *Physics of Surfaces and Interfaces*, Ibach, H., Ed. Springer Berlin Heidelberg: Berlin, Heidelberg, 2006; pp 149-205.

9.   Ren, T.; Patel, M.; Blok, K., Olefins from conventional and heavy feedstocks: Energy use in steam cracking and alternative processes. *Energy* **2006,** *31* (4), 425-451.

10.   Amghizar, I.; Vandewalle, L. A.; Van Geem, K. M.; Marin, G. B., New Trends in Olefin Production. *Engineering* **2017,** *3* (2), 171-178.

11.   Cavani, F.; Ballarini, N.; Cericola, A., Oxidative dehydrogenation of ethane and propane: How far from commercial implementation? *Catal. Today* **2007,** *127* (1), 113-131.

12.   Cavani, F.; Trifirò, F., The oxidative dehydrogenation of ethane and propane as an alternative way for the production of light olefins. *Catal. Today* **1995,** *24* (3), 307-313.

13.   Konya, T.; Katou, T.; Murayama, T.; Ishikawa, S.; Sadakane, M.; Buttrey, D.; Ueda, W., An orthorhombic Mo_3VO_x catalyst most active for oxidative dehydrogenation of ethane among related complex metal oxides. *Catal. Sci. Technol.* **2013,** *3* (2), 380-387.

14.   Védrine, J., *Heterogeneous Partial (amm)Oxidation and Oxidative Dehydrogenation Catalysis on Mixed Metal Oxides*. 2016; Vol. 6, p 22.

15.   Botella, P.; Dejoz, A.; Abello, M. C.; Vázquez, M. I.; Arrúa, L.; López Nieto, J. M., Selective oxidation of ethane: Developing an orthorhombic phase in Mo–V–X (X = Nb, Sb, Te) mixed oxides. *Catal. Today* **2009,** *142* (3–4), 272-277.

16.   Ishikawa, S.; Goto, Y.; Kawahara, Y.; Inukai, S.; Hiyoshi, N.; Dummer, N. F.; Murayama, T.; Yoshida, A.; Sadakane, M.; Ueda, W., Synthesis of Crystalline Microporous Mo–V–Bi Oxide for Selective (Amm)Oxidation of Light Alkanes. *Chem. Mater.* **2017,** *29* (7), 2939-2950.

17.   Ishikawa, S.; Kobayashi, D.; Konya, T.; Ohmura, S.; Murayama, T.; Yasuda, N.; Sadakane, M.; Ueda, W., Redox Treatment of Orthorhombic $Mo_{29}V_{11}O_{112}$ and Relationships between Crystal Structure, Microporosity and Catalytic Performance for Selective Oxidation of Ethane. *J. Phys. Chem. C* **2015,** *119* (13), 7195-7206.

18.   Grasselli, R., Fundamental Principles of Selective Heterogeneous Oxidation Catalysis. *Top. Catal.* **2002,** *21* (1-3), 79-88.

19.   Vogt, T.; Blom, D. A.; Jones, L.; Buttrey, D. J., ADF-STEM Imaging of Nascent Phases and Extended Disorder Within the Mo–V–Nb–Te–O Catalyst System. *Top. Catal.* **2016,** *59*, 1489–1495.

20.   Pyrz, W. D.; Blom, D. A.; Sadakane, M.; Kodato, K.; Ueda, W.; Vogt, T.; Buttrey, D. J., Atomic-level imaging of Mo-V-O complex oxide phase intergrowth, grain boundaries, and defects using HAADF-STEM. *P Natl Acad Sci USA* **2010,** *107* (14), 6152-6157.

21.   Masliuk, L.; Heggen, M.; Noack, J.; Girgsdies, F.; Trunschke, A.; Hermann, K. E.; Willinger, M.-G.; Schloegl, R.; Lunkenbein, T., Structural Complexity in Heterogeneous Catalysis: Cataloging Local Nano-Structures. *The Journal of Physical Chemistry C* **2017,** *121* (43), 24093-24103.

22.   He, Q.; Woo, J.; Belianinov, A.; Guliants, V. V.; Borisevich, A. Y., Better Catalysts through Microscopy: Mesoscale M1/M2 Intergrowth in Molybdenum-Vanadium Based Complex Oxide Catalysts for Propane Ammoxidation. *ACS Nano* **2015,** *9* (4), 3470-3478.

23.   Nguyen, T. T.; Deniau, B.; Baca, M.; Millet, J. M. M., Influence of Nb Content on the Structure, Cationic and Valence Distribution and Catalytic Properties of MoVTe(Sb)NbO M1 Phase Used as Catalysts for the Oxidation of Light Alkanes. *Top. Catal.* **2016,** *59* (17-18), 1496-1505.

24.   Aouine, M.; Epicier, T.; Millet, J. M. M., In Situ Environmental STEM Study of the MoVTe Oxide M1 Phase Catalysts for Ethane Oxidative Dehydrogenation. *ACS Catal.* **2016,** *6* (7), 4775-4781.

25.   Valente, J. S.; Armendáriz-Herrera, H.; Quintana-Solórzano, R.; Del Ángel, P.; Nava, N.; Massó, A.; López Nieto, J. M., Chemical, structural, and morphological changes of a MoVTeNb catalyst during oxidative dehydrogenation of ethane. *ACS Catal.* **2014,** *4* (5), 1292-1301.

26.   Zhu, Y.; Sushko, P. V.; Melzer, D.; Jensen, E.; Kovarik, L.; Ophus, C.; Sanchez-Sanchez, M.; Lercher, J. A.; Browning, N. D., Formation of Oxygen Radical Sites on MoVNbTeOx by Cooperative Electron Redistribution. *J Am Chem Soc* **2017,** *139* (36), 12342-12345.

27.   Hävecker, M.; Wrabetz, S.; Kröhnert, J.; Csepei, L.-I.; Naumann d'Alnoncourt, R.; Kolen'ko, Y. V.; Girgsdies, F.; Schlögl, R.; Trunschke, A., Surface chemistry of phase-pure M1 MoVTeNb oxide during operation in selective oxidation of propane to acrylic acid. *J. Catal.* **2012,** *285* (1), 48-60.

28.   Trunschke, A.; Noack, J.; Trojanov, S.; Girgsdies, F.; Lunkenbein, T.; Pfeifer, V.; Hävecker, M.; Kube, P.; Sprung, C.; Rosowski, F.; Schlögl, R., The Impact of the Bulk Structure on Surface Dynamics of Complex Mo–V-based Oxide Catalysts. *ACS Catal.* **2017,** *7* (4), 3061-3071.

29.   Malladi, S. R. K.; Tichelaar, F. D.; Xu, Q.; Wu, M. Y.; Terryn, H.; Mol, J. M. C.; Hannour, F.; Zandbergen, H. W., Quasi in situ analytical TEM to investigate electrochemically induced microstructural changes in alloys: AA2024-T3 as an example. *Corrosion Science* **2013,** *69* (0), 221-225.

30.   A. Crozier, P., *Nanocharacterization of Heterogeneous Catalysts by Ex Situ and In Situ STEM*. 2011; p 537-582.

31.   Qing-Hua, Z.; Dong-Dong, X.; Lin, G., Aberration-corrected scanning transmission electron microscopy for complex transition metal oxides. *Chin. Phys. B* **2016,** *25* (6), 066803.

32.   DeSanto, P.; Buttrey, D. J.; Grasselli, R. K.; Lugmair, C. G.; Volpe, A. F.; Toby, B. H.; Vogt, T., Structural characterization of the orthorhombic phase M1 in MoVNbTeO propane ammoxidation catalyst. *Top. Catal.* **2003**, *23* (1-4), 23-38.

33.   Murayama, H.; Vitry, D.; Ueda, W.; Fuchs, G.; Anne, M.; Dubois, J. L., Structure characterization of orthorhombic phase in MoVTeNbO catalyst by powder X-ray diffraction and XANES. *Appl. Catal., A* **2007**, *318* (0), 137-142.

34.   DeSanto, P.; Buttrey, D. J.; Grasselli, R. K.; Lugmair, C. G.; Volpe, A. F.; Toby, B. H.; Vogt, T., Structural aspects of the M1 and M2 phases in MoVNbTeO propane ammomidation catalysts. *Z. Kristallogr.* **2004**, *219* (3), 152-165.

35.   Pyrz, W. D.; Blom, D. A.; Vogt, T.; Buttrey, D. J., Direct imaging of the MoVTeNbO M1 phase using an aberration-corrected high-resolution scanning transmission electron microscope. *Angewandte Chemie-International Edition* **2008**, *47* (15), 2788-2791.

36.   Ueda, W.; Vitry, D.; Kato, T.; Watanabe, N.; Endo, Y., Key aspects of crystalline Mo-V-O-based catalysts active in the selective oxidation of propane. *Res Chem Intermediat* **2006**, *32* (3-4), 217-233.

37.   Ishikawa, S.; Ueda, W., Microporous crystalline Mo-V mixed oxides for selective oxidations. *Catalysis Science and Technology* **2016**, *6* (3), 617-629.

38.   Garlow, J. A.; Barrett, L. K.; Wu, L.; Kisslinger, K.; Zhu, Y.; Pulecio, J. F., Large-Area Growth of Turbostratic Graphene on Ni(111) via Physical Vapor Deposition. *Scientific Reports* **2016**, *6*, 19804.

39.   Cotter, T. P.; referee: Thomas, A.; referee: Schomäcker, R.; referee: Schlögl, R.; referee: Christmann, K. The reducibility of mixed Mo/V oxide materials to carbides and their reactivity in the activation of propane. phd, Technische Universität, Berlin, 2011.

40.   Ueda, W., Establishment of Crystalline Complex Mo-V-Oxides as Selective Oxidation Catalysts. *J. Jpn. Petrol. Inst.* **2013**, *56* (3), 122-132.

41.   Sadakane, M.; Watanabe, N.; Katou, T.; Nodasaka, Y.; Ueda, W., Crystalline Mo_3VO_x Mixed-Metal-Oxide Catalyst with Trigonal Symmetry. *Angew. Chem.* **2007**, *119* (9), 1515-1518.

42.   Lin, M. M., Selective oxidation of propane to acrylic acid with molecular oxygen. *Appl Catal a-Gen* **2001**, *207* (1-2), 1-16.

43.   Shannon, R., Revised effective ionic radii and systematic studies of interatomic distances in halides and chalcogenides. *Acta Crystallographica Section A* **1976**, *32* (5), 751-767.

44.   Amakawa, K.; Sun, L. L.; Guo, C. S.; Havecker, M.; Kube, P.; Wachs, I. E.; Lwin, S.; Frenkel, A. I.; Patlolla, A.; Hermann, K.; Schlogl, R.; Trunschke, A., How Strain Affects the Reactivity of Surface Metal Oxide Catalysts. *Angewandte Chemie-International Edition* **2013,** *52* (51), 13553-13557.

45.   Gorter, E. W., Classification, representation and prediction of crystal structures of ionic compounds. *Journal of Solid State Chemistry* **1970,** *1* (3), 279-305.

46.   Zhao, L.; Chiu, C.-c.; Genest, A.; Rösch, N., DFT cluster model study of MoVO-type mixed-metal oxides. *Computational and Theoretical Chemistry* **2014,** *1045* (0), 57-65.

47.   Pacchioni, G., Numerical Simulations of Defective Structures: The Nature of Oxygen Vacancy in Non-reducible (MgO, SiO2, ZrO2) and Reducible (TiO2, NiO, WO3) Oxides. In *Defects at Oxide Surfaces*, Jupille, J.; Thornton, G., Eds. Springer International Publishing: Cham, 2015; pp 1-28.

6.8 Supporting information
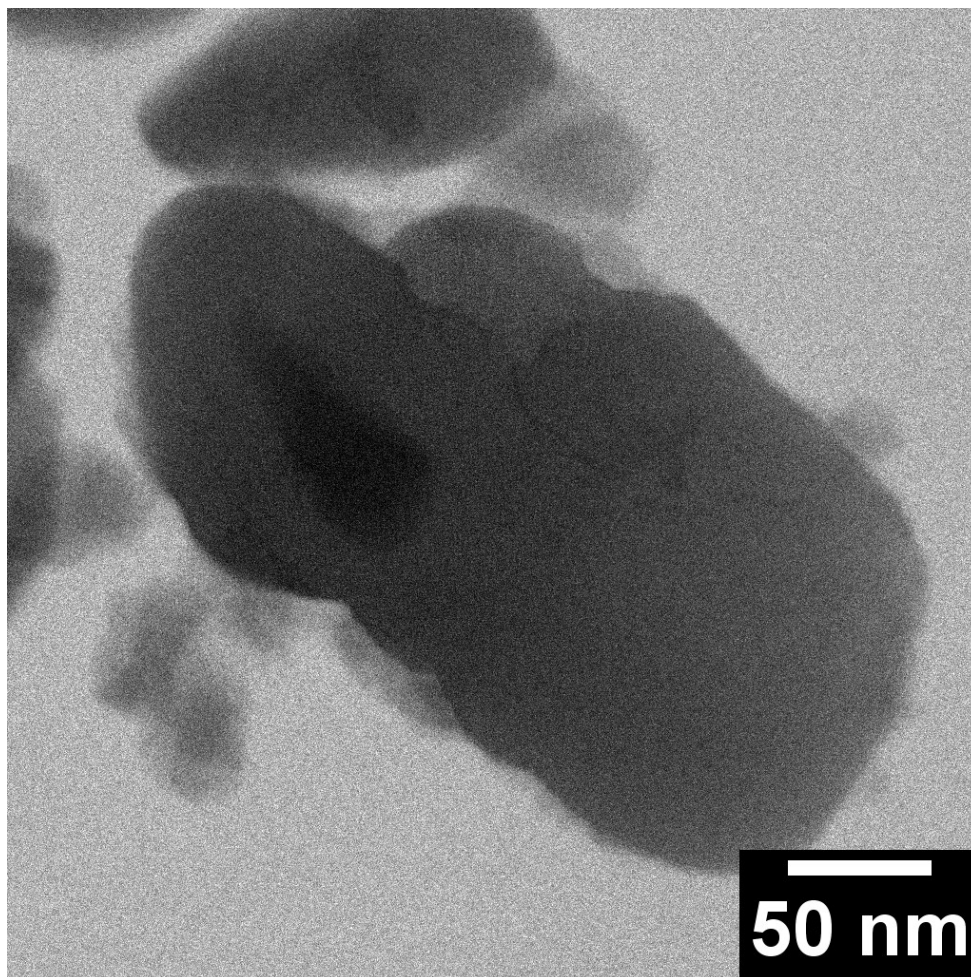
Figure S 6-1: Raw BF-STEM image of corresponding to Figure 6-3a.
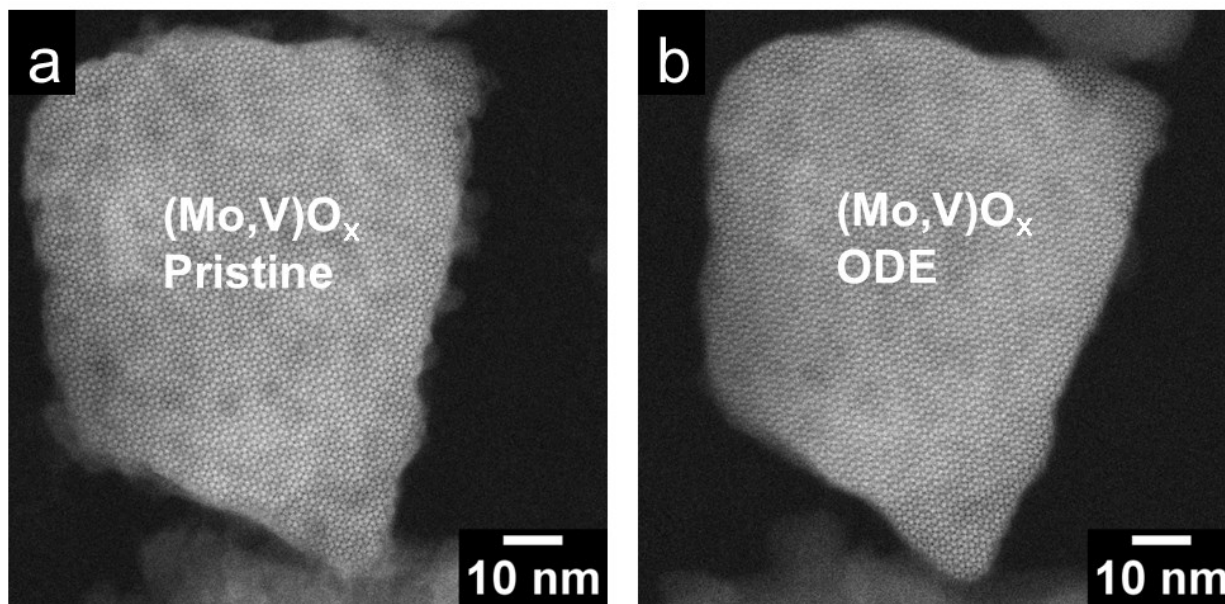
Figure S6-2: Overview identical location ADF-STEM images of the before (a) and after (b) ODE at 20% ethane conversion..
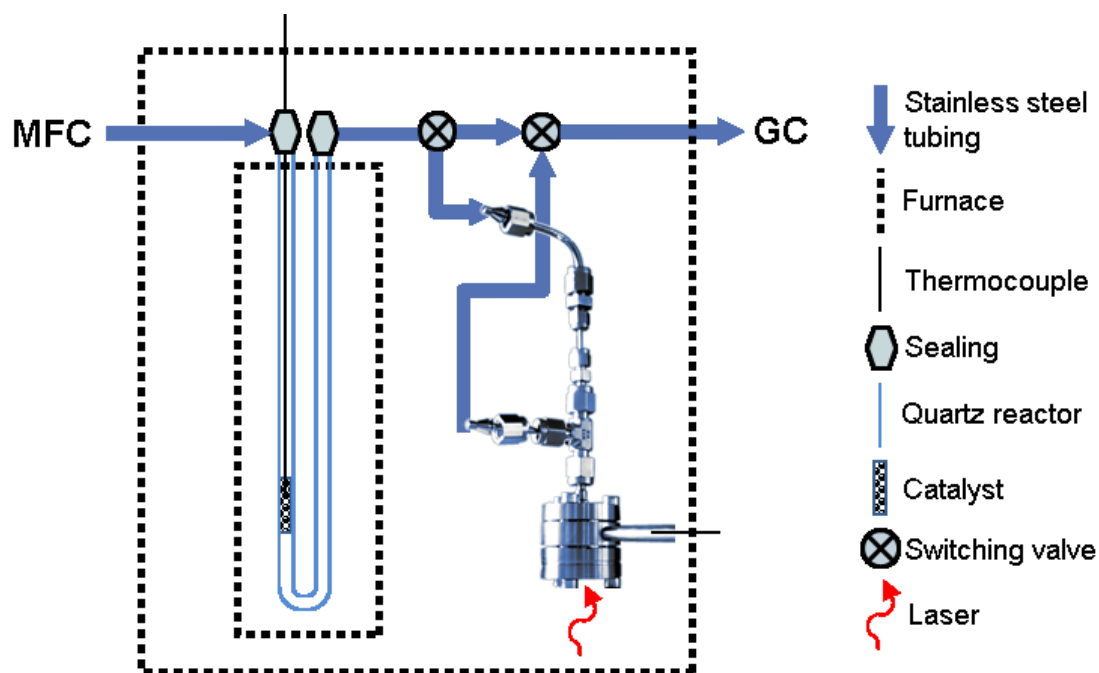
Scheme S6-1: Fixed bed reactor and TEM grid microreactor connection.

7 Conclusions

In this work the relationship between flexibility of the structure of the catalysts and performance of the catalysts was addressed using orthorhombic $(Mo,V)O_x$ and M1-type $(Mo,V,Te,Nb)O_x$ as model catalysts. The study was carried out by applying a specially designed TEM grid reactor, which was combined with *quasi in-situ* identical location imaging (ILI). The detailed analysis included the investigations of the structures or compositions of the pristine catalysts, exposure of the catalysts on the TEM grid to the desired relevant catalytic conditions and subsequent imaging of the identical locations of the samples after the reaction.

A plethora of geometric connectivities, which differ from the ideal crystallographic bulk structures of orthorhombic $(Mo,V)O_x$, were identified by scanning transmission electron microscopy (STEM). The concept of tiling was applied to identify and classify these connectivities. Local structural motifs as well as extended defects were detected. Local structural motifs were further classified as linear and triangular, depending on the structural connectivities of the pentagonal building blocks. Linear motifs lack or exhibit displaced linker sites between the pentagonal building blocks, while triangular motifs are characterized by trigonal arrangements of pentagonal building blocks similar to those that can be observed, for instance, in trigonal $(Mo,V)O_x$. The extended defects in the examined orthorhombic $(Mo,V)O_x$ are classified as intergrown phases, interstitial regions, extended surface defects, and (dis)inclinations. The structural arrangements, which were observed in orthorhombic $(Mo,V)O_x$, and their occurrence were summarized in a catalogue.

The examined M1-type $(Mo,V,Te,Nb)O_x$ exhibited only two kinds of extended defects: aperiodic intergrowth and dislocation. In addition, the surface of orthorhombic $(Mo,V)O_x$ is relatively rough and partially covered by single local motifs or complex arrangements of these motifs, while the surface of M1-type $(Mo,V,Te,Nb)O_x$ is rather smooth and defect-free. The main differences between the surface terminations of orthorhombic $(Mo,V)O_x$ and M1-type $(Mo,V,Te,Nb)O_x$ are linked to the occupation of structural channels, which seems to influence the flexibility of the surface-near bulk framework and preferred arrangements at the surface.

STEM imaging combined with electron energy loss spectroscopy (EELS) investigation of orthorhombic $(Mo,V)O_x$ have demonstrated local variations of the metal cations content. These variations both included local inhomogeneities related to the structure of the unit cell and

differences between the bulk structure and extended defects. The content of the metal cations in the intergrown areas was further correlated with their internal structure. While both Mo-rich and V-rich surface facets were detected, Mo enrichment can be considered as a preferential trend for the examined orthorhombic $(Mo,V)O_x$. Different enrichments can be attributed to the structures of the facets.

Model experiments were conducted to show the potential of *quasi in-situ* ILI studies using the TEM grid reactor for investigations of structure changes of the catalysts induced by the reaction under relevant conditions at the nanoscale. Thermal decomposition of lead carbonate was used to confirm the precise calibration of the temperature and reductive activation of $Cu/ZnO/Al_2O_3$ catalyst was used to show the possibility to transfer the sample between the reactor and the electron microscope without exposure to the ambient air. Catalytic conversion and structure changes at the nanoscale were detected for CO oxidation reaction over Pt foil and Pt nanoparticles.

The structure responses of orthorhombic $(Mo,V)O_x$ to different conditions were examined by *in-situ* and *quasi in-situ* ILI. Similarities of the structure responses to *in-situ* thermal treatment in high vacuum and *quasi in-situ* thermal treatment in N_2 suggested the mechanisms of the structure response to (mild) reducing conditions. The mechanisms include migration of metal cations into surface-near structural channels and the structural rearrangement towards the formation of potentially oxygen-deficient structural motifs. These rearrangements can include local strain or degradation of the surface-near orthorhombic bulk structure. Further *quasi in-situ* investigation of the structure response to the conditions relevant for the oxidative dehydrogenation of ethane (ODE) reaction has confirmed at least a partial reversibility of the structure rearrangements. Several differences between the structure responses observed *in-situ* and *quasi in-situ* validate the additional benefit of the TEM grid reactor approach as it allow for avoiding the pressure gap related effects.

A correlation between activities and adaptabilities of the catalysts was investigated by *quasi in-situ* ILI of the orthorhombic $(Mo,V)O_x$ and M1-type $(Mo,V,Te,Nb)O_x$ using ODE as a model reaction. The relevant mixture of the reactants and products for this investigation was obtained by coupling a fixed bed reactor and the TEM grid reactor. Orthorhombic $(Mo,V)O_x$ have exhibited high activity and a pronounced structure response even at 300°C. M1-type $(Mo,V,Te,Nb)O_x$ was activated over 350°C and remained almost unchanged even at 420°C. The

differences between the structure responses of orthorhombic $(Mo,V)O_x$ and M1-type $(Mo,V,Te,Nb)O_x$ are linked to the flexibility of the bulk framework, which seems to be determined by the occupation of the structural channels.

In conclusion, the study introduces a method for detecting structure responses of heterogeneous catalysts under relevant reaction conditions, which can unravel the mechanisms of the structure responses and can provide a way towards prospective tailoring of catalysts to obtain the desired activity and lifetime.

List of figures

168

List of supporting figures

List of tables

List of schemes

List of abbreviations

- o ABF – Annular bright field
- o AcrA – Acrylic acid
- o ADF – Annular dark field
- o BF – Bright field
- o EDX– Energy dispersive X-ray spectroscopy
- o EELS – Electron energy loss spectroscopy
- o EFTEM – Energy filtered TEM
- o ETEM – Environmental TEM
- o GC – Gas chromatograph
- o HAADF – High angle annular dark field
- o HRTEM – High resolution TEM
- o ILI – Identical location imaging
- o MEMS – Microelectromechanical system
- o ODE – Oxidative dehydrogenation of ethane
- o ODH – Oxidative dehydrogenation
- o PTR-MS – Proton transfer reaction mass spectrometer
- o STEM – Scanning TEM
- o TEM – Transmission electron microscopy
- o XPS – X-ray Photoelectron Spectroscopy
- o XRD – X-ray diffraction
- o XRF – X-ray Fluorescence Spectroscopy